Study of the exosphere of Mercury with the PHEBUS spectrograph on the BepiColombo mission

Rozenn Robidel

université PARIS-SACLAY

Study of the exosphere of Mercury with the PHEBUS spectrograph on the BepiColombo mission

Étude de l'exosphère de Mercure par le spectromètre PHEBUS de la mission BepiColombo

Thèse de doctorat de l'université Paris-Saclay

École doctorale n°127 : Astronomie et Astrophysique d'Île-de-France (AAIF)
Spécialité de doctorat: Astronomie et Astrophysique
Graduate School : Physique. Référent : Université de Versailles-Saint-Quentin-en-Yvelines

Thèse préparée dans l'unité de recherche **LATMOS (Université Paris-Saclay, CNRS)**, sous la direction de **Eric QUEMERAIS**, Directeur de recherche, et le co-encadrement de **Dimitra KOUTROUMPA**, Chargée de recherche

Thèse soutenue à Guyancourt, le 25 septembre 2023, par

Rozenn ROBIDEL

Composition du jury

Membres du jury avec voix délibérative

Karine BOCCHIALINI Professeure des universités, Université Paris-Saclay, IAS	Présidente
Nicolas ANDRE Chargé de recherche CNRS, HDR, Université Toulouse III - Paul Sabatier, IRAP	Rapporteur & Examinateur
Carl SCHMIDT Associate Professor, Boston University, Center for Space Physics	Rapporteur & Examinateur
Dominique DELCOURT Directeur de recherche CNRS, Université d'Orléans, LP2CE	Examinateur

THESE DE DOCTORAT

NNT : 2023UPASP074

université PARIS-SACLAY

ÉCOLE DOCTORALE
Astronomie
et Astrophysique
d'Île-de-France (AAIF)

Titre: Etude de l'exosphère de Mercure par le spectromètre PHEBUS de la mission BepiColombo
Mots clés: exosphère, Mercure, visible, spectroscopie, BepiColombo

Résumé: Mercure est la planète tellurique la moins explorée du système solaire, trois missions seulement l'ont survolée. Mariner 10 a effectué trois survols de la planète en 1974 et 1975, découvrant une atmosphère très mince, similaire à celle de la Lune, contenant de l'hélium (He) et de l'hydrogène (H). Le sodium (Na), le potassium (K) et le calcium (Ca) ont été détectés plus tard à partir d'observations depuis la Terre. La mission MESSENGER, lancée en 2004, a non seulement survolé Mercure à trois reprises mais a également orbité la planète durant quatre ans. Elle a détecté deux nouvelles espèces, le magnésium (Mg) et le manganèse (Mn). En parallèle, deux autres espèces ont été découvertes grâce à des observations depuis la Terre : le fer (Fe) et l'aluminium (Al).

BepiColombo est la troisième mission à destination de Mercure. Lancée en 2018, la mission conjointe ESA-JAXA doit effectuer six survols de Mercure avant de s'insérer en orbite fin 2025. Trois survols de Mercure ont déjà été réalisés lors desquels PHEBUS (Probing the Hermean Exosphere By Ultraviolet Spectroscopy) a pu observer l'exosphère de Mercure. L'instrument est composé de deux détecteurs UV (EUV et FUV) et de deux canaux visibles (c404 et c422). Le canal c404 est dédié à la ligne d'émission du K à 404,7 nm tandis que le canal c422 est dédié à la ligne d'émission du Ca à 422,8 nm.

La géométrie d'observation des deux premiers survols est similaire, la sonde approchant la planète côté nuit, traversant son ombre avant de se diriger côté jour. La sonde s'est approchée à ∼200 km de la surface au point le plus proche côté nuit. PHEBUS pointait vers le nord, dans une direction opposée au soleil.

Le taux de comptage enregistré par les deux canaux visibles illustre la géométrie d'observation, notamment le passage dans l'ombre de Mercure. Le maximum est atteint peu après la sortie d'éclipse. Le taux de comptage diminue ensuite à mesure que la sonde s'éloigne de Mercure. Lors des survols, les signaux des deux canaux sont pollués par des pics sporadiques dont l'origine reste incertaine.

Malgré ces pics, le canal c422 a clairement détecté du Ca. Le signal c422 montre non seulement une concentration de Ca à l'aube mais également une couronne de Ca très étendue du côté matin qui n'a pas été rapportée par MESSENGER. La hauteur d'échelle déduite de nos profils (2500-2800 km) est en accord avec la valeur rapportée par MESSENGER à un angle d'anomalie vraie similaire. En utilisant le modèle de Chamberlain, j'ai déterminé une température à l'exobase très élevée (>50 000 K), ce qui est en accord avec les résultats de MESSENGER. La grande hauteur d'échelle et la température à l'exobase élevée impliquent un processus de libération très énergétique. Les données semblent également indiquer une asymétrie jour/nuit qui pourrait signifier que la source de Ca est principalement du côté jour ou être la conséquence d'un décalage de la source de Ca par rapport à la région de l'aube. La prochaine étape consiste à utiliser un modèle exosphérique 3D prenant en compte la photoionisation et la distribution non uniforme du Ca. Enfin, le pointage de PHEBUS lors de ces deux premiers survols n'a pas permis d'observer la potentielle composante froide du Ca puisque les altitudes <200 km n'ont pas été explorées.

Le canal c404 a détecté une ou plusieurs espèces à basse altitude côté matin lors des survols, potentiellement du K ou du Mn. Cette ligne d'émission du K n'a jamais été détectée par MESSENGER. Quant au Mn, MESSENGER ne l'a pas observé continuellement, il n'a été détecté qu'à certaines saisons et dans certaines régions de l'exosphère. Ces conditions de détection sont bien différentes de celles de BepiColombo. Il est donc difficile d'identifier avec certitude l'espèce détectée. D'autres observations sont nécessaires. On peut tout de même mentionner que l'échelle de hauteur déduite du profil c404 est ∼135 km et que le modèle de Chamberlain appliqué au profil c404 semble indiquer une température à l'exobase <3000 K.

université PARIS-SACLAY
ÉCOLE DOCTORALE
Astronomie
et Astrophysique
d'Île-de-France (AAIF)

Title: Study of the exosphere of Mercury with the PHEBUS spectrograph on the BepiColombo mission

Keywords: exosphere, Mercury, visible, spectroscopy, BepiColombo

Abstract: Mercury is the least explored of the inner planets, only three spacecraft have explored it. Mariner 10 observed the planet during three close encounters in 1974 and 1975, unveiling a very thin atmosphere surrounding the planet, somewhat similar to that of the Moon, including hydrogen (H) and helium (He). Sodium (Na), potassium (K) and calcium (Ca) were later detected in Mercury's exosphere with ground-based telescopes. The MESSENGER mission, launched in 2004, not only performed three close encounters of the planet but also orbited it for four years. The mission added magnesium (Mg) and manganese (Mn) to the list of species detected in Mercury's exosphere. Iron (Fe) and aluminum (Al) were also discovered from ground-based observations around the same period.

BepiColombo is the third mission to visit Mercury. Launched in 2018, the ESA-JAXA joint mission is set to perform six flybys of Mercury before the insertion in orbit around the planet at the end of 2025. Three flybys of Mercury have already been performed, during which PHEBUS (Probing the Hermean Exosphere By Ultraviolet Spectroscopy) was able to observe the surface-bounded exosphere of Mercury. The instrument consists of two UV detectors (EUV and FUV) and two visible channels (c404 and c422). The c404 channel is dedicated to the K emission line at 404.7 nm while the c422 channel is dedicated to the Ca emission line at 422.8 nm.

The geometry of observation was similar during the first two flybys, the spacecraft approaching the planet from its nightside, crossing its shadow before moving to its dayside. The closest approach to the surface occurred in the shadow of Mercury at an altitude of ∼200 km. PHEBUS was pointing northward, slightly antisunward.

The count rate registered by both channels depicts the geometry of observation, notably the transit in the shadow of Mercury. The maximum is reached shortly after the spacecraft went out of eclipse. The count rate then decreases as the spacecraft moved away from Mercury. During the flybys, both signals are polluted by sporadic spikes whose origin remains uncertain.

Despite these spikes, Ca was clearly detected by the c422 channel. The c422 signal shows not only an enhancement of Ca at dawn but also a very extensive Ca corona on the morning side, which was not reported by MESSENGER. The scale height deduced from our Ca profiles (2,500–2,800 km) is in agreement with the value reported by MESSENGER at similar true anomaly angle. Using the Chamberlain model, I determined a high temperature at the exobase (>50,000 K), in agreement with MESSENGER results. Both the large scale height and temperature at the exobase imply a very energetic release process. I also report a day/night asymmetry in the Ca exosphere that could indicate that the source of Ca is predominantly on the dayside or be the consequence of a shift of the main source of Ca away from the dawn region. The next step consists in using a 3D exospheric model that will include the effects of photoionization and non-uniform distribution of Ca. Finally, PHEBUS pointing during the flybys did not allow to observe the potential cold component of Ca as the altitudes <200 km were not explored.

The c404 channel detected species at low altitudes on the morning side during the flybys, potentially K or Mn. This K emission line was never detected by MESSENGER. As for Mn, MESSENGER has not observed it continuously, its detection was confined to certain seasons and to certain regions of the exosphere. These detection conditions are very different from those of BepiColombo. It is therefore difficult to identify with certainty the detected species. Further observations are necessary. Note that the scale height deduced from the c404 profile is ∼135 km and that the Chamberlain model applied to the c404 profile seems to indicate a temperature at the exobase <3000 K.

À mes mamies

Acknowledgments

Realizing my thesis is coming to an end, I feel nostalgic. Those three years have passed so quickly! I would like to thank everyone who helped me during my PhD, starting with my supervisors, Éric Quémerais and Dimitra Koutroumpa. Thank you for entrusting me with this thesis. I am grateful I was able to discover Mercury and its environment thanks to you. Thank you for welcoming me to the PHEBUS team. It is one thing to process the data of an instrument, it is another to program the operations and deal with anomalies! Thank you for your involvement, your knowledge sharing and perpetual enriching discussions! And thank you Dimitra for always providing me with coffee after lunch!

I also want to thank the PHEBUS team. Jean-Yves Chaufray, thank you for your availability, for your constructive ideas and suggestions. Also, Jira and SPOT are all yours now! Special thanks to Aurélie Reberac, who has always taken the time to answer my incessant questions about PHEBUS and all the related tools. Thank you for your patience! Thanks also to Abdeladim El Aoumari for taking over from time to time. I was delighted to be the 'tester' of the PHEBUS tools! Thanks to Benjamin Lustrement for presenting me (the twin of) PHEBUS in the clean room, it is nice to see the models but it is even better to see it in real life! François Leblanc, thank you for following this thesis from a distance and for your always accurate and relevant questions and advice.

There are two people without whom this thesis would never have happened: Gabriel Tobie and Stéphane Le Mouélic. I enjoyed working with you on Cassini/VIMS data during my final-year internship, your passion is truly communicative. You made me want to become a researcher. For that, I would like to express my deepest gratitude. I take this opportunity to thank Corentin Buti because without your internship at LPG, I would not have done mine afterwards! Nicolas Altobelli and Claire Vallat, you are also a big part of this! I am very happy I will be able to work alongside you at ESAC for the next two years!

Speaking of ESAC, I would like to thank Sébastien Besse, Thomas Cornet and Inès Belgacem for their valuable advice when I applied to the ESA Fellowships.

Benoit Seignovert, a lot of my Python programming skills actually come from you, thank you for that! Also, it is always a pleasure to discuss with you and meet at conferences!

Special mention to the *Young Planetary Scientists* of LATMOS, to those who have passed, Loïc Rossi, Margaux Vals, Nicolas Oudart, Ashwin Braude, Aurélien Stcherbinine, and those who have arrived, Maélie Coutelier, Robin Sultana, Gwenaël Milcareck, Elise Knutsen, Lucile Conan, Koyena Das and all those who have come from time to time to the meetings! It was my pleasure to host these meetings! Thank you, Koyena, for taking over as organizer for the group meetings! Also, I loved chatting with you about k-dramas and Netflix shows, I wish you the very best for the last year of your PhD!

I would also like to adress a special mention to Ophélie Mcintosh: I was happy to share the (stressful) last weeks of preparation of defense with you!

Speaking of defense, I thank the members of my committee, Nicolas André, Karine Bocchialini, Dominique Delcourt and Carl Schmidt, for agreeing to be part of it. To my reviewers: Nicolas, thank you for your very detailed and thoughtful report. Carl, thank you for your interesting comments and suggestions: hopefully, I have answered your questions during the

defense!

Then, I would like to thank the BepiColombo mission members I met at conferences and SWT meetings, including Lina Hadid, Beatriz Sanchez-Cano, Sae Aizawa, Anna Milillo, Martina Moroni, Joe Zender, Jack Wright. Martina, I know your PhD is also coming to an end, so I wish you luck!

Finally, I would like to deeply thank my parents and sisters. Papa, Maman, thank you for your unfailing support, for encouraging me and allowing me to get the education I wanted (thank you Mum for questioning me about med school, it was clearly not the right choice for me!). Thank you for the coffee breaks (café, croissant?) when I was working from your home. Thank you Laura for being the best work from home colleague, even though you receive too many phone calls! Thank you Charlotte for the outings between 'Parisians', it is always a pleasure to come to your house to chat and relax a little after work!

And last but not least, Guillaume. Thank you for your unconditional love and support. Thank you for listening to me talk about my thesis over and over again, for reviewing my manuscript, for being my rehearsal audience, for your help when I was struggling with Python or Latex and most importantly for telling me that it is okay to take breaks sometimes!

Résumé long en français

L'exosphère de Mercure: découverte et précédentes observations

L'exosphère est une atmosphère très mince où la densité est si faible que les quelques atomes ou molécules qui la composent sont peu susceptibles d'entrer en collision les uns avec les autres. Dans le cas des corps ayant une atmosphère substantielle, comme Mars ou la Terre, l'exosphère est la couche supérieure de l'atmosphère. Dans le cas contraire, l'exosphère constitue la seule atmosphère.

La mission de la NASA Mariner 10 a découvert l'atmosphère très mince de Mercure lors de trois survols de la planète en 1974 et 1975. Son spectromètre UV a détecté de l'hydrogène et de l'hélium (Broadfoot et al., 1976). La détection d'oxygène suggérée par les données de Mariner 10 n'a jamais été confirmée. Le sodium et le potassium ont été détectés plus tard (Potter and Morgan, 1985, 1986) grâce à des observations effectuées depuis la Terre, tout comme le calcium (Bida et al., 2000). Durant les trois survols de Mercure effectués par la sonde MESSENGER, son instrument MASCS a découvert du magnésium (McClintock et al., 2009) et du calcium ionisé (Vervack et al., 2010). Le magnésium a par la suite été observé quasi-quotidiennement par MESSENGER/MASCS durant la phase orbitale (Merkel et al., 2017). Bida and Killen (2011) ont révélé la détection du fer et de l'aluminium grâce à des observations effectuées depuis la Terre. MESSENGER/MASCS n'a pas détecté de fer mais a confirmé la détection de l'aluminium (Vervack et al., 2016). Ces mêmes observations ont confirmé la présence de calcium ionisé et ont révélé la présence de manganèse.

L'exosphère de Mercure est continuellement renouvelée soit par des sources externes telles que le vent solaire ou encore les météorites, ou par des particules libérées de la surface par différents processus (Wurz et al., 2022). Les principaux processus de libération comprennent la désorption thermique, la désorption stimulée par les photons et les électrons, la vaporisation par impact et la pulvérisation (Killen et al., 2018). D'autres processus (photoionisation, échappement gravitationnel, accélération due à la pression de radiation solaire) viennent contrebalancer ces processus sources et désemplissent l'exosphère.

BepiColombo, nouvelle mission à destination de Mercure

BepiColombo est la troisième mission à destination de Mercure. Lancée en octobre 2018, la mission conjointe de l'ESA et de la JAXA est actuellement en route vers Mercure et devrait se mettre en orbite autour de la planète en décembre 2025 (Benkhoff et al., 2021). BepiColombo est composé de deux sondes : MPO, dirigée par l'ESA, et MMO, dirigée par la JAXA. MPO contient 11 instruments dont PHEBUS. Cet instrument, développé au LATMOS, a pour objectif d'étudier l'exosphère de Mercure, sa composition et sa dynamique ainsi que ses interactions avec le vent solaire et la surface de la planète (Chassefière et al., 2010; Quémerais et al., 2020). PHEBUS est composé de deux détecteurs fonctionnant dans l'UV (EUV et FUV) et de deux canaux visibles (c404 et c422). Le canal c404 est dédié à la ligne d'émission du potassium à 404,7 nm tandis que le canal c422 est dédié à la ligne d'émission du calcium à 422,8 nm.

Description des observations de PHEBUS durant les survols de Mercure

Durant la phase de croisière, BepiColombo doit survoler Mercure à 6 reprises. Trois survols ont déjà eu lieu en octobre 2021, juin 2022 et juin 2023. Durant ces survols, PHEBUS a pu observer l'exosphère de Mercure avec ses différents détecteurs. Ce manuscrit de thèse se concentre sur les résultats des observations des canaux visibles c404 et c422 lors des deux premiers survols.

La géométrie d'observation des deux premiers survols est similaire, la sonde approchant la planète côté nuit, traversant son ombre avant de se diriger côté jour. La sonde s'est approchée à environ 200 km de la surface au point le plus proche côté nuit. PHEBUS pointait vers le nord, dans une direction opposée au soleil. Le taux de comptage enregistré par les deux canaux visibles illustre la géométrie d'observation des survols, notamment le passage dans l'ombre de Mercure. Le maximum est atteint peu après la sortie de l'ombre. Le taux de comptage diminue ensuite au fur et à mesure que la sonde s'éloigne de la planète. Lors des deux survols, le signal de chaque canal est pollué par des pics sporadiques lorsque la sonde est sortie de l'ombre de Mercure côté matin. Ces pics semblent être liés à la lumière réfléchie sur des particules (potentiellement issues du dégazage de la sonde). Malgré ces pics, le profil du canal c422 indique clairement la détection du calcium lors des deux survols. Le signal du c422 montre non seulement une concentration de calcium à l'aube, mais aussi une exosphère de calcium très étendue du côté matin qui n'a pas été rapportée par MESSENGER. En ce qui concerne le canal c404, le signal est moins intense et plus confiné. Bien qu'affecté par les pics, le signal indique la détection d'une ou plusieurs espèces à basse altitude du côté matin.

Analyse des données du canal c422 durant les deux premiers survols de Mercure

L'analyse des données commence par la correction du signal de différentes contributions parasites (courant d'obscurité, lumère zodiacale et contribution stellaire) pour extraire le signal exosphérique. Une fois le signal corrigé, je convertis le taux de comptage en unité scientifique (rayleigh), ce qui nécessite l'étalonnage des canaux visibles. La sensibilité d'un instrument peut être exprimée comme une surface efficace, qui est le produit de la surface d'entrée et de l'efficacité spectrale de l'instrument. J'ai utilisé les données de plusieurs campagnes d'observations stellaires pour calculer la surface efficace des deux canaux visibles.

Pour comparer nos résultats à ceux de MESSENGER, je me suis concentrée sur les données à basse altitude côté matin. J'ai appliqué une fonction exponentielle ayant comme paramètres la hauteur d'échelle et l'intensité à la surface. Les paramètres permettant d'ajuster au mieux le profil sont similaires d'un survol à l'autre. La hauteur d'échelle déduite est comprise entre 2500 et 2800 km pour les deux survols ce qui est en accord avec les valeurs déduites par Burger et al. (2014) pour un angle d'anomalie vraie similaire. Une telle hauteur d'échelle indique une exosphère chaude, ce qui est en accord avec les précédents études de l'exosphère de calcium (Bida et al., 2000, Killen et al., 2005, Burger et al., 2012, 2014).

J'ai ensuite appliqué un modèle de Chamberlain (Chamberlain, 1963) à ces mêmes données pour calculer la température et densité à l'exobase. Malgré les limitations physiques du modèle lorsqu'appliqué à Mercure, il permet de donner une estimation de la température afin de la comparer aux résultats précédents. La température à l'exobase déduite pour le côté matin à basse altitude est similaire d'un survol à l'autre et très élevée (>50 000 K), en accord avec les températures déduites par Burger et al. (2012, 2014) à partir des observations de MESSENGER en phase orbitale. Une température si élevée implique un processus source très énergétique. Le processus le plus couramment évoqué par la communauté pour expliquer une telle température est un processus en deux étapes: la calcium est libéré de la surface sous forme moléculaire

puis dissocié (Killen et al., 2005). Le processus à l'origine du calcium moléculaire serait la vaporisation par impact météoritique (Killen & Hahn, 2015). Le processus de dissociation du calcium moléculaire reste débattu (Killen, 2016).

Le couple de paramètres (densité et température à l'exobase) déduit de ces données à basse altitude côté matin ne s'ajuste ni aux données à haute altitude côté matin ni aux données basse altitude côté nuit. La différence entre les données haute et basse altitude côté matin peut s'expliquer par la photoionisation qui n'est pas prise en compte dans le modèle de Chamberlain mais joue un rôle important pour le calcium. Le calcium a en effet un court temps de vie de photoionisation (<1h) c'est-à-dire qu'il faut moins d'une heure pour qu'un atome de calcium soit photoionisé. La différence entre les données à basse altitude côté matin et côté nuit semble indiquer une asymétrie jour/nuit qui pourrait être liée à la source du calcium qui serait localisée principalement côté jour. Les atomes de calcium côté nuit seraient alors les atomes transportés depuis le côté jour qui n'ont pas encore été photoionisés. Une autre hyptohèse est que la source de calcium est légèrement décalée par rapport à l'aube (Pokorný et al., 2018).

Analyse des données du canal c404 durant les deux premiers survols de Mercure

Il est difficile d'identifier la ou les espèces détectées par le canal c404. Sa bande passante est assez large pour observer les lignes d'émission de l'aluminium (394,51 et 396,26 nm), du calcium ionisé (393,48 et 396,96 nm), du manganèse (403,19, 403,42 et 403,56 nm) et du potassium (404,52 et 404,83 nm). L'aluminium, le calcium ionisé et le manganèse ont tous les trois été observés par MESSENGER/MASCS (Vervack et al., 2016). En comparant les profils rapportés par MESSENGER/MASCS à ceux de PHEBUS, j'ai éliminé l'aluminium et le calcium ionisé. Concernant le manganèse, les profils de MESSENGER/MASCS et de BepiColombo/PHEBUS présentent tous les deux une décroissance exponentielle avec l'altitude. Les hauteurs d'échelle que j'ai déduites des profils issus des deux instruments sont similaires (entre 100 et 150 km). Toutefois, MESSENGER/MASCS n'a détecté le manganèse qu'à certaines saisons et dans certaines régions de l'exosphère qui ne correspondent pas à celles des survols effectués par BepiColombo. Quant au potassium, MESSENGER/MASCS n'a jamais détecté cette ligne d'émission au cours de ses 4 années de phase orbitale. Seule une limite supérieure de quelques rayleigh a été déduite. Les lignes d'émission plus brillantes du potassium, aux environs de 765 nm, n'ont été observées que depuis le sol. Elles sont toutefois en dehors de la gamme spectrale de BepiColombo/PHEBUS et de MESSENGER/MASCS.

J'ai appliqué le modèle de Chamberlain au profil du second survol, côté matin après la sortie de l'ombre de Mercure. La température à l'exobase permettant d'ajuster le profil au mieux est de 1500 K pour le potassium et 2500 K pour le manganèse. La température déduite pour le manganèse est en adéquation avec la température attendue pour du manganèse issu d'impact météoritique (Berezhnoy, 2018). Les résultats de MESSENGER suggèrent en effet que le manganèse exosphérique viendrait de poussière cométaire impactant la surface de Mercure. La température déduite pour le potassium est relativement comparable à celle déduite par Lierle et al. (2022) à partir d'observations depuis la Terre (entre 700 et 1000 K). Cette gamme de température semble indiquer la photodésorption ou désorption thermique comme processus source dominant.

Conclusions et perspectives

La correction des données des canaux visibles des premiers survols a necessité de développer un modèle empirique car le niveau du bruit était bien différent de celui estimé à partir des précédentes observations en vol.

En ce qui concerne le canal c422, nous avons détecté la ligne d'émission du calcium lors des trois premiers survols de Mercure. Les observations ont révélé une couronne de calcium très étendue du côté matin et concentrée dans la région de l'aube. La température à l'exobase (>50 000 K) ainsi que la hauteur d'échelle (2500-2800 km) déduites des données des deux premiers survols indiquent un processus très énergétique à l'origine du calcium atomique, en accord avec les conclusions de MESSENGER. La prochaine étape consiste à utiliser un modèle exosphérique 3D prenant en compte la photoionisation (Chaufray, Leblanc, et al., 2023). Un modèle 3D permettra de mieux représenter la distribution spatiale du calcium et les effets de l'heure locale. Enfin, la potentielle composante froide du calcium (Cassidy, 2018) n'a pas été observée durant ces survols. Des campagnes d'observations à basse altitude sont prévues durant la phase orbitale. La résolution spatiale sera alors meilleure puisque la vitesse de la sonde par rapport à Mercure sera plus faible que lors des survols.

En ce qui concerne le canal c404, une ou plusieurs espèces ont été détectées à basse altitude côté matin durant les trois premiers survols, potentiellement du potassium ou du manganèse. La ou les espèces n'ont toutefois pas été formellement identifiées à partir des données des survols seulement. On peut tout de même mentionner que la hauteur d'échelle est relativement faible (∼130 km) et que la température à l'exobase est inférieure à 3000 K. Il est nécessaire d'accumuler plus d'observations pour déterminer la ou les espèces. Des observations simultanées depuis la Terre pourraient également aider à différencier le potassium du manganèse.

BepiColombo/MPO doit se mettre en orbite autour de Mercure en décembre 2025 pour une phase nominale d'un an. Une première extension d'un an est déjà prévue et une seconde extension d'un an est également envisagée (cela dépendra du statut de la sonde et notamment de sa température). PHEBUS observera alors quotidiennement l'exosphère de Mercure. La phase orbitale permettra d'observer de potentielles variations saisonnières des différentes espèces exosphériques. D'autre part, des évènements d'érosion spatiale (liés au vent solaire, météorites ...) pourraient avoir lieu: il sera alors intéressant d'observer leurs effets sur les différentes espèces, comme cela avait été le cas lors de la phase orbitale de MESSENGER (Cassidy et al., 2021).

Contents

List of Figures

List of Tables

List of Abbreviations and Acronyms

AU	Astronomical Units
CA	Closest Approach
ESA	European Space Agency
EUV	Extreme UltraViolet
FD	Flight Dynamics
FoV	Field of View
FUV	Far UltraViolet
FWHM	Full Width at Half Maximum
HIP	Hipparcos identification number
HRP	High-reflectance red plains
HV	High Voltage
IP	Intermediate plains
JAXA	Japan Aerospace Exploration Agency
LATMOS	Laboratoire Atmosphères et Observations Spatiales
LBP	Low-reflectance blue plains
LOS	Line of Sight
LRM	Low-reflectance material
MASCS	Mercury Atmospheric and Surface Composition Spectrometer
MCP	Micro-Channel Plate
MEA	Mercury Electron Analyzer
MESSENGER	MErcury Surface, Space ENvironment, GEochemistry and Ranging
MMO	Mercury Magnetospheric Orbiter

MOC	Mission Operations Centre
MOSIF	Mercury Magnetospheric Orbiter's Sunshield and Interface Structure
MPO	Mercury Planetary Orbiter
MSB	Mercury Swing-By
MSE	Mean Squared Error
MSO	Mercury-centric Solar Orbital
MTM	Mercury Transfer Module
MTP	Medium Term Planning
MUV	Middle UltraViolet
NASA	National Aeronautics and Space Administration
NUV	Near UltraViolet
OGS	Operations Ground Segment
OR	Operation Request
PHEBUS	Probing of Hermean Environment By Ultraviolet Spectroscopy
PHESOC	PHEBUS Science Operations Centre
PMT	Photo-Multiplier Tube
POR	Payload Operation Request
PSF	Point Spread Function
PSR	Permanently Shadowed Region
RAE	Resistive Anode Encoder
SEP	Solar-Electric Propulsion
SGS	Science Ground Segment
SNR	Signal-to-noise ratio
SPOT	Science Planning Operation Tool
STP	Short Term Planning
TAA	True Anomaly Angle
URF	Unit Reference Frame
WOL	Wheel Off-Loading

List of Constants

$e = 0.2056$	Eccentricity of Mercury's orbit
$a = 57.909 \times 10^6$ km	Semimajor axis of Mercury's orbit
$c = 2.9979 \times 10^{10}$ cm.s^{-1}	Speed of light
$e = 4.8032 \times 10^{-10}$ statcoul	Elementary charge
$m_e = 9.1094 \times 10^{-28}$ g	Electron mass
$k = 1.3807 \times 10^{-23}$ J.K^{-1}	Boltzmann constant
$G = 6.6726 \times 10^{-11}$ m^3.s^{-2}.kg^{-1}	Gravitational constant
$M_S = 1,988,500 \times 10^{24}$ kg	Mass of the Sun
$\Omega = 4.175$ deg^2	PHEBUS solid angle
$R_M = 2440.5$ km	Equatorial radius of Mercury
$m = 0.33010 \times 10^{24}$ km	Mass of Mercury

Introduction

Mercury is the closest planet to the Sun and also the smallest. It has been visited by only two missions, both from NASA (National Aeronautics and Space Administration): Mariner 10 (3 flybys 1974 and 1975) and MESSENGER (MErcury Surface, Space ENvironment, GEochemistry and Ranging) (3 flybys in 2008 and 2009, orbital phase from 2011 to 2015). The MESSENGER mission, despite its numerous observations, left many questions open, hence the interest of a new mission to Mercury. The BepiColombo mission was launched in October 2018 on a 7-year cruise to Mercury. The mission is composed of two spacecraft: the European-led MPO (Mercury Planetary Orbiter) and the Japanese-led MMO (Mercury Magnetospheric Orbiter) (also known as Mio). On its journey to Mercury, the ESA (European Space Agency)-JAXA (Japan Aerospace Exploration Agency) mission will make gravity assist maneuvers at Earth, Venus and Mercury. The encounters with Mercury will have various geometries that offer a variety of science investigations to be performed by instruments on board the MPO and Mio spacecraft.

Mercury is a special terrestrial planet, owing to its thin collisionless atmosphere, or exosphere. The latter is generated by possible transient sources (e.g. volatile activity) and surface release processes driven by external sources (e.g. sun radiation, impacting ions, and micrometeoroids). These surface release processes are influenced by the magnetosphere: the exosphere and magnetosphere of Mercury represent a highly dynamic, coupled system that is unique among the terrestrial planets. Mercury's exosphere is the object of study of PHEBUS (Probing of Hermean Environment By Ultraviolet Spectroscopy), one of the 11 instruments on board MPO. The UV spectrometer, built by LATMOS (Laboratoire Atmosphères et Observations Spatiales) in cooperation with IKI (Spaces Physics Institute, Moscow, Russia) and the Department of Planetray Sciences at the University of Tokyo, aims to study the exosphere of Mercury, its composition and dynamics and its interaction with the solar wind.

Six flybys of Mercury will be conducted during the journey to the planet, providing a foretaste of the Hermean environment. These flybys will be the occasion for PHEBUS to observe Mercury with its various detectors, covering the extreme to middle ultraviolet ranges. Additional visible lines (potassium at 404.7 nm and calcium at 422.8 nm) will also be measured. The instrument was operated during the first three flybys, the last three having not yet taken place.

This thesis manuscript presents the results of these first flybys and focuses on the data of visible channels. The manuscript is organized in seven parts: first, I will establish the context by describing the planet Mercury in the first chapter and the BepiColombo mission in the second chapter. I will subsequently describe the PHEBUS instrument in a third chapter as well as the in-flight calibration of its visible channels and FUV (Far UltraViolet) detector in the fourth chapter. The fifth chapter will focus on the planning and results of the first two flybys of Mercury. The last two chapters will be devoted to the analysis of the visible channels data and its comparison with the results of the MESSENGER mission and ground observations. Appendices present the theory of exospheres developed by Chamberlain (1963) and demonstrate that the exosphere of Mercury is optically thin for the emission lines considered here.

Chapter 1

Mercury, closest planet to the Sun

Mercury is one of the four rocky planets of our solar system and is quite unusual. It has the most eccentric orbit and is the only planet in the inner solar system (other than the Earth) to possess an internally generated magnetic field. Mercury is the lightest and smallest planet in the solar system. Although the closest to the Sun, Mercury is not the hottest planet, it is Venus. The planet likes to keep it simple: it has no moons, no rings and a very thin atmosphere. The planet is often compared to the Earth's Moon due to its similarity (size, cratered surface, exosphere).

In this chapter, I will present the planet, its characteristics and exploration and will develop a very characteristic aspect of the planet, namely its exosphere.

1.1 Characterisation of the planet

1.1.1 Motion and temperature

The orbit of Mercury is very special, if not abnormal. It is very eccentric (0.2058) and also quite inclined on the ecliptic plane[1] (7°). Interestingly, its eccentricity and inclination have evolved over periods of a few million years. Unlike the orbits of large planets, those of the inner planets are irregular (Laskar, 1989, 1990). Mercury's is particularly chaotic, its eccentricity can rise to very high values (potentially close to 1), allowing for collision of the planet with Venus, resulting in a possible ejection out of the solar system in less than 5 Gyr (Laskar, 1994, 2008). Due to the large eccentricity of Mercury's orbit, its distance to the Sun varies from 46 million km (0.307 AU (Astronomical Units)) at perihelion to 70 million km at aphelion (0.467 AU). Since the intensity of the sunlight is inversely proportional to the distance between the Sun and the planet, the solar flux received by Mercury varies a lot along the planet's orbit (Table 1.1).

Mercury orbital period is 88 Earth days but it takes 58 Earth days for the planet to turn on its axis (Mercury rotation period). Mercury is the only known object in our solar system in 3:2 spin-orbit resonance: the planet makes three rotations on its axis for every two orbits around the Sun (Colombo, 1965). The spin-orbit resonance of Mercury is related to both its highly elliptical orbit and its shape (non-spherical). As a consequence of this resonance, Mercury solar day lasts 176 Earth days i.e. it takes 176 days for the Sun to return to the same spot in the sky, as seen from a fixed point on the surface.

[1] The plane on which the Earth moves around the Sun.

Table 1.1: Quick look facts about Mercury and comparison with Earth. Values from https://nssdc.gsfc.nasa.gov/planetary/factsheet/mercuryfact.html

Parameters	Mercury	Earth
Mass [kg]	0.33×10^{24}	5.97×10^{24}
Equatorial radius [km]	2,440	6,378
Density [kg.m^{-3}]	5,430	5,515
Gravity [m.s^{-2}]	3.70	9.81
Average distance to Sun [AU]	0.387	1
Orbit inclination[°]	7	0
Orbit eccentricity	0.206	0.017
Obliquity [°]	0.03	23.4
Average surface temperature [°]	167	15
Solar irradiance at aphelion [W.m^{-2}]	6,272	1,321
Solar irradiance at perihelion [W.m^{-2}]	14,446	1,413
Rotation period (Earth days)	58	1
Orbital period (Earth days)	88	365
Solar day (Earth days)	176	1

The axis of rotation of Mercury is almost vertical, its tilt being close to 0°. This very small obliquity implies that:

1. Mercury does not experience seasons (as on Earth or Mars). There are, however, thermal seasons as the distance of the planet to the Sun varies.

2. Some regions at its poles never receive sunlight, they are called the PSR (Permanently Shadowed Region). As a result, water ice is thought to be present in some high-latitude craters (Harmon and Slade, 1992; Paige et al., 1992, Lawrence et al., 2013; Neumann et al., 2013).

Although the closest planet to the Sun, Mercury is not the hottest planet but experiences the greatest range in surface temperature. It can go up to about 450°C during the daytime while it can go down to nearly -180°C at night. This huge temperature difference is due to its proximity to the Sun, its long solar day and its lack of atmosphere (which would promote the transport of heat from one side to the other). Mercury indeed has a very tenuous atmosphere, without comparison with that of the Earth. The Earth has different layers within its atmosphere: the troposphere, stratosphere, mesosphere, thermosphere, and finally the exosphere that is beyond 600 km, at the interface with interstellar space. At Mercury, the base of the exosphere merges with the surface of the planet. It is then called a surface-bounded exosphere. A thorough description of the Hermean exosphere is given in Section 1.1.4.

Like other planets of the solar system, Mercury's orbit precesses around the Sun but with an anomalous rate: there is a 43″ per century discrepancy between the observed and calculated

precession. That discrepancy could not be explained by Newtonian mechanics and perturbations of know planets. Le Verrier (1859) proposed that an unknown planet or group of asteroids orbiting inside Mercury's orbit were perturbing the orbit. The hypothetical planet, named Vulcan, was searched for decades before Einstein's theory of relativity came to explain the perihelion advance of Mercury.

1.1.2 Surface

1.1.2.1 Impact craters

Mercury's surface resembles that of the Moon with its many impact craters, resulting from collisions with meteoroids and comets. The planet has no significant atmosphere to stop impacts and is then heavily weathered by the harsh space environment. Mercury is the most cratered planet in the solar system. The ages of these craters are varied: some, the oldest, have eroded ramparts, while others have sharp ramparts, and are therefore much younger.

Very large impact basins (e.g. Caloris Basin, roughly 1,550 km wide, one of the largest impact basin in our solar system) were created by asteroid impacts on the planet's surface early in the solar system's history. At the Caloris antipode (i.e. point diametrically opposite), hilly and lineated terrain has been found (Murray et al., 1974). Surprisingly, this type of terrain has not been identified antipodal to any other basin of Mercury. However, new analysis of high spatial resolution MESSENGER imagery and laser altimeter topography unveiled multiple hilly and lineated terrains with no impact antipodal impact bassins (Rodriguez et al., 2020).

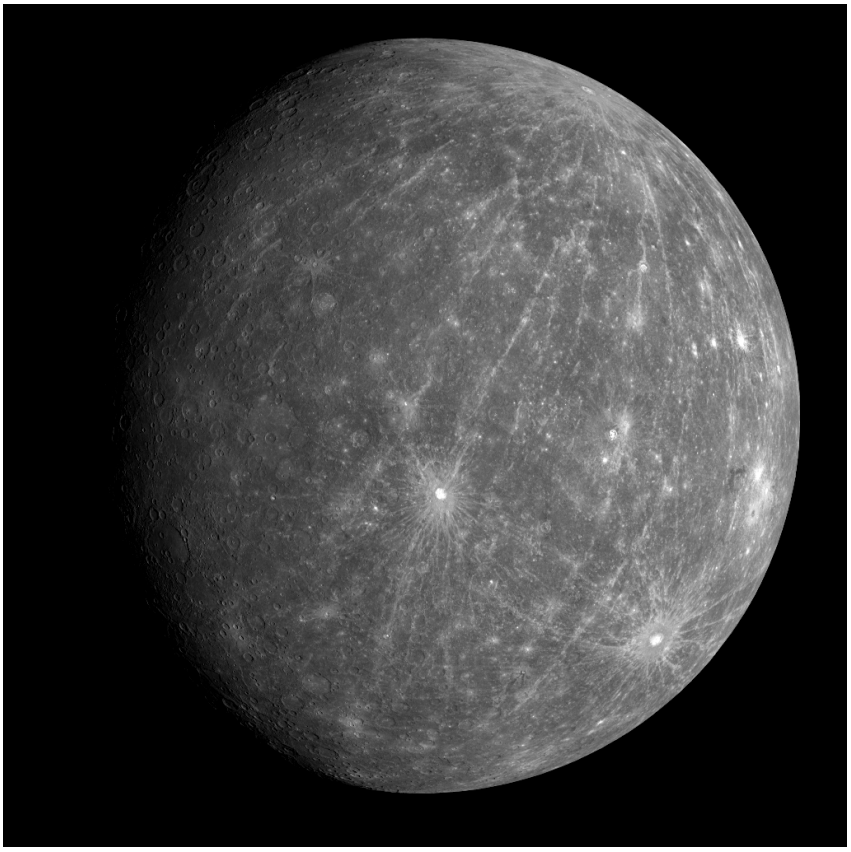

Figure 1.1: Image acquired by Wide Angle Camera (WAC) of Mercury Dual Imaging System (MDIS) during MESSENGER's second Mercury flyby. At the center, lies the bright Kuiper Crater (62 km in diameter). To the southeast of Kuiper, near the limb of the planet, lies the Debussy Crater (85 km in diameter), imaged for the first time by a spacecraft. Credit: NASA/Johns Hopkins University Applied Physics Laboratory/Carnegie Institution of Washington.

Fresh impact craters show light-coloured rays extending away from its centre (e.g. Debussy and Kuiper craters, Figure 1.1). These rays form when meteoroids or comets strike the surface, crushing rocky material beneath the point of impact. Some of this fresh material is ejected out of the crater and falls back to the surface, forming the rays. Those bright rays darken with time as a result of space weathering. Mercury presents fewer rayed craters than the Moon, implying that hermean regolith matures faster than lunar regolith as the planet is more exposed to the solar wind and micrometeoroid bombardment. The rayed craters on Mercury were first observed by Mariner 10 (Murray et al., 1974; Strom, Murray, et al., 1975). With a more complete coverage of the planet, MESSENGER was able to unveil many other rayed craters.

Some deep craters at the poles host water ice. In fact, ground-based observations revealed radar-bright polar deposits, suggesting that water ice is present at the surface of Mercury (Harmon and Slade, 1992; Slade et al., 1992). In the PSRs near the poles, there are deep impact craters where sunlight does not reach the bottom. It is cold enough to preserve water ice, especially if a layer of organic-rich volatile compounds insulates the water ice below, as suggested by the MESSENGER observations (Neumann et al., 2013; Chabot et al., 2014). The origin of these deposits is not yet assessed although a recent large impact event is the most favoured hypothesis.

1.1.2.2 Volcanic and tectonics

Mercury's ancient, cratered surface shows signs of past volcanic and tectonic activity.

Smooth plains are found within and surrounding most of the known basins. Based on Mariner 10 images, the origin of the deposits was debated: either solidified impact melt (Wilhelms, 1976) or volcanic origin (Murray et al., 1975; Strom, 1977). MESSENGER returned global coverage of Mercury's surface at resolutions far higher than those of Mariner 10 data, bringing definite evidence of volcanic activity on Mercury, either effusive (smooth plains) or explosive (pyroclastic vents) volcanism (Head et al., 2008; Murchie et al., 2008; Robinson et al., 2008).

While the smooth plains cover around 27% of the surface of Mercury (Denevi et al., 2013), Mercury's surface is also filled with tectonic features such as wrinkle ridges, high-relief ridges, and lobate scarps (Watters et al., 2009). These landforms are the result of a tectonic regime dominated by global contraction and show a decrease in the volume of the planet by internal cooling (Strom, Trask, et al., 1975). The number and morphology of the tectonic features make it possible to estimate the decrease of the planetary radius between 5 and 7 km (Byrne et al., 2014). Earlier estimates from more limited data from Mariner 10 rather suggested a decrease in planetary radius <2 km (Strom, Trask, et al., 1975).

1.1.2.3 Surface composition

The composition of Mercury's surface appears different from those of other terrestrial planets. MESSENGER's geochemical observations indicated "higher Mg/Si ratio and lower Al/Si and Ca/Si ratios than the terrestrial and lunar crusts"[2] (Nittler et al., 2011). Unexpectedly, the observations showed an abundance of sulfur and low amounts of iron on the planet's surface. The combination of these two conditions is strong evidence that Mercury's surface is highly chemically reduced. With low surface abundances of iron and titanium, Mercury relatively dark surface could be explained by the abundance of carbon (Murchie et al., 2015; Peplowski, Lawrence, Evans, et al., 2015).

Images and spectral measurements revealed compositional variations among surface materials that manifest themselves as differences in albedo and red, lunar-like spectral slope (indicative of mature, space-weathered material) (Figure 1.2). Mercury's surface presents three geomorphic units: smooth plains, intercrater plains and the rims, walls and ejecta of impact craters and

[2]Mg stands for magnesium, Si for silicon, Al for aluminum and Ca for calcium.

basins. These geomorphic units can be divided in four spectral units: LBP (Low-reflectance blue plains), IP (Intermediate plains), HRP (High-reflectance red plains) and LRM (Low-reflectance material) (Robinson et al., 2008; Denevi et al., 2009; Murchie et al., 2015). Low-albedo, less-red LRM is associated with impact craters and their ejecta. The other three spectral units (LBP, IP and HRP) form the smooth and intercrater plains. Denevi et al. (2009) explain that IP "have reflectance and color properties similar to the global mean", while LBP "have reflectances 15% below the global mean and spectral properties intermediate to IP and LRM". The HRP have reflectances of up to 20% above the global mean and steeper spectral slope.

MESSENGER measurements surprisingly revealed that Mercury is a volatile-rich planet, despite the high temperatures of the planet. Highly volatile elements, such as hydrogen, are limited to the PSRs, while moderately volatile species, including sulfur, sodium, potassium and chlorine are more abundant and widespread. The spatial distribution of volatile elements on Mercury does not appear to correlate with changes in surface temperature (Peplowski, Lawrence, Feldman, et al., 2015; Weider et al., 2015).

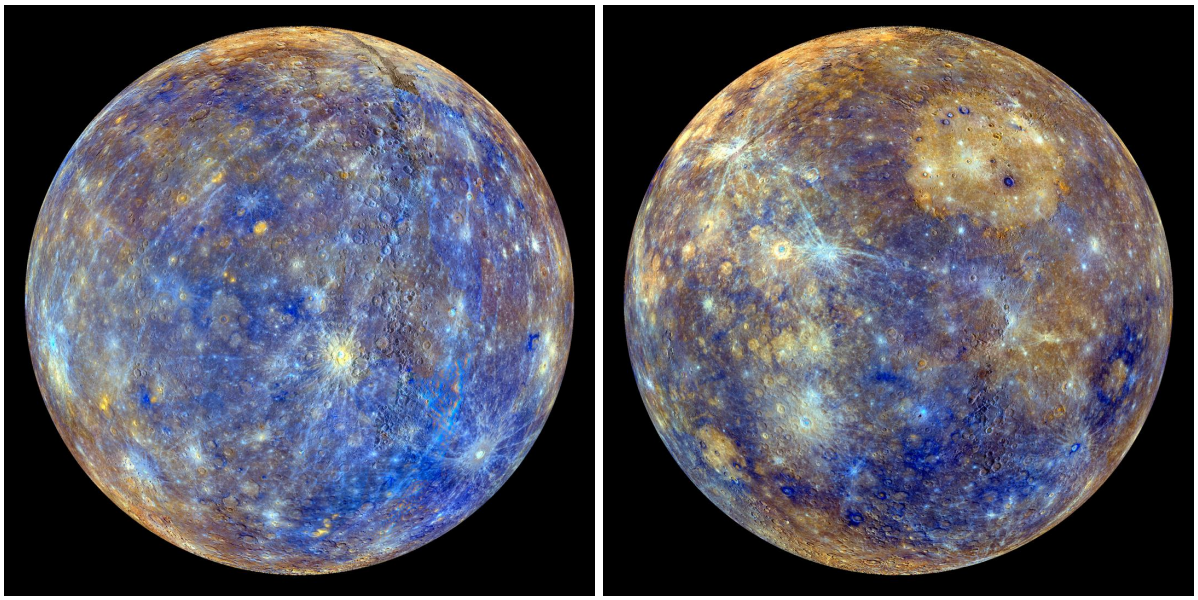

(a) **(b)**

Figure 1.2: Enhanced color mosaic of Mercury in orthographic projection centered on latitude 0° and longitude 320°E (a) and longitude 140°E (b). The views are based on images acquired by the Wide Angle Camera (WAC) of the Mercury Dual Imaging System (MDIS) during MESSENGER's primary mission. The colors enhance the chemical, mineralogical, and physical differences between the rocks that make up Mercury's surface. Young crater rays appear light blue or white while medium- and dark-blue areas correspond to the LRM, thought to be rich in a dark, opaque mineral. Tan areas are plains formed by eruption of highly fluid lavas. Hokusai crater, whose rays stretch across the planet, is located in the upper right of image (a). The giant Caloris basin is the large circular tan feature located just to the upper right of center of image (b). Credit: NASA/Johns Hopkins University Applied Physics Laboratory/Carnegie Institution of Washington.

1.1.3 Internal structure, magnetic field and magnetosphere

Mercury is the second densest planet, after Earth (Table 1.1). If gravitational compression is taken into account, Mercury is then the densest planet in the Solar System, with an uncompressed density of 5.3 g.cm^{-3} when that of Earth is 4.1 g.cm^{-3}. This relatively high density means that Mercury contains a large metallic core, with a larger fraction of iron than any other planet or satellite in the solar system. It has been estimated that the core is about 83% of the planet's diameter. Note that the iron core of Earth is only 54% of its diameter. Mercury's outer

shell (silicate mantle and crust), is only about 400 km thick. The crustal thickness, derived from MESSENGER's low-altitude measurements, is greater near the equator (between 50 and 80 km) and less toward the north polar region (between 20 and 40 km). The thickness of the crust in the southern hemisphere could not be estimated due to the lack of low-altitude measurements.

The large liquid core of Mercury generates, through a dynamo effect, a weak but stable dipolar magnetic field. With Earth, Mercury is the only terrestrial planet to possess an internally-generated magnetic field. Its strength is however much lower than that of Earth, by a factor of ∼100. MESSENGER's measurements confirmed that Mercury's magnetic field is largely dipolar, with the same polarity as Earth's magnetic field. The dipole is almost aligned with Mercury's rotational axis (less than 0.8° tilt) and is offset relative to the planet's equator (∼0.2 R_M) as revealed by MESSENGER's measurements, implying that the south pole is more exposed to the solar wind than the north pole.

The dynamic pressure exerted by the solar wind is obviously stronger at Mercury than at Earth. Mercury's magnetic field is strong enough to deflect the solar wind around the planet, generating a magnetosphere. Although much smaller than that of Earth, Mercury's magnetosphere presents the same architecture, with a bow-shock, a magnetopause and a magnetotail (Figure 1.3). Mercury's magnetosphere is very dependent on solar activity due to its proximity with the Sun and varies with the position of the planet along its orbit. Magnetic reconnections between the magnetic field of the planet and the interplanetary magnetic field have a higher intensity than at Earth. These interactions allow the penetration of solar wind plasma into the magnetosphere. The cusps in the polar regions expose the surface to direct bombardment by the solar wind.

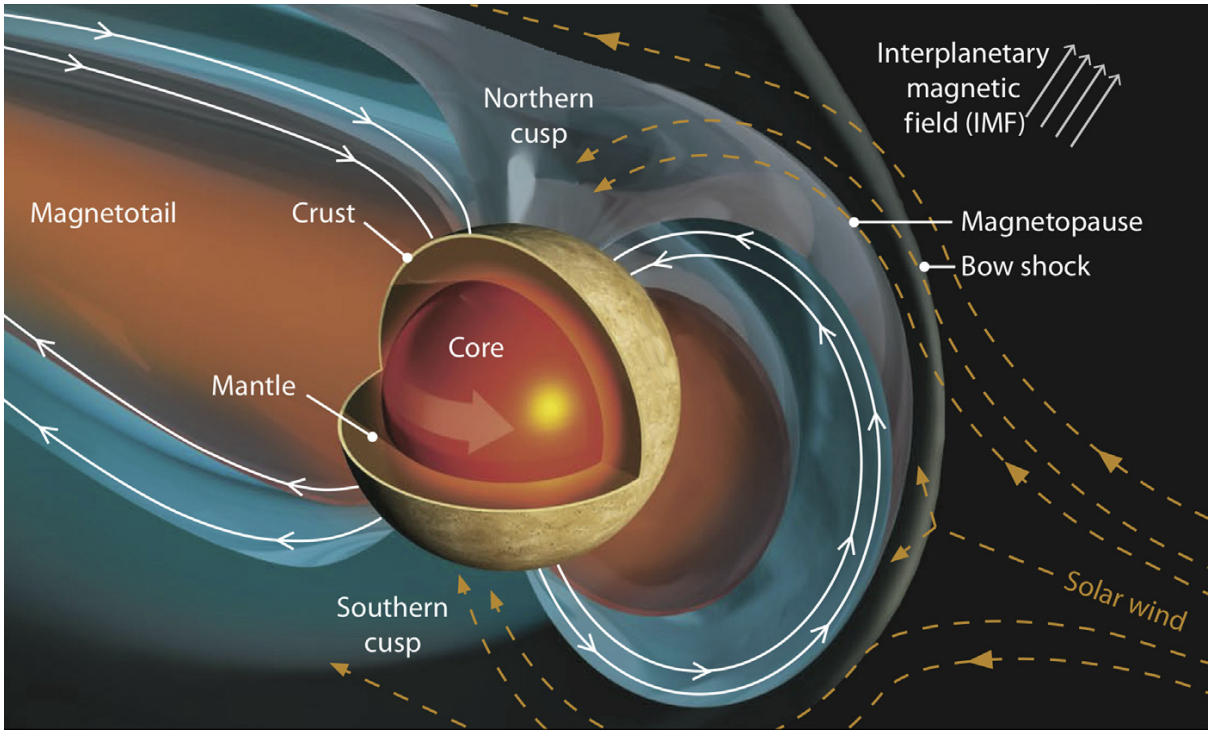

Figure 1.3: Mercury's magnetosphere and its interactions with the solar wind. From Murchie et al. (2014).

1.1.4 Exosphere

The exosphere is a thin atmosphere where the density is so low that its few atoms or molecules are unlikely to collide with each other. In the case of bodies with substantial atmospheres (e.g.

Earth or Mars), the exosphere is the highest part of the atmosphere where it thins out and merges with outer space. However, in the case of airless bodies (e.g. Mercury or the Moon), the exobase (i.e. the lower boundary of the exosphere) coincides with the surface: it is then called a surface-bounded exosphere.

The ultraviolet airglow and occultation experiment on board Mariner 10 (Section 1.2.1) unveiled the surface-bounded exosphere of Mercury, making it the only planet of our solar system not to possess a substantial atmosphere. The surface gravity of Mercury (3.7 $m.s^{-2}$) is too low for it to have kept an atmosphere: molecules are more likely to escape into space or collide with the surface of the planet than with each other.

1.1.4.1 Composition

To determine the constituents of the exosphere, in-situ mass spectrometers are used as well as remote sensing observations, either from the ground or space. The remote sensing instruments measure the resonantly scattered radiance, i.e. the intensity of sunlight that is resonantly scattered by the atoms (or molecules). When an atom in its fundamental state absorbs a photon, it results in a transition to its excited state. The atom quickly returns to the ground state by emitting a photon of equal energy. The contribution of the solar radiation reflected from the planet's surface to the observed exospheric intensity is small and usually neglected. The contribution of electron impact excitation to the observed emission is also neglected as "the electron density in Mercury's magnetosphere is too low for it to be significant" (McClintock et al., 2018).

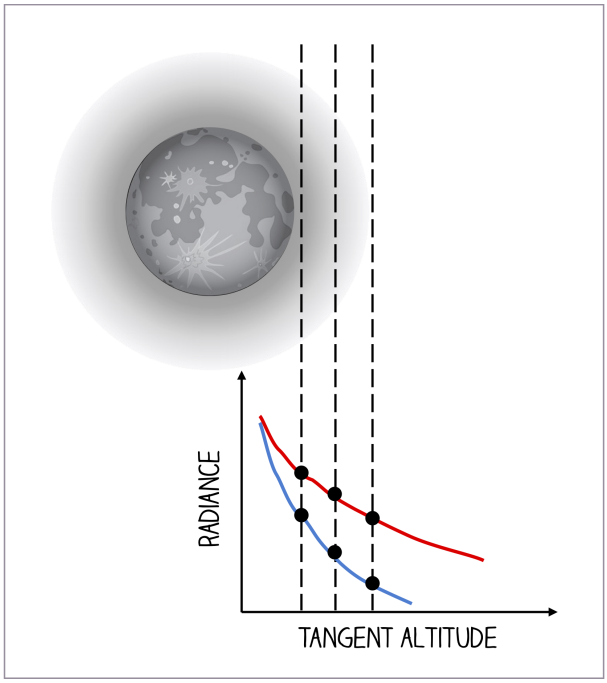

Figure 1.4: Illustration of limb scan for two components of the exosphere: the blue line represents the colder exosphere, while the red one represents a hotter exosphere.

Both Mariner 10 (section 1.2.1) and MESSENGER (Section 1.2.2) UV spectrometers relied on limb-scan viewing to study the exosphere of Mercury (Figure 1.4). The instrument pictures the exosphere with its entrance slit along a line of sight that passes above the surface at a given altitude. An emission limb profile (i.e. radiance versus tangent altitude[3]) is deduced from consecutive limb scans. The slope of the profile is indicative of its temperature: a shallow slope

[3]The minimal distance from the planet's surface to the instrument's line of sight.

suggests a warm exosphere. Space-based observations offer the undeniable advantage of not having the contamination of the Earth's atmosphere (sunlight reflected by Earth's atmosphere). Owing to absorption by Earth's atmosphere, some species cannot be observed from ground (hydrogen, helium and magnesium). Ground-based observations also need to account for the sunlight reflected by Mercury's surface when extracting the exospheric signal.

Mercury's exosphere is composed almost entirely of atoms rather than molecules. Nine neutral species were detected in the exosphere of Mercury: helium (He), hydrogen (H), sodium (Na), potassium (K), calcium (Ca), magnesium (Mg), aluminum (Al), iron (Fe) and manganese (Mn). Na, K, Ca and Mg are the most studied ones, Na and Ca from both the ground and space, K from the ground and Mg from space. The other ones are more difficult to observe due to their weak emission and/or abundance.

He and H were the first neutral species to be measured by Mariner 10 Ultraviolet Spectrometer (Broadfoot et al., 1976). PHEBUS, the UV spectrometer of the ESA-JAXA joint mission BepiColombo, recently observed He in the exosphere of Mercury (Quémerais et al., 2023), nearly 50 years after the first detection by Mariner 10. MESSENGER could not observe He, its emission line at 58.4 nm falling out of the wavelength range of the MASCS (Mercury Atmospheric and Surface Composition Spectrometer) instrument (McClintock and Lankton, 2007). Exospheric H Lyman-α (121.6 nm) is not easy to observe at Mercury as the observed H Lyman-α can come from three sources: exospheric emission, scattered solar H Lyman-α from the dayside surface, and background interplanetary H Lyman-α. More than thirty years after Mariner 10 observations, MESSENGER detected neutral hydrogen during the flybys (McClintock et al., 2008) and throughout the orbital phase (Vervack et al., 2018). The potential detection of oxygen (O) during Mariner 10 flybys of Mercury was unconfirmed (Broadfoot et al., 1976). MESSENGER/MASCS regularly searched for O throughout the orbital mission but could not detect it. Only an upper limit was derived: $\sim$2 R at 130.4 nm (Vervack et al., 2016). Vervack et al. (2016) also stated that the levels of O reported by Mariner 10 would have easily been seen. However, the Fast Imaging Plasma Spectrometer (FIPS) of the Energetic Particle and Plasma Spectrometer (EPPS) on board MESSENGER observed ionized oxygen (Raines et al., 2013), suggesting that some neutral oxygen is in the exosphere. Note that Raines et al. (2013) also reported the detection of sodium ions.

Na and K were the next exospheric species discovered with ground-based telescopes (Potter and Morgan, 1985, 1986), as was the calcium (Ca) (Bida et al., 2000). The observations of Ca in Mercury's exosphere are further developed in sections 6.1 and 6.2, while the observations of K are further developed in Section 7.1. Na is the most observed species in the exosphere of Mercury owing to its intense intrinsic brightness. The extended tail of Na was first observed by Potter et al. (2002). Interestingly, results from ground-based observations sometimes conflict with those from MESSENGER observations. MESSENGER's orbital phase data revealed a dawn/dusk asymmetry of the Na exosphere, contrary to many observations from Earth (Cassidy et al., 2015). In addition, MESSENGER has not observed short-term spatial and temporal variations in the Na exosphere, which is in total contradiction with observations from Earth (Solomon and Anderson, 2018). This disagreement suggests that the variations observed from Earth occur on the day side at medium and high latitudes, areas not surveyed by MESSENGER (Solomon and Anderson, 2018).

During the three flybys of Mercury, MESSENGER/MASCS yielded detection of Mg and ionized calcium (Ca^+) (McClintock et al., 2009; Vervack et al., 2010). During its orbital phase, MESSENGER conducted near-daily observations of exospheric Mg (Merkel et al., 2017).

Bida and Killen (2011) reported first-time detections of Al and Fe by ground-based observations. Fe was not observed by MESSENGER/MASCS but the detection of Al was confirmed by MESSENGER/MASCS observations during the orbital phase (Vervack et al., 2016). The same observations yielded first detection of manganese (Mn) and confirmed the detection of Ca^+. The detections of Al, Mn and Ca^+ are further developed in Section 7.1.

1.1.4.2 Processes

The exosphere of an airless body is transient and is continuously fed by several processes. Without these processes, the exosphere would disappear completely within a few days. An exosphere is supplied both by incoming sources (solar wind, micrometeoroids and meteoroids, comets) and by particles released from the surface through different processes (photon, thermal and electron-stimulated desorption, sputtering and meteoroid impact vaporization). These source processes are balanced by loss processes (Figure 1.5), which include surface implantation, ionization followed by transport along magnetic field lines, thermal escape and acceleration by solar radiation pressure to escape velocity.

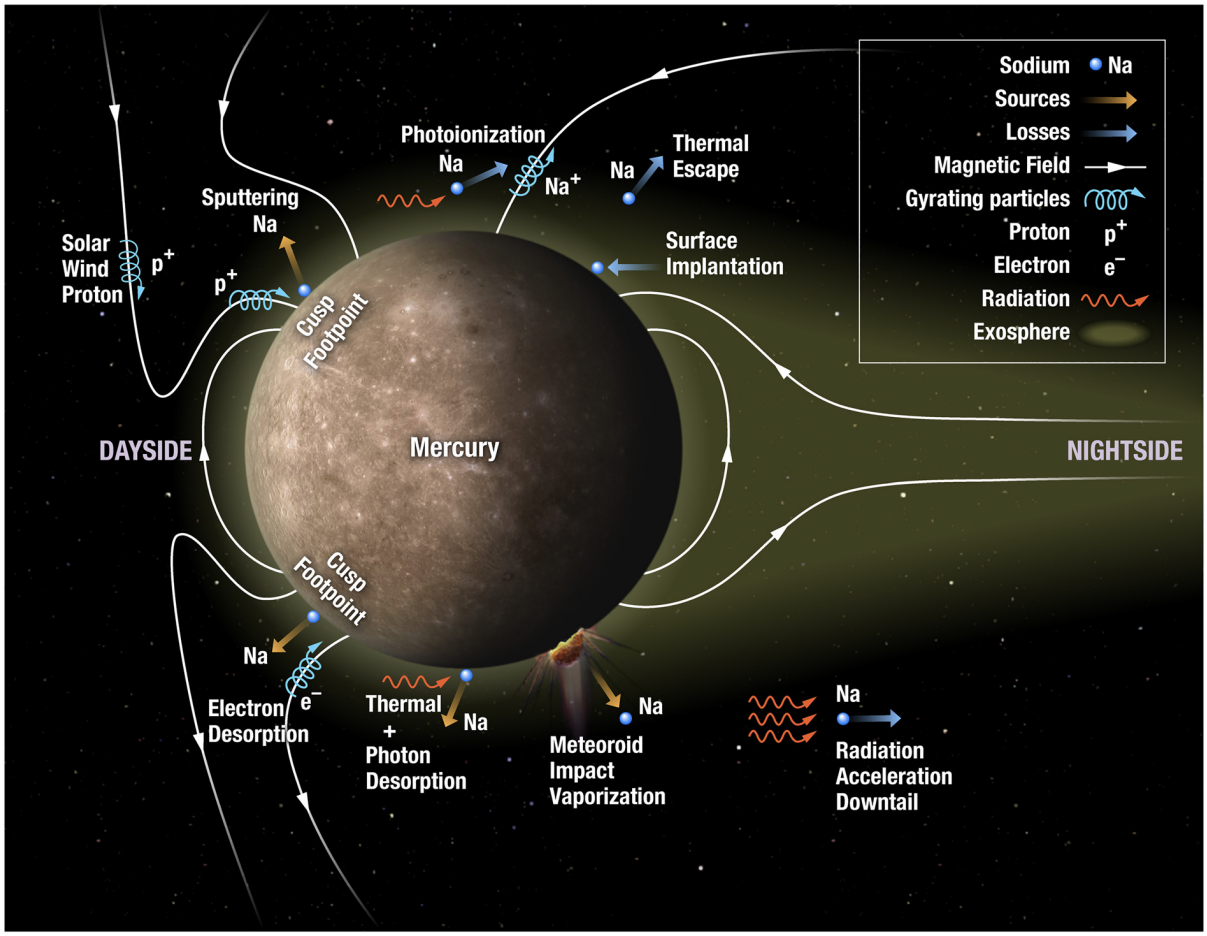

Figure 1.5: Illustration of the major sources and loss processes that generate and maintain the exosphere of Mercury. From Jasinski et al. (2021).

The processes that release atoms or molecules affect them differently depending on the element. The chemical bonds of refractory elements (e.g. Ca, Mg, Al, Fe and Mn) require high-energy processes (such as ion sputtering and meteoroid impact vaporization) to release them from the surface. The released material can then reach high altitudes. The weak bonds of the volatile elements (e.g. He, H, Na and K) require lower energies to be broken (e.g. thermal and photon-stimulated desorption). The released material then reaches only low altitudes and usually returns to the surface.

The processes releasing neutrals species in the exosphere depend on the species, local time, orbital position, and solar wind conditions. Both ground- and space-based observations indicated a highly variable exosphere, on both spatial and temporal scales. The spatial distribution of the elements in Mercury's exosphere is very different (e.g. Potter and Morgan, 1997; McClintock et al., 2009; Vervack et al., 2010; Lierle et al., 2022). The temporal variations are either

short- (day-to-day or even shorter variations, e.g. Mangano et al., 2013; Cassidy et al., 2021) or long-timescale (year-to-year, e.g. Burger et al., 2014; Cassidy et al., 2015; Merkel et al., 2017; Milillo et al., 2021) changes.

Source processes:

The exosphere of Mercury is generated by the interaction of the surface with incoming particles, including ions, meteoroids and photons. There are four main processes that release neutrals from the planet's surface: thermal desorption, photon-stimulated desorption, impact vaporization and ion sputtering.

When the sunlight strikes the planet's surface, it releases material through two low-energy processes: thermal desorption or photon-stimulated desorption. **Thermal Desorption** is the release of adsorbed atoms from a surface through heating. The thermal agitation in the first microns of the surface is sufficiently energetic that some of the volatiles can escape from the surface and populate the exosphere. Surprisingly, MESSENGER observations showed no evidence for thermal desorption for any species (Killen et al., 2018). Yakshinskiy et al. (2000) suggested that space weathering could inhibit thermal desorption.

Photon-Stimulated Desorption (PSD) and **Electron-Stimulated Desorption** (ESD) refer to the ejection of an atom or a molecule from a surface initiated by the adsorption of individual photons or electrons. PSD is important for the volatile elements, especially Na and K. The vapor resulting from PSD is much hotter than that resulting from thermal desorption, but is cooler than that resulting from **impact vaporization**.

Mercury is particularly sensitive to meteoroids impacts as the planet does not have an atmosphere to slow down and disintegrate meteoroids. Large meteoroid impacts release much material and are expected to produce localized and transient enhancements in the exospheric density (Mangano et al., 2007). These events are rare and their contribution to the global exosphere is considered negligible. However, small dust particles from interplanetary space constantly impact Mercury's surface (Cintala, 1992; Marchi et al., 2005; Borin et al., 2009), releasing neutral species in the exosphere of Mercury. A meteoroid impact induces a heat wave in the regolith, resulting in the vaporization of a part of the meteoroid and the surface at the impact site, releasing high-energy atoms to high altitudes. As the impacts vapourize deeper layers of regolith than other processes, the composition of the cloud of impact vapour provides valuable information about the surface composition. The characteristics of the vapour cloud induced by meteoroid impact depend on the impactor mass, velocity and composition. Meteoroids impacting the surface of Mercury derive from different sources, including Jupiter Family Comets, Main Belt Asteroids, Halley Type and Oort Cloud Comets (Pokorný et al., 2018).

The solar particles penetrating the magnetosphere of Mercury are likely to impact the planet's surface, preferably at high latitudes, and induce the ejection of matter from the surface, especially the most volatile (e.g. Na). When the ion impacts the surface, it transfers energy resulting in another particle being released. **Ion sputtering** yields are highly dependent on the impacting ion species, their energy and impact angle, and also on the grain size distribution, space weathering history, and composition of the regolith (Killen et al., 2018).

Quémerais et al. (2023) recently showed that neutrals present in the interplanetary medium (He and H mainly) can have a significant contribution to the exosphere. For certain values of the TAA of Mercury, this contribution would be more important than that of solar wind ions capture.

Loss processes:

Neutral species do not remain in the exosphere indefinitely: they can fall back to the surface

or, depending on their mass and source process, can be lost to space by **kinetic escape** (when the particle's speed exceeds the planet's escape velocity). They are also affected by different processes. First, they are subjected to solar **radiation pressure**: the solar photons push atoms in the antisunward direction, forming a comet-like tail. The effects of solar radiation are different depending on the species, Na and K being strongly affected whereas Mg hardly at all. The Na tail experiences variations following the seasons of Mercury (Potter et al., 2007). Ca atoms are affected by the radiation pressure but only to a certain extent, owing to its short photoionization lifetime: the Ca atoms are more likely to be photoionized before radiation acceleration effects become significant. The **photoionization** is "the process by which solar photons remove electrons from neutral atoms and create pickup ions that are governed by electrodynamic forces rather than gravitational forces" (Killen et al., 2018). The ions are then accelerated toward the planet, impacting the surface, or away from the planet, lost to interplanetary space. Note that there are uncertainties in the photoionization lifetime for each species (discussed in Killen et al., 2018).

1.2 Exploration

Due to its proximity with the Sun and its small size, Mercury is difficult to observe from Earth. It remains low on the horizon (maximum elongation of 28°) and appears there only relatively little time (at dawn and twilight).

Using telescopes, it is possible to observe the transit of Mercury on the Sun. However, due to the orbital inclination, there are only 13 transits of Mercury per century.

From Earth, radar observations allow to determine the movements of the planet around the Sun, and on itself. Optical telescopes provide global information, through spectroscopy, on the chemical composition of the planet's surface and exosphere.

It is also difficult to approach Mercury and put a spacecraft into orbit as it must compete with the Sun gravitational force. The proximity of the planet to the Sun also poses a problem in terms of intense heat that the spacecraft would experience. So far, the planet was visited by only three probes: NASA Mariner 10 and MESSENGER, and ESA-JAXA BepiColombo. The BepiColombo mission, currently on a cruise to Mercury, is presented in Chapter 2.

1.2.1 Mariner 10

Mariner 10 was the last spacecraft of NASA Mariner program to explore the inner planets of the solar system, (Mars, Venus and Mercury). It was the first spacecraft to visit two planets (Venus and Mercury), the first mission to use gravity assist maneuver and the first spacecraft to explore Mercury.

1.2.1.1 Trajectory

As a direct trajectory to Mercury would require too much fuel and heavy launcher, it was suggested to use Venus for a gravity assist to reach Mercury (Minovitch et al., 1963; Sturms and Cutting, 1966). The concept of gravity assist trajectory was theorized for decades but never used before. The Venus gravity assist concept was therefore developed in the 1970s. A unique Earth-Venus-Mercury trajectory opportunity was found for 1973. The initial plan included a unique flyby of Mercury through the gravitational assistance of Venus. However, the calculations of Guiseppe Colombo, an Italian scientist, mathematician and engineer, showed that not only one, but three close encounters with Mercury were achievable within the same mission. Mariner 10 eventually conducted three successful flybys of Mercury in 1974 and 1975.

Mariner 10 lifted off from Cape Canaveral, Florida, on November 3, 1973, to begin its journey to Venus and Mercury. The spacecraft passed Venus on February 5, 1974 at a distance of 5,768 km at CA (Closest Approach) (Figure 1.6).

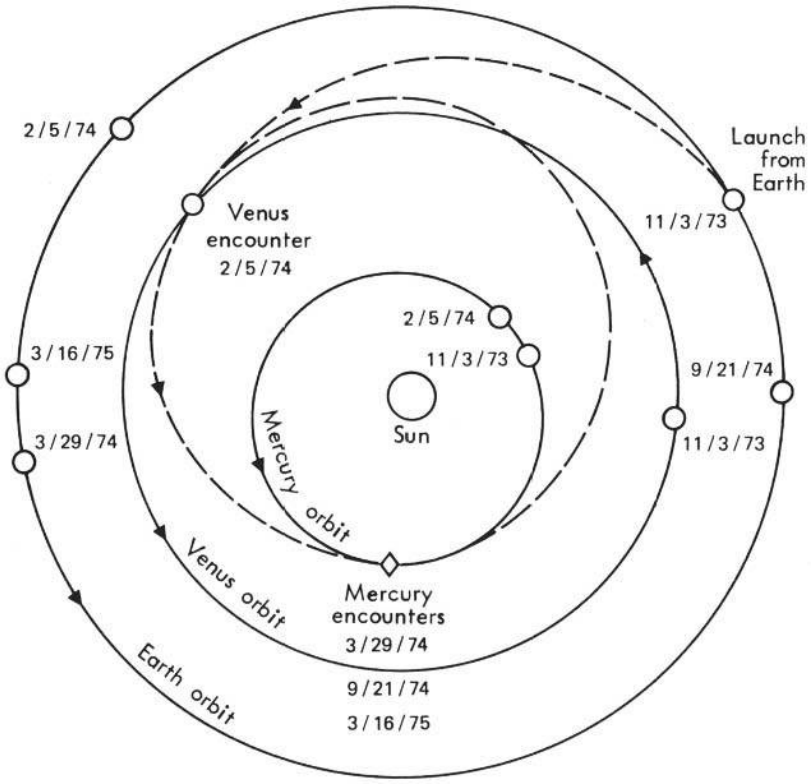

Figure 1.6: Mariner 10 trajectory. Image: NASA.

It returned the first close-up images of Venus. This flyby allowed the spacecraft to slow down and to change its trajectory towards Mercury. Then, it performed three flybys of Mercury on March 29 and September 21, 1974, and March 16, 1975. The first flyby of Mercury occurred at a distance of 705 km at CA, the second one at a larger distance (48,069 km) and the third and final flyby was the closest to the surface, down to 327 km of altitude at CA. The encounters were spaced exactly one Mercury solar day apart, so the same sunlit hemisphere was presented to the spacecraft. They occurred at Mercury's greatest distance from the Sun. Shortly after the final encounter with Mercury, on March 24, 1975, communication with the spacecraft was terminated after a final signal to turn it off.

1.2.1.2 Objectives and payload

The main objective of Mariner 10 was to explore Mercury's atmosphere (if any), surface, environment and physical characteristics and to make similar investigations of Venus. Another objective was to redefine more precisely the mass and radius of Mercury. The greatest scientific priority was given to the study of the interaction between Mercury and the solar wind. This type of information not only helps us understand the environment in which Mercury evolves, but also its internal structure.

To investigate Mercury, Mariner 10 embarked on board seven instruments:

- **TV Cameras**. To image the surface of the planet.
- **Infrared Radiometer**. To measure the infrared radiation and derive the temperature of Venus' atmosphere and Mercury's surface.
- **Ultraviolet Spectrometers**. To detect any atmosphere around Mercury.
- **Plasma Detectors**. To study the interaction of the solar wind with the planet.

- **Magnetometer**. To detect a magnetic field around Venus and Mercury and analyze the interplanetary magnetic field between the various flybys.
- **Charged Particle Telescope**. To detect charged particles in the planet's surrounding environment.

1.2.1.3 Main results

Venus

Although Venus was not the main target of the Mariner 10 mission, the spacecraft used the flyby to take the first close-up images of the planet. The observations revealed, among other, that a Hadley-type circulation existed in Venus' atmosphere and showed that Venus had at best a weak magnetic field, and that the ionosphere interacted with the solar wind to form a bow shock.

Mercury

Mariner 10 obtained images of about 45% of Mercury's surface at an average resolution of 1 km per pixel. Less than 1% of the surface was imaged with a resolution better than 500 m per pixel (Dunne and Burgess, 1978). The images revealed Mercury to be a Moon-like body, with craters, ridges and chaotic terrain (Figure 1.7). As the cameras were equipped with various filters, it highlighted spectral contrasts of the surface. These contrasts may be associated with variations in the surface composition and/or correlated with surface morphology (Robinson and Lucey, 1997).

The Mariner 10 mission discovered the planet's internally generated global magnetic field (Ogilvie et al., 1974; Simpson et al., 1974; Ness et al., 1974, 1975, 1976). This result was completely unexpected due to the size of Mercury and its rotation period. Theoretically, planets generate magnetic fields only if they spin quickly and possess a molten core. However, the rotation period of Mercury is 58 days and its size is so small that its core should have cooled off long ago. An unusual interior could help to explain the differences in Mercury's magnetic field when compared to Earth.

Another great discovery of the mission was the detection of Mercury's exosphere, through observations of emission from atoms of hydrogen and helium (Broadfoot et al. 1974, 1976).

In short, Mercury's lunar appearance suggests that the planet has been extinct and solidified for several years. However its magnetic field indicates an internal structure and dynamics rather similar to that of the Earth. Other questions raised or unanswered by the Mariner 10 mission have initiated the need for a new mission that would place a spacecraft in orbit around Mercury.

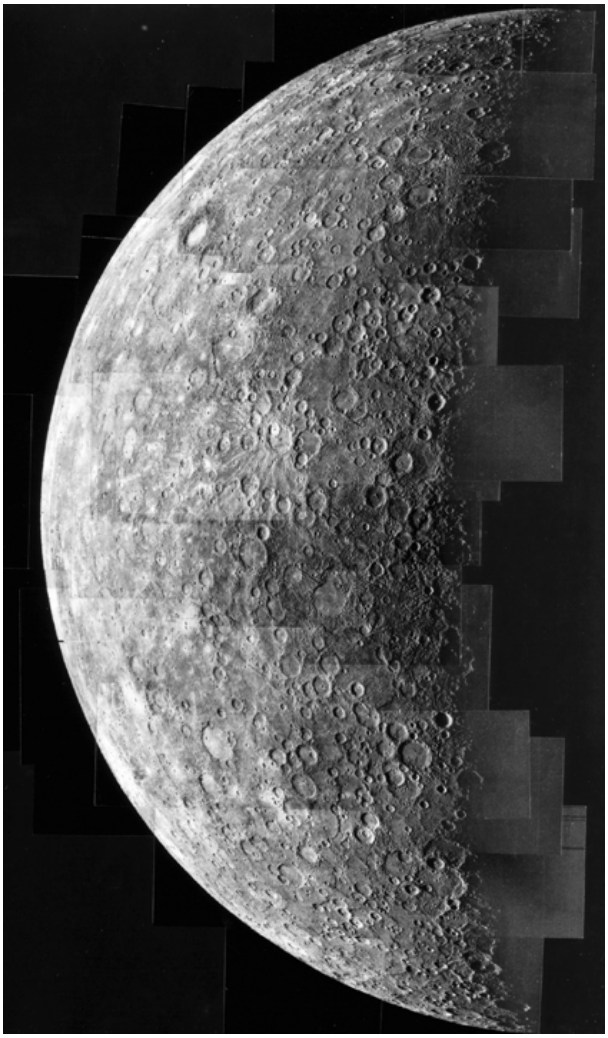

Figure 1.7: Mariner 10 mosaic of Mercury, incoming view from the first encounter. Image: NASA.

1.2.2 MESSENGER

Between the mid-1980s and early 1990s, multiple gravity-assist trajectories were discovered that could achieve Mercury orbit insertion with chemical propulsion systems (Yen, 1989) and important discoveries were made by ground-based astronomy, including the sodium (Na) and potassium (K) components of Mercury's exosphere (Potter and Morgan, 1985, 1986) and the radar-reflective deposits at Mercury's poles (Harmon and Slade, 1992; Slade et al., 1992). All these findings motivated a Mercury orbiter mission. The MESSENGER mission was first proposed in 1996 and then again in 1998 before finally being selected in 1999. The development, integration and testing of the spacecraft began in 2000. Three decades after the first flyby of Mercury by Mariner 10, the MESSENGER mission towards the innermost planet of the solar system was launched. It was the first mission to orbit Mercury. MESSENGER delivered great results, meeting all its scientific objectives. Originally planned for a year, the mission was extended twice, orbiting Mercury from 2011 to 2015, before crashing on its surface.

1.2.2.1 Trajectory to Mercury and orbital phase

The MESSENGER spacecraft was launched on August 3, 2004 on a nearly 7-year cruise to Mercury. Its journey to Mercury included multiple gravity assist maneuvers (Earth, Venus and Mercury) and five major course-correction maneuvers prior to Mercury orbit insertion on March 18, 2011 (Figure 1.8).

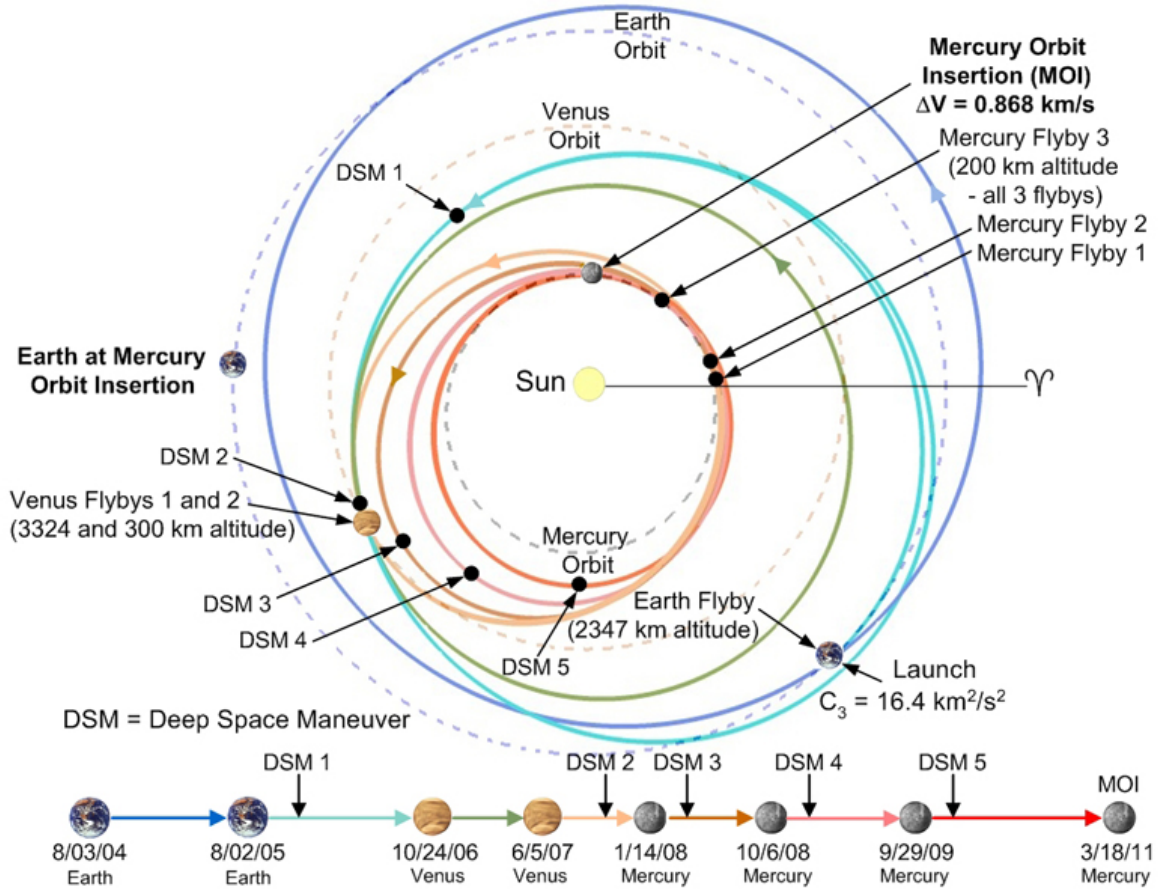

Figure 1.8: MESSENGER trajectory. Image: NASA.

The gravity assist flyby of Earth occurred on August 2, 2005. Instruments used the Earth-Moon system for calibration. It was followed by two flybys of Venus on October 24, 2006 and June 5, 2007 that helped resizing and rotating its trajectory closer to Mercury's orbit. MESSENGER executed three flybys of Mercury, on January 14 and October 6, 2008 and September 29, 2009. The spacecraft approached the planet at ∼200 km on the nightside (Figure 1.9). The encounters provided the first close-up looks at Mercury in more than 30 years. During the flybys, MESSENGER operated all of its instruments and imaged areas of Mercury unseen by Mariner 10. Each flyby was followed by a course-correction maneuver roughly two months later.

On March 18, 2011, MESSENGER was inserted into a 12 hr orbit around Mercury, with a periapsis altitude of ∼200 km and a periapsis latitude of 60°N (Figure 1.10). The highly elliptical orbit allowed the spacecraft to cool down after each close pass over Mercury's hot dayside surface. The orbit was 80° inclined with respect to the planet's orbital plane. During the primary mission (i.e. the first year of operations), the altitude of the periapsis gradually increased and its latitude moved northward, highlighting the effects of the Sun's gravitation pull on the spacecraft's trajectory. A series of maneuvers made it possible to maintain the periapsis between 200 and 500 km of altitude.

At the end of the nominal mission (March 18, 2012), the spacecraft as a whole (payload and platform) was in good health and there was enough propellant left for at least another year of orbital operations. It was then decided to extend the mission by one year. The average altitude was lowered by reducing the spacecraft orbital period from 12 hr to 8 hr (Figure 1.10).

At the end of the first extended mission (March 18, 2013), the scenario repeated itself: the spacecraft and its instruments were in good health and there was still propellant. The mission

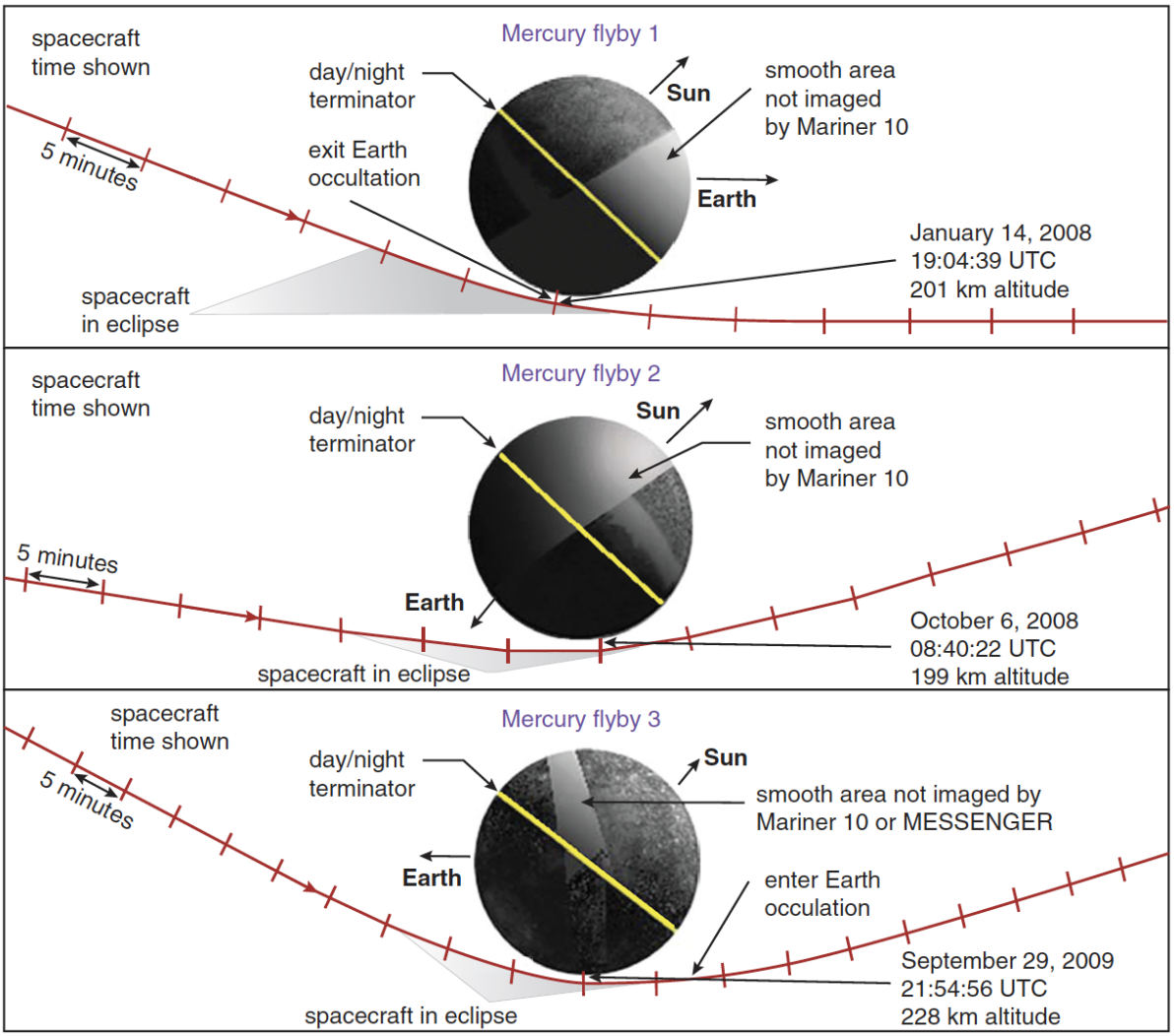

Figure 1.9: Trajectories of the three flybys of Mercury as viewed from above Mercury's north pole. From McAdams et al. (2011).

was granted an additional two-year extension. As MESSENGER's closest approach distance progressively decreased, orbit-correction maneuvers were necessary to raise the orbit. These maneuvers were no longer possible once propellant ran out. The spacecraft eventually impacted the planet on April 30, 2015.

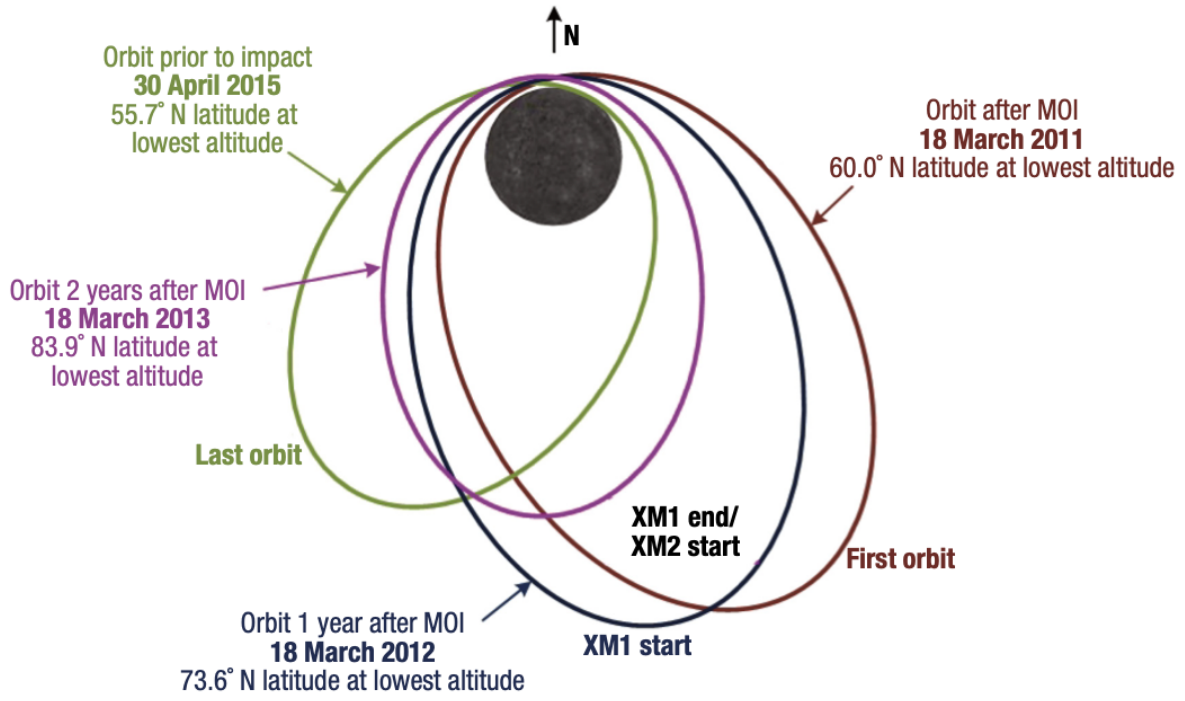

Figure 1.10: Illustration of the orbits of MESSENGER throughout the mission.

1.2.2.2 Objectives and payload

The MESSENGER mission was designed to address six scientific questions (Solomon et al., 2001, 2007) that were driven by the knowledge of the planet at the time the mission was proposed. The questions and their associated objectives are given in Table 1.2. To meet the objectives and requirements of the primary mission, MESSENGER carried seven scientific instruments and a radio science experiment:

- **MDIS**: Mercury Dual Imaging System (Hawkins et al., 2007). Composed of the a monochrome narrow-angle camera (NAC) and a wide-angle camera (WAC). To image the surface of Mercury and investigate the diversity of geological terrains on the planet's surface.

- **GRNS**: Gamma-Ray and Neutron Spectrometer (Goldsten et al., 2007). Composed of separate Gamma-Ray Spectrometer (GRS) and Neutron Spectrometer (NS) sensors. To collect data on the elemental composition of Mercury's crust.

- **XRS**: X-Ray Spectrometer (Schlemm et al., 2007). To study the upper layer of Mercury's crust and monitor X-rays from the Sun bombarding the planet.

- **MAG**: MAGnetometer (Anderson et al., 2007). To characterize Mercury's magnetic field.

- **MLA**: Mercury Laser Altimeter (Cavanaugh et al., 2007). To determine the planet's topography.

- **MASCS**: Mercury Atmospheric and Surface Composition Spectrometer (McClintock & Lankton, 2007). Composed of an Ultraviolet and Visible Spectrometer (UVVS) and Visible and Infrared Spectrograph (VIRS). To detect species in Mercury's exosphere and minerals on its surface.

- **EPPS**: Energetic Particle and Plasma Spectrometer (Andrews et al., 2007). Composed of an Energetic Particle Spectrometer (EPS) and a Fast Imaging Plasma Spectrometer (FIPS). To measure the composition, distribution, and energy of charged particles around Mercury.
- **RS**: Radio Science (Srinivasan et al., 2007). To measure gravity and the state of the core by precisely tracking the spacecraft's trajectory. Note that the telecommunications subsystem was not primarily designed as a scientific instrument.

Table 1.2: Key questions that framed MESSENGER's primary mission.

Guiding question	Associated scientific objective
What planetary formation processes led to Mercury's high ratio of metal to silicate?	Characterize the chemical composition of Mercury's surface, to help in understanding the planet's formation and to test competing hypotheses for why it is so dense
What is the geological history of Mercury?	Determine the planet's geological history by globally imaging the surface at a resolution of hundreds of meters or better
What are the nature and origin of Mercury's magnetic field?	Determine the structure of Mercury's magnetic field by measuring the magnetic perturbations near the planet and throughout the magnetosphere and determine how the magnetic field is generated
What are the structure and state of Mercury's core?	Determine the properties of Mercury's core including its diameter and whether there is an outer fluid core
What are the radar-reflective materials at Mercury's poles?	Determine the nature of the polar deposits including their composition by assaying the volatile inventory at Mercury's poles
What are the important volatile species and their sources and sinks on and near Mercury?	Measure Mercury's exosphere and how it interacts with the magnetosphere and surface

By the end of the primary mission, all of the objectives had been achieved. The results of the nominal mission raised new questions (Solomon and Anderson, 2018) that framed the first extended mission:

1. What are the sources of surface volatiles on Mercury?
2. How late into Mercury's history did volcanism persist?
3. How did Mercury's long-wavelength topography change with time?
4. What is the origin of localized regions of enhanced exospheric density at Mercury?
5. How does the solar cycle affect Mercury's exosphere and volatile transport?
6. What is the origin of Mercury's energetic electrons?

The goals of the second extended mission were based not only on the results from the primary and the first extended missions but also on the particular solar environment of the following years (solar cycle maximum) and the foreseen lower periapsis altitudes that would bring the spacecraft closer to the surface than ever and would allow observations of regions at higher resolutions. The objectives were then captured in seven science questions (Solomon & Anderson, 2018):

1. What active and recent processes have affected Mercury's surface?
2. How has the state of stress in Mercury's crust evolved over time?
3. How have the compositions of volcanic materials on Mercury evolved over time?
4. What are the characteristics of volatile emplacement and sequestration in Mercury's north polar region?
5. What are the consequences of precipitating ions and energetic electrons at Mercury?
6. How do Mercury's exosphere and magnetosphere respond to both extreme and stable solar wind conditions during solar maximum and the declining phase of the solar cycle?
7. What novel insights into Mercury's thermal and crustal evolution can be obtained with high-resolution measurements from low altitudes?

1.2.2.3 Main results

The impact of the spacecraft with the surface of Mercury on April 30, 2015 marked the end of the successful MESSENGER mission after operating for 10 years. The spacecraft spent 4 years at Mercury, whereas only one year was originally planned. The mission fulfilled its objectives and even exceeded expectations with remarkable discoveries and ultimately a better knowledge of the innermost planet. The key results of the mission are presented below.

Volatile-rich planet
MESSENGER measurements have revealed that Mercury is surprisingly abundant in volatile elements, including potassium, sodium, sulfur (S) and chlorine (Cl) (Nittler et al., 2011, Peplowski et al., 2012, Evans et al., 2015). One of the most surprising results regarding the composition of the surface of Mercury is its high S concentration.

Polar deposits
MESSENGER has provided several indicators as to the nature of the deposits in shadowed craters at Mercury's poles. Illumination models and surface temperature derived from the topography show that the radar-bright deposits are located in permanently shadowed craters and that the craters have thermal environments that allow water ice to be stable (Chabot et al. 2012, 2013, Paige et al., 2013). Neutron Spectrometer data showed evidence for the presence of hydrogen (as in water ice) in Mercury's polar region (Lawrence et al., 2013). Multiple volatile organic compounds are present in addition to water ice (Chabot et al., 2016).

Offset magnetic field
MESSENGER's magnetometer observations revealed that Mercury's magnetic dipole is offset from the planet's equator by $\sim$0.2 R_M, therefore, the magnitude of Mercury's magnetic field is $\sim$3 times higher at the north pole than at the south pole (Anderson et al., 2012).

Hollows
MESSENGER identified new surface features that appear to be young and unique to Mercury: the hollows (Blewett et al., 2011). Hollows are shallow, irregular depressions and are

a geologic landform. Their formation seems to be recent and to involve loss of volatile materials.

Volcanic deposit
MESSENGER observed surface features that are consistent with past volcanic activity (Head et al., 2008; 2011). The Mg-rich nature of Mercury's surface materials also suggest that hot lavas formed the surface volcanic deposits (Nittler et al., 2011).

Global contraction
MESSENGER found that Mercury has shrunk by as much as 7 km in radius, a number well above the values previously reported, as its interior cooled and contracted (Byrne et al., 2014).

Seasonal exosphere
The three easiest species to detect in the exosphere of Mercury, namely Ca, Na and Mg, exhibit a relative persistence from year to year and experience seasonal variations with Mercury's distance from the Sun (Burger et al., 2014, Cassidy et al., 2015, Merkel et al., 2017).

Dynamic magnetosphere
MESSENGER results showed a highly dynamic magnetosphere because of the small size of the planet's magnetic field and its proximity to the Sun (Slavin et al., 2012).

Energetic electrons
Mariner 10 had witnessed bursts of energetic particles but due to instrumental limitations, could not determine the nature of the particles or their energy. MESSENGER did. The energetic particles are electrons, not ions, and they have energies from tens to hundred of keV. Largest events were observed around local midnight and at high latitudes, and such events were rare to absent near dawn and dusk (Ho et al., 2012). Smaller events were also seen in the equatorial region at most local times. Electron bursts are thus a quasi-permanent feature of Mercury's magnetosphere.

Field-aligned currents
Magnetic field observations by the MESSENGER spacecraft revealed flow of electric currents along magnetic field lines over Mercury's northern hemisphere (Anderson et al., 2014).

Chapter 2

The BepiColombo mission: a pair of spacecraft to investigate Mercury

The BepiColombo is the third mission to explore Mercury. It was named after the late Giuseppe "Bepi" Colombo, whose trajectory calculations made possible the three close encounters of Mariner 10 with Mercury instead of the only flyby originally planned. The ESA-JAXA joint mission was launched in October 2018 and should be inserted in orbit around Mercury in December 2025 to study the planet during a nominal phase of one Earth year.

In this chapter, I will first describe the development of the mission and its objectives. I will give a brief description of the two science orbiters of the mission: the Mercury Planetary Orbiter (MPO) and the Mercury Magnetospheric Orbiter (MMO or Mio). I will then explain the trajectory of the spacecraft, from the launch to the insertion into orbit of the two spacecraft.

2.1 ESA/JAXA joint mission

The first proposal for a European mission to Mercury came in May 1993. ESA made a Mercury orbiter one of its three new cornerstone missions when the Horizon 2000 science programme was extended in 1994. In October 2000, ESA approved a package of missions for 2008–2013, including the BepiColombo mission. In February 2007, the mission was approved as part of the Cosmic Vision programme. During the design phase in 2008, the mission's mass increased, requiring to change the launch vehicle (Ariane 5 was preferred to the initial Soyuz-Fregat). Final approval for the redesigned mission was given by ESA's Science Programme Committee in November 2009. The initial target launch of July 2014 was pushed back several times, mostly because of delays on the development of the solar electric propulsion system. The BepiColombo mission was finally launched in October 2018 and is now on its way to Mercury.

BepiColombo is the third mission to visit Mercury after NASA's Mariner 10, which flew past the planet three times between 1974 and 1975, and NASA's MESSENGER, which also flew past Mercury three times between 2008 and 2009 before orbiting the planet from 2011 to 2015.

The BepiColombo mission is an ESA-JAXA collaboration to investigate Mercury, the innermost and least explored planet in the inner Solar System. The observations of Mercury from Earth or space have revealed the complexity of the planet and the important interactions between its interior, surface, magnetosphere, and exosphere. The BepiColombo mission is dedicated to the study of Mercury, covering all the layers of the closest planet to the Sun: its interior (internal structure and physical characteristics), surface (composition and evolution) and dynamical environment (magnetosphere and exosphere). The main scientific objectives and questions can be grouped under the following topics:

- Origin and evolution of a planet close to its parent star,

- Structure and composition of the planet's interior,
- Characteristics and origin of its internal magnetic field,
- Structure, composition, origin and dynamics of its exosphere,
- Structure and dynamics of its magnetosphere,
- Exogenic and endogenic surface modifications such as cratering, tectonics, polar deposits and volcanism,
- Test of Einstein's Theory of General Relativity.

The mission aims to enhance our understanding of not only the planet itself but also the process of planetary formation and evolution in the hottest part of the protoplanetary nebula. The study of the planet's surface (impact cratering, volcanism and tectonics) will help to reconstruct the geological history of Mercury. Deciphering the composition of its surface, together with a better understanding of its interior structure and evolution, will provide new insights into the formation of planets. Once in orbit, BepiColombo will take high-resolution (spatial and temporal) observations of the planet, providing the information necessary to compare Mercury's magnetosphere to that of the Earth. Among the planets with a magnetic field (Mercury, Earth, Jupiter, Saturn, Uranus and Neptune), Mercury has the most compressed magnetosphere, allowing the solar wind to interact directly with the planetary surface. Determining the volatile budget of Mercury, its nature and evolution through time is a critical aspect for understanding the source and distribution of volatiles in the Solar System.

All of those important scientific investigations are to be addressed by BepiColombo. Such information cannot be obtained from observations made from Earth. The BepiColombo mission will provide simultaneous measurements from two spacecraft, offering an unprecedented opportunity to investigate magnetospheric and exospheric dynamics at Mercury as well as their interactions with the solar wind, radiation, and interplanetary dust. The mission is in fact composed of two spacecraft, the Europe-led MPO (Section 2.1.1) and the Japan-led MMO (Section 2.1.2). MPO and MMO will travel together to Mercury, attached to the MTM (Mercury Transfer Module), which provides power and propulsion (Figure 2.1). The SEP (Solar-Electric Propulsion) is mission-enabling for the journey to Mercury. Without it, it would not be possible to bring the two spacecraft to Mercury using a conventional launcher. Ion thrusters on the MTM will provide the needed low thrust over long durations of the cruise phase. They will accumulate the highest total impulse ever achieved in a space mission! The mission is very challenging due to its proximity with the Sun. The enormous gravity of the Sun makes it difficult to place a spacecraft into a stable orbit around Mercury. BepiColombo has to constantly brake against the gravitational pull of the Sun. It requires a lot of energy, even more than sending a mission to Pluto! In addition, because of the high temperatures, the solar arrays cannot directly face the Sun for long periods without becoming degraded. Therefore, they have to be rotated away from the Sun (sun incident angle up to 80°), thus requiring a greater area to achieve the same power requirements.

The two-spacecraft interdisciplinary approach of the BepiColombo mission will enable simultaneous measurements at different positions. This resolves a range of spatial and temporal ambiguities that would arise from single point observations, especially for exospheric and magnetospheric observations. In addition, a simultaneous measurement of the magnetic field distinguishes between internal and external sources, thus resolving ambiguities in the internal magnetic field. Characterizing the magnetic field properties with respect to the dynamic solar environment and the implication of Mercury's magnetosphere in the modification and preservation of the Hermean exosphere will explain the role and importance of Mercury's core dynamo.

The specific orbits of the two spacecraft, and more particularly the low altitude orbit of MPO, enable a significantly increased capability for detailed observations (together with a

higher performance of the instruments compared to previous missions). The larger telemetry capability of BepiColombo allows the increased volume of observations to be fully exploited. Moreover, compared with MESSENGER, the southern hemisphere of Mercury will be observed from much lower altitudes. Finally, both MPO and Mio spacecraft carry instruments that were not included in the MESSENGER payload (e.g. thermal infrared spectrometer, a full complement of plasma physics instrumentation, and a radio-science instrument, see sections 2.1.1 and 2.1.2).

All combined (the spacecraft orbits and scientific payload), this allows a wider range of scientific questions to be addressed than those that could be achieved by the individual instruments acting alone, or by previous missions.

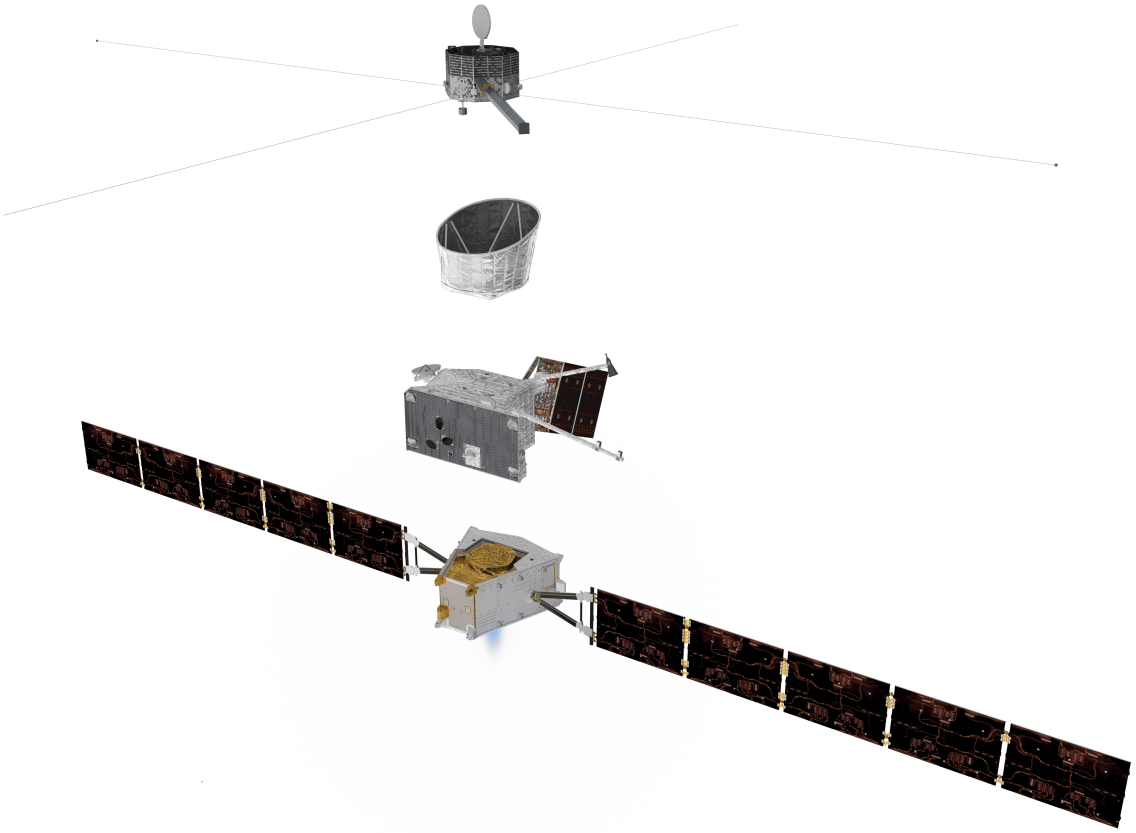

Figure 2.1: Exploded view of the BepiColombo spacecraft components. From bottom to top, these are: MTM, MPO, Sunshield and Interface Structure, and MMO. The spacecraft are shown with solar arrays and instruments deployed. Credit: ESA/ATG medialab.

2.1.1 Mercury Planetary Orbiter

MPO focuses on a global characterisation of Mercury through the investigation of its interior, surface, exosphere and magnetosphere. The three-axis stabilised spacecraft will orbit Mercury in an inertial polar orbit (480×1,500 km) of 2.3 hr period (Benkhoff et al., 2021). It accommodates 11 instruments suites (Figure 2.2), several of which have multiple subsystems:

- **BELA**: BepiColombo Laser Altimeter (Thomas et al., 2021). To characterize the topography and surface morphology of Mercury.

- **ISA**: Italian Spring Accelerometer (Santoli et al., 2020). To study Mercury's interior structure and test Einstein's theory of relativity.
- **MPO-MAG**: Mercury Planetary Orbiter Magnetometer (Heyner et al., 2021). To provide a detailed description of Mercury's magnetosphere and of its interaction with the planetary magnetic field and the solar wind.
- **MERTIS**: MErcury Radiometer and Thermal Infrared Spectrometer (Hiesinger et al., 2020). To determine Mercury's mineralogical composition and obtain a global map of the surface temperature.
- **MGNS**: Mercury Gamma-ray and Neutron Spectrometer (Mitrofanov et al., 2021). To determine the elemental compositions of distinguishable regions over the entire surface of Mercury and to determine the regional distribution of volatile depositions in the polar areas.
- **MIXS**: Mercury Imaging X-ray Spectrometer (Bunce et al., 2020). To obtain a global map of the surface atomic composition.
- **MORE**: Mercury Orbiter Radio-science Experiment (Iess et al., 2021). To determine Mercury's gravity field and the size and physical state of its core.
- **PHEBUS**: Probing of Hermean Exosphere by Ultraviolet Spectroscopy (Quémerais et al., 2020). To characterize the composition and dynamics of Mercury's exosphere.
- **SERENA**: Search for Exospheric Refilling and Emitted Natural Abundances (Orsini et al., 2021) (ELENA: Emitted Low-Energy Neutral Atoms; MIPA: Miniature Ion Precipitation Analyser; PICAM: Planetary Ion Camera; STROFIO: Start from a Rotating Field Mass Spectrometer). To study the interactions among the surface, exosphere, magnetosphere, and the solar wind.
- **SIMBIO-SYS**: Spectrometer and Imagers for MPO BepiColombo Integrated Observatory System (Cremonese et al., 2020). To provide global, high-resolution, and infrared imaging of the surface.
- **SIXS**: Solar Intensity X-ray and particle Spectrometer (Huovelin et al., 2020). To perform measurements of solar X-rays and energetic particles at high time resolution.

During the cruise, and outside the SEP periods, the ISA, MAG, MGNS and MORE instruments are fully operative. Some instruments or sensors (PHEBUS, SERENA and SIXS) are partially or totally obstructed by the MTM and, hence, are not fully operative. When partially blocked, the instruments (or sensors) can still acquire scientific measurements.

MPO is designed to take scientific measurements in all parts of the orbit throughout the Mercury year, implying that most of instruments, on the -Z side of the spacecraft (i.e. facing towards Mercury) are continuously nadir pointing. As a consequence, 5 out of 6 spacecraft faces may be illuminated by the Sun at some point. This leaves only one spacecraft side for a radiator to allow radiation towards deep space and to minimize absorption of heat radiated from Mercury. During the interplanetary cruise phase, the radiator panel of MPO (-Y side) is pointing anti-sunwards, the +Y axis is therefore directed towards the Sun.

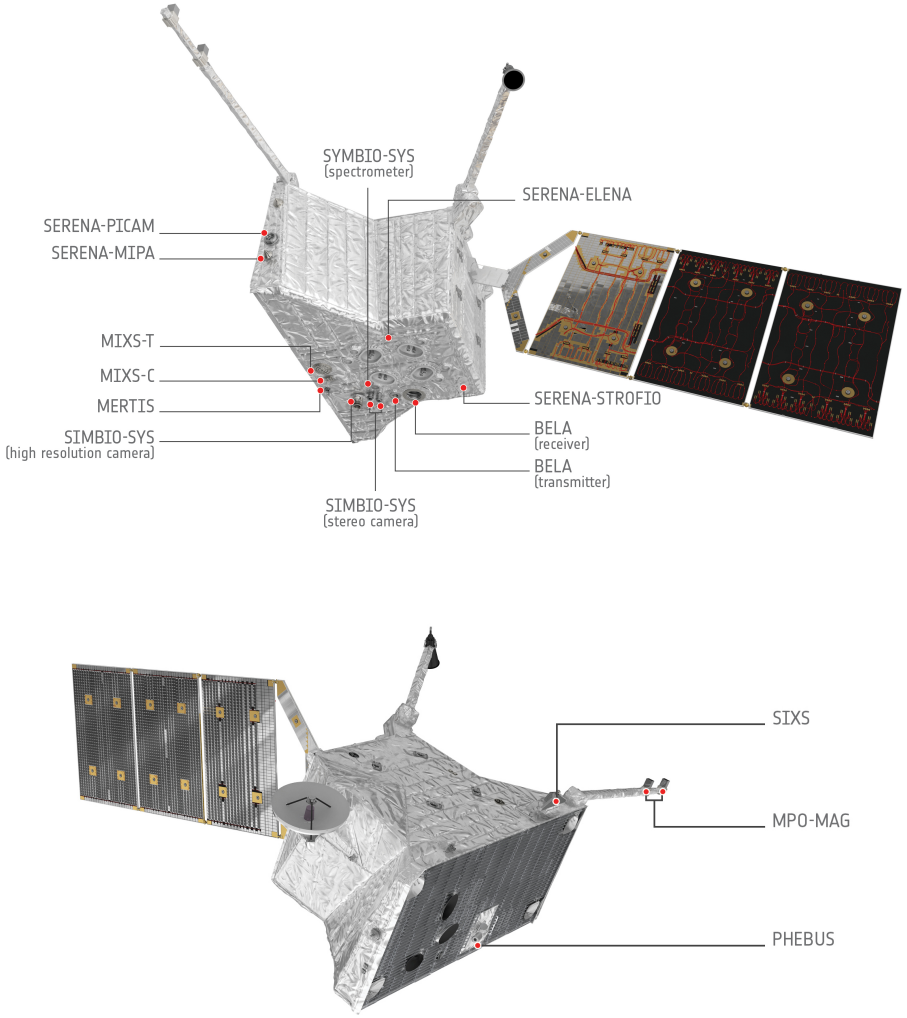

Figure 2.2: The science instruments of BepiColombo's MPO. Credit: ESA/ATG medialab.

2.1.2 Mercury Magnetospheric Orbiter

MMO (also known as Mio) is optimized for in situ plasma and electromagnetic fields and waves measurements in Mercury's orbit. The spin-stabilised spacecraft will operate from a 9.3 hr elliptical polar orbit that will take it between 590 and 11,640 km above the planet's surface. It will make 15 rotations per minute, with its spin axis nearly perpendicular to Mercury's orbital plane (Benkhoff et al., 2021).

Mio has five science instruments (Figure 2.3) dedicated to the study of the planet's exosphere and magnetosphere, and their interactions with the solar wind and the planet itself:

- **MDM**: Mercury Dust Monitor (Nogami et al., 2010). To study the distribution of interplanetary dust in the orbit of Mercury.
- **MMO-MAG**: Mercury Magnetometer (Baumjohann et al., 2010). To provide a detailed description of Mercury's magnetosphere and of its interaction with the planetary magnetic field and the solar wind.
- **MPPE**: Mercury Plasma Particle Experiment (Saito et al., 2010). To study plasma and energetic particles in the magnetosphere and the interaction between the solar wind and Mercury's magnetosphere. Note that this instrument is composed of seven sensors.

- **MSASI**: Mercury Sodium Atmosphere Spectral Imager (Yoshikawa et al., 2010). To measure the abundance, distribution and dynamics of sodium in Mercury's exosphere to investigate its sources and related processes.

- **PWI**: Mercury Plasma Wave Instrument (Kasaba et al., 2010). To perform in-situ and remote-sensing analysis of electric fields, plasma waves and radio waves in Mercury's plasma environment.

During the cruise to Mercury, Mio is partly shielded by the MOSIF (Mercury Magnetospheric Orbiter's Sunshield and Interface Structure), an ESA-built component which provides not only thermal protection but also mechanical and electrical interfaces for Mio. Only a few instruments can then be turned on (MPPE sensors and MDM). Their field of view is however limited by the MOSIF: the instruments can observe only within a conical field of view around the spacecraft -Z axis (Murakami et al., 2020). The MGF and PWI instruments are not deployed yet.

JAXA is responsible for the operations of Mio throughout the mission. For support during the cruise, a subset of the mission control system has been deployed at ESA. Direct interactions between the JAXA Control Center and Mio will occur after Mio's separation in late 2025 (see the following section).

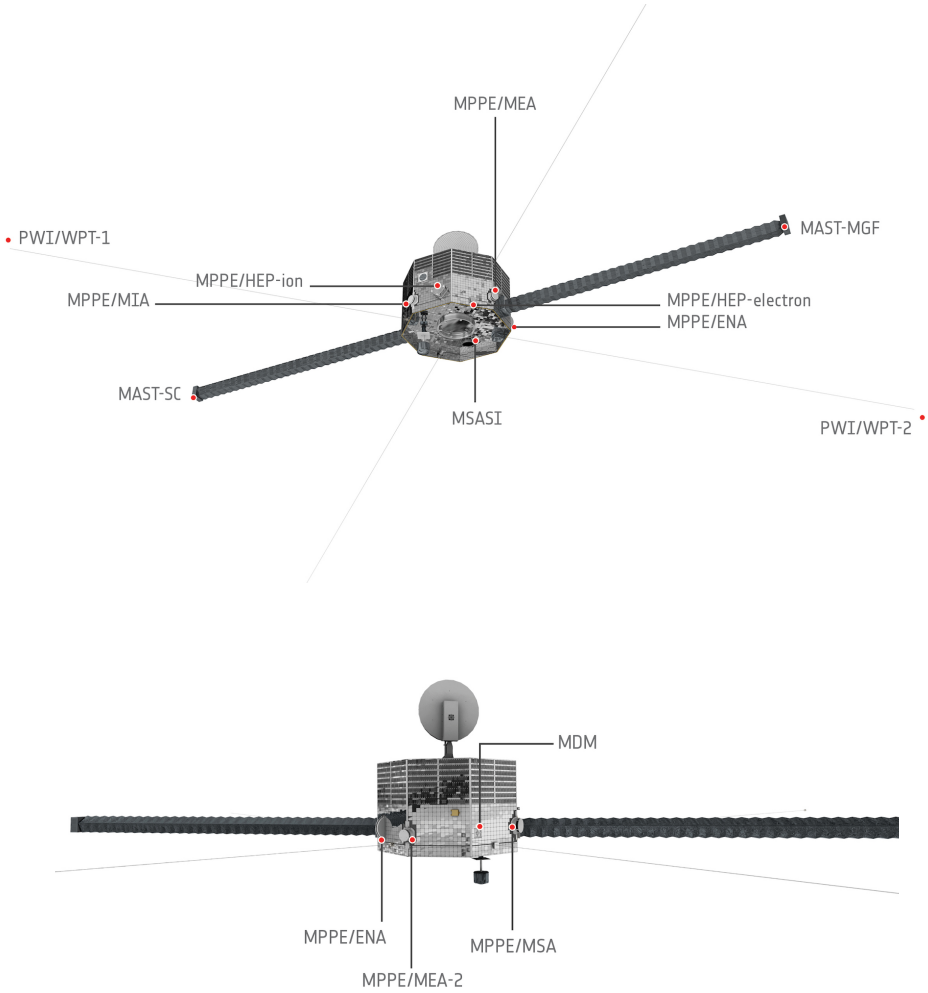

Figure 2.3: The science instruments of BepiColombo's MMO. Credit: ESA/ATG medialab.

2.2 Journey to Mercury

BepiColombo was launched on October 20, 2018 from Kourou, French Guiana, aboard an Ariane 5. The BepiColombo spacecraft will take more than 7 years to reach Mercury and orbit the planet, for a total distance of 9 billion kilometers! To reach its final destination, BepiColombo will use the gravity of Earth, Venus and Mercury (Figure 2.4) in combination with the thrust provided by SEP.

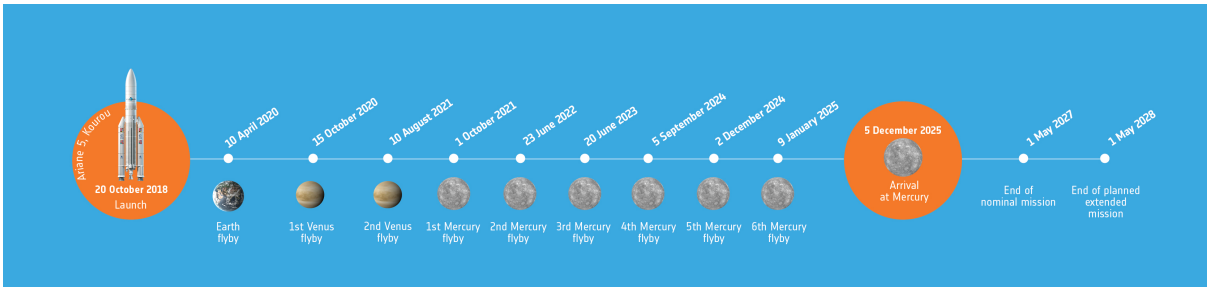

Figure 2.4: BepiColombo timeline. Credit: ESA

The flyby of Earth occurred on April 10, 2020 at a distance of 12,685 km at CA. It was followed by two flybys of Venus, the first on October 15, 2020 (10,631 km at CA), and the second on August 10, 2021 (550 km at CA). Six Mercury flybys, spanned between October 2021 and January 2025, will conclude this sequence of gravity assist flyby maneuvers before arriving in orbit at the end of 2025. Between the planetary encounters, the spacecraft performs SEP thrust arcs. During Earth flyby, the instruments operated for the first time simultaneously, mainly for calibration purpose (the environments of the Earth and the Earth-Moon system are well known). The two flybys of Venus were different in terms of altitude and trajectory. These flybys offered the opportunity to collect valuable science data at Venus (e.g. atmospheric measurements of composition, temperature and wind vertical profiles). The six flybys of Mercury will allow the first observations of the planet up to four years in advance before the spacecraft is placed in orbit. They will provide a taste of the Hermean environment, offering geometric configurations of observations that will not be possible once in orbit. It will also allow investigations of regions that have never been investigated by previous missions.

During the long cruise, the only operation scheduled was the solar conjunction experiment, to be performed by MORE. However, it appeared that certain opportunities for observations had to be seized. As BepiColombo is travelling towards Mercury, different portions of the solar cycle will be covered, starting from the late declining phase of cycle 24 up to the rising phase of cycle 25, expected to peak in July 2025. This represents a unique opportunity to study interplanetary physics under different conditions of the solar activity. In addition, the cruise is the perfect opportunity for coordinated science observations (whether heliospheric or planetary multi-point observations) together with other spacecraft or ground facilities. The opportunity to obtain measurements simultaneously at many different heliospheric locations inside 1 AU (Parker Solar Probe, Solar and Heliospheric Observatory (SoHO), Solar Orbiter) is unprecedented. Also, in addition to Venus flybys, coordinated observations of Venus were made, together with JAXA's Venus orbiter Akatsuki, and with Earth-based telescopes. The different platforms provided different viewing geometries, so that day and night sides of Venus could be captured simultaneously. They also allowed observations with overlapping wavelength range. Mangano et al. (2021) reviews the science objectives to be addressed during the cruise, whether with the planetary flybys or in specific configurations with other spacecraft.

Figure 2.5 depicts the arrival at Mercury timeline. When approaching Mercury, the MTM will be jettisoned and the two science orbiters, still together, will be captured into a polar orbit around the planet. Their altitude will be adjusted using MPO's thrusters until MMO's desired

elliptical polar orbit of 590×11,640 km above the planet is reached. At that point, MMO will be separated in the required attitude, leaving the MOSIF attached to MPO. Later, MPO separates the MOSIF in a safe direction and descend to its own 480×1,500 km orbit using its thrusters. The fine-tuning of the orbits is then expected to take three months. Once the orbit is reached, the final commissioning of the MPO and its payload is performed. Nominal mission science operations in Mercury's orbit are scheduled to last one Earth year (four Mercury years) with the possibility of a one-year extension. The orbital period of MPO is approximately 2.3 hr, which means that ten orbits around Mercury will be performed per Earth day.

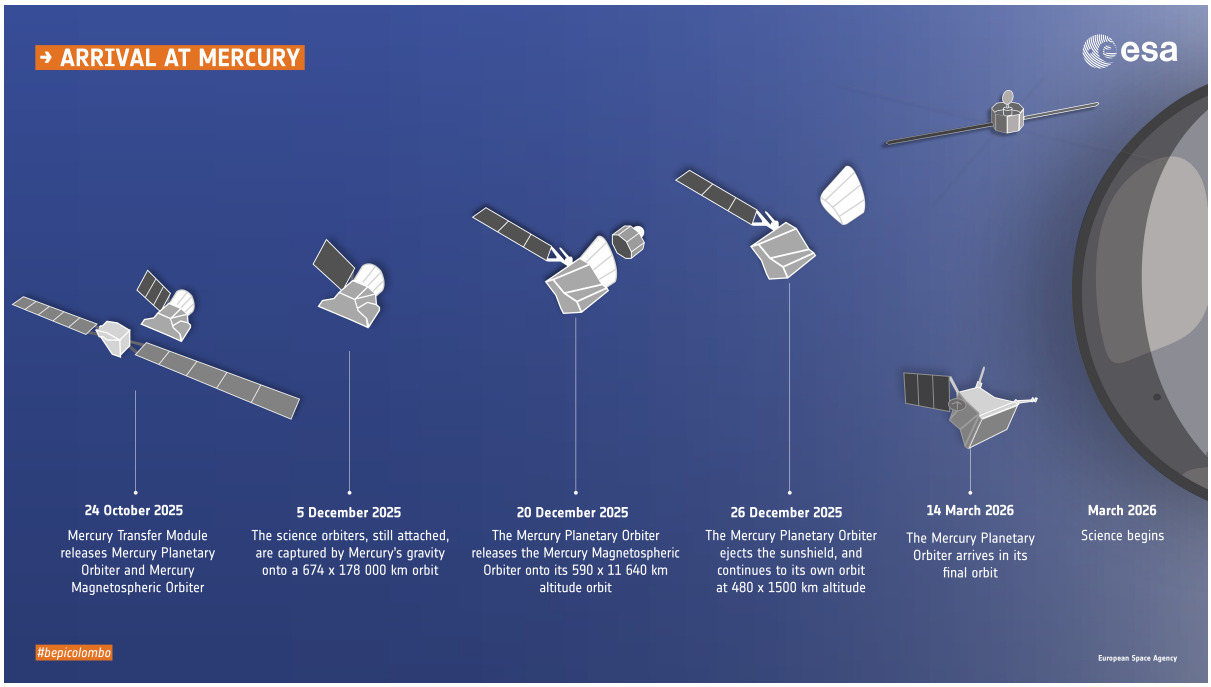

Figure 2.5: BepiColombo arrival at Mercury timeline. Credit: ESA

The orbit of Mercury around the Sun, which takes about 88 Earth days, is divided into four major seasons: Aphelion, Perihelion, and the Terminator seasons in between (Figure 2.6). Since Mercury is in a 2/3 resonance with respect to the Sun, it will be possible to observe almost the whole planet in each of the seasons. The terminator seasons can be treated alike, while the observing and resource conditions of the Perihelion and Aphelion seasons differ significantly.

The observation plan for the nominal mission needs to take into account the environmental conditions and operational constraints. Environmental conditions encompass Earth occultations (Earth is behind Mercury as seen from the spacecraft), Superior and Inferior Conjunctions (Earth behind Sun as seen from the spacecraft), Solar occultations (eclipses) (Sun is behind Mercury as seen from the spacecraft), and the state of the magnetosphere (the orbits of MPO and MMO relative to the Hermean magnetosphere are different depending on the positions around the Sun). Operational constraints encompass mission profiles for data-volume downlink (depending on the distance between Mercury and Earth, the data-rates change), limitations of the Solid State Mass Memory, power limitations and limitations on pointing (off-pointing observations).

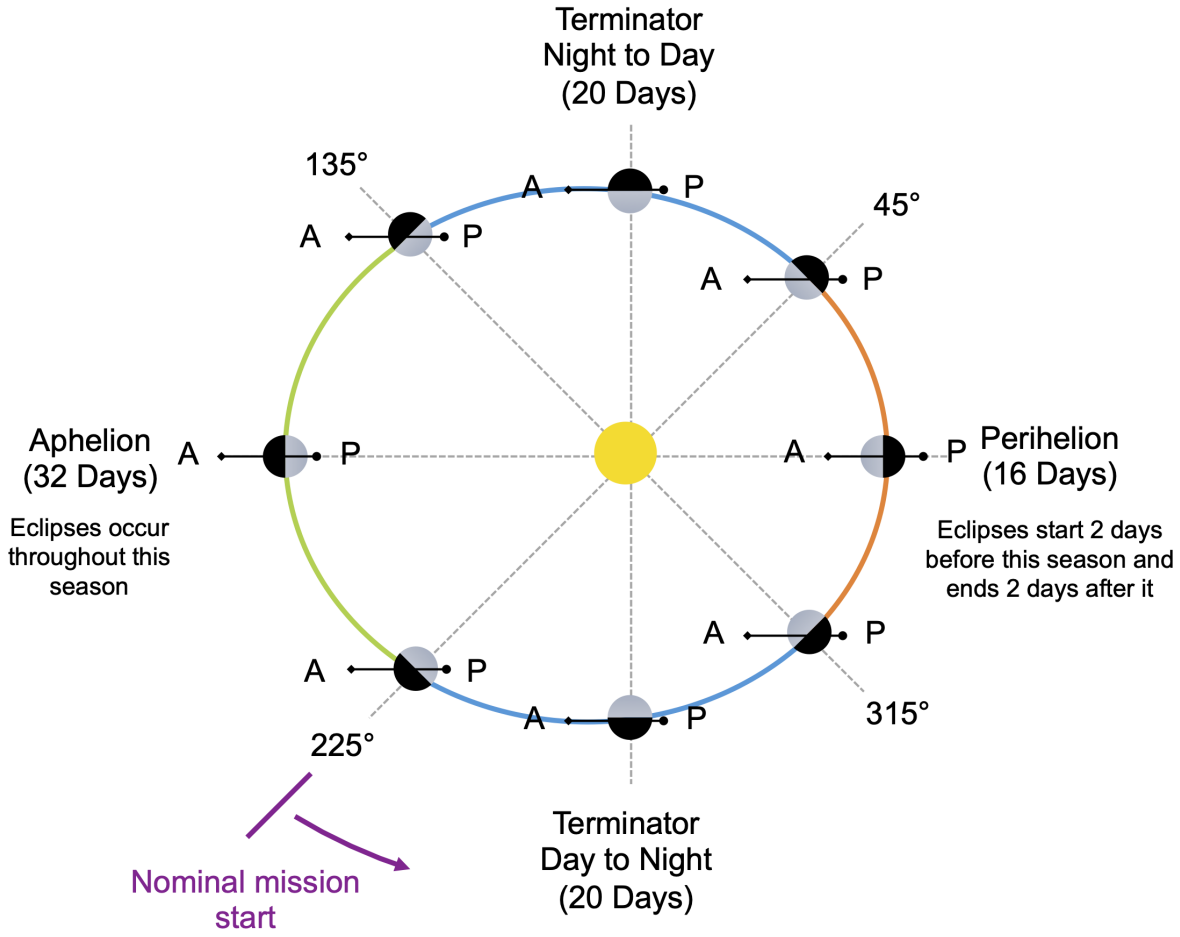

Figure 2.6: Orbit of Mercury around the Sun divided in seasons. The variation of the periherm and apoherm throughout the Mercury year is represented by the black solid lines. The apoherm is denoted by the letter A and the periherm is denoted by the letter P. Note that at perihelion, the MPO's apoherm is on the dayside, while at aphelion, the periherm is on the dayside. Note that apoherm and periherm refer to MPO's orbit around Mercury.

Chapter 3

PHEBUS, the UV spectrometer on board BepiColombo

PHEBUS, an acronym for Probing the Hermean Exosphere By Ultraviolet Spectroscopy, is an ultraviolet spectrometer on board MPO, with two additional visible channels. It has been developed as a cooperation between three institutes from France, Japan and Russia. Italy provided ground facilities for calibration in the vacuum ultraviolet. The instrument design, along with its objectives, ground calibration and planned measurements are presented in Chassefière et al. (2010) and Quémerais et al. (2020). Parts of this chapter are freely inspired by these papers.

In this chapter, I will give a brief history of the instrument development, then highlight the scientific objectives of the instrument. I will subsequently detail the optical layout of the instrument and describe the different sub-systems composing PHEBUS. Finally, I will discuss the operations, both in cruise and in-orbit, along with the tools that have been developed to prepare the operations.

3.1 Development of the instrument

Under French responsibility, the PHEBUS spectrometer was designed in cooperation with Japan, Russia and Italy. From 2004 to 2007, the instrument went through a series of prototypes before the final design was selected. It follows almost 7 years of developing different models (optical prototype, structural and thermal model, electric model) before obtaining a qualified model, then a model suitable to be embarked on a spacecraft, a flight model. Once the instrument was assembled at LATMOS, it underwent a series of environmental tests to validate the expected mechanical requirements, verify the robustness during launch, the resistance to high temperatures and the electronic performance.

After 10 years of development and validation, PHEBUS was integrated in spring 2015 on the MPO spacecraft. A new series of tests was then performed with the fully assembled spacecraft.

3.2 Scientific objectives

The PHEBUS instrument aims to better understand the coupling between the surface, the exosphere and the magnetosphere of Mercury. Its scientific objectives can be summarized as follows:

- **Composition and vertical structure of the exosphere**: PHEBUS will perform vertical scans of the exosphere all over the planet. Such scans will provide information about the composition, temperature, and release processes (variations with altitude would denote the presence of populations generated by different sources).

- **Exosphere dynamics**: PHEBUS complete coverage of the planet in terms of longitude (i.e. local time) and latitude, will allow to track the different species in the exosphere of Mercury from dayside to nightside. It will provide information about local transient active regions (e.g. the cusp regions) and episodic transport in the exosphere.
- **Orbital variation and variations due to transient events**: By measuring the densities of the species present in the exosphere of Mercury over several Mercury years (four years at least), we shall be able to differentiate the effects of the different release processes. For example, the release of species by interplanetary dust vaporization is seasonally variable while sputtering in cusp regions is variable on shorter timescales, as related to solar wind (variable) and solar events (sporadic) (Orsini et al., 2018).
- **Exosphere-Magnetosphere coupling**: In synergy with other instruments on board MPO and MMO, PHEBUS will study the coupling between the exosphere and the magnetosphere of Mercury. It will track planetary ions, from their formation regions in the exosphere (by neutral ionization), through the magnetosphere, until their escape or reimplantation onto the surface of the planet.
- **Escape, source-sink balance, geochemical cycles**: In synergy with the results of geochemical instruments (e.g. MIXS), PHEBUS results will be used to characterize the composition of eroding regolith. Comparing the escape rate and the exospheric density for each species, it will be possible to estimate the residence time of a given species in the regolith-exosphere system, and, more generally geochemical cycles and source/sink balance.
- **Surface studies**: PHEBUS will observe Mercury nightside, especially the PSRs, to search for water ice which may be present in some high-latitude craters. If present, water ice will be detected by variations of the surface albedo at the Lyman-α line (121.6 nm): at this wavelength, the emission from the surface should lower in presence of water ice.

We can also mention secondary objectives related to solar and heliospheric physics:

- **Interaction of the interstellar gas with the solar environment**: PHEBUS will measure the sky background at resonance lines of He (58.4 nm) and H (121.6 nm). The measurements will be done from locations never explored before, providing unprecedented information on the interstellar gas in the heliosphere and its interactions with the solar wind.
- **Stellar physics**: PHEBUS will observe hot UV stars (especially during stellar calibration).
- **Comets and small bodies**: If the opportunity arises, PHEBUS will make UV observations of comets and asteroids in the inner heliosphere.
- **Zodiacal light**: PHEBUS will monitor the zodiacal light with its visible channels. This objective was recently added, following observations made during the cruise. The Bepi-Colombo will provide unprecedented vantage points at small solar distance.

3.3 Instrument description

PHEBUS is a double spectrometer (EUV and FUV detectors) with two additional visible lines at 404.7 nm and 422.8 nm (c404 and c422 channels). The EUV detector actually operates in the EUV (Extreme UltraViolet) and FUV (Far UltraViolet) (55-155 nm) while the FUV detector operates in the FUV, MUV (Middle UltraViolet) and NUV (Near UltraViolet) (145-315 nm) (see Figure 3.1).

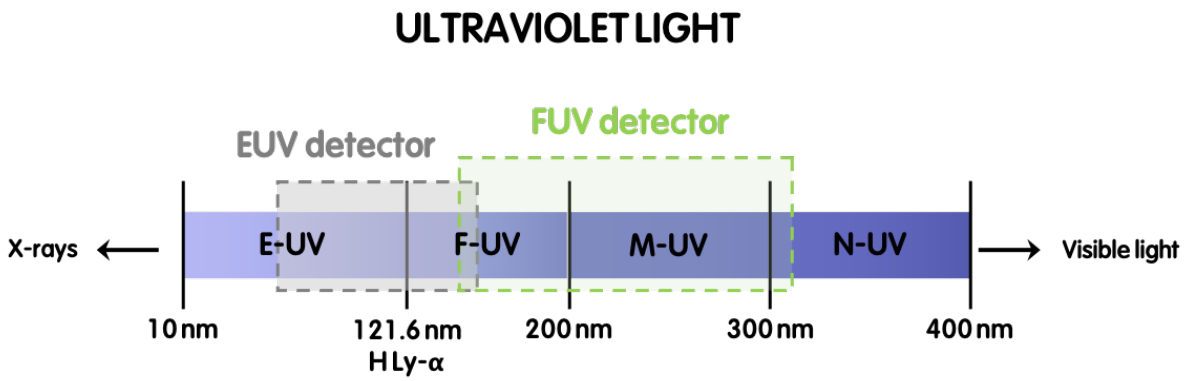

Figure 3.1: Spectral range of PHEBUS UV detectors.

The instrument is located on the radiator panel of MPO, with a rotating baffle extending outside the radiator panel. A combination of a rotating primary mirror and baffle allows changing the pointing direction of PHEBUS FoV (Field of View). When the instrument is not operating, the baffle is positioned in front of a parking bracket which blocks the light. This is called the safe position.

PHEBUS is an instrument for detecting light emission from Mercury's exosphere whose measuring principle is emission spectroscopy (Figure 3.2). When one of the electrons of a chemical species (atom, ion, molecule) of the exosphere of Mercury absorbs a photon from the Sun, this electron passes from the basic energy level (state of rest) to a higher energy level (excited state). The lifetime of an excited state being very short (1 to 100 nanoseconds), the electron falls back into its resting state by emitting in turn a photon whose wavelength is specific to the chemical species. These are the photons that PHEBUS will detect. To count these photons according to their wavelength is to identify the chemical species that emitted them.

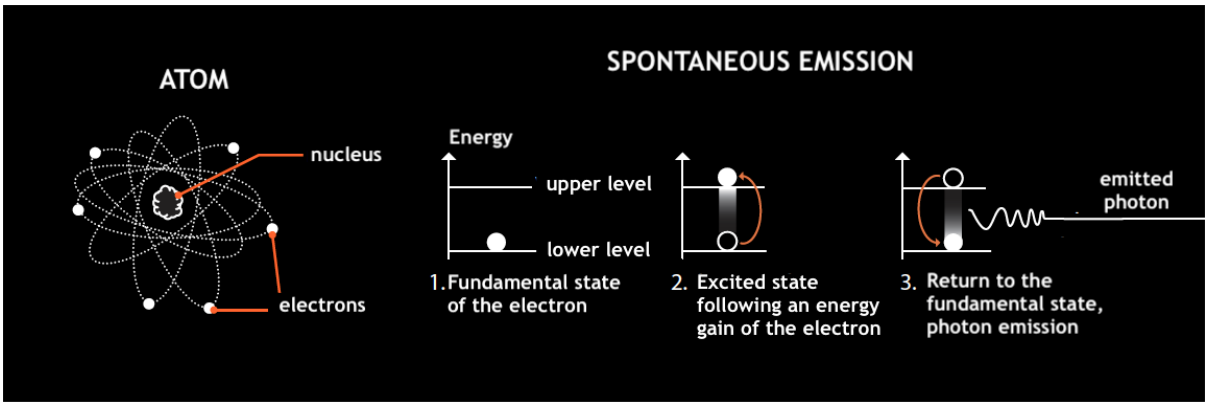

Figure 3.2: Emission spectroscopy. Credit: PHEBUS team.

3.3.1 Optical layout

The optical configuration of PHEBUS can be divided in two parts: the collecting part and the spectrometer part (Figure 3.3). The collecting part consists of a straylight rejection baffle, an entrance pupil and an off-axis parabolic mirror. The spectrometer part is composed of an entrance slit, two holographic gratings and the detectors (including the visible channels paths).

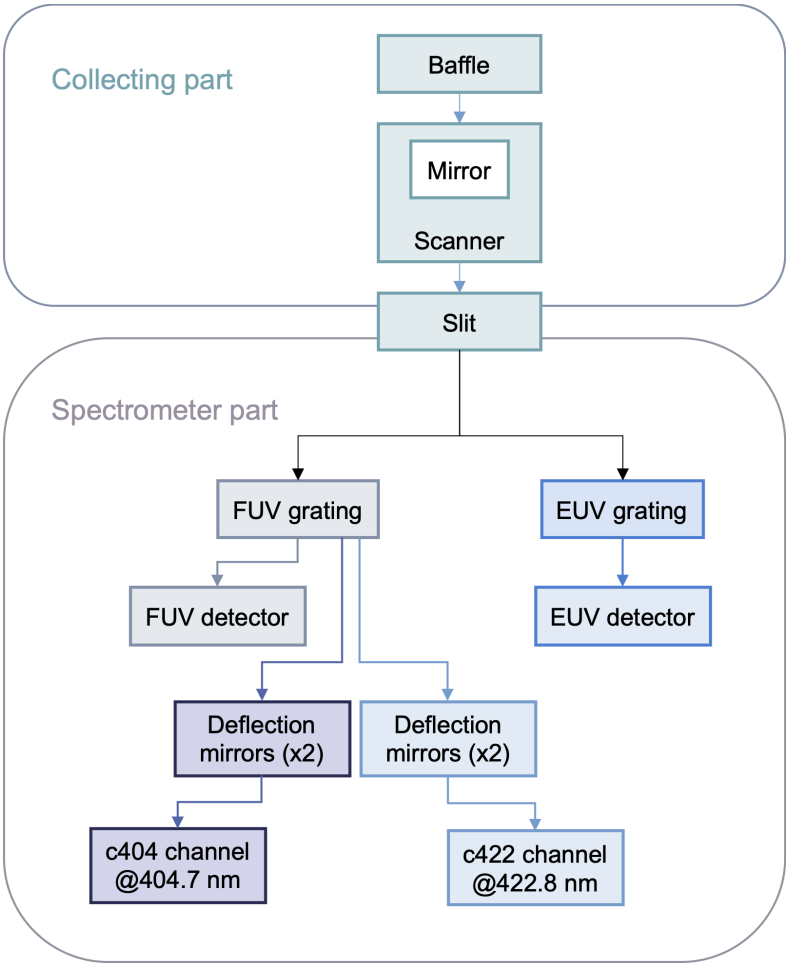

Figure 3.3: PHEBUS optical schematic

Photons from the observed source enter the baffle and reach the primary mirror (Figure 3.4). They are subsequently focused on the slit at the focal plane of the primary mirror. Then, they reach one of the two holographic gratings that share the pupil. Both gratings focus the photons at a position depending on their wavelength. The two UV detectors are positioned along the focal planes of the gratings according to the desired spectral range. By design, photons measured by the two visible channels (c404 and c422) are reflected by the FUV grating and are caught by two mirrors positioned to the spots corresponding to the 404 nm and 422 nm wavelengths. The separation between the two mirrors is large enough so that we would expect that there is no cross-talk between the two channels for photons scattered by the FUV gratings. However, visible photons are also scattered by the EUV grating and the positions of the mirrors allow photons at 422 nm to be caught by the mirror of c404. This is why there is a small contamination (cross-talk) of the c404 channel by the Ca emission.

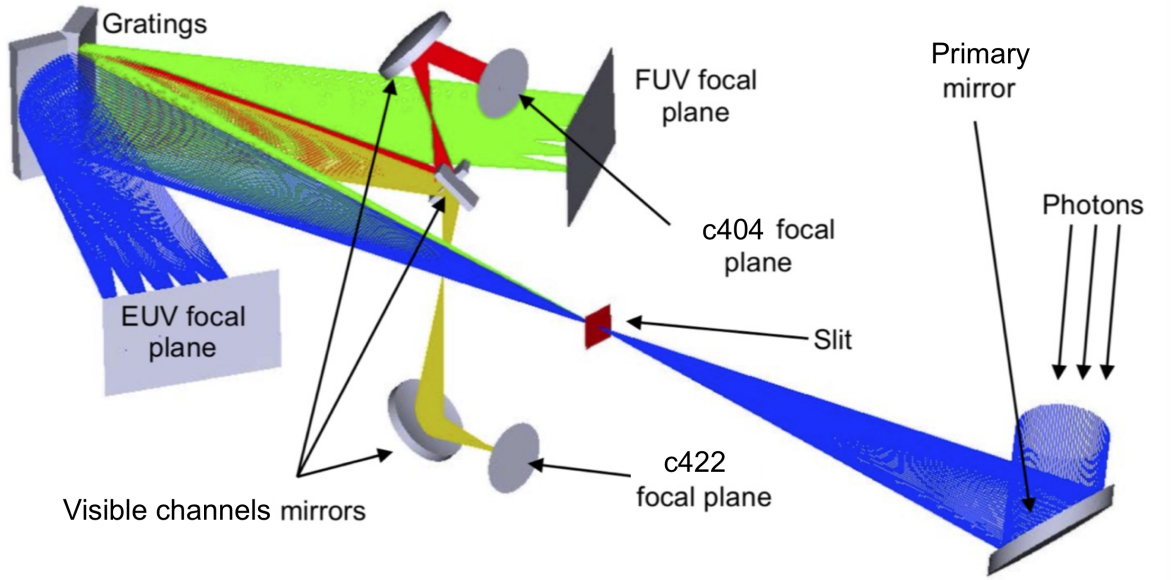

Figure 3.4: 3D view of PHEBUS optical layout. Adapted from Quémerais et al. (2020).

In order to limit the straylight inside the instrument, some internal baffles are accommodated along the optical path between the slit and the detectors. The main one is located just in front of the gratings, in order to avoid second-order pollution of one spectrometer to the other one (Figure 3.5). Another baffle is installed around the slit. A zero order trap is also installed on each detector, still with the objective to reduce the straylight level.

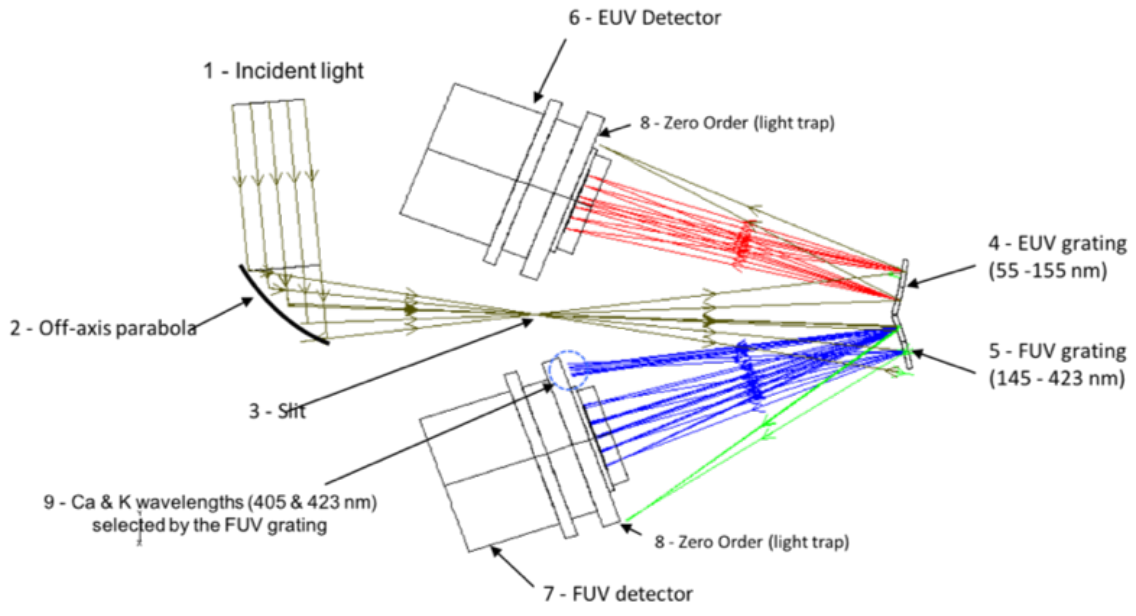

Figure 3.5: 2D view of PHEBUS optical layout. Adapted from Mariscal et al. (2019).

3.3.2 Sub-systems

3.3.2.1 Entrance baffle

The entrance baffle has the difficult task to avoid direct illumination of the entrance mirror due to bright sources located outside a rejection angle of ±8.3°. In addition, the diffused straylight induced inside the baffle must be mitigated as much as possible before reaching the entrance mirror thanks to multi-reflections. To fill these optical constraints, the baffle was designed as a cylindrical body composed of four stages and five diaphragms (Figure 3.6).

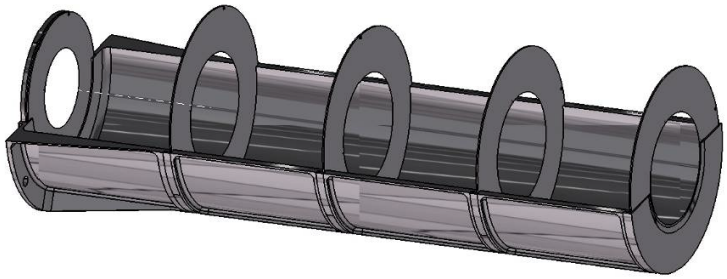

Figure 3.6: Mechanical drawing of the entrance baffle. The leftmost diaphragm is the entrance pupil. Adapted from Mariscal et al. (2019).

For light coming from outside the rejection angle, this geometry enforces a minimum of two diffuse reflections on the surfaces before entering the instrument and only one diffuse reflection on the edges (Figure 3.7). The high level of attenuation is reached thanks to the high quality of the inner surfaces. Such a level of attenuation is necessary to perform exospheric observations as close as the guard angle value from Mercury's illuminated surface.

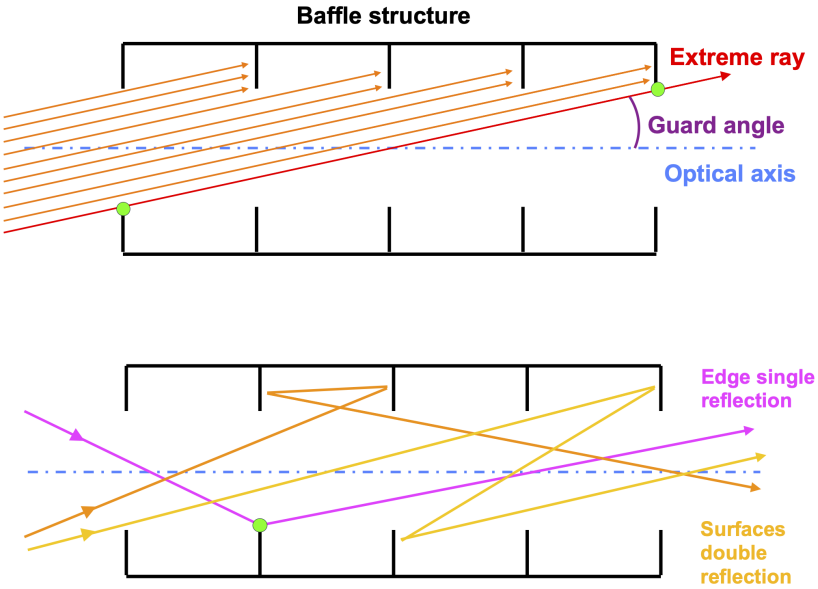

Figure 3.7: Illustration of the geometrical properties of the entrance baffle: rejection angle and minimum number of reflections on surfaces and edges.

3.3.2.2 Entrance mirror

The entrance mirror is positioned just after the baffle exit and is accommodated inside the rotating mechanism. This subsystem has to focus the light beam onto the entrance slit. The mirror substrate is made of Silicon Carbide (SiC). To improve its reflectivity, it is coated with SiC powder. It offers a homogeneous mirror in terms of material and thermal behavior, which is very important in the PHEBUS case, since the mirror is accommodated on the outside part of the spacecraft so within a difficult thermal environment. The design of the mirror was driven by two main constraints:

- surface reflective roughness (for nominal exospheric observations, to avoid as much as possible straylight inside the instrument),
- surface figure error (for stellar calibration, to limit the star image size within the focal plane)

3.3.2.3 Scanner mechanism

The main function of the PHEBUS scanner mechanism is to point the spectrometer's boresight to the desired location. It allows the baffle and the mirror to rotate 360° around the optical axis of the spectrometer. As the mirror rotates, the projection of PHEBUS FOV over the sky varies with the scanner angle.

Figure 3.8 illustrates the geometry in MPO reference frame (X,Y,Z). PHEBUS is mounted on the -Y side (i.e. radiator side). The scanning motor rotation axis is defined by the -Y axis. The scanner position is defined by its angle in the (X,Z) plane. The reference position of the scanning mechanism (i.e. origin of the angle) is defined by the position of the parking bracket. It is placed at 45° from the -Z axis. The motor steps are defined on 12 bits (4096 values), one step value corresponding to an angle of $\frac{360}{4096}$°.

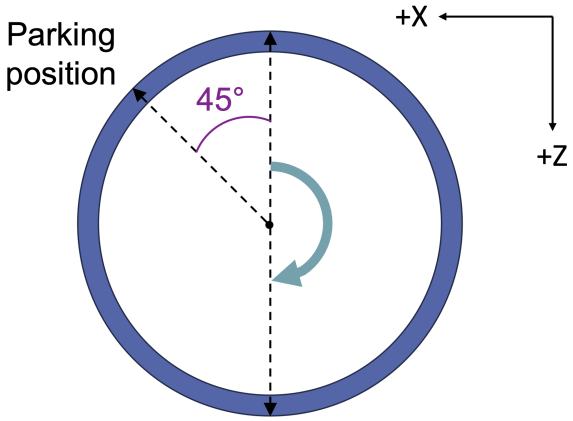

Figure 3.8: Angle and orientation definition. The arrow shows the positive direction, i.e. positive angle around +Y.

The scanner mechanism is equipped with a photometer to monitor the luminosity level, and with a high-speed shutter to the detectors of the spectrometer against inadmissible levels of light exposure (e.g. from Mercury lit surface or the Sun). If the light level detected by the photometer is higher than a pre-defined threshold, the shutter is closed.

3.3.2.4 Slit

The slit is accommodated at the focal plane of the entrance mirror. The slit width of 0.1° is optimized for in-orbit exospheric observations in order to maximize the spectrometer resolution.

For star calibration while in orbit around Mercury, the (apparent) angular velocity of a star in the frame of MPO is about 0.04°/s (due to the orbital period of 2.3 hr). Knowing that the angular width of the nominal slit is 0.1°, it results that a star cannot remain within the slit more than 2s in a passive configuration. To solve this problem and get 100% of the star flux, it is then necessary to significantly increase the FOV. To do so, the slit is mounted on a rotating mechanism which is linked to a two-positions actuator (*Across* or *Removed*), allowing to remove it for the observation of stars. In that case, the FOV is only limited by the scanner internal parts (i.e. the entrance pupil at the end of the baffle). By removing the slit, we can increase the solid angle of the instrument by a factor 22, which means that the count rate on an extended source increases by the same factor. It also decreases the spectral resolution for an extended source by a factor 10.

The FOV of the PHEBUS corresponds to the slit projection on the sky, through the entrance pupil. The paraxial FOV is 2° by 0.1°. When the slit is removed, the FOV is extended: 3.1° by 1.4° (Figure 3.9).

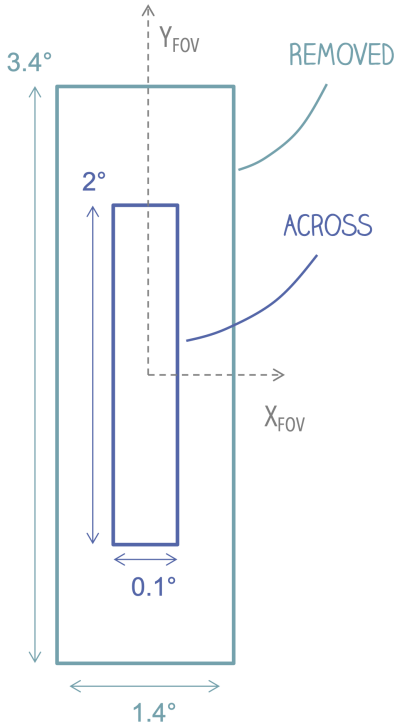

Figure 3.9: Definition of the PHEBUS FOV with the slit across or removed (not to scale).

The FOV direction is represented by 3 vectors in the URF (Unit Reference Frame), forming a right-handed reference frame:

- X_{FOV} defines the direction of the spectral axis (perpendicular to the slit),
- Y_{FOV} defines the direction of the spatial axis (along the slit),
- Z_{FOV} defines the direction of the center of the FOV.

In the URF, the vector coordinates are expressed as follows:

$$Z_{FOV} = \begin{bmatrix} \sin D \cos\left(S - \frac{\pi}{4}\right) \\ \cos D \\ -\sin D \sin\left(S - \frac{\pi}{4}\right) \end{bmatrix}$$

$$Y_{FOV} = \begin{bmatrix} \sin^2(D/2)\cos(2S) \\ -\sin D \sin\left(S - \frac{\pi}{4}\right) \\ -\sin^2(D/2)\sin(2S) - \cos^2(D/2) \end{bmatrix}$$

$$X_{FOV} = Y_{FOV} \times Z_{FOV}$$

where D is the deviation angle of the parabolic entrance mirror (D = 100°) and S is the position angle of the scanner, knowing that the reference position (S = 0°) is defined in front of the parking bracket and centered at 45° between the +X and -Z axes of the spacecraft (Section 3.3.2.3).

The URF is related to the MPO reference frame as follows:

$$\begin{pmatrix} x_{\text{MPO}} \\ y_{\text{MPO}} \\ z_{\text{MPO}} \end{pmatrix} = \begin{pmatrix} -z_{\text{URF}} \\ y_{\text{URF}} \\ x_{\text{URF}} \end{pmatrix}$$

3.3.2.5 Gratings

Light dispersion is performed by two aberration corrected holographic gratings. This technology allows a low level of scattering, which is required to perceive some faint emission lines close to some bright other lines. Also, having only one component that spreads and focuses the spectrum from the slit onto the detector helps to limit losses due to reflection losses.

The spherical holographic diffraction gratings diffuse at all wavelengths, the position of the detector with respect to its grating defines the bandwidth.

3.3.2.6 UV detectors

The EUV and FUV detectors share the same architecture (Figure 3.10):

- A photocathode to generate photo-electrons (CsI for EUV, CsTe for FUV),
- A 5-stage MCP (Micro-Channel Plate) to multiply electrons,
- A RAE (Resistive Anode Encoder) to collect the electron cloud in terms of charge and position.

The spectrum detection is based on the photon counting method. The principle is the following: an incident photon strikes the photocathode, emitting photo-electrons that will be amplified by the MCPs in order to generate a cascade of electrons. At each impact on the MCPs, the electron is accelerated and multiplied several million times thanks to a high voltage (up to 5 kV) to form an electron cloud output. The electron cloud is then collected by the conductive area of the resistive anode, on which it disperses creating electric currents to its four corners. These currents are measured by an encoder (RAE) which calculates the position of the stacking point on the anode that mirrors the point of impact of the photon on the photocathode. Discriminators are used to filter the events according to their charge. Figure 3.11 shows Pulse Height Distributions measured for the FUV Flight Model at different HV (High Voltage) during ground calibrations. As the HV increases, the peak moves to higher gain (i.e. total charge of the electron cloud generated by a single photo-electron). The discriminator value is close to 0.5 pC. The nominal value of the HV is chosen when the peak gain is close to 2 pC. Increasing the HV would not increase the number of photo-electron counted.

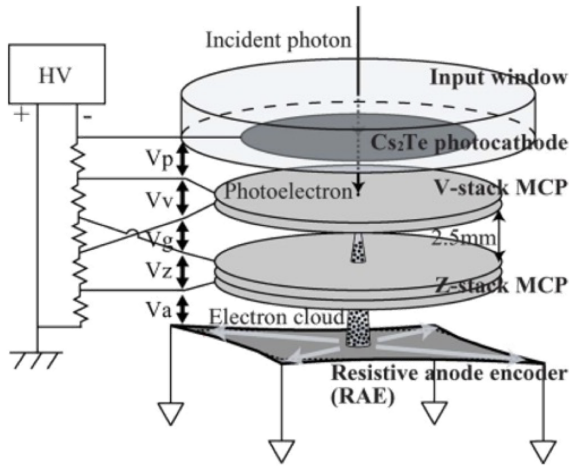

Figure 3.10: Illustration showing the architecture of the UV detectors. Credit: PHEBUS team.

An Analog-to-Digital Converter (ADC) is used to determine the impact position of the electron cloud. A barycenter calculation (4 outputs, one at each corner of the RAE) allows a 2-D localization of the electron cloud but note that the two axes are measuring different things. One axis gives a spectral dimension, and the other a spatial dimension. We call the resulting data *virtual pixels*. The active region of both detectors is 40×25 mm^2, which is equivalent to an array of 1024×512 virtual pixels (spectral×spatial). The 2° slit is imaged onto the central pixels while the remaining pixels are used for dark current[1] monitoring.

The detectors require a power-supply to accelerate the electrons. The nominal voltage at the beginning of the mission is around 3.5 kV for the EUV, 4.8 kV for the FUV.

The EUV and FUV detectors cannot be operated simultaneously as the instrument Data Processing Unit (DPU) cannot process two images simultaneously. Moreover, this would have required too much power from the spacecraft platform.

[1]The dark current is a residual current due to thermal agitation of electrons.

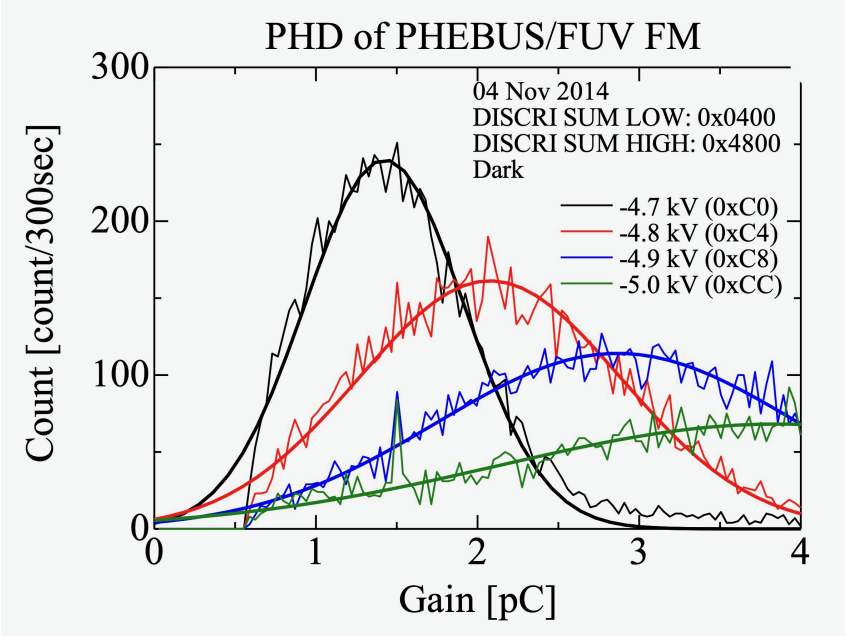

Figure 3.11: Pulse Height Distribution (PHD) for various HV values. The nominal HV is the one with a peak at a gain of 2 pC (i.e. 4.8 kV). The gain represents the charge of the electron cloud. The discriminator (a.k.a. discri) is proportional to this gain. The selection of the discri allows to filter the electron cloud according to their charge. By increasing the discri, the electron cloud with low charge are not counted.

3.3.2.7 Visible channels

Two visible channels (previously denominated NUV channels, standing for Near UltraViolet) complete the instrument. Both channels are very similar. Each visible channel uses a set of two mirrors to deviate the specific rays of potassium (K) at 404.7 nm and calcium (Ca) at 422.8 nm from the spectrum dispersed by the FUV grating. A PMT (Photo-Multiplier Tube) operated in photon-counting mode is used on each channel to measure the intensity of each line.

A PMT consists of a photoemissive cathode (photocathode) as a photon-electron conversion element, an electron multiplier as amplifier and an anode as electron collector, assembled in a vacuum tube (Figure 3.12). When a photon strikes the photocathode, photoelectrons are created and emitted from the photocathode. These photoelectrons are directed by focusing electrode voltage towards the electron multiplier (i.e. a series of dynodes), whose purpose is to transform the photoelectron in a packet of electrons. The collision of the photoelectron with the dynode releases several new electrons, which are subsequently accelerated into another dynode. Finally, the secondary electrons are collected by the anode as output pulses.

In the rest of this manuscript, the channel dedicated to potassium will be denoted as c404 channel, while the channel dedicated to calcium will be denoted as c422 channel.

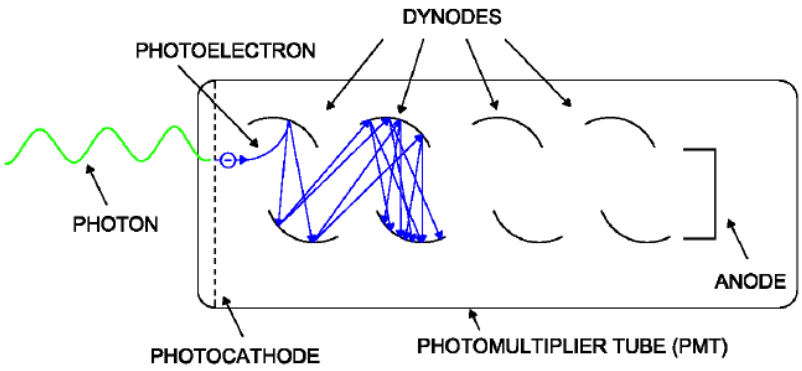

Figure 3.12: Photomultiplier tube scheme with secondary electron emissions. From Bednarski et al. (2014).

3.3.3 Anomalies

3.3.3.1 EUV discharges

From the commissioning of the detectors in 2019, "events" spontaneously occurred on the EUV detector. These events manifest as a count rate increase along with an HV drop. The symptoms are quite stable but the conditions under which the events occur (e.g. temperature, HV value, HV ramp procedure, mode - whether during science acquisition or HV ramp) are not similar. We have conducted test campaigns with the same parameters as those used during observations without an event, but this time, events occurred. The conditions are then not reproducible.

Fortunately, the occurrence of the event does not damage the detector and the detector recovers right after the occurrence. However, the root cause is still unidentified and several assumptions are currently being investigated. Since October 2021, we have suspended the use of the EUV detector.

3.3.3.2 FUV dark current

From the commissioning of the detectors in 2019, the FUV detector has shown a high level of noise, 100 to 1000 times higher than measured on ground. This shortens the lifetime of the detector. In addition, the spatial distribution of the counts is not homogeneous, which makes it difficult to subtract noise for the analysis of the "useful" data. Furthermore, the noise increases with the HV, so we avoid using the nominal voltage so as not to damage the detector too much before the nominal phase of the mission. If the noise corresponds to counts having a low charge (which is usually the case), increasing the discriminators (discri) thresholds would partially remove it and increase the signal to noise ratio. We have therefore tested several configurations of HV/discri couple. Increasing the discri value has a positive effect on the detector's performance, but does not allow recovering the expected performances.

3.3.3.3 Scanner pointing accuracy

During several observations, a pointing error caused the target not to be in PHEBUS FOV. During most observations, the scanner positions show variations of a few steps even though no movement is commanded. It is not clear yet if those variations are actual movement of the scanner or error in its position determination (i.e. noise from the encoders that measure the scanner position). Note that the scanner mechanism of PHEBUS also has internal backlash ($\pm 0.5°$).

3.4 Observation modes

3.4.1 Cruise observations

The cruise phase is crucial to achieve readiness to Mercury. For the instruments that can be operated during the cruise, it allows to find and resolve anomalies, to characterise the instrument and to gain experience and confidence in operating it. The cruise is a rehearsal for the orbital phase. The cruise offers the opportunity to test and improve the tools to 1) prepare the products, the so-called POR (Payload Operation Request), and 2) analyse the data.

Thanks to its accommodation on MPO (i.e. radiator side) and its ability to move its scanning mechanism, PHEBUS is able to observe during the cruise. As the radiator side is always pointed away from the Sun, PHEBUS is constantly shielded from direct sunlight, thus avoiding straylight. Therefore, no special precaution or spacecraft attitude are required to operate the instrument safely during the cruise phase. Yet, a specific spacecraft attitude may be requested when the target is behind the MTM (Section 3.5.1). PHEBUS observations are limited only by the SEP arcs and operational constraints.

The targets of interest of PHEBUS during the cruise phase are presented below.

3.4.1.1 Stellar observations

We use stellar observations for the calibration of PHEBUS detectors. These observations make it possible to characterize the spectral response of the detectors and to follow its evolution during the journey to Mercury. The initial calibration phase (after launch) makes it possible to monitor changes or contamination that could have occurred since the ground calibration performed before the launch (FUV and NUV detectors only, the EUV detector has not been calibrated in detail on the ground due to lack of time). Changes in the instrument sensitivity are monitored by making observations of stars with well-known spectra. The stellar observations made during the cruise will be used as reference spectra for the in-orbit sensitivity monitoring. The stars of interest depend on the detector spectral range and the sources (i.e. data from other instruments and from models). A spectral database was developed at LATMOS based on various measurements of other EUV and FUV instruments on board current or previous missions (e.g. Spectroscopy for Investigation of Characteristics of the Atmosphere of Mars (SPICAM) on board Mars Express, Spectroscopy for Investigation of Characteristics of the Atmosphere of Venus (SPICAV) on board Venus Express, International Ultraviolet Explorer (IUE), Far Ultraviolet Spectroscopic Explorer (FUSE), UltraViolet Spectrometer (UVS) on board Voyager 1 & 2, MESSENGER/UVVS ...), and/or on data modelling. Note that there are very few sources below 90 nm.

3.4.1.2 Interplanetary observations

The Sun sends a constant flow of charged particles (i.e. plasma) into interplanetary space. This so-called solar wind forms a giant bubble around the Sun and its planets, known as the heliosphere. From the termination shock, the solar wind is abruptly slowed to the heliopause, where a balance of pressure between interstellar plasma and the solar wind is established. The heliopause forms the outer boundary of the heliosphere, beyond which lies the interstellar space. Figure 3.13 shows the different boundaries and their scale.

The neutrals of the interstellar medium (mostly hydrogen, followed by helium and other heavy species such as oxygen and neon) penetrate freely into the heliosphere. In fact, these atoms have mean free paths of the scale of the heliosphere and can therefore penetrate the heliosphere in the form of an interstellar wind. As they penetrate the heliosphere, these neutral atoms undergo charge exchanges with interstellar and solar wind protons. Therefore, their distribution evolves in terms of density, velocity and temperature.

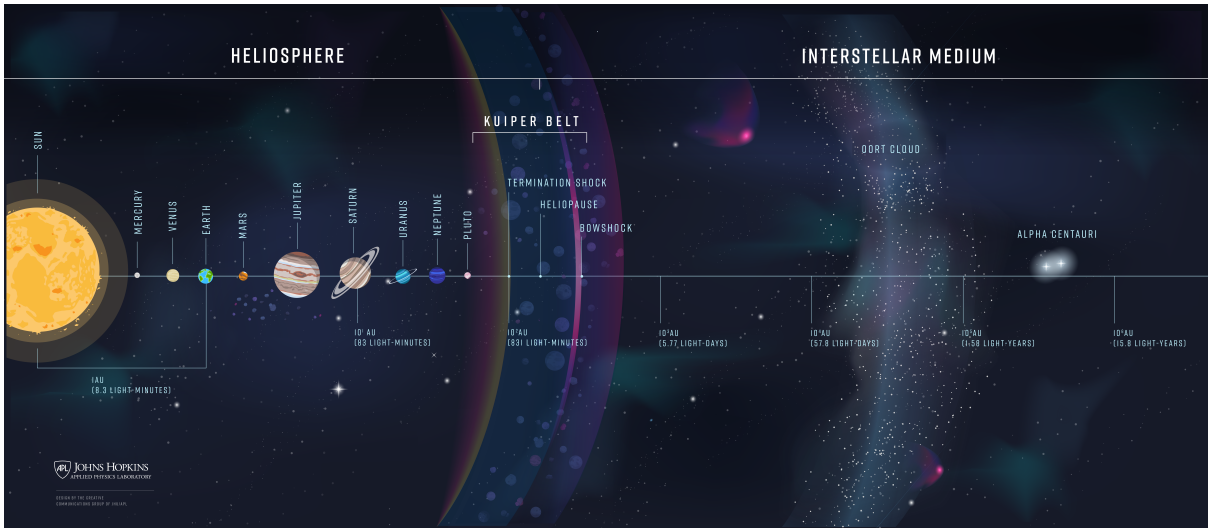

Figure 3.13: Scale of the Solar system and beyond. The scale bar is in AU. Credit: Johns Hopkins APL.

A key cruise science objective is to study the distribution of the neutral hydrogen and helium populations in the interplanetary medium. These observations are useful for the observations of Mercury's exosphere with the EUV detector. This allows to segregate the He and H atoms of Mercury's exosphere from those of the interplanetary medium, seen in the background.

3.4.1.3 Planetary flybys

Planetary flybys offer good opportunities to check the instrument performance and optimize upcoming operations during the nominal mission. The six scheduled flybys of Mercury will allow observations that will not be possible once in orbit, such as the observation of the extended exosphere. PHEBUS will make scans of Mercury's exospheric tail to characterize the acceleration induced by solar pressure in the tail and the escape rates of species. The scans will allow to reconstruct the variability of the exosphere induced by solar wind conditions (significant density inhomogeneity in the tail is the signature of change in the exosphere). Doing these scans during each flyby of Mercury would allow to reconstruct the tail geometry at different TAA (True Anomaly Angle).

The planning and results of the first two flybys of Mercury are discussed in the chapters 5, 6 and 7.

At the early stage of the cruise, BepiColombo performed flybys of Earth and Venus. These flybys represented a challenge for PHEBUS as these two planets, having dense atmospheres, were expected to be too bright for safe observation with the FUV detector. Therefore, during the Earth flyby in April 2020, PHEBUS observed the Moon with the FUV detector instead. During the two flybys of Venus in October 2020 and August 2021, PHEBUS was meant to use its EUV detector to perform a nightside coronal scan and a nightside stellar occultation. For the second flyby, the nightside coronal scan was successful but the subsequent stellar occultation failed as the star was not in PHEBUS FoV. As for the first flyby, the instrument was put into safe mode even before the start of acquisitions (due to light in scanner).

3.4.1.4 Distant observations of Venus and Mercury

Few days after the first flyby of Mercury, PHEBUS was able to conduct disk-integrated observations of the planet ($\sim$0.03 AU) to measure the EUV reflectance of Mercury's surface (Chaufray, Quémerais, et al., 2023). Attempts to observe Mercury with the FUV detector during this period failed because of the use of non-optimal detector parameters. The same type of operation

was requested after the second and the third flybys. The request was rejected for the second flyby due to payload operational constraints. It was accepted for the third flyby, subject to MOC (Mission Operations Centre) constraints.

The dayside of Venus is too bright for PHEBUS so it was not possible to observe it during the flybys. Observations of Venus dayside were attempted during several observation campaigns at a large distance. Figure 3.14 lists the scheduled observations along with the distance at which Venus was observed. Unfortunately, during some observations, Venus was not in the FoV of PHEBUS.

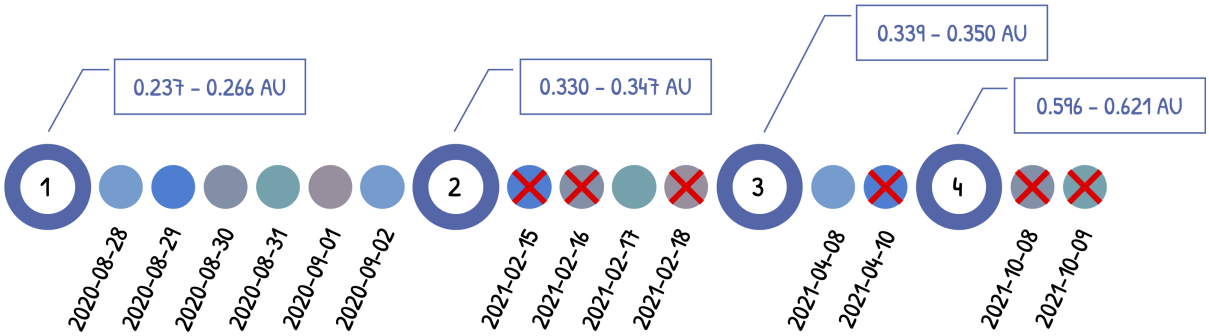

Figure 3.14: Timeline of PHEBUS distant observations of Venus. The red crosses mean Venus was missed. The distance at which Venus was observed is given in AU.

Those observation campaigns were requested by a guest investigator in order to conduct coordinated observations of Venus from the ground and from space (Lee et al., 2022). The goal was to investigate the unknown absorber in Venus atmosphere and to retrieve the disk mean SO_2 gas abundance. The FUV detector was therefore used for these observations. I processed the data from these observations (including correction of the inherent dark current and calibration at the different HV) to retrieve the spectrum of Venus (Section 4.1).

3.4.1.5 Zodiacal light observations

The zodiacal light is produced by sunlight scattered by interplanetary dust particles (known as cosmic dust) in the solar system. It was not a PHEBUS target of interest prior to the launch of the mission. However, observations of the sky with the visible channels during BepiColombo flip maneuvers (Section 4.2.2) unexpectedly revealed the observation of the zodiacal light (Section 4.2.4.2.1). Following these observations, we programmed regular observations of the zodiacal light. These data are currently analyzed and compared to models in the frame of an internship (Lucas Gomez).

Zodiacal light observations are mainly from the ground. Few (if any) spacecraft still active make observations of zodiacal light. PHEBUS data is therefore a real asset for the scientific community. Furthermore, they are the first observations of the zodiacal light at such distance from the Sun.

It is also necessary to estimate its contribution in order to be able to remove it from exospheric data during Mercury flybys.

3.4.2 In-orbit observations

Continuous operation of the instrument in orbit is not possible due to power budget restrictions and data volume constraints. A typical observation of the PHEBUS instrument will last about 30 minutes and will be programmed during most of the orbits. Depending on the science case, the operation can be placed at various times along the orbit (periherm, apoherm, MPO in the shadow of Mercury, etc). The aim of PHEBUS is to observe sources (emission lines from atoms

and ions) in the exosphere of Mercury or in the interplanetary medium, the nightside surface of Mercury but also to observe stars (mainly for calibration) or comets (if opportunities arise). The scanning mechanism allows to select the pointing direction without moving the spacecraft. This will allow to obtain vertical profiles in the exosphere of Mercury independently of the spacecraft attitude. Some operations, like stellar calibration, will require inertial pointing of the spacecraft platform.

Different modes of observation will be used sequentially (Figure 3.15):

1. Measurements of the interplanetary species background glow (H, He) in sky scanning mode.
2. Water ice detection in polar craters always in the shade (PSRs).
3. Determination of the composition and vertical structure of Mercury's exosphere by day observations at different altitudes above the surface.
4. Determination of the composition and vertical structure of Mercury's exosphere by night observations at different altitudes above the surface.
5. Star observations at MPO's apoherm for calibration and PHEBUS performance monitoring.

These modes are defined to optimize the science return while keeping the instrument safe from degradation. The brightest sources of light are the Sun and the lit surface of Mercury. Both sources will be kept away from the LOS (Line of Sight) at all times. During the orbital phase, the instrument will be regularly calibrated on well chosen stars, in such a way to quantitatively estimate the overall degradation of the sensitivity of the instrument. The nominal PHEBUS plan is to perform one calibration per day. The stellar observations will be made preferentially at MPO's apoherm because 1) there will be few operations of the other instruments on board MPO and 2) it corresponds to the location where there is the least possible contamination by Mercury's exosphere.

The eclipse season at aphelion and perihelion are of great importance for the PHEBUS science return. At perihelion, thermal desorption is expected to be a major source of the exospheric species, therefore observations during that period are extremely important for the science return of the PHEBUS instrument. The PSRs will be observed during terminator seasons.

The orbital phase offers vantage points for the study of the zodiacal light. The distribution of zodiacal light depends on the heliocentric distance and the elongation[2]. While the elongation is almost constant ($\sim$100°) during the cruise, it varies during the orbital phase, with very low values at aphelion and perihelion (10°) and values similar to cruise during the terminator seasons ($\sim$100°). At low elongation, the zodiacal light is $\sim$10 times brighter. It is therefore crucial to observe it throughout the orbit to be able to subtract its contribution to exospheric data.

[2]Angle between the LOS and the Sun direction

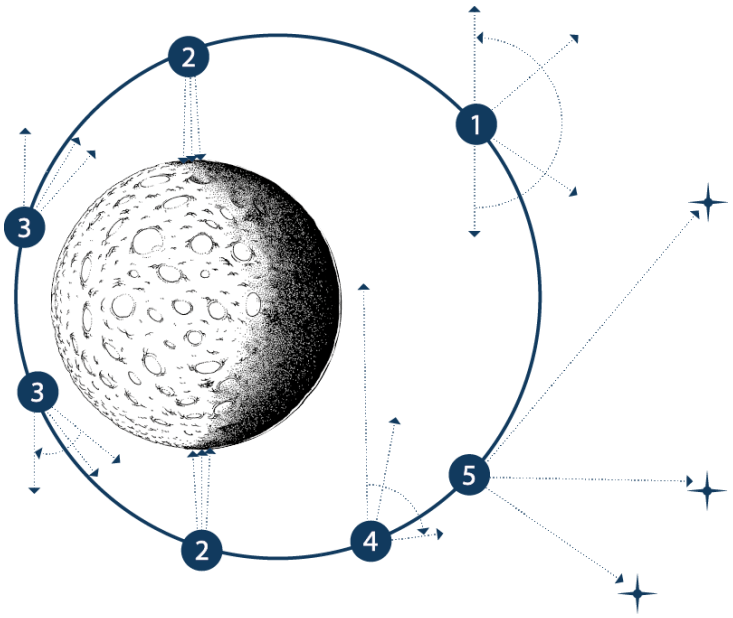

Figure 3.15: PHEBUS in-orbit observation modes. Credit: PHEBUS team.

3.5 Operations during cruise

3.5.1 Processes

To plan the payload activities during the cruise phase, instrument teams send requests every six months covering science observations, anomaly troubleshooting / instrument characterisation and software updates. Checkout and flybys science operations are excluded from regular planning as dedicated processes are in place. A checkout is a series of tests conducted to monitor the health of the instrument. For example for PHEBUS, we test the ignition of the instrument, its communication with the platform, the scanner positions, etc. A one-week checkout is performed every six months.

When sending the requests, instrument teams must specify: 1) expected data volume, 2) duration, 3) constraints in term of start/end date and 4) attitude change requirements. PHEBUS can ask for pointing requirement when the target is behind the MTM. In fact, during the cruise, the spacecraft is in stacked configuration and some positions of PHEBUS scanner (185° to 290°) are blocked by the MTM (Figure 3.16).

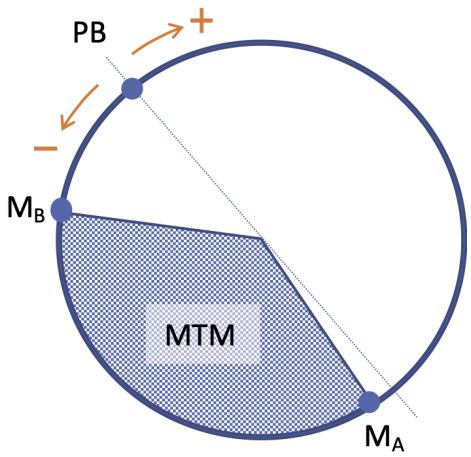

Figure 3.16: PHEBUS scanner position. PB = Parking Bracket (0°), M_A = Entry in MTM cone (185°), M_B = Exit of MTM cone (290°). The orange arrows indicate the rotation direction, '+' means positive and '-' means negative.

The Project Scientist and OGS (Operations Ground Segment) teams evaluate the Principal Investigator (PI) request. Requests can be accepted, partially accepted or refused. Payload operations are limited by spacecraft constraints (SEP arcs, solar conjunction, reduced data rate and flyby preparation). The level of payload operations that can be supported during the cruise is also constrained by the limited ground station time available and limited manpower available for payload operations (planning/coordination/implementation). Initially, payload operations during cruise were restricted to checkout and radio-science campaign during one solar conjunction. OGS tools and processes are therefore not optimized for sustained payload operations in cruise.

OGS subsequently send the final plan with start/end date, data volume along with the tentative STP (Short Term Planning) cycle and its start/end date. The cruise is indeed divided in STP (Short Term Planning) cycles (roughly corresponding to a month). Each cruise science request is associated with an STP cycle. STP and payload plan may change at short notice due to operational reasons resulting in cancelled or delayed observations. OGS communicates final dates for STP start/end and FD (Flight Dynamics) products delivery enough time in advance. FD usually delivers products (e.g. WOL (Wheel Off-Loading) times, slews ...) two days prior to delivery deadline. PORs are to be delivered via SPOT (Science Planning Operation Tool). Instrument teams notifies the MOC by email about the delivery. PORs are then ingested as part of mission planning process and uplinked to Mission Time Line (MTL). Instrument teams are fully responsible of POR content as no manual check is done by OGS. Mission Planning System (MPS) only checks basic constraints such as WOL or incorrect state transitions.

For flybys science operations, the process is different. The observations are not linked to a specific STP cycle. The instrument teams send their request to the Project Scientist and OGS months prior to the flyby, specifying duration with respect to CA, estimated data volume and pointing requirement, if any. After gathering requests from all the instrument teams, FD provides the pointing timeline. After iterations on the pointing timeline, FD provides MTP (Medium Term Planning) products. The instrument team first provide draft products. In the case of cruise science operations, the products are defined with absolute times, whereas for flyby science operations, they are planned against the CA of the flyby. The absolute time of the CA can vary between the MTP products and the consecutive STP products. The events relative times with respect to the CA do not change between MTP and STP products.

I built and submitted the operation requests of different observation campaigns (stellar observations, distant observations of Mercury and Venus, observations during flip maneuvers

dedicated to zodiacal light or stars) and of the first three flybys of Mercury. The planning of Mercury flybys is detailed in the section 5.1.

3.5.2 Tools

3.5.2.1 SPOT

The BepiColombo SGS (Science Ground Segment) team has developed SPOT, a tool that supports the SGS and instrument teams in the generation of operational products. SPOT allows to create, clone, edit or delete PORs and to deliver them to ESOC. Each POR contains (Figure 3.17):

1. The name of the instrument(PHEBUS)
2. The name of the POR, giving a concise description of the operation,
3. The description of the operation, with the main parameters of observation (e.g. detector, HV, slit mode ...),
4. The operations, with the definition of the time (absolute or relative to an event) and the operations commanding. The operations commanding contains sequences, timings and parameters included in the sequences.

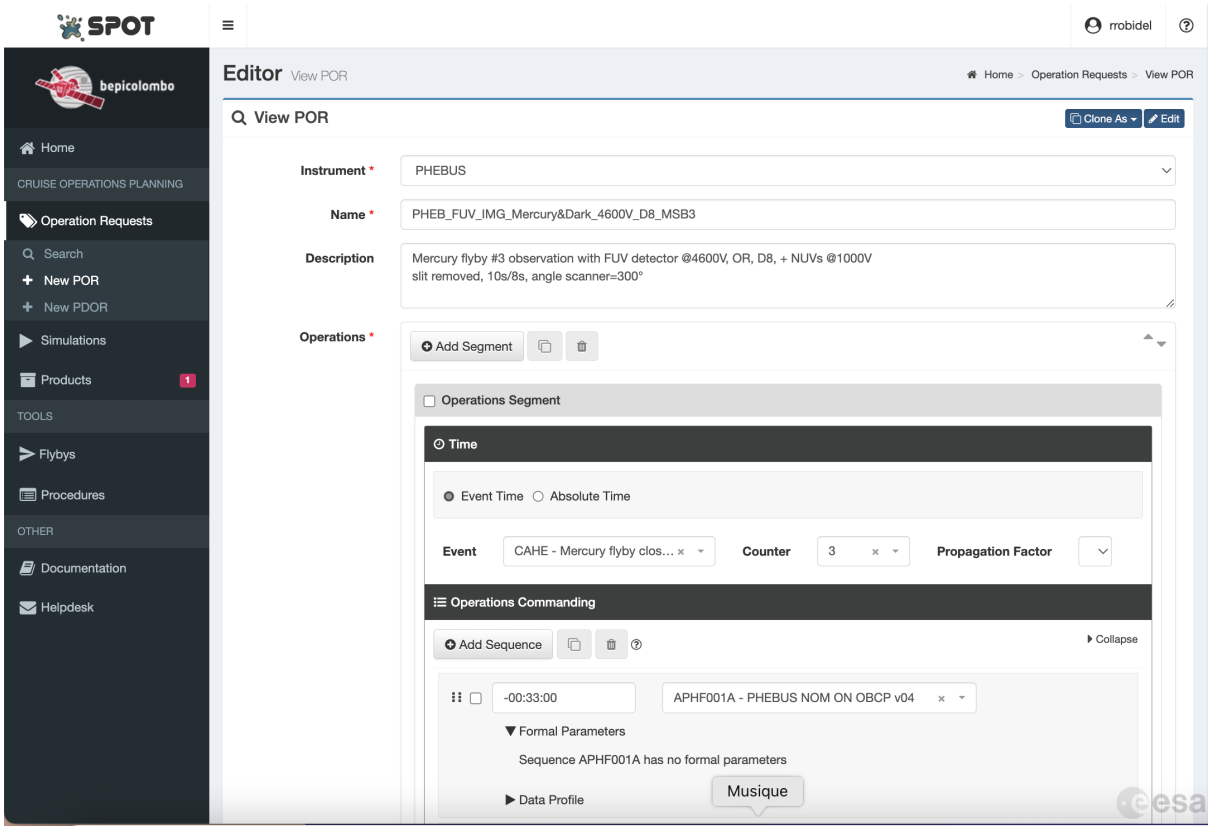

Figure 3.17: SPOT user interface.

At the beginning of my thesis, PORs were created from scratch or cloned from a previous POR. Later, tools developed by the PHESOC (PHEBUS Science Operations Centre) team allowed to directly import a CSV file containing all the sequences, timings and parameters attached to the sequences. With these imported data, SPOT automatically populates the fields of the POR being created, which makes the creation process more efficient and convenient. The

only things left to fill are the instrument, name, description and time. These tools are described in the following sections.

3.5.2.2 PHEBUS Operations Planner

PHEBUS Operations Planner tool was developed alongside my thesis by the PHESOC team (A. Reberac and A. El Aoumari). It aims to help planning, managing and reporting on PHEBUS operations. The tool gives a first level of verification of conflicts. If it detects inconsistencies with regards to the schedule or the selected values, observation sequence overlapping or wrong wait time, it sends a notification to the user. It provides a history of all PHEBUS operations, their parameters and status (OK, Partially OK (POK)[3], Not OK (NOK)[4] or CANCELLED).

I start by defining an Operation Plan, filling in the period it covers and the type of operation to conduct. The Operation Plan can contain several OR (Operation Request) (Figure 3.18). I will focus only on the ones I used during my thesis i.e. EUV, FUV and NUV. An OR contains one or several observations configured for a specific goal (science observation, calibration, EUV outgassing, good health test...).

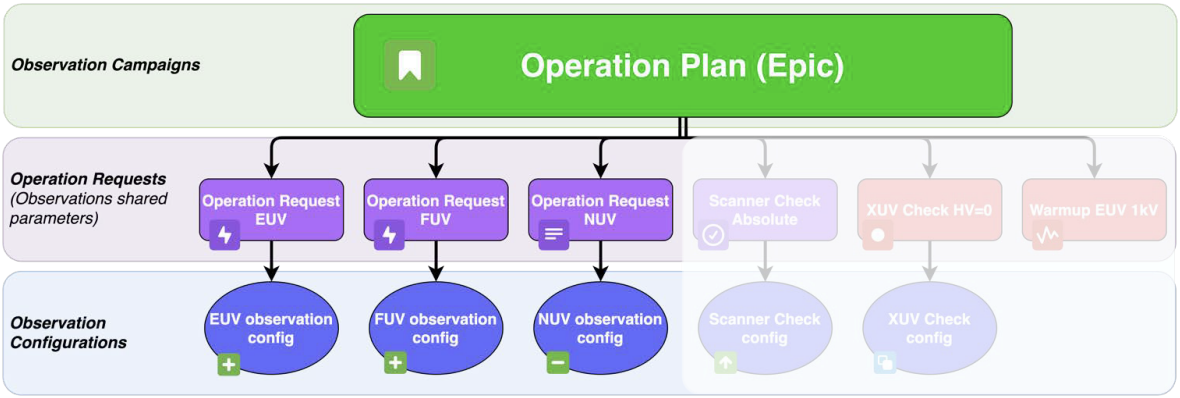

Figure 3.18: PHEBUS Operation Planner hierarchy levels

An OR is usually delimited by a SWITCH ON/OFF of the instrument. During this time, only one of the UV detectors can be activated (or none, and with or without the visible channels activated) and detector configuration parameters cannot be changed from an observation to another. Parameters that cannot be modified from one observation to another ("shared parameters") are defined at OR level. They are listed hereafter:

- *Discri*: discriminator value,
- *HV init*: initial HV value of the detectors used,
- *XUV max count rate*: the instrument is put into safe mode when the count rate of the selected detector reaches this threshold,
- *NUV activation*: visible channel(s) to be used (none, one or both),
- *Downlink mode*: priority for downlink (high or low),

Some of these shared parameters are defined only when one of the UV detectors is used. Other parameters are defined at Observation Configuration level such as the observation rate, the slit mode, the exposure time or the shutter mode. They also encompass information related to binning, compression, windowing and scanner activation.

[3]The observation is exploitable despite the anomaly observed.
[4]The observation is not exploitable at all.

Then, I define the scanner position considering the error relative to the position. There can in fact be a discrepancy between the commanded position and the actual position of the scanner returned by the encoder (Section 3.3.3.3). To estimate this discrepancy and determine its relation with the commanded position, we perform a test during the checkouts. It consists in commanding the scanner back and forth from the parking position to a different position, increasing the value of this position by a step of 200 at each iteration to cover all the possible positions. The test is performed twice: a positive rotation is used in one case and a negative rotation in the other. The results are displayed in Figure 3.19.

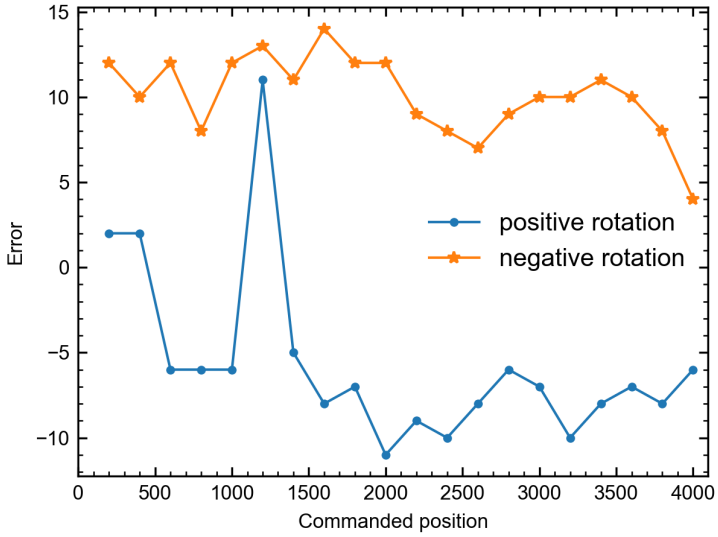

Figure 3.19: Relative error of PHEBUS scanner position depending on the commanded position and the direction of rotation.

Along with the scanner position, I define the first direction (positive or negative) and the first safe direction[5] (positive or negative). These directions are chosen depending on the location of the scanner positions. The rules are represented in Figure 3.20.

When we operate the EUV or FUV detectors, the high voltage is gradually increased (in steps) to avoid a power surge. The HV ramp is different depending on the UV detector when it comes to the HV value or duration. Therefore, for EUV or FUV observations only, I subsequently define the XUV HV (High Voltage) ramp: the HV value to reach, the procedure to use along with the HV ramp details.

[5]The safe direction is the direction the scanner must take if the instrument goes into safe mode.

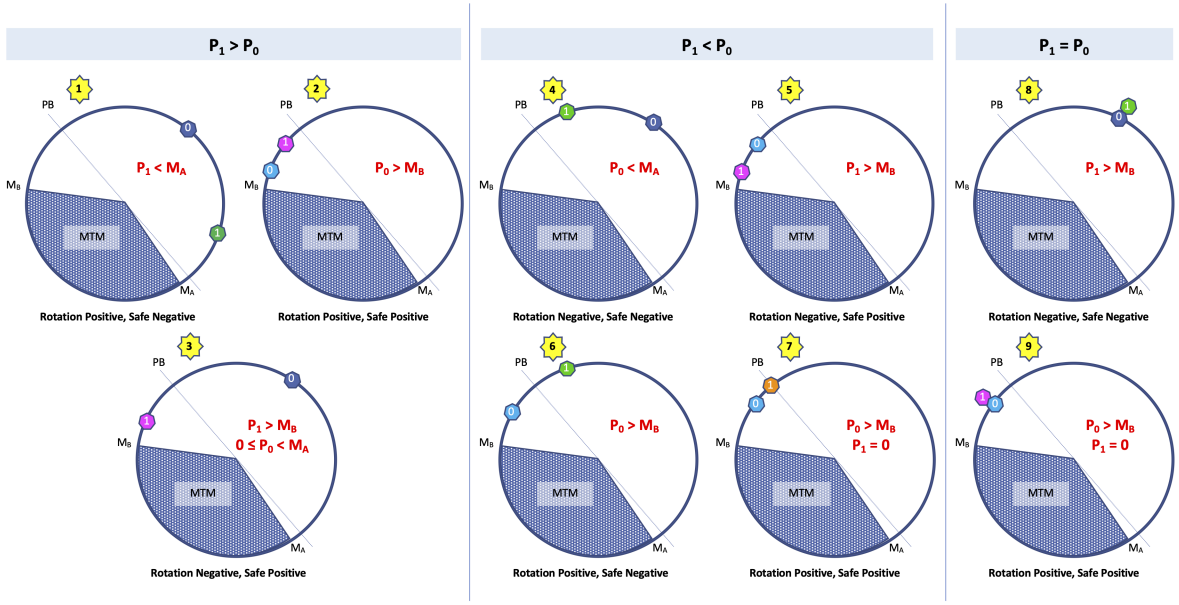

Figure 3.20: Scanner rotation check in spacecraft stack configuration (i.e. with the MTM). P_B = Parking Bracket, M_A = Entry in MTM cone (185°), M_B = Exit of MTM cone (290°), P_0 = Previous position, P_1 = Position to reach.

3.5.2.3 PHEBUS Web tools: SPOT import and POR checker functionalities

Once the OR is defined in the PHEBUS Operations Planner tool, I use the "SPOT IMPORT" functionality to generate a CSV file based on the OR data.

Once the POR is created in SPOT, I use the "POR CHECKER" functionality to check the consistency of the product with respect to WOL events, operation timings, observation parameters values and to detect mismatch between parameters values filled in the PHEBUS Operations Planner tool and the ones filled in SPOT.

To sum up:

1. Create an Operation Plan with one or more ORs in PHEBUS Operations Planner tool,
2. Generate a CSV file for each OR using the SPOT IMPORT functionality of the PHEBUS Web application,
3. Import the CSV file in SPOT to create a POR,
4. Check the consistency of each POR using the POR CHECKER functionality of the PHEBUS Web application,
5. If multiple PORs, gather them in a Command Request File Group (CRFG),
6. Before sending the CRFG file to the MOC, verify its consistency (e.g. no overlapping of operations, respect of waiting times between two consecutive operations) with the POR CHECKER functionality of the PHEBUS Web application,
7. Finally send the CRFG file to the MOC on SPOT and notify them by email.

Chapter 4

In-flight calibration of the detectors

To evaluate the health of the instrument and monitor its performance, we regularly perform in-flight calibration using stellar observations. In this chapter, I present the study of distant observations of Venus (mentioned in Section 3.4.1.4) which required the calibration of the FUV detector at multiple HV. The results of the calibration are used to analyze the FUV data from the second and third flybys of Mercury, but this falls out of the scope of this thesis. I also present the calibration of the visible channels, required to analyze the data from Mercury flybys. I will then describe how the effective areas of the FUV detector and of each visible channel have been retrieved.

4.1 FUV in-flight calibration and distant observations of Venus

4.1.1 August and September 2020 observation campaign

PHEBUS has performed several campaigns of observations of Venus. The first one took place from August 28, 2020 to September 2, 2020, at a distance of 0.237 to 0.266 AU from Venus with a phase angle of ∼60°. Each day, PHEBUS performed a half-hour observation with an acquisition every 10 sec and an integration time of 8 sec. Each observation comprises 180 image acquisitions at 4.55 kV. Each acquisition consists of a 512×256 matrix, mapping the number of photon counts registered in a pixel onto each of the pixels of the Region of Interest (ROI) of FUV detector image as a function of time (i.e. each slice represents an image acquired at a specific time of the observing sequence). To obtain the mean count rate, all the acquisitions are summed then divided by the exposure time and the number of acquisitions.

Figure 4.1 represents the mean count rate registered by the FUV detector during the August 28 operation. The row pixel number represents the spatial dimension while the column pixel number represents the spectral dimension. The center of the detector has initially been set to zero to remove a spike.

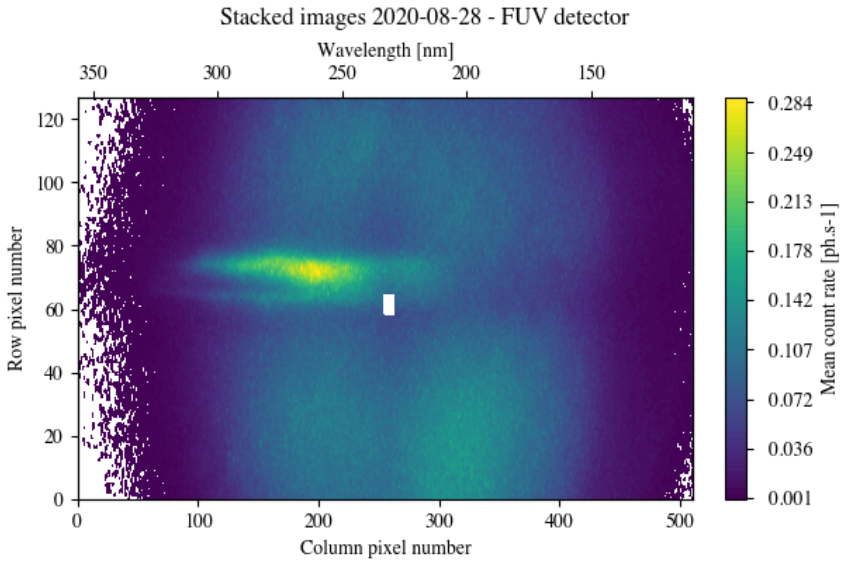

Figure 4.1: Distant observation of Venus with the FUV detector, acquired on August 28, 2020 at 4.55 kV.

4.1.1.1 Data correction

To derive the spectrum of Venus from the data, the first step consists in correcting the data from the dark current. Although it is the only contribution to the FUV detector background, it was not an easy task to remove it. The dark current is much stronger than what was observed on ground and is very unstable. No observation of the dark (i.e. at the parking position) was made just before or after the observations of Venus. Therefore, I consider the most recent dark observation with the same HV, performed on July 8, 2020 (Figure 4.2).

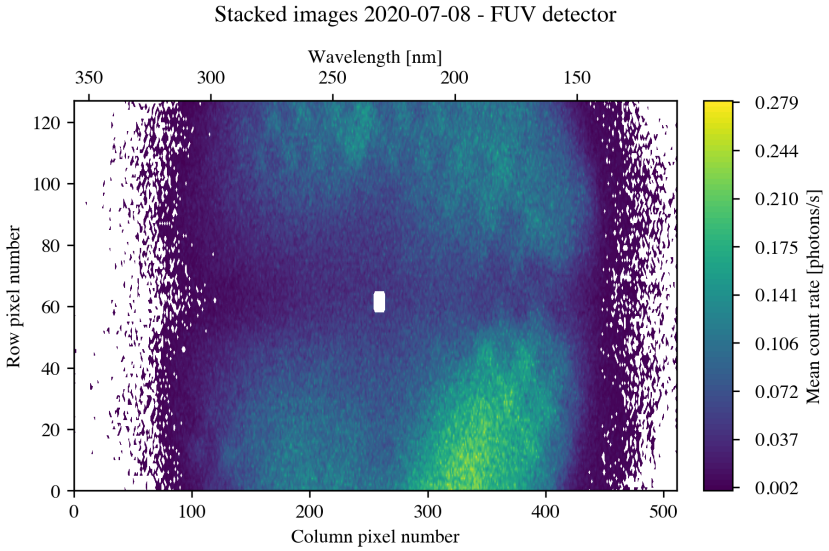

Figure 4.2: Observation at the parking position with the FUV detector, acquired on July 8, 2020 at 4.55 kV.

If I directly subtract the dark to the observation of Venus, we notice that too much dark is removed, resulting in a negative count rate on some pixels (Figure 4.3). I then have to manually correct this residual bias. I have tested two types of correction. The first one consists in setting a null average on the edges of image. The other one consists in removing a model of the dark, based on the shape of the dark observation from July 8, 2020.

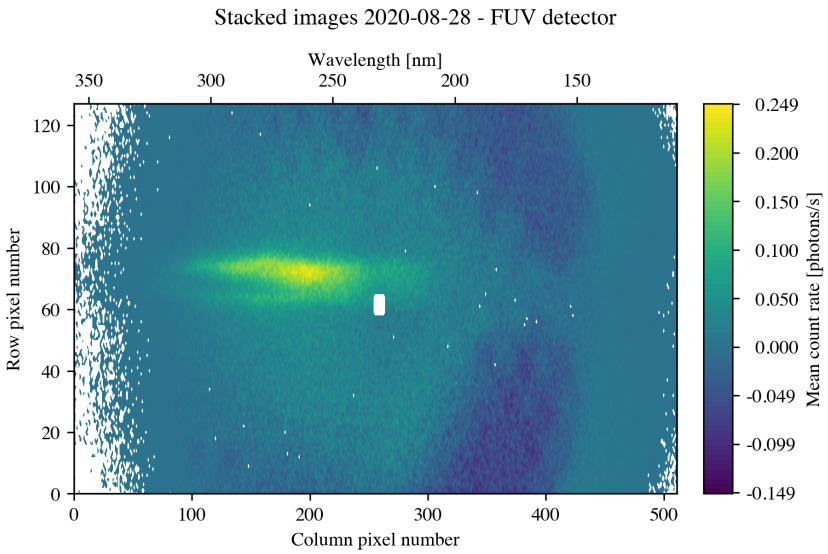

Figure 4.3: Distant observation of Venus with the FUV detector acquired on August 28, 2020 corrected for the dark observation of July 8, 2020.

Let's consider the first correction. Figure 4.4a illustrates the photon counts registered on column 150 (where we see Venus) as a function of the row pixel number. Then, I consider 10 values in the lower part of the detector (i.e. short row pixel number) and another 10 in the upper part (i.e. large row pixel number) for both the dark and Venus data (Figure 4.4b). For each observation, I compute the mean of these 10 values. The idea is to compute the function to apply to the dark so that the upper (resp. lower) mean value of the dark equals the upper (resp. lower) mean value of Venus data (Figure 4.4c).

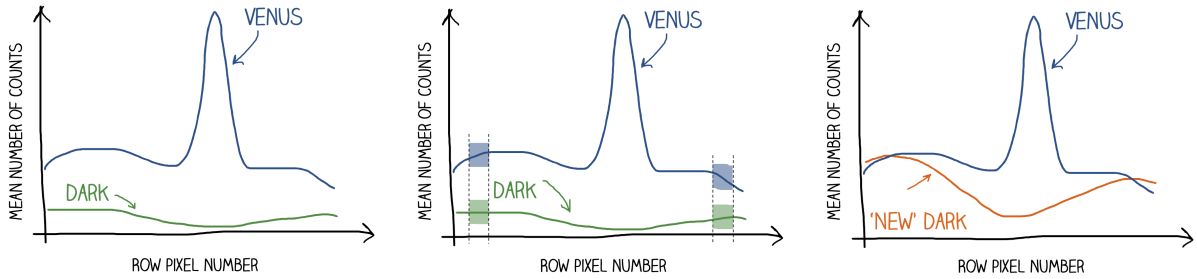

Figure 4.4: Illustration of the first correction applied to Venus data.

I subsequently remove the 'new' dark to Venus data. As can be seen on Figure 4.5, the correction is not fully satisfactory. The dark current seems to have changed too much between the two observations.

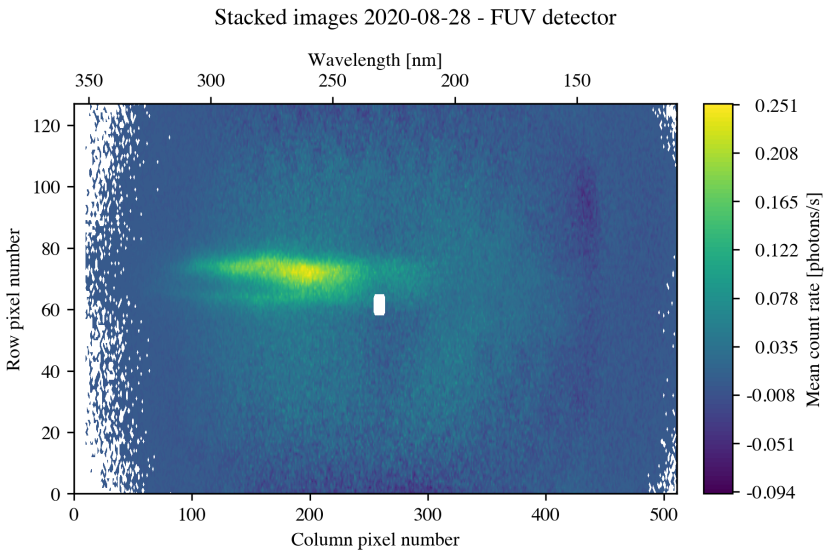

Figure 4.5: Distant observation of Venus with the FUV detector acquired on August 28, 2020 corrected with the first empirical correction of the dark current.

That brings us to the second empirical correction. The dark current can be modelled by a polynomial of degree 5. The idea is then to remove this polynomial for each column. To do so, I first consider the photon counts registered on each column (Figure 4.6a). To compute the polynomial fit, I exclude the rows where Venus is located (Figure 4.6b). I compute a polynomial fit of degree 5 (Figure 4.6d) on the selected values (Figure 4.6c).

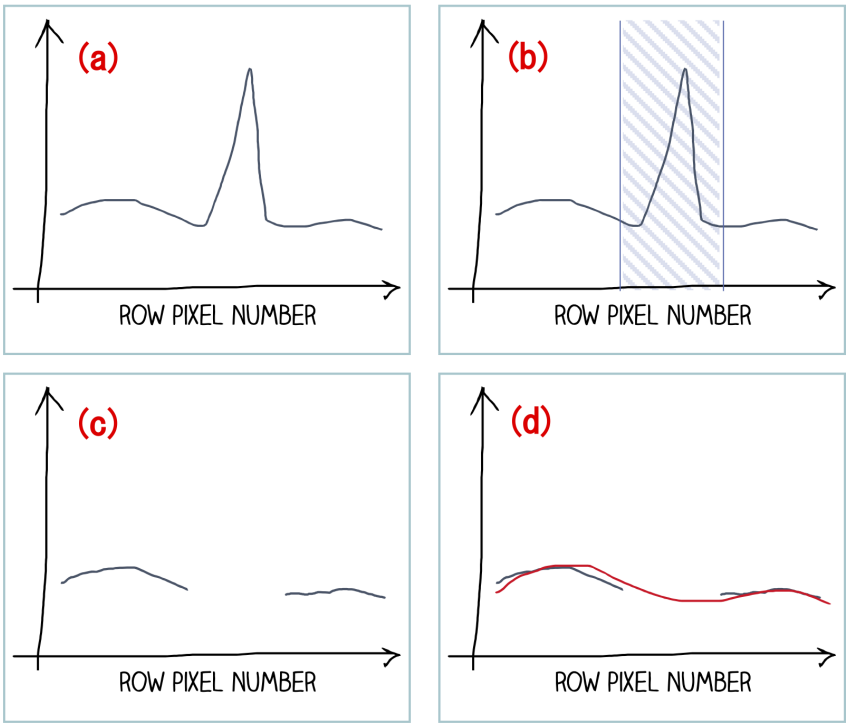

Figure 4.6: Illustration of the second correction applied to Venus data.

I remove the polynomial to Venus data but, as it can be seen on Figure 4.7, there is a trough on central lines around column 350.

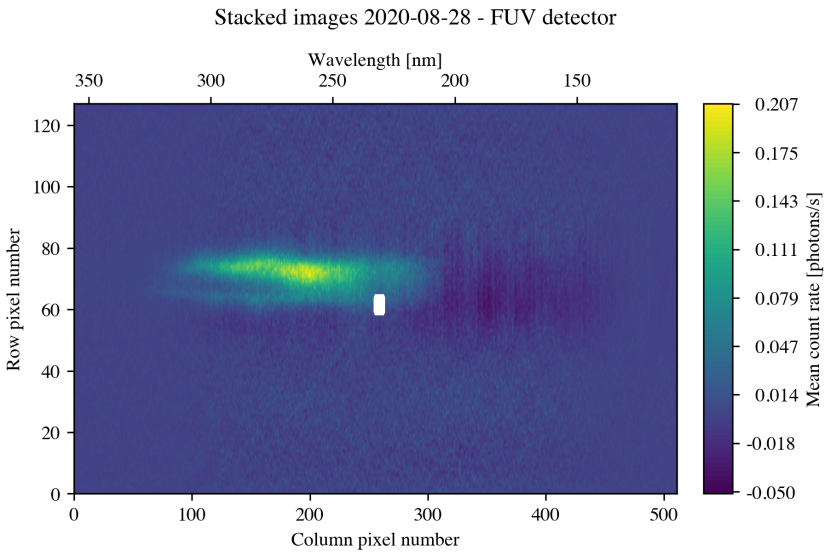

Figure 4.7: Distant observation of Venus with the FUV detector acquired on August 28, 2020 corrected with the second empirical correction of the dark current.

By plotting the spatial contribution of the column 350 (blue curve on Figure 4.8), it appears that the dark is not well represented by a polynomial of degree 5 (orange curve on Figure 4.8). I then have to apply an additional correction.

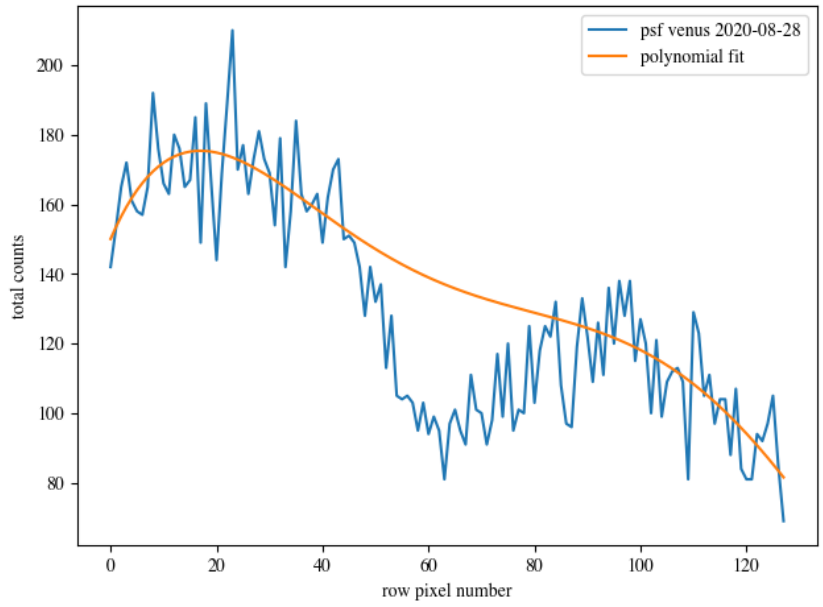

Figure 4.8: Spatial contribution computed on column 350 (blue curve) along with a polynomial fit of degree 5 (orange curve).

To determine the shape of this trough, I average columns 350 to 400 and compute the ratio of the polynomial fit to the data. So, to get the right correction, instead of simply subtracting the polynomial of degree 5, I remove this polynomial multiplied by the ratio and apply it on all the columns. Figure 4.9 shows the result.

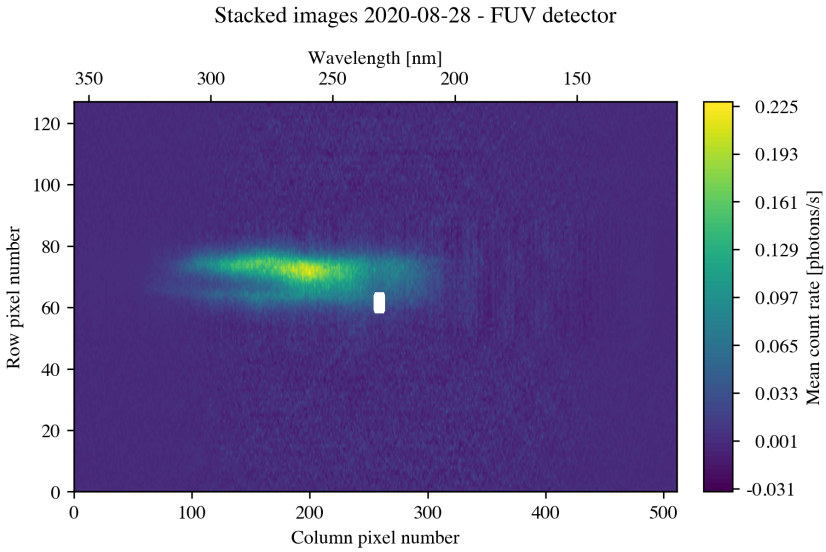

Figure 4.9: Distant observation of Venus with the FUV detector acquired on August 28, 2020 corrected with the final empirical correction of the dark current.

Now that the background is removed, I correct the unexpected spike at the center of the image using interpolation (Figure 4.10).

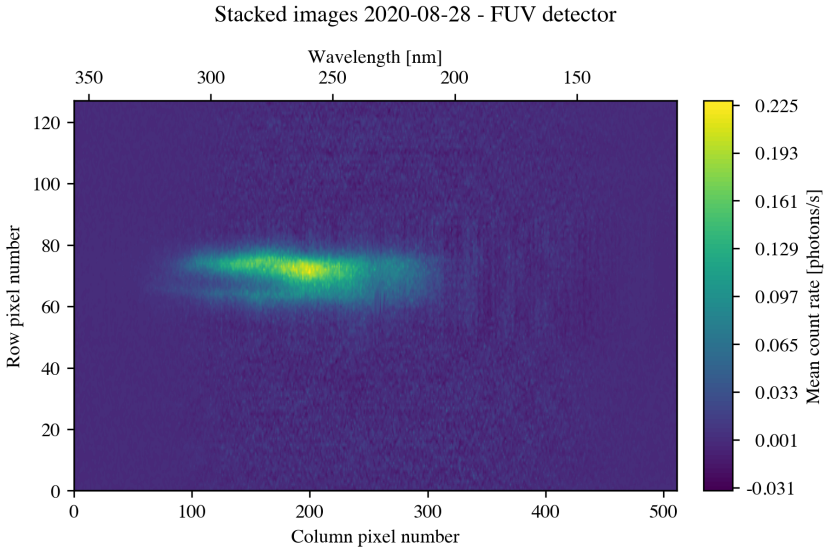

Figure 4.10: Distant observation of Venus with the FUV detector acquired on August 28, 2020 corrected with the final empirical correction of the dark current and the central spike.

Finally, I retrieve the spectrum of Venus (Figure 4.11) by summing the lines where the planet is located i.e. from line 67 to line 78 (Figure 4.10). We can notice there is no signal under 200 nm which is consistent with the atmosphere of Venus (strong CO_2 absorption below 200 nm).

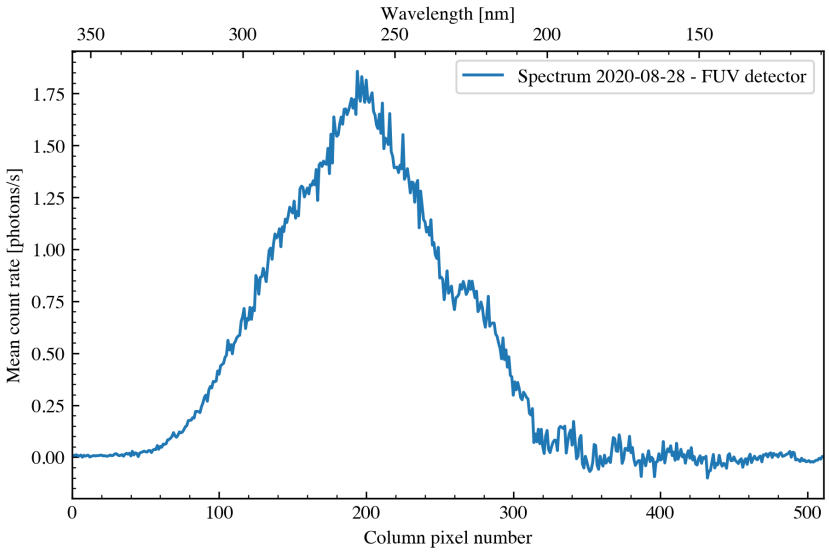

Figure 4.11: Spectrum of Venus deduced from the August 28, 2020 FUV observation.

I apply the same process for the other observations (Figure 4.12). It is clear that the target is not located at the center of the detector and appears slightly tilted. Note that Venus sometimes appear in the superior half plane (Figures 4.12a and 4.12i) and other times in the inferior half plane (Figures 4.12c, 4.12e, 4.12g and 4.12k). This is simply due to the spacecraft attitude, a flip maneuver has been performed in between PHEBUS observations.

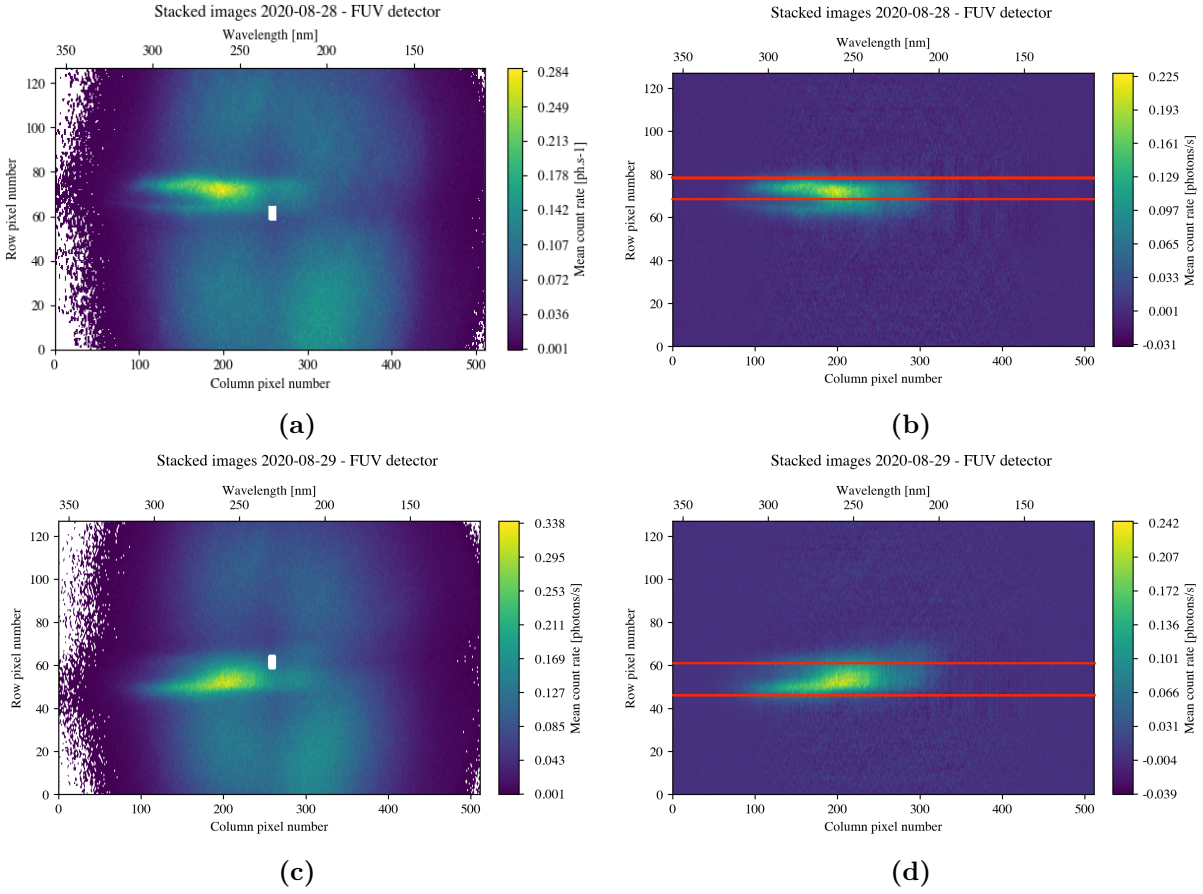

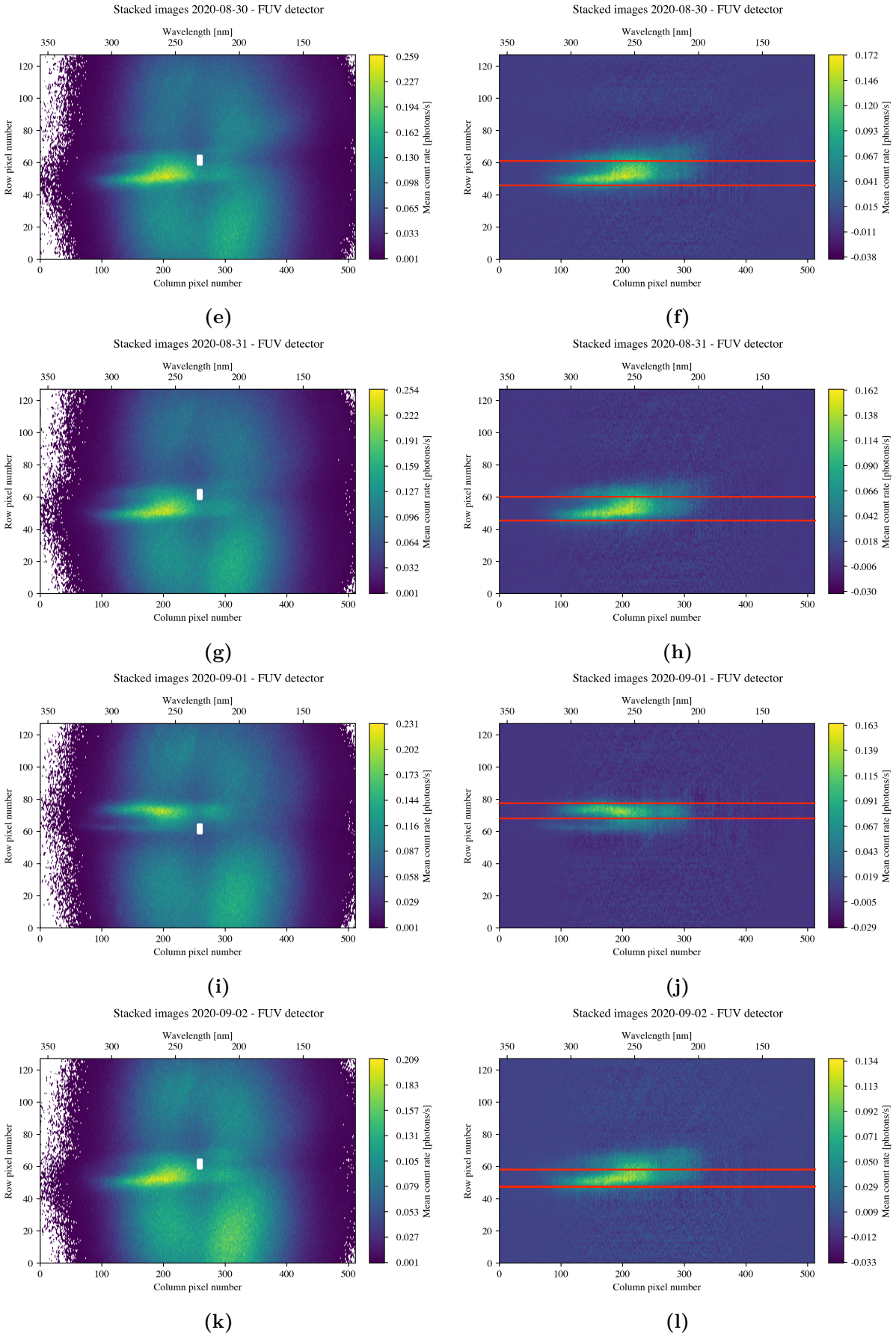

Figure 4.12: The left panels represent the mean count rate observed with the FUV detector on August 28 (a), August 29 (c), August 30 (e), August 31 (g), September 1 (i) and September 2 (k) 2020. The right panels represent the mean count rate observed with the FUV detector corrected for the dark background and the central spike. The red solid lines picture the area on which the count rate is summed to derive the spectrum of Venus.

4.1.1.2 Spectrum comparison

To observe the evolution of Venus over several days, the normalized spectra are compared (Figure 4.13). The spectra are normalized such that the integral equals 1. Note that the spectrum of the observation of September 1 stands out particularly from the others, having a bump between 210 and 230 nm. The one of August 28 also presents a bump, but less prominent. These observations correspond to two different scanner positions (related to the spacecraft attitude). A possible explanation is a variation of sensitivity according to the scanner position (expected).

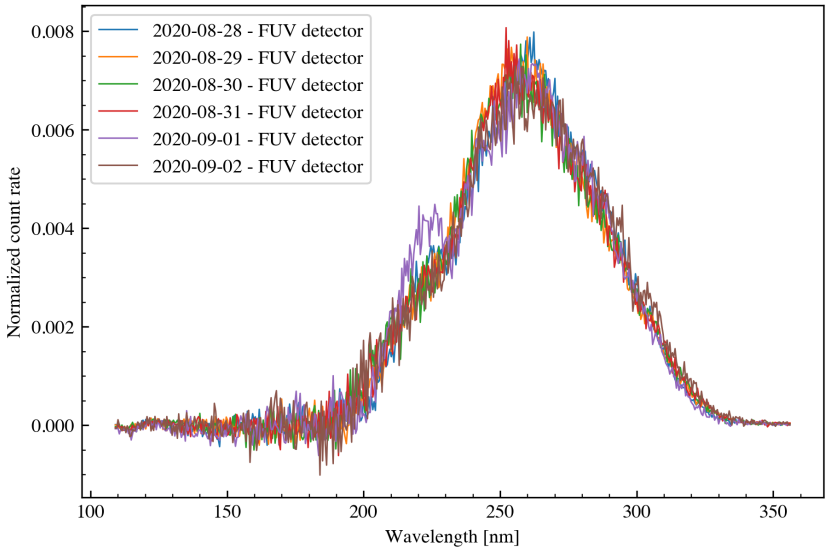

Figure 4.13: Normalized spectra of Venus deduced from FUV observations during the August and September 2020 observation campaign. The different colors indicate the different days of observation.

4.1.1.3 Comparison with visible channels count rate

To compare the response of the FUV detector and the visible channels, I plot the mean count rate registered by the detectors for each day of observation (Figure 4.14). Note the FUV mean count rate decreases over the days. This overall decrease of the signal may be due to a decrease in gain, which is expected for young detectors (i.e. which have not had time to evolve). It should stabilize over time. However, the amplitude of the decrease ($\sim$40%) is too large to be explained by this effect only.

Regarding the visible channels, the counts on the two detectors show variations that change from one observation to the other (positive or negative slopes, but always correlated between the two detectors). It has yet to be determined whether these variations are due to the solar flux or a possible variation in the emission of Venus.

However, no correlation between the FUV detector and both visible channels is found. Another likely explanation is linked to the fact that Venus is not located at the center of the detector, but most likely on the edges. The detector then receives only a part of the planet's flux.

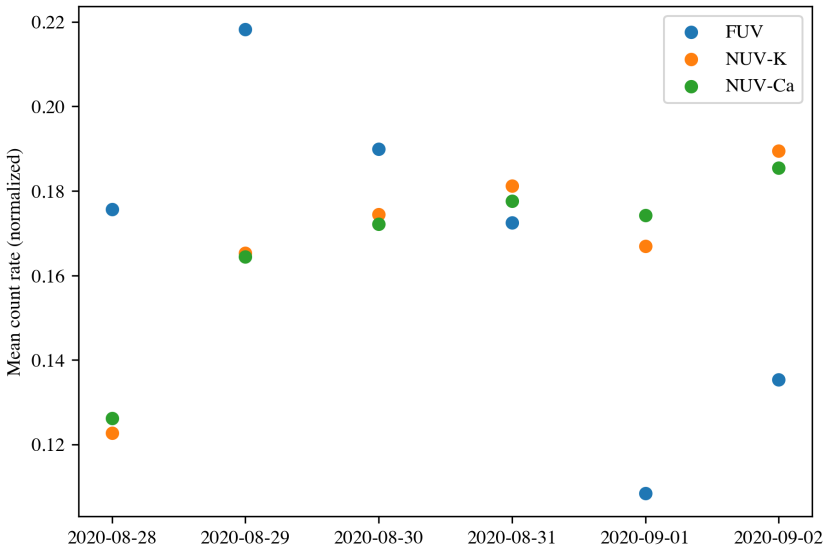

Figure 4.14: Comparison of the FUV detector and visible channels mean count rate.

4.1.1.4 FUV in-flight calibration

For the calibration of the FUV detector, I use observations of the Alpha Virginis star (also known as Spica), which is bright enough to be detected by the FUV detector. The observation, performed on February 4, 2020 at 4.55 kV, comprises 156 image acquisitions. Each acquisition consists of a 1024×128 matrix. All the acquisitions are summed then divided by the exposure time and the number of acquisitions (Figure 4.15).

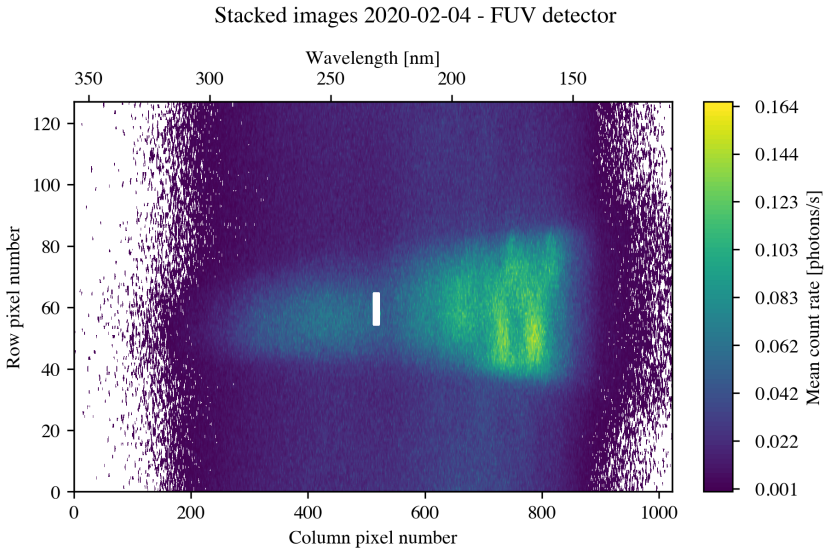

Figure 4.15: Observation of Spica with the FUV detector, acquired on February 4, 2020 at 4.55 kV.

I consider the dark observation acquired prior to Spica observation. It comprises 156 image acquisitions at 4.55 kV. Each acquisition consists of a 1024×128 matrix. I then subtract the dark current to Spica data and correct the spike at the center of the detector using interpolation (Figure 4.16).

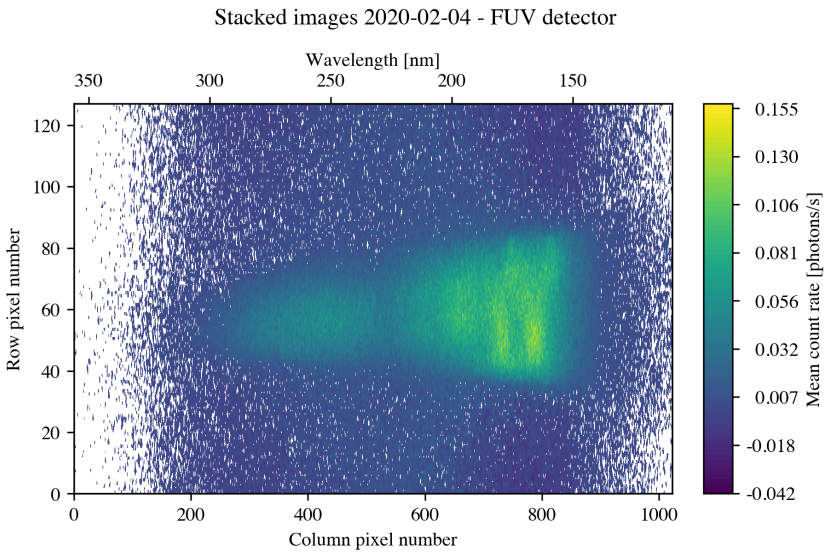

Figure 4.16: Observation of Spica with the FUV detector acquired on February 4, 2020 corrected for the dark observation acquired on the same day and corrected for the central spike.

However, as the dark current is not stable between the two observations, strictly subtracting the dark current results in negative count rate. I thus apply a correction that consists in forcing a null average at the edges of the image (Figure 4.17).

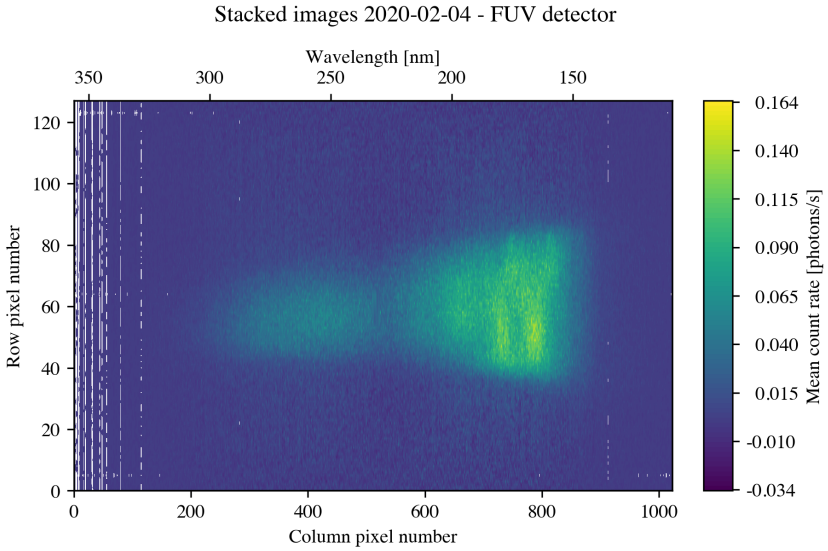

Figure 4.17: Observation of Spica with the FUV detector on February 4, 2020 corrected with the final empirical correction of the dark current and the central spike.

To extract the spectrum of Spica, I sum the count rate over the lines where the star is located (lines 37 to 83 here) and plot the result as a function of the wavelength (Figure 4.18).

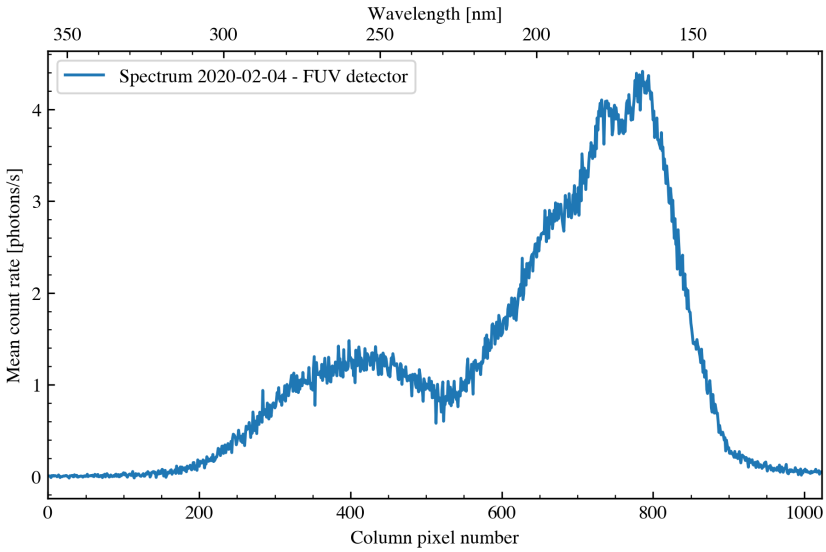

Figure 4.18: Spectrum of Spica deduced from the February 4, 2020 FUV observation.

In addition to Spica's spectrum deduced from PHEBUS observation, the calibration of the FUV detector requires the calibrated reference spectrum of the star. To do so, I use the catalog built by the PHEBUS Science team based on past or current UV instruments (see section 3.4.1.1). From the catalog, I retrieve the SPICAM reference photon flux of Spica (photons/cm^2/s/nm) and interpolate on PHEBUS reference spectrum wavelengths grid. I can then compute the theoretical spectrum of Spica:

$$N_p(\lambda) = A_{eff}(\lambda)\,\phi(\lambda)\,\Delta\lambda \tag{4.1}$$

Where N_p is the number of photoevents per second reported by the FUV detector, λ the wavelength in nm, A_{eff} is the theoretical effective area of the FUV detector, which was computed on ground prior to the integration on the BepiColombo spacecraft, ϕ is the incident stellar flux in photons.s^{-1}.cm^{-2}.nm^{-1} through the aperture and $\Delta\lambda$ is the pixel size in nm. $\phi(\lambda)\,\Delta\lambda$ represents the flux of the star interpolated on PHEBUS/FUV wavelength grid.

On Figure 4.19, several differences can be noted between the spectrum derived from PHEBUS observation and the expected spectrum. The first difference (1) around 150 nm could be due to the light trap located near the gratings that causes a photons loss (i.e. photons that cannot be reflected by the gratings to the detector). The second difference (2), between 200 and 250 nm, can certainly be explained by the grid effect (i.e. the position of the anodes on the detector) which should disappear as we operate at nominal voltage. Finally, it seems that the effective area is underestimated between 270 and 320 nm (3). The ratio between the two curves gives the ratio between the theoretical effective area (calculated on the ground) and the effective area computed in flight. The average ratio is 10.8, implying that we work at ∼10% of the nominal sensitivity).

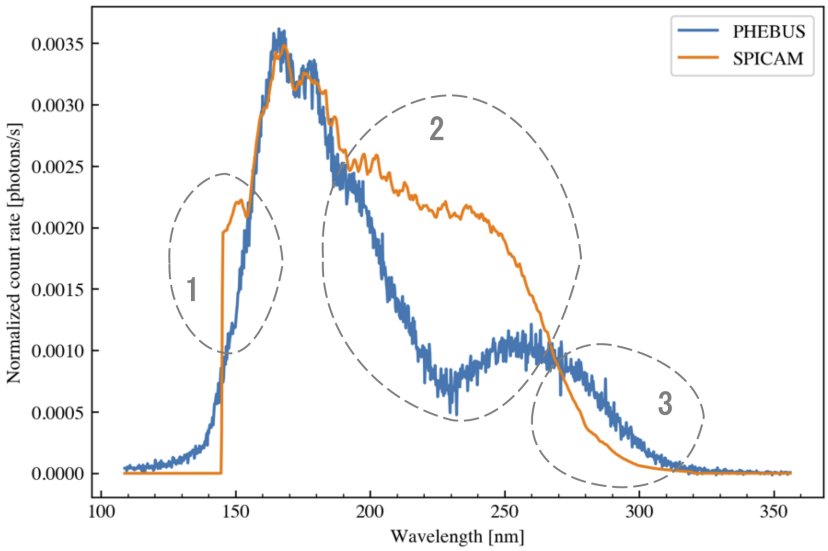

Figure 4.19: Spica spectra obtained with PHEBUS/FUV (blue curve) and SPICAM/UV (orange curve).

4.1.1.5 Instrument response function

To derive the response of the detector, I need to compare the spectrum of Venus derived from the observations to a modelled spectrum of Venus. To model the spectrum of Venus, I use Eq. (4.1), where A_{eff} is the effective area of the FUV detector determined in flight by cross calibration with SPICAM spectrum of Spica (Figure 4.20), and ϕ is the flux of the planet.

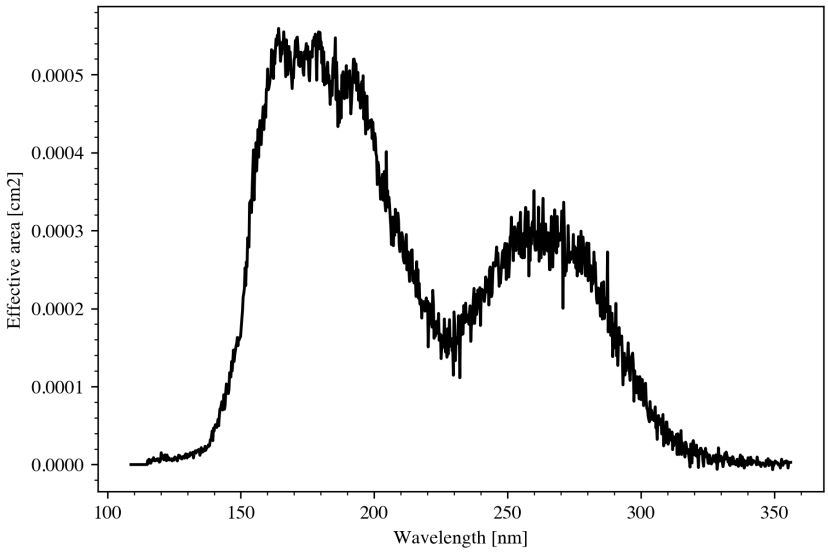

Figure 4.20: PHEBUS/FUV effective area at 4.55 kV.

The planet flux can be defined as follows:

$$\phi(\lambda) = \phi_{Sun}(\lambda) A_L(\lambda)$$

Where:

- ϕ_{Sun} is the solar spectral flux, retrieved from Killen et al. (2009) (Figure 4.21). It contains a combination of calculated and measured high-resolution line shapes with pixel widths

of 2 mÅ(1Å= 0.1 nm) resolution in the EUV/FUV. The solar flux used is a mean at solar minimum, it does not represent the solar flux at the moment of the observation. At the time of the study, the high resolution solar irradiance reference spectrum from Coddington et al. (2023) had not been published but would be more appropriate to use.

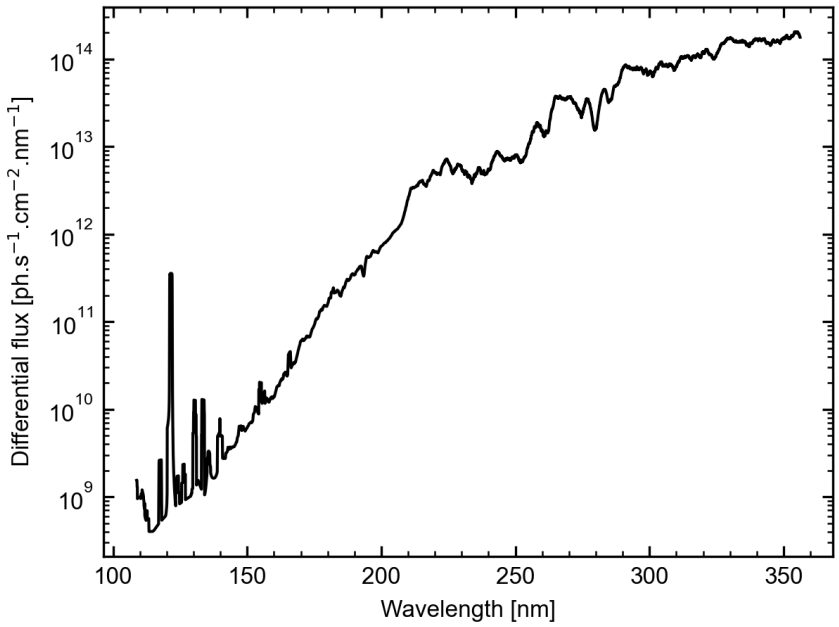

Figure 4.21: Solar spectral flux from Killen et al. (2009). The wavelength range corresponds to that of PHEBUS/FUV.

- A_L is the Venus albedo (Figure 4.22), deduced from the radiance factor measured by SPICAV/UV (E. Marcq, personal communication).

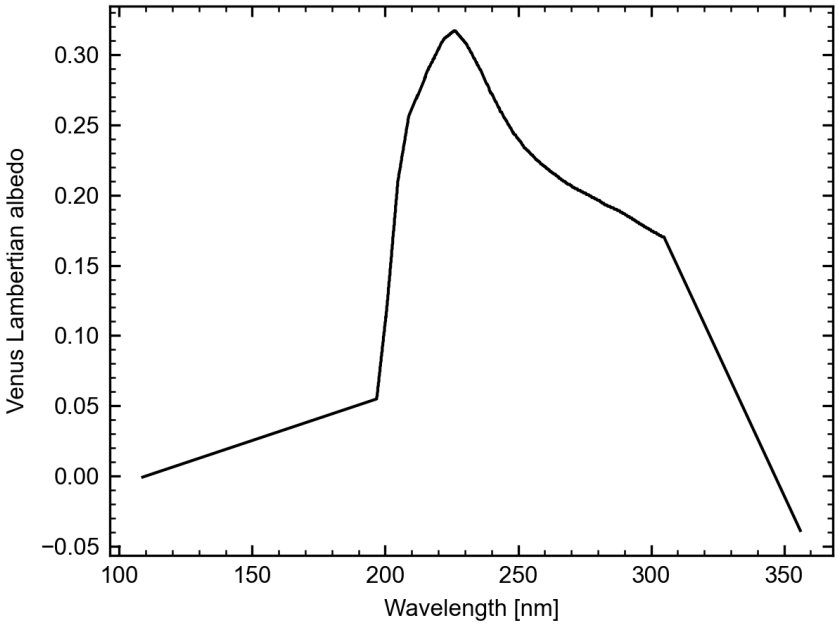

Figure 4.22: SPICAV/UV Lambertian albedo. The wavelength range corresponds to that of PHEBUS/FUV.

With all these elements, I can compare the model with the observations (e.g. Figure 4.23).

A spectral shift can be noticed. The next step consists in convolving the model (orange curve on Figure 4.23) with a function – to be determined – that will represent the response of the instrument.

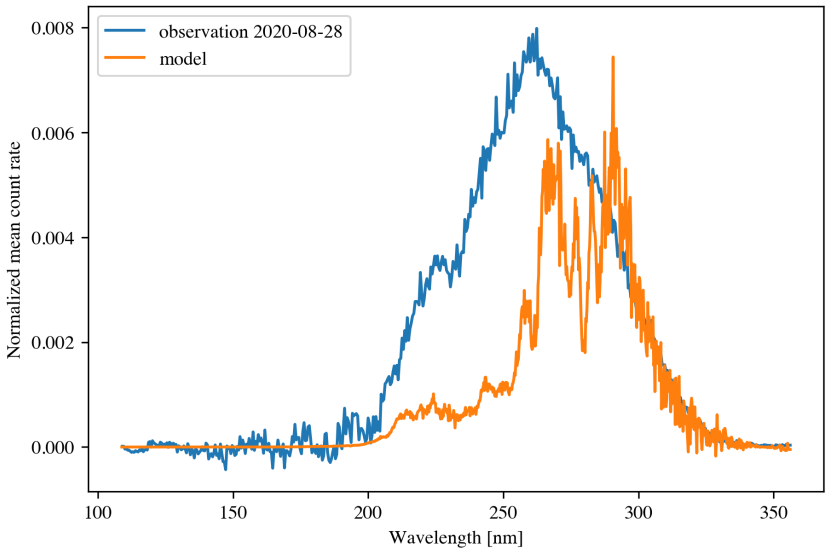

Figure 4.23: Comparison between the spectrum of Venus derived from the August 28, 2020 FUV observation (blue curve) and the modelled spectrum of Venus (orange curve).

4.1.1.5.1 Convolution with a step function

The first function I am testing is a step function with a varying width. This function implies two parameters: the wavelength shift and the FWHM (Full Width at Half Maximum) of the function. To measure how well the models agree with the data, I use the MSE (Mean Squared Error). The results are summarized in Table 4.1.

Table 4.1: Parameters of the step function representing the instrument response function for each observation.

Date	Shift	FWHM	MSE
2020-08-28	17.5	55.5	3.44×10^{-8}
2020-08-29	19.5	56	4.73×10^{-8}
2020-08-30	19.5	60	4.09×10^{-8}
2020-08-31	19	59	4.17×10^{-8}
2020-09-01	19	62	5.54×10^{-8}
2020-09-02	17	62.5	4.34×10^{-8}

Figure 4.24 shows the step function for August 28, 2020 observation (blue curve), along with the other functions that are described in the two followings sections (Gaussian function in orange and PSF (Point Spread Function) in green).

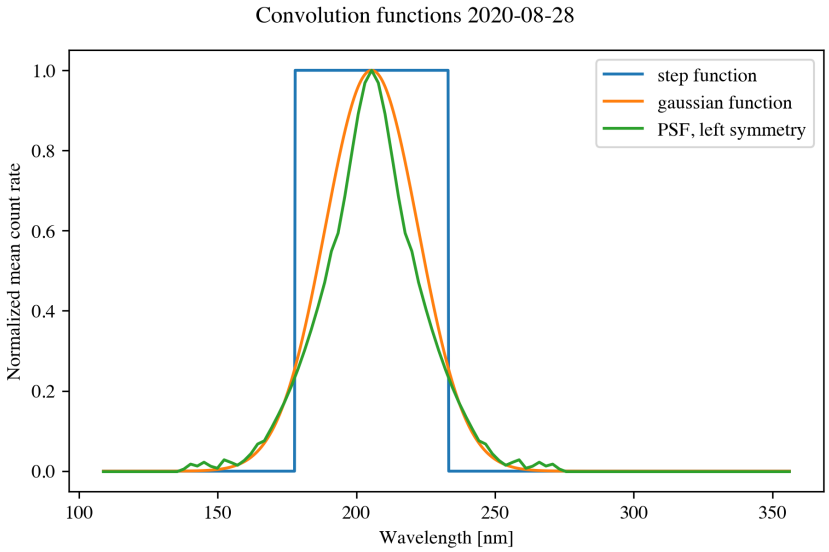

Figure 4.24: Convolution functions minimizing the MSE for August 28, 2020 observation.

4.1.1.5.2 Convolution with a Gaussian function

The second function I am testing is a Gaussian function:

$$f(x) = ke^{-((x-x_1)/x_2)^2}$$

Where k is a normalizing constant, x_1 is the wavelength and x_2 defines the width. k is defined such that $\int_{-\infty}^{+\infty} f(x)\,dx = 1$. Knowing that:

$$\int_{-\infty}^{+\infty} e^{-x^2} dx = \sqrt{\pi}$$

we can deduce that:

$$\int_{-\infty}^{+\infty} ke^{-((x-x_1)/x_2)^2} dx = kx_2\sqrt{\pi}$$

Therefore:

$$k = \frac{1}{x_2\sqrt{\pi}}$$

Regarding the FWHM, it is defined as follows:

$$\text{FWHM} = 2x_i$$

With x_i such that:

$$e^{-(x_i/x_2)^2} = \frac{1}{2}$$

Therefore:

$$\text{FWHM} = 2\sqrt{\ln 2}x_2$$

I evaluate the best couple (shift, FWHM) for each observation by computing the MSE. The maximum likelihood estimate of the model parameters is obtained by minimizing the MSE. The results are summarized in Table 4.2.

Table 4.2: Parameters of the Gaussian function representing the instrument response function for each observation.

Date	Shift	FWHM	MSE
2020-08-28	17	39.5	3.74×10^{-8}
2020-08-29	19.5	39.5	4.75×10^{-8}
2020-08-30	19	43	3.93×10^{-8}
2020-08-31	19	42	4.06×10^{-8}
2020-09-01	19	44	6.61×10^{-8}
2020-09-02	17	45	4.17×10^{-8}

4.1.1.5.3 Convolution with a Point Spread function (PSF)

Finally, I test the PSF (Point Spread Function) assuming the PSF (spatial) and the Line Spread Function (LSF) are identical. The PSF is computed for each day (averaged over column pixel number 120 to 260).

The first problem I face is the maximum of the PSF does not occur at the same line pixel number for each column pixel number. I then have to recenter the maximum of the PSF for each column pixel number before computing the mean.

The second problem is the asymmetry of the PSF (e.g. Figure 4.25). The question is to know in which direction to apply the function during the convolution. I also try realizing a symmetry on one side of the function.

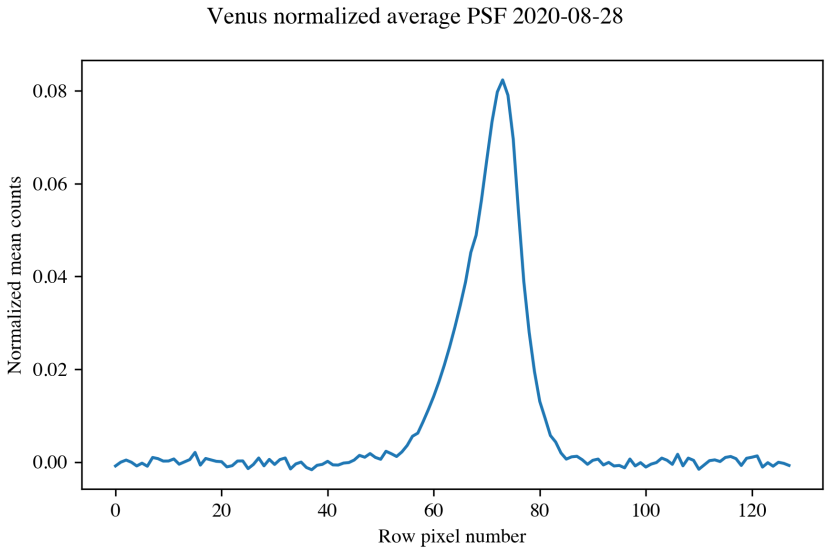

Figure 4.25: Asymmetrical normalized mean PSF derived from the August 28, 2020 observation.

The maximum likelihood estimate of the model parameters is obtained by minimizing the MSE. When combining all the different possibilities (recenter the function or not, flip the function or not, perform a symmetry or not and if so, on which side of the function), it is not easy to state which combination gives the best result. Overall, it seems the left-symmetrical non-recentered PSF is the best solution. This is the one used in the calculations of the MSE

(Table 4.3).

Table 4.3: Parameters of the PSF representing the instrument response function for each observation.

Date	Shift [nm]	k	FWHM [nm]	MSE
2020-08-28	17	5	30.5	4.48×10^{-8}
2020-08-29	19.5	8	31.7	5.37×10^{-8}
2020-08-30	19	8	36.1	4.24×10^{-8}
2020-08-31	19	7.5	27.7	5.13×10^{-8}
2020-09-01	19	6.5	32.5	7.02×10^{-8}
2020-09-02	17	9.5	34.1	4.49×10^{-8}

Considering the PSF, the FWHM of the FUV detector at 4.55 kV is ∼30 nm, far from the 2 nm calculated on the ground (at the nominal HV, i.e. 4.8 kV). Figure 4.26 pictures the result of the convolution of Venus model with the PSF (orange curve).

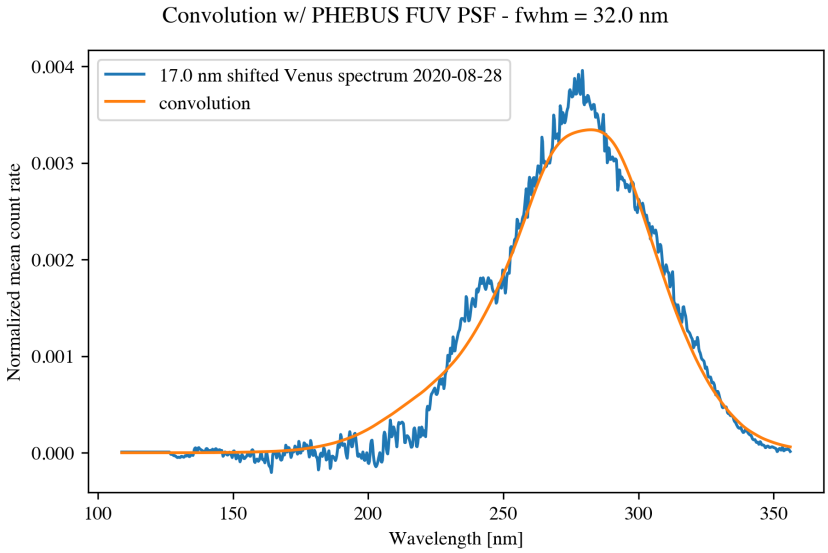

Figure 4.26: Comparison between the spectrum of Venus derived from the August 28, 2020 FUV observation (blue curve) and the modelled spectrum of Venus convolved with a PSF that minimizes the MSE (orange curve).

4.1.2 February 2021 observation campaign

The second campaign took place on February 2021 (Figure 3.14). Out of the four scheduled observations for this campaign, only one was successful. It is the February 17, 2021 observation at distance of 0.335 AU, with a phase angle of 52.3°. The observation lasted for half an hour, with an acquisition every 10 sec and an integration time of 8 sec. The observation comprises 180 image acquisitions at 4.6 kV. Each acquisition consists of a 512×256 matrix (spectral×spatial). To obtain the mean count rate, all the acquisitions are summed then divided by the exposure time and the number of acquisitions. Figure 4.27a corresponds to the observation mean count rate registered by the FUV detector. As for the August and September 2020 observations, I

model the dark current of the FUV detector by a polynomial of order 5 and subtract it to Venus data. I apply the additional correction for columns 350 to 400 and correct the central spike using interpolation (Figure 4.27c). I deduce the spectrum of Venus (Figure 4.27e) by summing the lines where Venus is located, here 49 to 64.

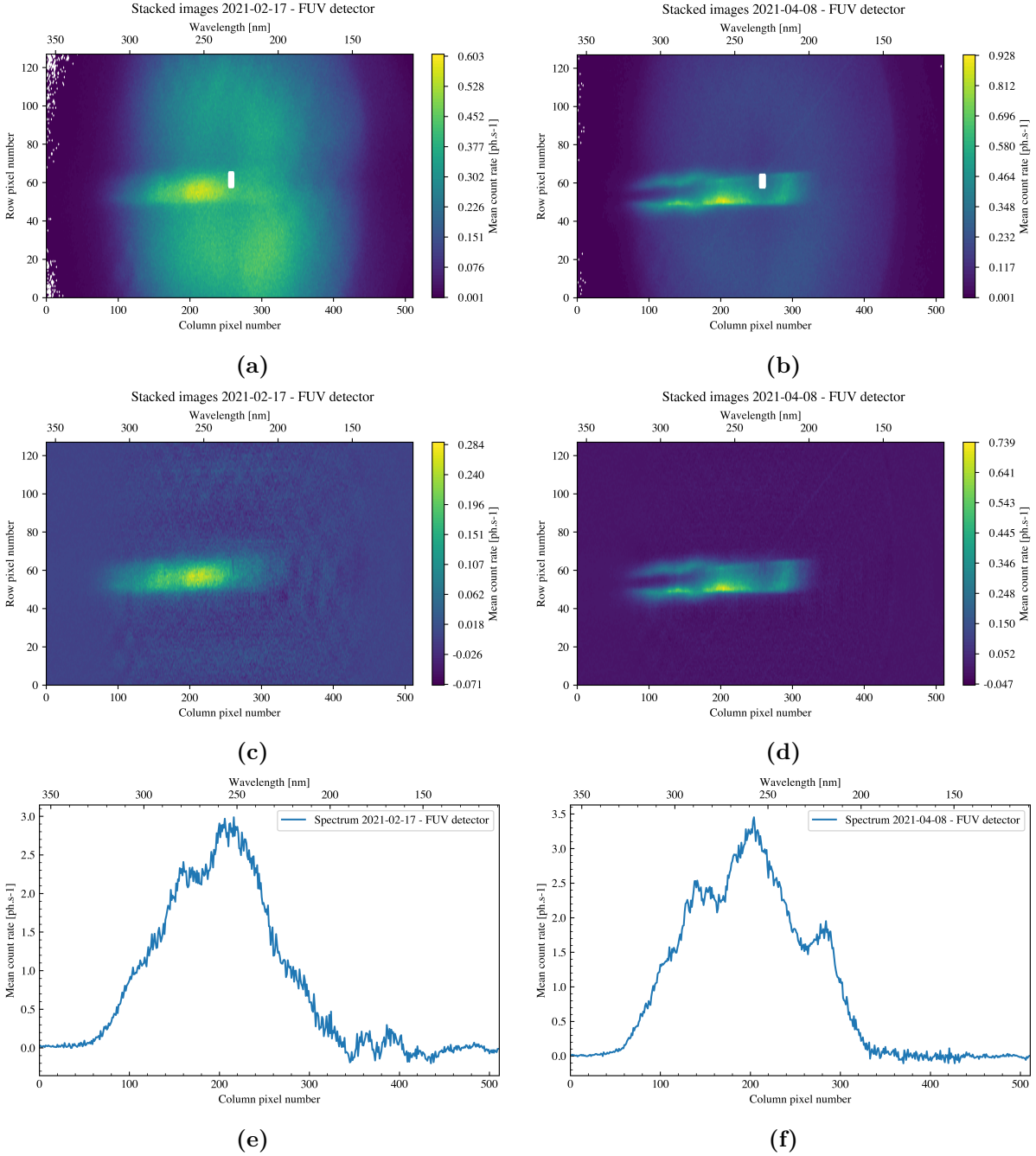

Figure 4.27: The left panels concern the observation of February 17, 2021: (a) mean count rate matrix, (c) mean count rate matrix corrected for the dark current and the central spike and (e) derived spectrum of Venus. The right panels concern the April 8, 2021 observation: (b) mean count rate matrix, (d) mean count rate matrix corrected for the dark current and the central spike and (f) derived spectrum of Venus.

To compute the effective area at 4.6 kV, I use the observation of the star Alpha Eridani (also known as Achernar) performed on February 14, 2021 (Figure 4.28b). This star was observed sequentially at different HV. Figure 4.28 clearly highlights the importance of the HV and its impact on the SNR.

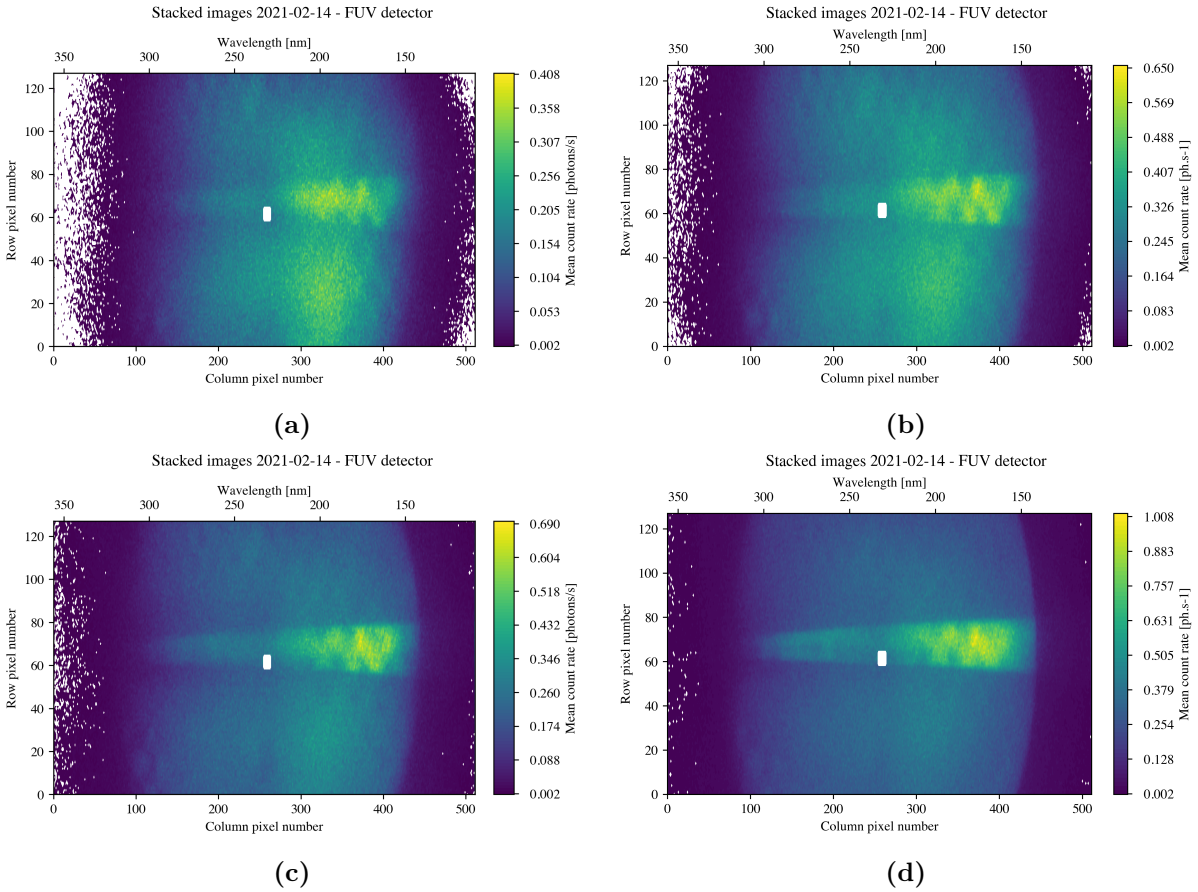

Figure 4.28: Observations of Achernar with the FUV detector acquired on February 14, 2021 at different HV: 4.55 kV (a), 4.6 kV (b), 4.7 kV (c) and 4.8 kV (d).

The observation of Achernar comprises 61 image acquisitions at 4.6 kV, each acquisition consisting of a 512×256 matrix. As for the Spica observation, I subtract the dark observation performed on the same day and subsequently force a null average at the edges. I deduce the spectrum (Figure 4.29) by summing lines from 58 to 75.

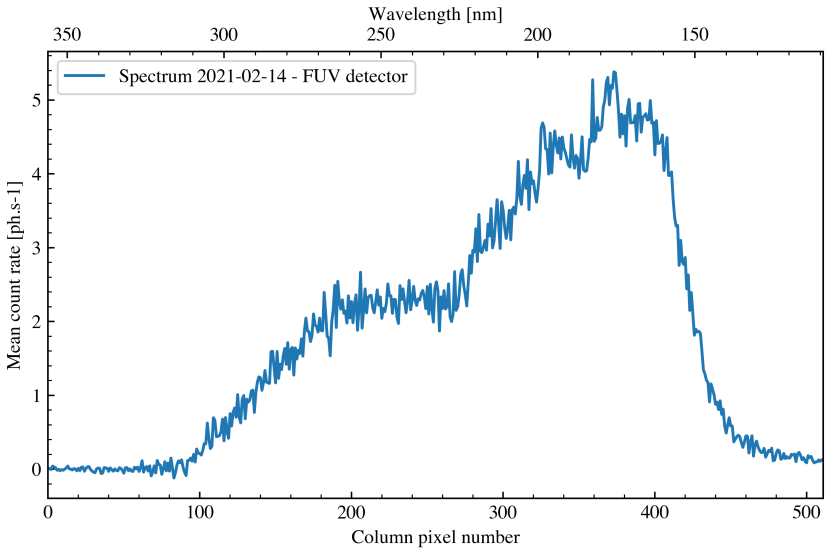

Figure 4.29: Spectrum of Achernar deduced from the February 14, 2021 FUV observation at 4.6 kV.

Then, I retrieve the SPICAM reference photon flux of Achernar and interpolate it on PHEBUS/FUV reference spectrum wavelength grid. I can then deduce the effective area of the FUV detector at 4.6 kV (Figure 4.30) using Eq. (4.1).

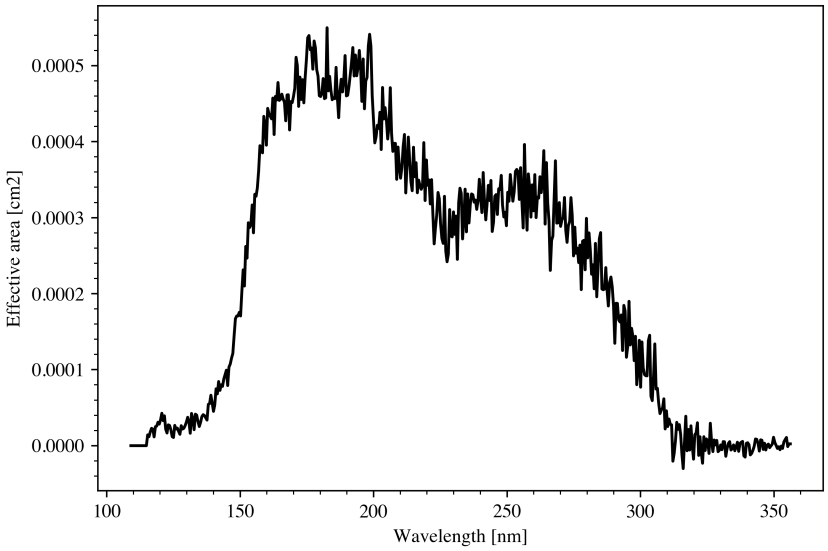

Figure 4.30: PHEBUS/FUV effective area at 4.6 kV.

I use a Gaussian function to convolve the model. When minimizing the MSE, I obtain a shift of 11 nm and a FWHM of 39 nm (Figure 4.31).

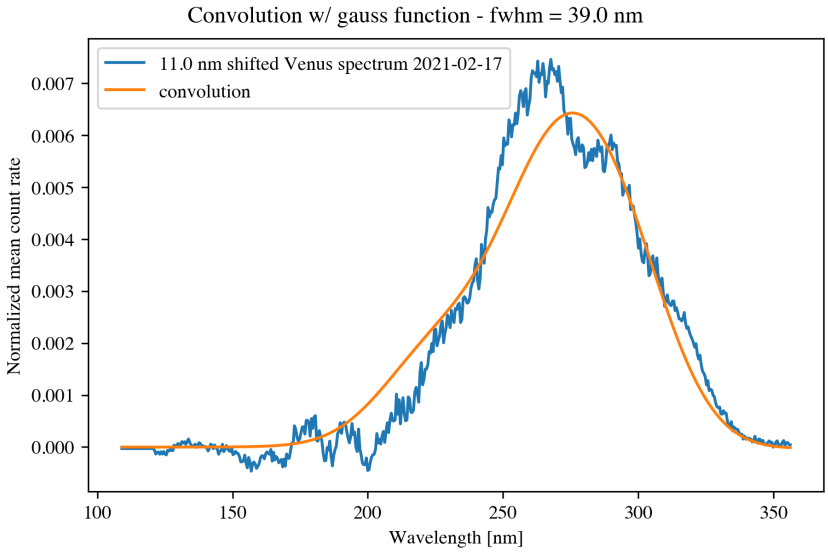

Figure 4.31: Comparison between the spectrum of Venus derived from the February 17, 2021 FUV observation (blue curve) and the modelled spectrum of Venus convolved with a Gaussian function that minimizes the MSE (orange curve).

4.1.3 April 2021 observation campaign

The third campaign took place on April 2021 (Figure 3.14). Of the two observations originally planned, only one was successful. It is the April 8, 2021 observation at distance of 0.339 AU, with a phase angle of 52.7°. The observation lasted for half an hour, with an acquisition every 10 sec and an integration time of 8 sec. The observation comprises 180 image acquisitions at 4.7 kV. Each acquisition consists of a 512×256 matrix (spectral×spatial). To obtain the mean count rate, all the acquisitions are summed then divided by the exposure time and the number of acquisitions. Figure 4.27b corresponds to the observation mean count rate registered by the FUV detector. I model the dark current of the FUV detector by a polynomial of order 5 and subtract it to Venus data. I apply the additional correction for columns 350 to 400 and correct the central spike using interpolation (Figure 4.27d). This observation is a bit odd. At first, we thought Venus had moved in the FOV of PHEBUS during the observation, but after looking individually at each acquisition, it appears not. It seems to be a spread that may be due to the central spike. It was also visible on some observations of August and September 2020 (Figure 4.12). To deduce the spectrum of Venus (Figure 4.27f), I sum the lines where the target is located, here 47 to 54.

To compute the effective area at 4.8 kV, I use the observation of Achernar performed on February 14, 2021 (Figure 4.28d). The observation comprises 60 image acquisitions at 4.8 kV, each acquisition consisting of a 512×256 matrix. As for the Spica observation, I subtract the dark observation performed on the same day with the same voltage and subsequently force a null average at the edges. I deduce the spectrum (Figure 4.32) by summing lines from 60 to 73.

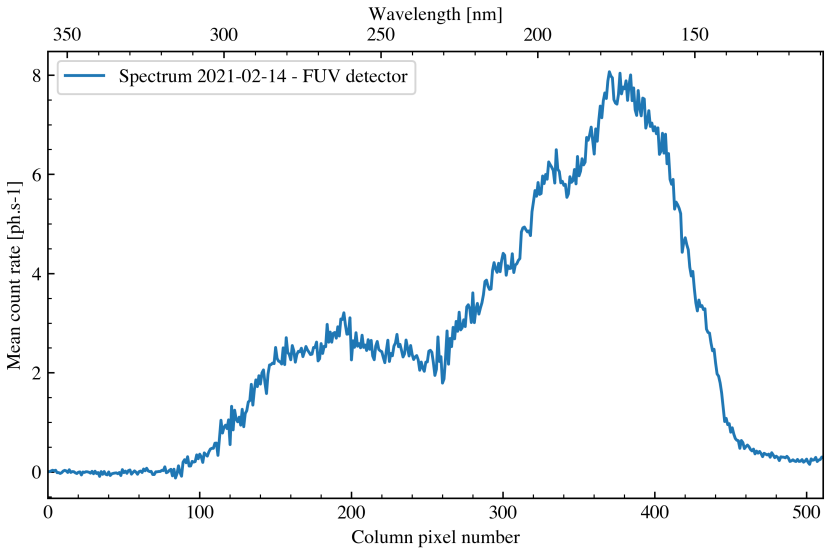

Figure 4.32: Spectrum of Achernar deduced from the February 14, 2021 FUV observation at 4.8 kV.

Knowing the SPICAM reference photon flux of Achernar interpolated on PHEBUS/FUV reference spectrum wavelengths grid, I can then deduce the effective area of the FUV detector at 4.8 kV (Figure 4.33) using Eq. (4.1).

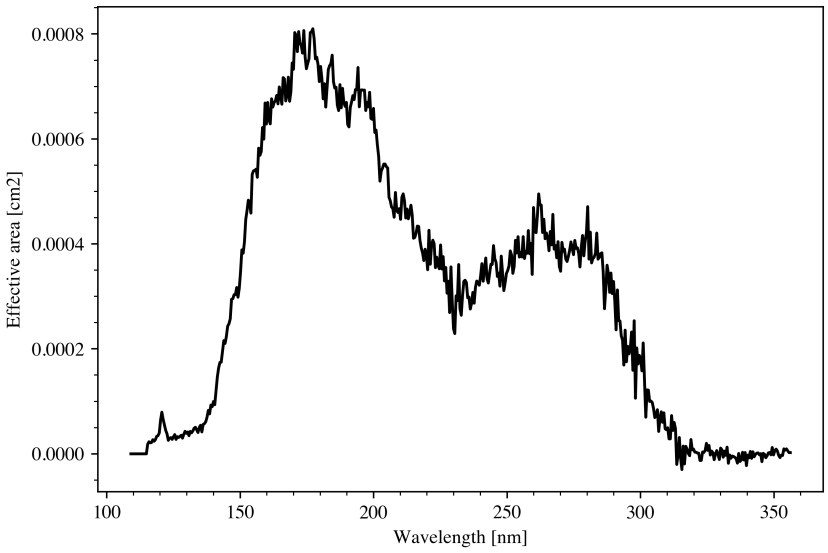

Figure 4.33: PHEBUS/FUV effective area at 4.8 kV.

Regarding the convolution, it is very difficult to determine a function to convolve the model with as the spectrum of Venus is atypical.

4.2 Visible channels in-flight calibration

4.2.1 Calibration stars

The in-flight calibration of PHEBUS visible channels is made through stellar observations. In our case, we are interested in bright stars in the visible range. Most of them are part of the main sequence of the Hertzsprung-Russell diagram, a diagram illustrating the state of the stars during their life (Figure 4.34). It graphically depicts the relationship between luminosity (i.e.

the energy released by the star per second), surface temperature and star radius. The radius increases diagonally from the bottom left to the top right. The distinct groups (e.g. supergiants, dwarfs ...) represent different stellar phases. Few stars are found outside these groups as they spend little time in a transient state. Furthermore, stars spend most of their life in the main sequence: 90% of the stars observed in the sky are in the main sequence. The spectral type of a star, allowing to classify the stars according to their temperature, is indicated by a letter (OBAFGKM), from the hottest to the coldest types. The classification of a star is based on the shape of its spectrum and the intensity of its lines.

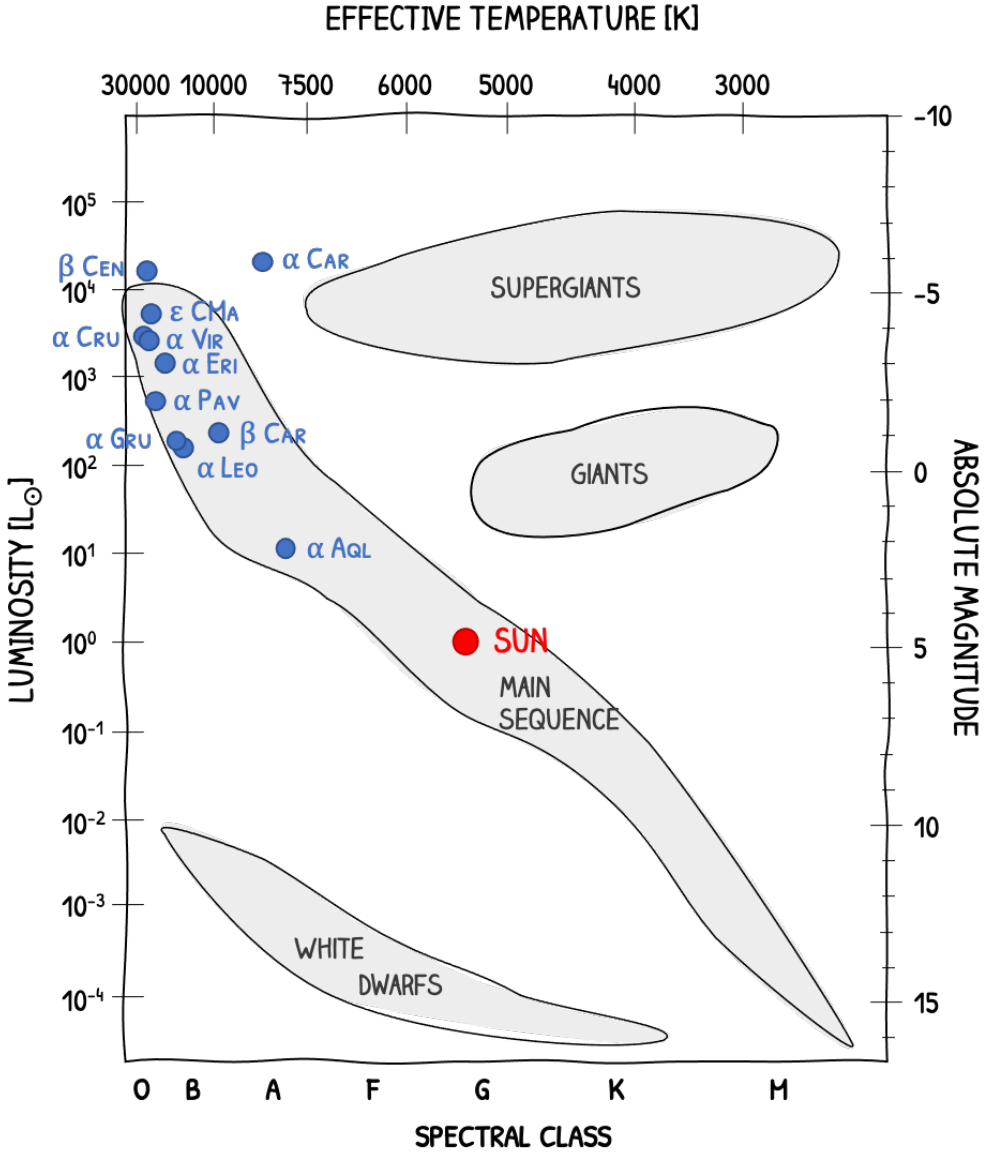

Figure 4.34: Schematic Hertzsprung-Russell diagram with the stars used for the visible channels calibration.

4.2.2 Flip maneuvers

Performed twice a day by BepiColombo, the flip maneuver offers a good opportunity for PHEBUS to observe stars. The flip strategy consists in a 180° rotation of the spacecraft around its +Y axis (facing the Sun), performed twice a day with the use of reaction wheels. The slew lasts for ∼3 hr. The spacecraft then keeps its attitude, namely "cruise attitude", for 9 hr before the

maneuver is performed again in the reverse direction. This process aims to reduce the angular momentum load on the spacecraft's reaction wheels due to the solar radiation pressure and thus to save fuel. In fact, by reducing the load acting on the reaction wheels, it is necessary to perform WOL less often. These WOLs consume fuel since they consist in discarding part of the angular momentum accumulated in the spacecraft's reaction wheels by transferring it to a momentum induced by a thrust of the spacecraft's chemical propulsion system.

Figure 4.35 depicts the two possible scenarios of observation during the flip maneuvers. The first one (Figure 4.35a) uses a single scanner position, allowing to observe several stars during the same observation. It is called a sky scan. The second scenario (Figure 4.35b) involves multiple positions, allowing to observe the same star several times during the same observation. It requires the computation of the scanner angle for which the targeted star is at the center of the FOV every 10 min. This way, the star crosses PHEBUS FOV differently. For the study, I have used only the observations during the flip maneuvers with the slit across, a high voltage of 1 kV and an exposure time of 1 sec.

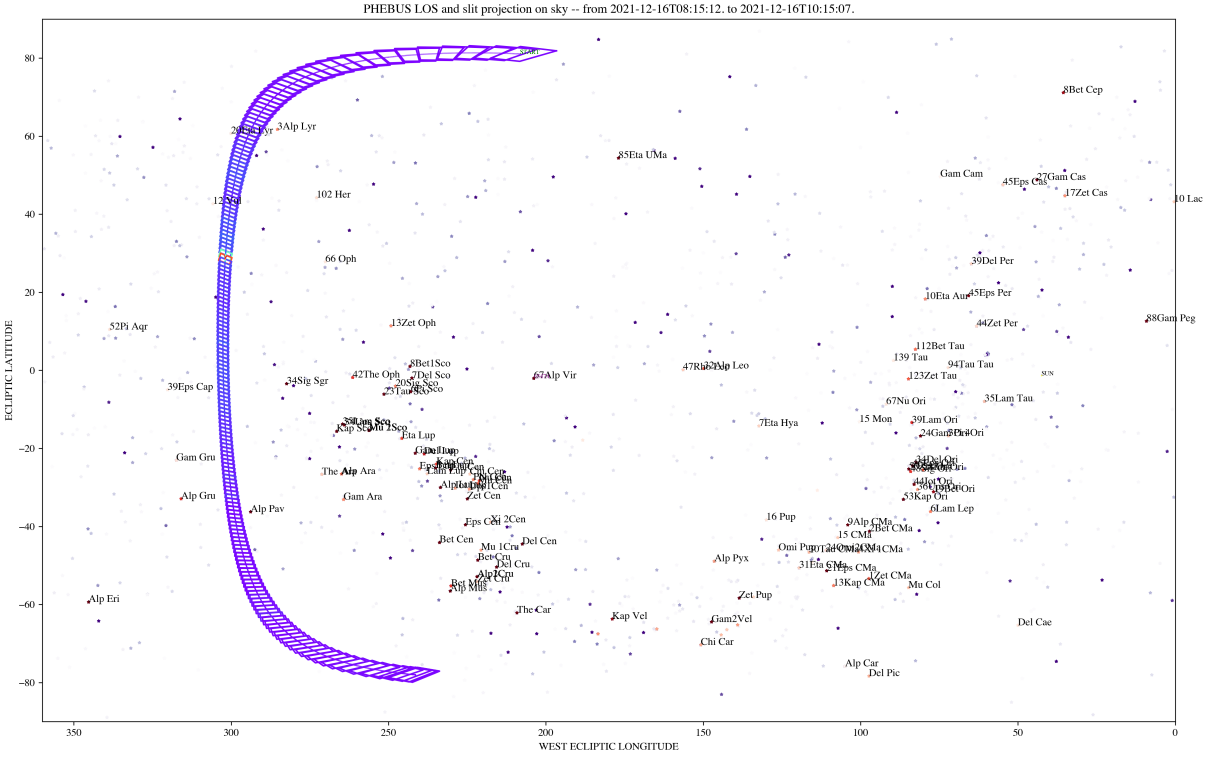

(a)

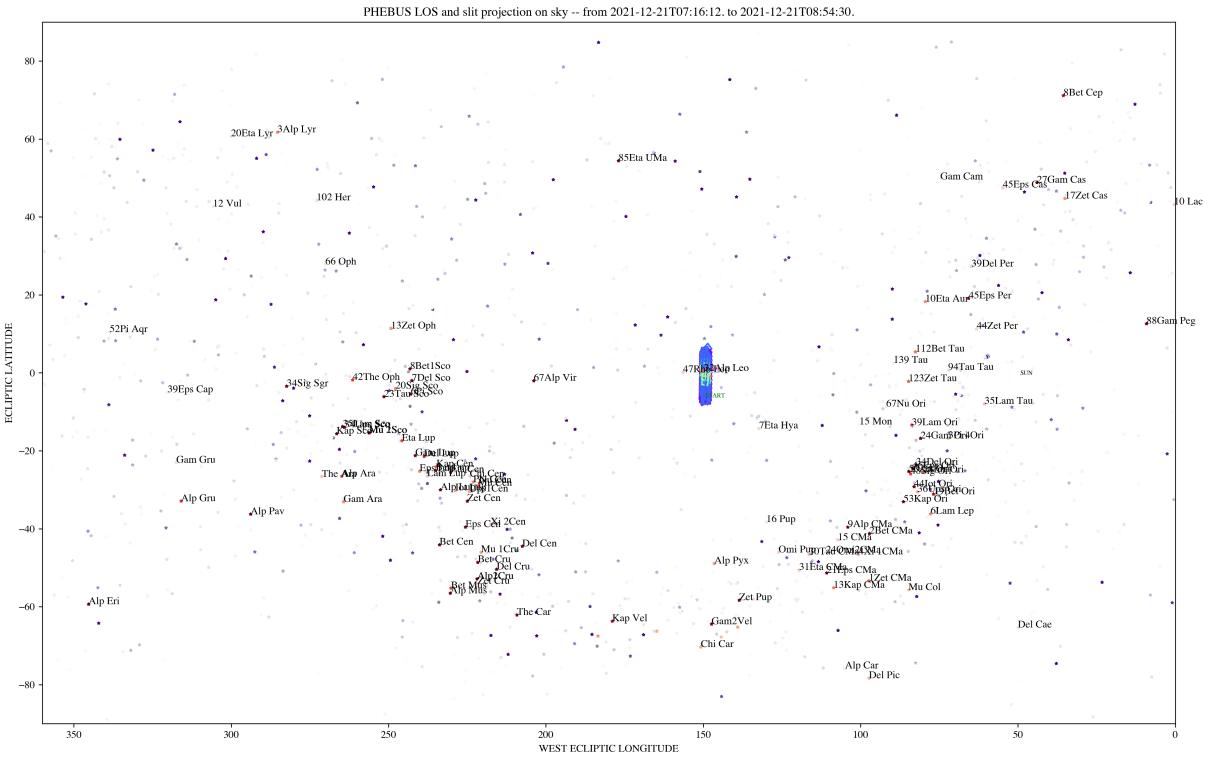

(b)

Figure 4.35: Projection of PHEBUS FOV on the sky: first case scenario with a single scanner position (a) and second case scenario with multiple scanner positions (b).

4.2.3 Stars identification

The crossing of a star in the FOV of PHEBUS results in a peak in the count rate of both visible channels. For single position flips, there may be multiple peaks. Is is then necessary to identify to which star each peak corresponds. For a given peak, I retrieved the associated time of acquisition and the coordinates of the LOS of PHEBUS. We consider that a star is in the FOV of PHEBUS with the slit across when the angle between the LOS and the direction of the star is lower than 1°. I used a catalogue adapted from The Hipparcos Catalogue (ESA, 1997), that provides the ecliptic coordinates of more than 100,000 stars along with their HIP number and their flux at 400 nm. The original catalogue gathers more information (e.g. positions, proper motions, magnitudes, astrometric and photometric data). Using the projection of PHEBUS FOV on the sky at the time of the peak and the positions of the stars in the adapted Hipparcos catalog, I was able to identify the stars, except for one. This may be due to the pointing error of the instrument or simply the fact that the star is not in the adapted Hipparcos catalog. The identified stars are summarized in Tables 4.4 and 4.5.

4.2.4 Effective area computation

The effective area, corresponding to the detector sensitivity, is the product of the entrance area by the spectral efficiency of the detector, that includes the entrance mirror, the FUV grating, the deflection mirrors and the detector. As a star is a punctual source, we can compute the effective area of the detectors by using the following equation:

$$CR = A_{eff} F \tag{4.2}$$

With CR the count rate associated with the star (units of s^{-1}), A_{eff} the effective area of the detector (units of cm^2) and F the transmitted flux of the star on the channels (units of

$s^{-1}.cm^{-2}$).

4.2.4.1 Stars transmitted flux

The transmitted flux F is expressed as:

$$F = \int \phi(\lambda) T(\lambda) d\lambda \tag{4.3}$$

Where ϕ is the photometric flux of the star, T the bandwidth of the visible channels and λ the wavelength. The spectral response of the visible channels was measured on ground with the slit across (Figure 4.36). I retrieved the photometric fluxes of the stars at multiple wavelengths in Burnashev (1985). However, there is not a single catalog where all the stars observed by PHEBUS are available. Therefore, the spectrum of some stars was not available.

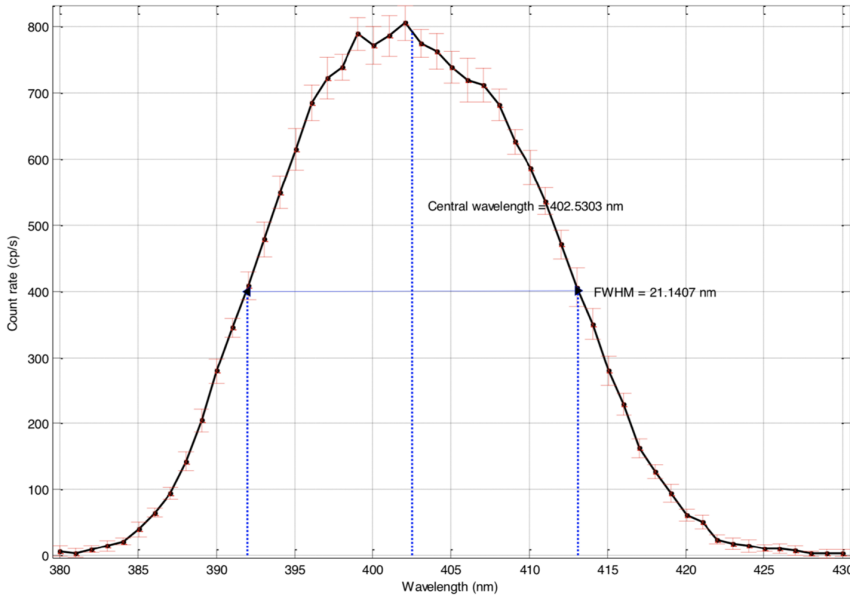

(a)

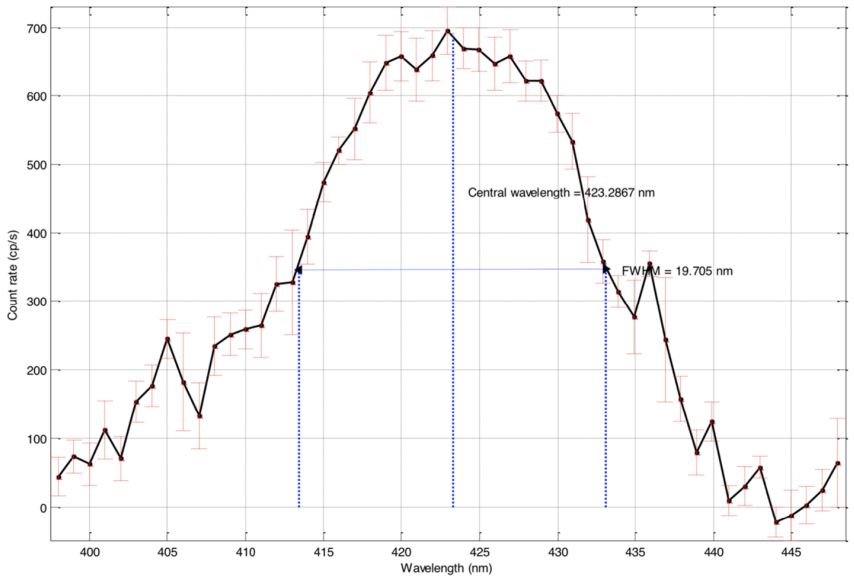

(b)

Figure 4.36: c404 (a) and c422 (b) channels spectral responses as measured on the ground. From Quémerais et al. (2020).

4.2.4.2 Correction of the data

The number of counts registered by the visible channels does not correspond directly to the signal of the observed star. There is a contribution from the dark current and the zodiacal light.

4.2.4.2.1 Zodiacal light

During the flip maneuvers, we have performed not only observations with the slit across but also with the slit removed to determine the ratio between the two slit modes. Surprisingly, the observations during the flip maneuvers with the slit removed have highlighted the zodiacal light. As a matter of fact, when the slit is across, the count rate is globally constant with the ecliptic latitude (Figure 4.37a). However, when the slit is removed, the count rate increases as the LOS gets closer to the ecliptic plane (Figure 4.37b). This "bump" corresponds to the zodiacal light.

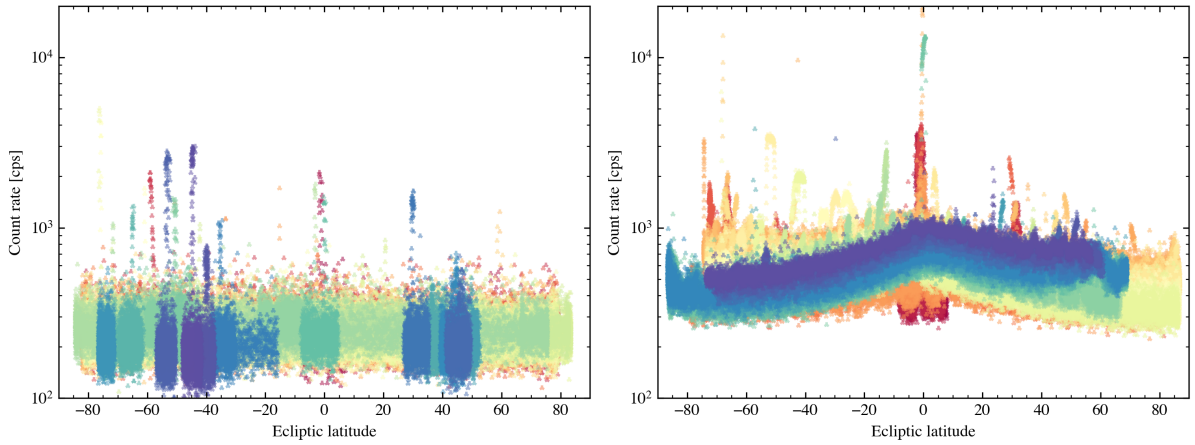

Figure 4.37: c404 count rate as a function of PHEBUS boresight ecliptic latitude registered during flip maneuvers with the slit across (a) / removed (b). Peaks correspond to stars crossing the FoV of PHEBUS. Each colour corresponds to a single observation.

The zodiacal light depends on the heliocentric distance and the elongation (Section 3.4.1.5). A model of zodiacal light has been computed based on Leinert et al. (1998). Its contribution is estimated between ∼50 counts per second (towards the ecliptic poles) and ∼100 counts per second (towards the ecliptic equator) for an observation at 0.5 AU from the Sun (i.e. during the cruise phase). When the slit is across, the contribution of the zodiacal light is divided by a factor of 22.

4.2.4.2.2 Dark current

To measure the dark current in-flight, we have conducted several campaigns of observations at the parking position (Section 3.3). We have varied the observation parameters during these campaigns (e.g. slit mode, exposure time). Even though the slit mode should not have an impact for this type of observation, Figure 4.38 clearly shows a difference. When the slit is across, the dark current seems to converge to an average value of ∼230 counts per second for both detectors. However, when the slit is removed, some outliers prevent convergence of the dark count rate.

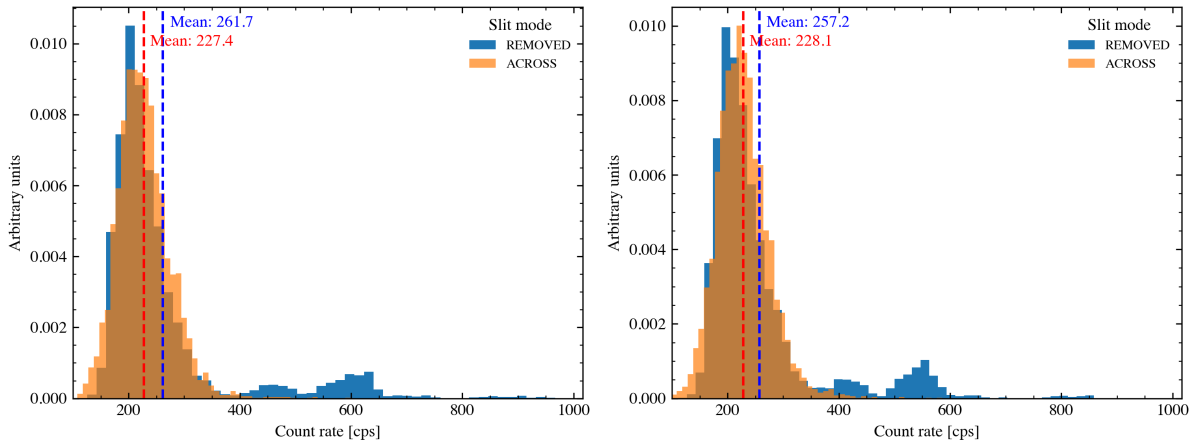

Figure 4.38: Distribution of the count rate during the observations at the parking position for the c404 (a) and c422 (b) channels.

One possible explanation for this difference is that some photons enter the baffle in the parking position, when it should not be the case. To monitor if light was coming in the baffle, we have performed two consecutive observations at the parking position, one with the shutter[1] open and the other one with the shutter closed. This type of observation was repeated eight times, for different sets of slit mode and exposure time. No difference was noted between the shutter open and close. We concluded that there was no light entering the baffle.

Another explanation is the dependence with temperature: the hotter the detector, the more counts it registers. The temperature is partly related to the heliocentric distance at the moment of the operation. The problem with this hypothesis lies in the fact that the temperature sensors are not on the PMT but right next to them, giving only an indication of the temperature of the surrounding environment. As it can be seen on Figure 4.39, there is no obvious relationship between the count rate and the temperature. It should also be noted that during the ground test campaigns (in 2014), dark observations were carried out at several operating temperatures without impacting the count rate. However, the number of counts per second observed was much lower (only a few counts per second on ground compared to hundreds of counts per second in flight).

I identified several unusual observations (indicated with red circles on Figure 4.39) that presented a relatively high count rate with no obvious link to temperature. These are observations at the parking position made with the slit removed, an exposure time of 8 sec and with a UV detector (either FUV or EUV) in addition to the visible channels. They are dated October 8, 9 and 10, 2021 and March 28, 2022. I have decided to consider the solar environment at the time of those observations. Using data from BepiColombo Radiation Monitor (BERM) and the online tool *The Space Weather Database Of Notifications, Knowledge, Information* (DONKI) (https://kauai.ccmc.gsfc.nasa.gov/DONKI/), I noticed that there were solar events around the periods of observation of PHEBUS. However, there are also solar events around other PHEBUS observation periods without any consequences on the count rate (the observation parameters were somewhat different). It is important to note that PHEBUS sensitivity to charged particles depend on their nature[2] and their energy. So, depending on the solar event, the instrument will be affected differently. It is therefore difficult to conclude on the origin of these unusual observations.

Ultimately, I used the dark observations made with the same parameters as the flip maneu-

[1] See Section 3.3.2.3 for description of the shutter.
[2] The MCP and PMT are sensitive to electrons whereas the RAE is sensitive to ions.

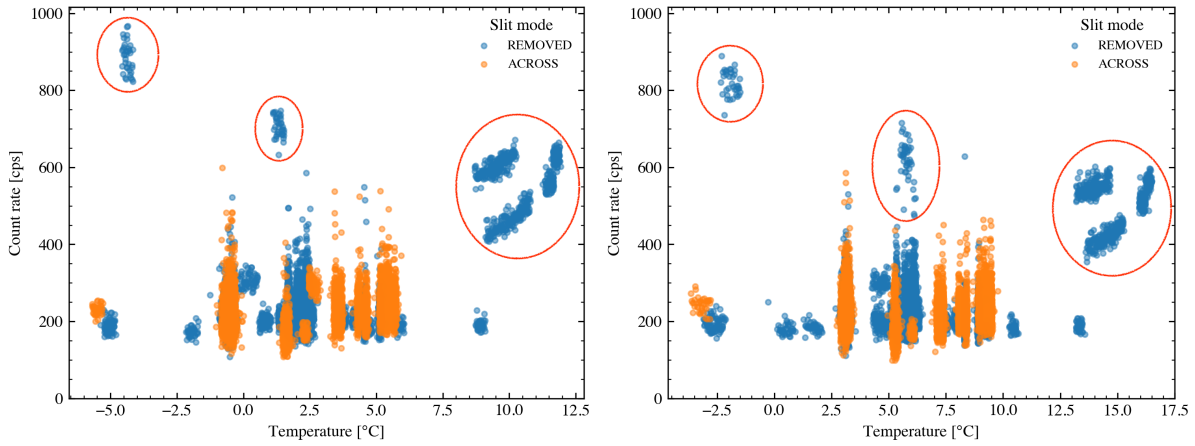

(a) **(b)**

Figure 4.39: c404 (a) and c422 (b) count rate registered during observations at the parking position as a function of the detector's temperature. The blue (resp. orange) dots indicate observations made with the slit removed (resp. across).

vers (i.e. slit across and exposure time of 1 second) to deduce the mean value of the dark and its associated error (the error corresponds to the standard deviation). The estimates of D_{404}, the dark on the c404 channel, and D_{422}, the dark on the c422 channel, are then:

$$\begin{aligned} D_{404} &= 228.5 \pm 47.4 \text{ counts} \\ D_{422} &= 229.0 \pm 47.1 \text{ counts} \end{aligned} \tag{4.4}$$

4.2.4.3 Results and uncertainties

Table 4.4 lists the stars identified during the flip observations, their name and Hipparcos identification number, the count rate observed on c404 corrected for the background, along with the flux of the star transmitted on c404 and the effective area deduced from the measurements. Table 4.5 contains the same information for the c422 channel. When a star has been observed several times, I considered the maximum value. From the count rate and the transmitted flux, I deduced the effective area (Eq. 4.2) from each star. Stars whose deduced effective area is within $\pm 1\sigma$ of the mean value are marked with an asterisk in Tables 4.4 and 4.5. By computing the average of the effective area deduced from these marked stars, I obtain $A_{eff_{404}} = 1.19 \times 10^{-2}$ cm^2 and $A_{eff_{422}} = 0.96 \times 10^{-2}$ cm^2.

Table 4.4: Star name, Hipparcos identification (HIP id.), observed count rate on c404 during flip maneuvers (CR_{404}), transmitted flux on c404 (F_{404}) and its deduced c404 effective area (A_{eff}).

Name	HIP id.	CR_{404} [ph.s^{-1}]	F_{404} [ph.s^{-1}.cm^{-2}]	$A_{eff} = CR_{404}/F_{404}$ [cm^2]
α Eridani *	7588	1876.6	1.65×10^5	1.14×10^{-2}
α Carinae	30438	4776.6	4.99×10^5	9.57×10^{-3}
ϵ Canis Majoris *	33579	1255.6	1.02×10^5	1.24×10^{-2}
β Carinae *	45238	821.6	6.53×10^4	1.26×10^{-2}
α Leonis *	49669	1286.6	1.09×10^5	1.19×10^{-2}
α Crucis *	60718	2583.6	2.05×10^5	1.26×10^{-2}
α Virginis *	65474	1886.6	1.70×10^5	1.11×10^{-2}
β Centauri *	68702	2770.6	2.37×10^5	1.17×10^{-2}
α Aquilae *	97649	1412.6	1.24×10^5	1.14×10^{-2}
α Pavonis	100751	876.6	6.84×10^4	1.28×10^{-2}
α Gruis *	109268	901.6	7.32×10^4	1.23×10^{-2}

Table 4.5: Star name, Hipparcos identification (HIP id.), observed count rate on c422 during flip maneuvers (CR_{422}), transmitted flux on c422 (F_{422}) and its deduced c422 effective area (A_{eff}).

Name	HIP id.	CR_{422} [ph.s^{-1}]	F_{422} [ph.s^{-1}.cm^{-2}]	$A_{eff} = CR_{422}/F_{422}$ [cm^2]
α Eridani	7588	1138	2.08×10^5	5.48×10^{-3}
α Carinae	30438	3517	4.75×10^5	7.41×10^{-3}
ϵ Canis Majoris *	33579	770	8.37×10^4	9.20×10^{-3}
β Carinae	45238	660	5.90×10^4	1.12×10^{-2}
α Leonis *	49669	911	9.35×10^4	9.74×10^{-3}
α Crucis *	60718	1707	1.69×10^5	1.01×10^{-2}
α Virginis *	65474	13076	1.40×10^5	9.80×10^{-3}
β Centauri *	68702	1786	1.96×10^5	9.10×10^{-3}
α Aquilae *	97649	1051	1.18×10^5	8.89×10^{-3}
α Pavonis *	100751	612	5.82×10^4	1.05×10^{-2}
α Gruis *	109268	611	6.42×10^4	9.52×10^{-3}

To compute the uncertainty associated to the effective area, I consider the propagation of errors that shows that the variance σ_f^2 in the value of any function will be:

$$\sigma_f^2 = \sum_i \sigma_i^2 \left(\frac{\partial f}{\partial y_i}\right)^2 \tag{4.5}$$

I apply it to the effective area (Eq. 4.2):

$$\sigma_{A_{eff}}^2 = \left(\frac{1}{F}\right)^2 \sigma_{CR}^2 + \left(\frac{-CR}{F^2}\right)^2 \sigma_F^2 \tag{4.6}$$

The errors on the spectrum measurements σ_F were unfortunately not available, so I considered them as null, leading to:

$$\sigma_{A_{eff}}^2 = \left(\frac{1}{F}\right)^2 \sigma_{CR}^2 \tag{4.7}$$

The count rate CR and its uncertainty σ_{CR} are defined as follows:

$$\begin{aligned} CR &= \frac{N_{corr}}{\Delta t} \\ \sigma_{CR}^2 &= \frac{\sigma_{N_{corr}}^2}{\Delta t^2} \end{aligned} \tag{4.8}$$

w-Where Δt corresponds to the exposure time and N_{corr} corresponds to the number of counts registered by the detector corrected for the dark current. N_{corr} and its uncertainty $\sigma_{N_{corr}}$ are defined as follows:

$$\begin{aligned} N_{corr} &= N - D \\ \sigma_{N_{corr}}^2 &= \sigma_N^2 + \sigma_D^2 \end{aligned} \tag{4.9}$$

Where D is the dark current and σ_D its associated uncertainty. Their values are given in Eq. (4.4). The visible channels being composed of a PMT to detect photons, the number of counts registered by the visible channels does not correspond exactly to the number of incident photons. The relation between the number of counts N, the number of photons P and the dark current D is as follows:

$$N = kP + D \tag{4.10}$$

I derived the coefficient k using observations of different stars. For each observation, I retrieved the mean value of the number of counts registered by both visible channels ($\langle N_{404} \rangle$ and $\langle N_{422} \rangle$) and computed the variance ($\sigma_{N_{404}}^2$ and $\sigma_{N_{422}}^2$). The values are summarized in Table 4.6. I then applied a linear regression between $\langle N_{404} \rangle$ and $\sigma_{N_{404}}^2$ to derive the coefficient k_{404} associated to the c404 channel. I applied the same method to the other channel (i.e. the c422 channel). The coefficients k_{404} and k_{422} are nearly equal to 1. In the rest of this chapter, I considered them equal to 1.

The uncertainty σ_N associated to the number of counts N is equal to:

$$\sigma_N^2 = \sigma_P^2 + \sigma_D^2 \tag{4.11}$$

The detected photons in a photomultiplier tube follow a Poisson distribution. The error σ_P associated with the number of photons detected by the channels corresponds to photon noise and is equal to:

$$\sigma_P = \sqrt{P} \tag{4.12}$$

Combining Eq. (4.7), (4.8), (4.9), (4.11) and (4.12), we finally get:

$$\sigma_{A_{eff}}^2 = \left(\frac{1}{F}\right)^2 \frac{N_{corr} + 2\sigma_D^2}{\Delta t^2} \tag{4.13}$$

For both channels, I computed the uncertainty associated with each considered star (marked by an asterisk in Tables 4.4 and 4.5) and computed the average value. I finally deduced the effective area of both detectors $A_{eff_{404}}$ and $A_{eff_{422}}$:

$$\begin{aligned} A_{eff_{404}} &= 1.19 \times 10^{-2} \pm 2.3 \times 10^{-4} \text{ cm}^2 \\ A_{eff_{422}} &= 0.96 \times 10^{-2} \pm 2.8 \times 10^{-4} \text{ cm}^2 \end{aligned} \tag{4.14}$$

Table 4.6: Mean value of the number of counts registered by each visible channel ($\langle N_{404} \rangle$ and $\langle N_{422} \rangle$) along with the variance ($\sigma^2_{N_{404}}$ and $\sigma^2_{N_{422}}$). Each row corresponds to a different stellar observation.

$\langle N_{404} \rangle$	$\sigma^2_{N_{404}}$	$\langle N_{422} \rangle$	$\sigma^2_{N_{422}}$
6,921.3	20,829.3	5,854.3	16,261.6
6,117.7	15,524.0	5,406.9	24,139.5
18,947.0	31,331.2	13,657.7	22,721.1
19,398.0	38,786.4	13,399.6	24,389.7
3,635.5	18,743.6	3,273.4	23,277.5
11,668.8	25,623.4	7,919.5	18,540.2
7,291.6	16,627.4	5,213.7	17,180.5
4,714.1	18,678.6	4,544.7	21,906.4
5,048.3	20,056.1	4,787.2	19,475.8
4,820.4	17,634.8	4,727.0	19,693.1
5,831.0	13,211.1	5,349.8	15,225.6
7,632.1	13,674.9	6,890.4	14,620.2
7,460.3	15,678.4	6,775.7	18,739.4
5,977.4	17,533.3	5,432.2	21,304.8
10,082.7	26,252.5	7,866.2	23,355.1
15,899.3	29,404.4	9,744.2	30,920.4
16,580.8	31,095.1	10,116.2	25,108.0
15,701.6	15,761.6	9,618.8	21,200.2
16,330.7	38,858.4	9,879.6	36,038.8
20,139.9	40,490.3	12,438.3	34,065.4
20,534.4	28,005.3	12,699.2	31,695.4
21,936.8	31,202.4	13,245.1	22,506.4
19,117.9	41,402.1	11,859.7	25,051.4
21,514.3	25,104.3	13,231.4	30,999.1

Chapter 5

Mercury flybys with BepiColombo

In this chapter, I will describe the preparation of Mercury flybys from an operational point of view. I will then comment on the data acquired by PHEBUS visible channels during the first two flybys of Mercury by BepiColombo. I will subsequently explain how I process these data to convert them into scientific unit. The specific analysis of the results of the c422 is done in Chapter 6 and those of the c404 channel in Chapter 7.

5.1 Planning the flybys

To prepare PHEBUS observations during a flyby of Mercury, a set of parameters has to be defined. We select the detectors to operate, along with their high voltage. We define the observation sequence, i.e. the duration with respect to the CA. We then select the scanner angle, considering some geometrical constraints. Finally, we define additional parameters such as the slit mode, the observation rate and the integration time.

5.1.1 Selection of the detectors

The selection of the detectors must be made considering that the EUV and FUV detectors cannot operate simultaneously (Section 3.3.2.6). As for the visible channels, they can be operated along with one of the UV detectors. Several scenarios are therefore possible. Along with the visible channels, we can use one of the UV detectors or decide to operate the UV detectors one after the other. This last scenario is however not ideal during a flyby as it implies a time during which no data can be acquired (Figure 5.1). In fact, to change the UV detector, it is necessary to switch off the instrument and then switch it on again. There is a time margin of 2 min between the switch off and the switch on. Moreover, it is necessary to take into account the high voltage ramp (8 min for the FUV, 30 min for the EUV). Thus, this last scenario wastes between 15 and 35 min of observation time and does not allow continuous observation.

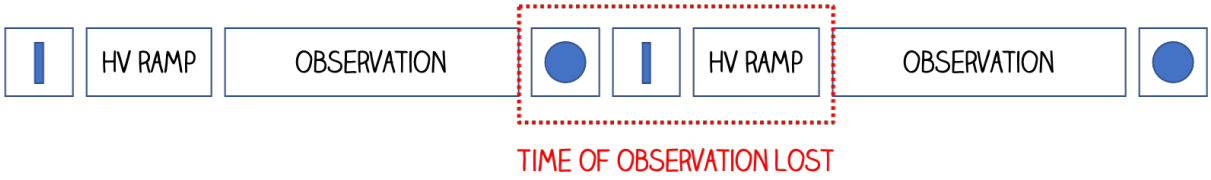

Figure 5.1: Visualisation of the observing time lost due to the switch of the UV detector.

The choice of the detector is also related to the species we can detect (Table 5.1). As helium has not been observed in the exosphere of Mercury since Mariner10 in the 1970s, we have decided to use the EUV detector along with the visible channels for the first flyby (Quémerais

et al., 2023). For the second and third flybys, we have decided to use the FUV along with the visible channels.

Table 5.1: Species that can be detected by PHEBUS

Detector	Species	Vacuum wavelength [nm]
EUV	He	58.4
	H	121.6
FUV	Mg	285.3
c404	Mn	403.190
		403.421
		403.563
	K	404.528
		404.835
c422	Ca	422.8

5.1.2 Selection of the high voltage

Each detector has a nominal operating voltage which was determined on ground prior to the launch:

- 1 kV for the visible channels,
- 3.6 kV for the EUV,
- 4.8 kV for the FUV.

During the cruise, we have conducted several stellar observation campaigns to determine the best high voltage/discriminator couple. Whether for the EUV or the FUV, when increasing the high voltage, the SNR (Signal-to-noise ratio) is improved. But it also implies that there are more photo-events, which damages the MCP faster. Considering that we are at the beginning of the mission, still in cruise, we decided to employ a conservative approach and selected a high voltage of 3.4 kV for the EUV and 4.6 kV for the FUV. The discriminator is the same, namely 8.

5.1.3 Selection of the observation parameters

For the first flyby, we have decided to observe during an hour, starting 30 minutes before the closest approach. We have selected a sampling frequency of 10 seconds. The integration time for each individual measurement was 8 seconds, the remaining 2 seconds being used by the instrument to process the detector images and transmit them to the spacecraft. The slit was removed in order to optimize the count rate (Section 3.3.2.4).

For the second flyby, we have decided to extend the time of observation: two hours, starting an hour before the closest approach. However, to avoid a strong dark current on the FUV detector (Section 3.3.3.2) at the most important moment of the operation (i.e. the closest approach), we have decided to switch on the FUV only shortly after the entry in the shadow of Mercury. Moreover, we have chosen to add a dark observation (i.e. at the parking position) at the end of the operation to monitor the performance of the dark current after almost two hours of observation. The sampling frequency, integration time and slit mode are the same as for the first flyby.

The third flyby sequence will be a repetition of the second one. The difference lies in that the FUV is turned on earlier than during MSB (Mercury Swing-By) 2, slightly before entering the shadow of Mercury.

5.1.4 Selection of the scanner angle

Regarding the selection of the scanner angle, we are facing multiple constraints:

1. The first one is related to the stacked configuration of the spacecraft during the cruise. It implies that some positions of the instrument (from 185° to 290°) are blocked by the MTM (Figure 3.16). I thus excluded the scanner angles from 185° to 290°.

2. The second constraint is related to the geometry of the instrument. Positions between ±10° around the parking bracket (i.e. 0°) can not be used as they are partly obstructed by the parking bracket (Section 3.3). I thus excluded the scanner angles from 350° to 10°.

3. Another constraint lies in the UV detectors. The LOS of PHEBUS can not intercept the lit surface of Mercury as it would damage the detectors. I thus excluded scanner angles where the angle between the LOS and Mercury's center is smaller than the apparent angular radius of Mercury. The difference includes the guard angle of the baffle (i.e. ±8.3°, ±10° with margins, Figure 3.7). The apparent angular radius of Mercury α is defined as follows:

$$\sin(\alpha) = \frac{R_M}{R_M + z} \tag{5.1}$$

   where R_M is Mercury's radius and z is the altitude of the spacecraft above the surface.

Finally, we choose the scanner angle so as to maximize the intensity of the species we want to observe, while respecting the constraints previously mentioned (Figure 5.2a). For each scanner angle tested, I therefore calculated the radiance I_R (units of Rayleigh) of the species (Mg and Ca), defined as follows:

$$I_R = \frac{4\pi}{10^6} I \tag{5.2}$$

With $4\pi I$ the emission brightness. For an optically thin medium (Appendix B), the emission brightness is defined as follows:

$$4\pi I = gN \tag{5.3}$$

Where N is the illuminated column density (cm^{-2}) and g is the excitation rate that equals the number of photons one atom scatters per unit time (s^{-1}).

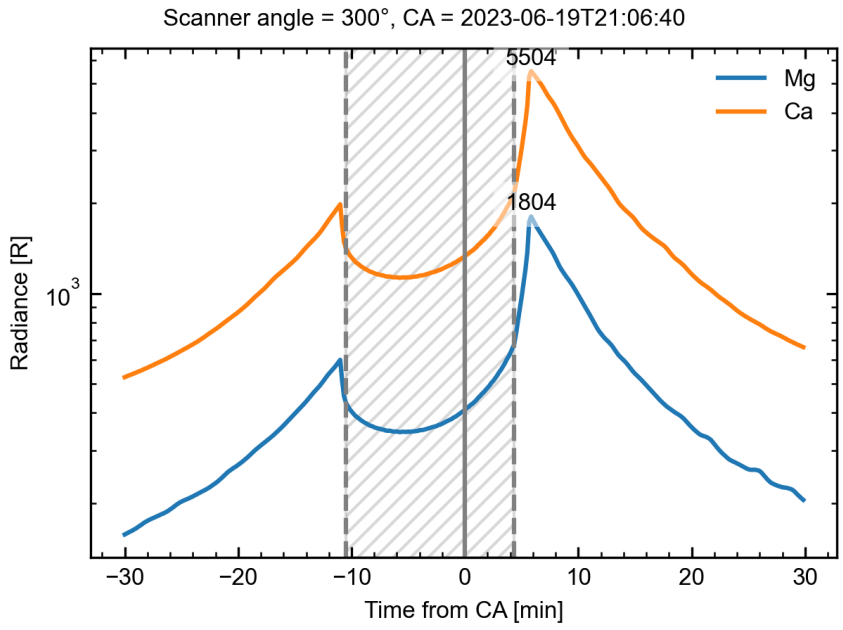

(a)

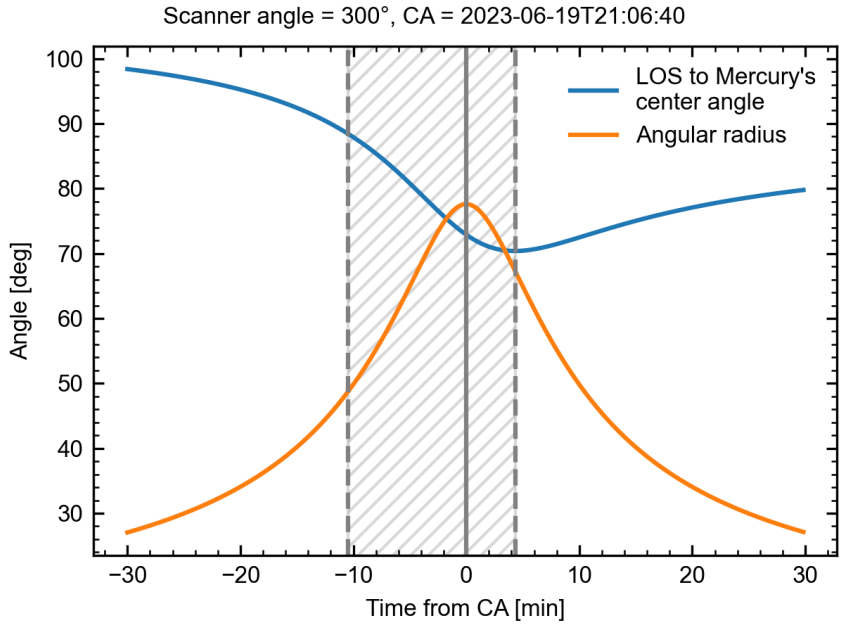

(b)

Figure 5.2: Selected angle for MSB3 based on the intensity (a) and the geometry (b) computations. The gray hatched area corresponds to the transit in the shadow of Mercury. The solid gray line represents the CA.

We have decided to employ a conservative approach and add a safety margin of 10° to the scanner angle responding to all the constraints mentioned above. Regarding the third flyby, the spacecraft is in the northern hemisphere at the beginning of the operation (Figure 5.3). Therefore, we have decided to look southward to integrate over a longer distance. There was no scanner angle to look at the southern hemisphere without the line of sight intercepting the surface of Mercury. So we chose a scanner angle that allows the instrument to look southward and with which the line of sight intercepts only Mercury nightside (during the eclipse)(Figure 5.2b).

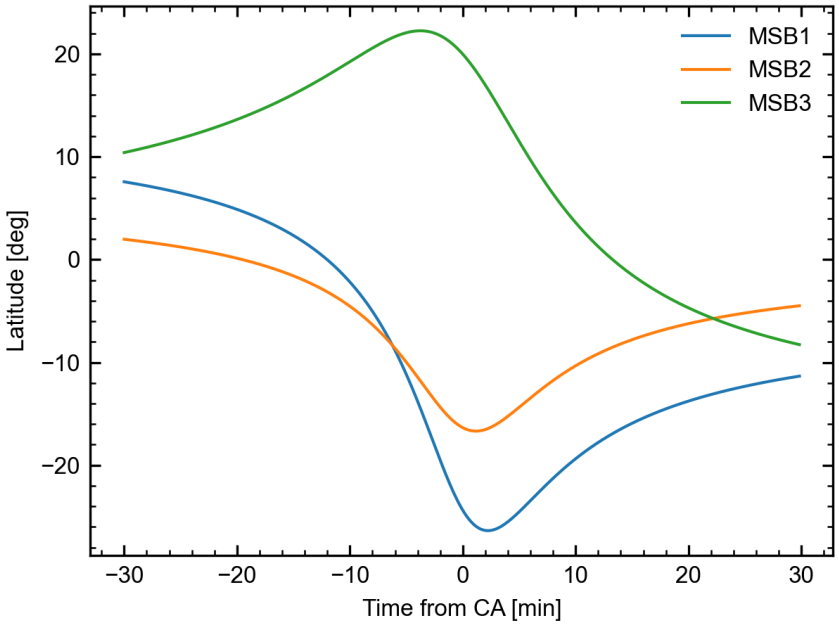

Figure 5.3: Latitude of MPO spacecraft as a function of time during MSB1 (blue curve), MSB2 (orange curve) and MSB3 (green curve). The latitude is expressed in the MSO (Mercury-centric Solar Orbital) reference frame[1].

5.1.4.1 Computation of the g-values

The g-value is defined as the solar photon scattering probability, related to the transition from a ground state to an excited state. The solar flux at Mercury at the rest frequency of the transition varies with Mercury's Doppler shift, owing to Mercury's eccentric orbit. g-values are dependent on the instantaneous heliocentric radial velocity of an atom, which varies as a function of 1) Mercury's heliocentric radial velocity and of 2) the atom's velocity as it is ejected from the surface and subsequently affected by gravity and radiation pressure. We have made the assumption that the atoms are at rest with respect to Mercury (Killen et al., 2009). As mentioned by Burger et al. (2014) and Chaufray et al. (2022), this assumption is not entirely valid for calcium atoms, which are ejected energetically. The g-value obtained under the assumption of no radial motion is underestimated.

The variation in g-value as a function of TAA then results from both changing Doppler shift and changing solar distance (Figure 5.4).

[1]The MSO coordinate system is defined by the +X axis pointing from Mercury towards the Sun, the +Y axis being perpendicular to the +X axis and opposite to the direction of Mercury's orbital velocity and the +Z axis completing the right-handed system, pointing northward. The origin of the frame is the center of mass of Mercury.

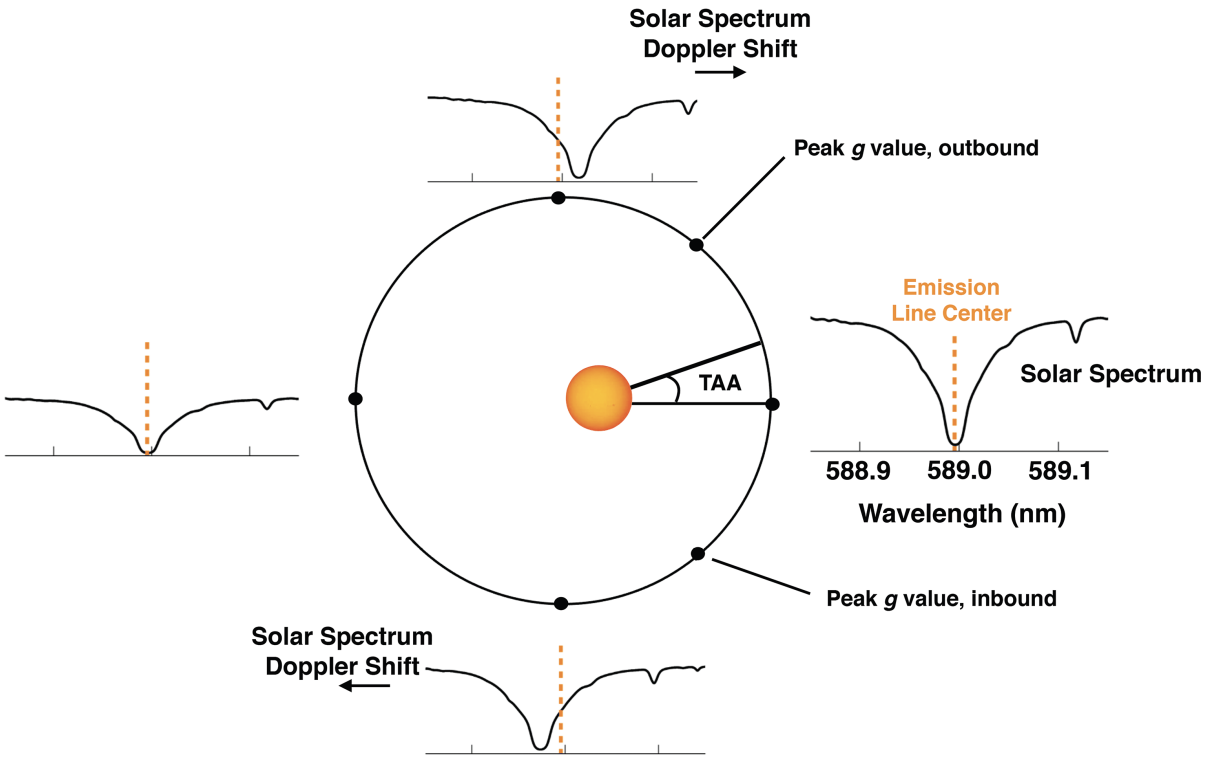

Figure 5.4: Mercury's distance from the Sun plotted as a function of the TAA (central figure). An example of the changes on solar irradiance and Doppler shift effects is shown for the sodium D2 resonance transition. As the planet moves around the Sun, both the solar irradiance and the planet's radial velocity (hence the Doppler shift) are modified. Adapted from Killen et al. (2018).

The g-value can be derived as:

$$g = \frac{F_\lambda}{r^2}\frac{\lambda^2}{c}\left(\frac{\pi e^2}{m_e c}\right) f \tag{5.4}$$

Where F_λ is the solar irradiance at the radiation wavelength λ at 1 AU from the Sun, r is the distance from the Sun, c is the speed of light, e is the elementary charge, m_e is the electron mass, f is the oscillator strength factor and $\frac{\pi e^2}{m_e c}$ is the total cross section of the transition (CGS units). The oscillator strength f is one measure of the strength of a spectral transition: the greater the oscillator strength, the more likely the transition will occur. λ corresponds to the Doppler shifted wavelength, i.e.:

$$\lambda = \frac{\lambda_0}{(1 + \frac{\bar{v}}{c})} \tag{5.5}$$

Where λ_0 is the wavelength of the transition and $\bar{v}$ is the radial velocity component. I computed the radial velocity $\bar{v}$ as:

$$\bar{v} = \frac{dr}{dt} = \frac{\partial r}{\partial \theta}\frac{\partial \theta}{\partial t} \tag{5.6}$$

Where r is defined as follows:

$$r = \frac{a\,(1 - e^2)}{1 + e\cos\theta} \tag{5.7}$$

With semimajor axis of Mercury's orbit, e the eccentricity of Mercury's orbit and θ the TAA.

The radial velocity is thus expressed as follows:

$$\bar{v} = e\sin\theta\sqrt{\frac{GM_S}{a\,(1 - e^2)}} \tag{5.8}$$

Where G is the gravitational constant and M_S is the mass of the Sun. Mercury's radial velocity varies between -10 and +10 km.s^{-1} (Figure 5.5).

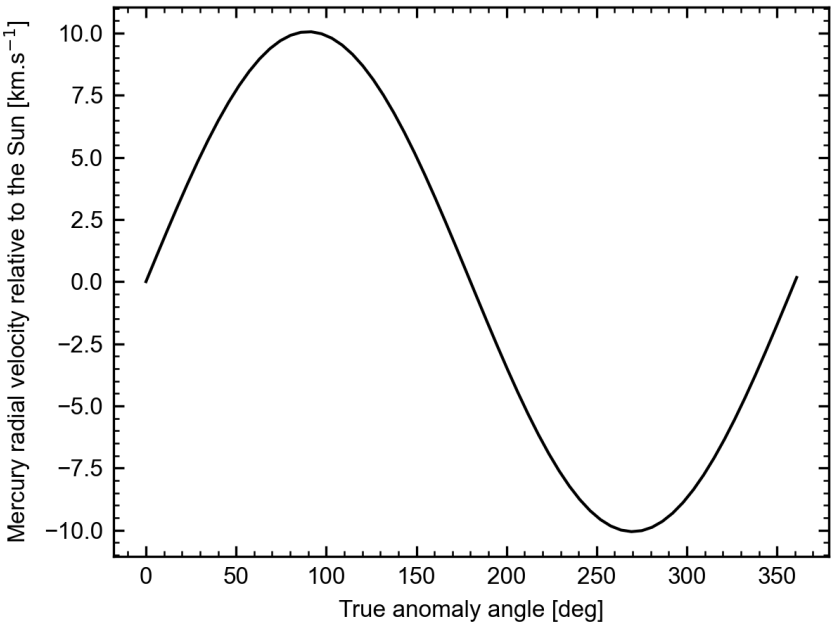

Figure 5.5: Mercury's radial velocity with respect to the Sun as a function of Mercury's TAA.

For each flyby, I computed the g-value associated with the emission line of Ca at 422.8 nm. During the first flyby, Mg could not be observed due to the choice of the UV detector. Therefore, I computed the g-value associated with the emission line of Mg at 285.3 nm only for the second and third flybys. For the computations of the g-values, I used the high-resolution solar spectrum TSIS-1 Hybrid Solar Reference Spectrum (Coddington et al., 2023) and retrieved the values of the oscillator strength from the NIST database (Kramida et al., 2022). Finally, I computed the geometry of each flyby (Table 5.2). The g-values given in Table 5.3 were calculated for the Mercury heliocentric distance and TAA of each flyby.

Table 5.2: Parameters of the flybys. "Time CA" corresponds to the time of the closest approach, TAA θ, Sun-target-observer angle γ and local time are given at CA of each flyby. For flybys n°4, 5 and 6, the values given are provisional and may vary due to operational constraints and/or activities.

Flyby n°	Time CA [UTC]	Distance [km]	θ [°]	$\bar{v}$ [km.s^{-1}]	r [AU]	γ [°]	Local time
1	2021-10-01T23:34:42	200	262.6	-9.97	0.381	136.0	02:31:28
2	2022-06-23T09:44:22	200	264.8	-10.02	0.378	122.2	03:45:13
3	2023-06-19T19:34:25	235	311.5	-7.54	0.326	147.1	01:47:45
4	2024-09-05T06:12:20	200	332.6	-4.63	0.313	90.0	05:59:56
5	2024-12-01T23:41:36	40,000	331.1	-4.85	0.314	4.4	12:10:35
6	2025-01-09T00:44:50	385	150.3	4.99	0.451	134.8	23:34:36

Table 5.3: g-values for the Ca and Mg emission lines computed for the first three flybys of Mercury along with the oscillator strength and atomic mass assumed for the calculations. The g-values are given for Mercury heliocentric distance and TAA corresponding to each flyby.

Species	Wavelength in vacuum λ_0 [nm]	Oscillator strength f	Atomic mass m [u]	g-value at MSB1 [s^{-1}]	g-value at MSB2 [s^{-1}]	g-value at MSB3 [s^{-1}]
Mg	285.296	1.80	24.3050	-	0.321	0.414
Ca	422.792	1.75	40.078	17.54	17.86	19.50

5.1.4.2 Computation of the column density

To compute the illuminated column density, I consider the geometry of flybys. For each acquisition, I retrieve the position of MPO and deduce the coordinates of the LOS of PHEBUS. For each LOS, I calculate the column density N, i.e. the density n integrated along the LOS:

$$N = \int n \, \mathrm{d}z$$

For this, I calculate the density at each point of the LOS. I chose a variable step $\mathrm{d}z$ to speed up the calculations. The calculation stops when the LOS intercepts the surface of Mercury or exceeds the region of interest (a sphere of radius 10 R_M centered at Mercury). The densities of Ca and Mg come from a 3D profile derived from Monte Carlo simulations (Chaufray et al., 2022). The density is a function of spherical coordinates, expressed in the MSO reference frame.

Considering the geometry of observations, the LOS can be partially in the shadow of Mercury. The excitation factor is then null, since there is no sunlight. Figure 5.6 displays the predicted illuminated column density of Ca and Mg considering the geometry of MSB3 and the column density of Ca and Mg when the effect of Mercury shade is not taken into account. In the latter case, we note that the distribution is symmetrical (in relation to the density profiles of the species).

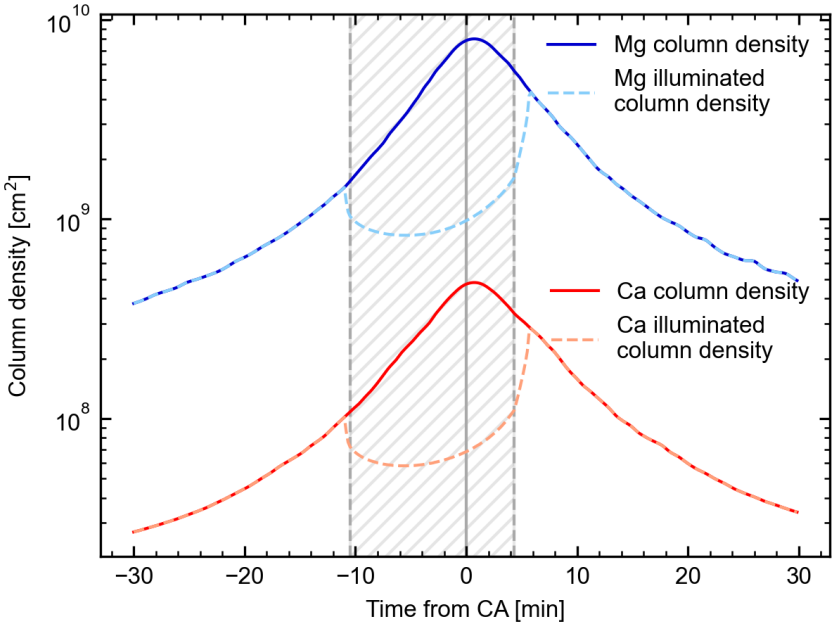

Figure 5.6: Predicted column density of Mg and Ca as a function of the time relative to the CA during MSB3. The colored dashed lines represent the illuminated column density, while the colored solid lines represent the column density. The gray hatched area corresponds to the transit in the shadow of Mercury. The solid gray line represents the CA.

5.2 Geometry of observation and preliminary results

In this section and the following one, I will describe the results of the first and the second flybys only. At the time of writing, the third flyby took place but the data have not yet been processed.

5.2.1 Mercury Swing-By #1 (MSB1)

The first flyby of Mercury by BepiColombo occurred on October 1, 2021. The spacecraft arrived on the planet's nightside, crossed its shadow and then moved to its dayside (Figure 5.7). The closest approach to the surface took place at 23:34 UTC at an altitude of ∼200 km, a few minutes before the spacecraft crossed the terminator. Figure 5.7 represents the geometry of the first flyby of Mercury in BepiColombo MSO frame.

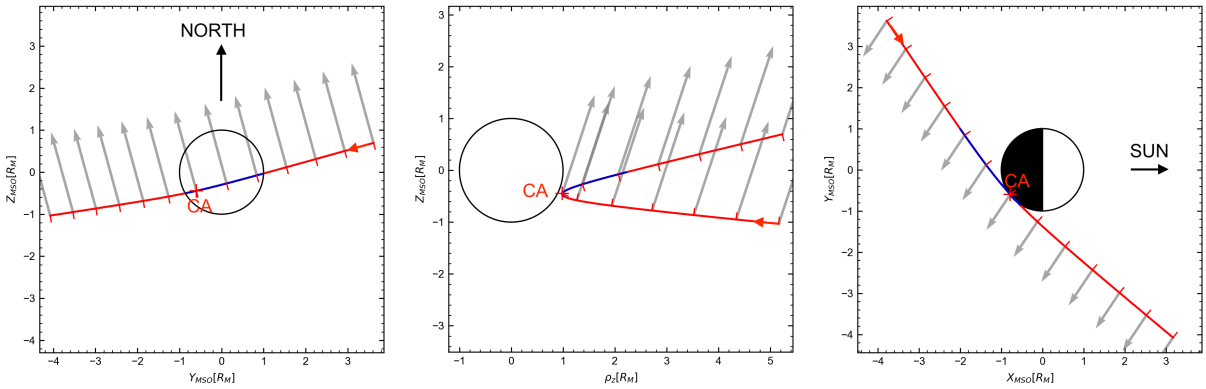

(a) **(b)** **(c)**

Figure 5.7: Geometry of the first flyby of Mercury. The black circle represents the planet, the gray arrows represent PHEBUS boresight, the red line represents the trajectory of BepiColombo and the blue line represents the transit in the shadow of Mercury.

The c422 count rate profile (Figure 5.8a) clearly indicates the geometry of the flyby, notably the transit in the shadow of Mercury. The maximum is reached shortly after the spacecraft went out of eclipse. It does not occur immediately out of eclipse as a part of the LOS is still in the planet's shadow as it was expected from our estimates. Then, as the spacecraft moves away from Mercury, the count rate decreases. Unfortunately, the signal is polluted by many spikes, some of them even spreading over several acquisitions. The origin of these spikes is discussed in Section 5.2.4. In spite of these peaks, the c422 profile strongly points to the detection of the emission line of calcium at 422.8 nm and shows an enhancement on the dawn side. The c422 signal extends far from the planet, which means that the Ca exosphere is very widespread on the morning side. As for c404, the signal is less intense and more confined. The signal being very polluted by the peaks, it is difficult to know if it reflects the detection of species. We can however notice the geometry of the flyby and the exit of the eclipse of Mercury in particular.

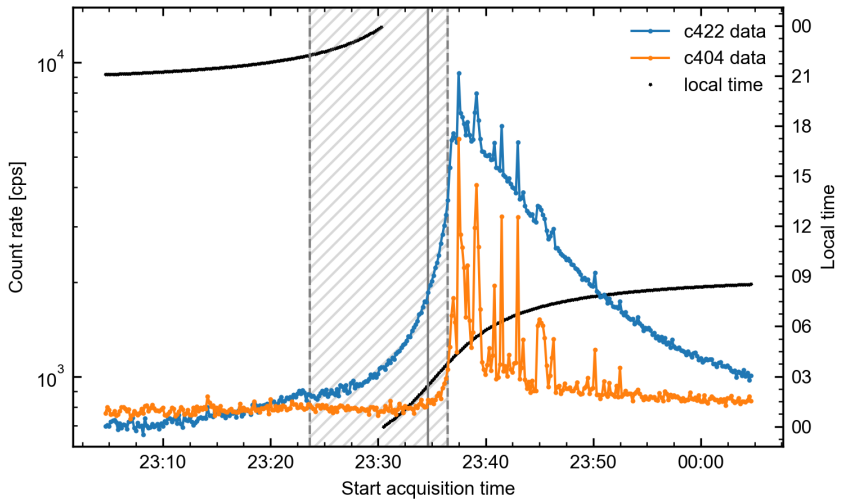

(a)

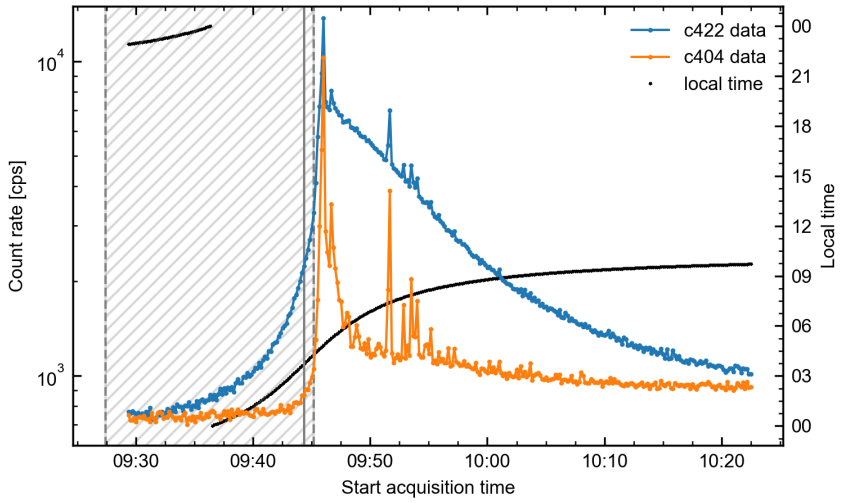

(b)

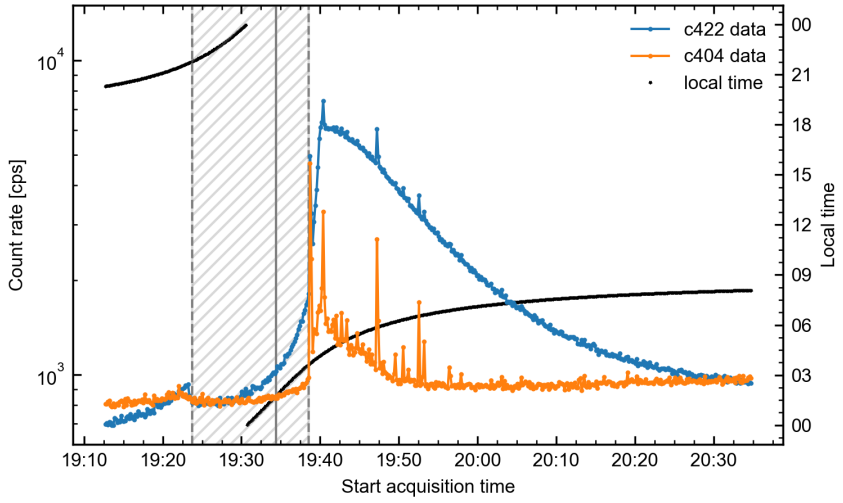

(c)

Figure 5.8: Visible channels count rate as a function of the time during MSB1 (a), MSB2 (b) and MSB3 (c). The blue curve represents the c422 data while the orange curve represents the c404 data. The black dots represent the local time. The gray hatched area corresponds to the transit in the shadow of Mercury. The solid gray line represents the closest approach.

5.2.2 Mercury Swing-By #2 (MSB2)

The second flyby occurred on June 23, 2022. The geometry of observation was similar to the first flyby: the spacecraft approached the planet from its nightside, crossed its shadow and then moved to its dayside (Figure 5.9). The closest approach occurred in Mercury's shadow at 09:44 UTC, about 200 km above the surface. PHEBUS was pointing northward, slightly antisunward. Unfortunately, PHEBUS observation was interrupted about 20 min earlier than planned, as the instrument was commanded to Safe configuration from an on board Fault Detection, Isolation and Recovery (FDIR). The FUV detector has indeed reached the limit value of count rate, set at 32,768 counts per second. This prompted us to increase the threshold for the third flyby.

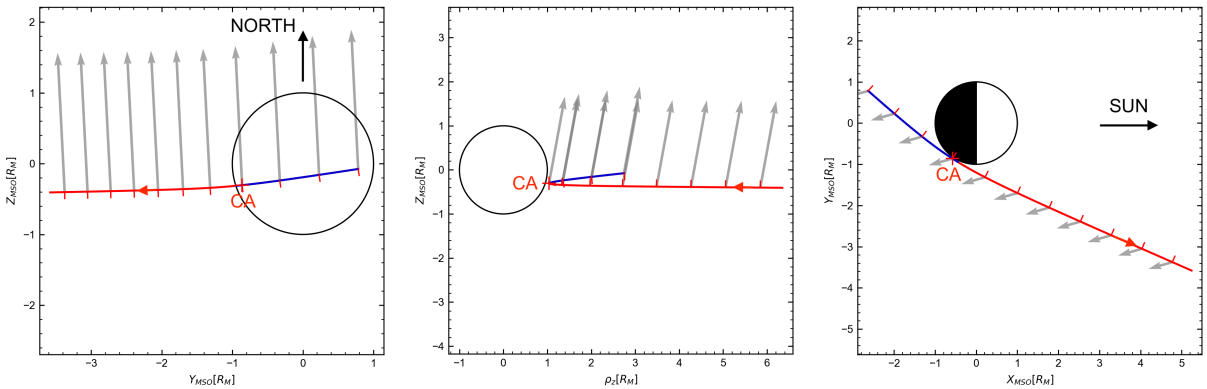

Figure 5.9: Geometry of the second flyby of Mercury. The black circle represents the planet, the gray arrows represent PHEBUS boresight, the red line represents the trajectory of BepiColombo and the blue line represents the transit in the shadow of Mercury.

As with the first flyby, the count rate profiles of the visible channels indicate the observation geometry of the flyby; the transit in the shadow of Mercury and the maximum of the emission on the morning side after the CA (Figure 5.8b). Calcium was again detected with the c422 channel, confirming the extent of the Ca exosphere on the morning side, up to ∼13,000 km. Again, we note multiple spikes on top of the general emission profile once out of the planet's shadow. Their occurrence is nevertheless less frequent than during MSB1 which allows to notice that the c404 and c422 signals are different. The c404 data clearly reflect the detection of additional species at low altitudes on the morning side, which was not obvious during the first flyby.

5.2.3 Mercury Swing-By #3 (MSB3)

The third flyby occurred on June 19, 2023. The geometry of observation was similar to the first two flybys: the spacecraft approached the planet from its nightside, crossed its shadow and then moved to its dayside (Figure 5.10). The closest approach occurred in Mercury's shadow at 19:34 UTC, about 235 km above the surface. PHEBUS was pointing southward, slightly antisunward.

Again, the count rate profiles (Figure 5.8c) clearly depict the geometry of observation, especially the transit in Mercury's shadow. The maximum is reached shortly after the exit of eclipse. The c422 channel again detected calcium, showing an enhancement near the dawn region and revealing a very widespread Ca corona on the morning side. The c404 channel detected species at low altitudes on the morning side. Again, we note that both signals are polluted by sporadic spikes when the spacecraft is out of the planet's shadow on the morning side.

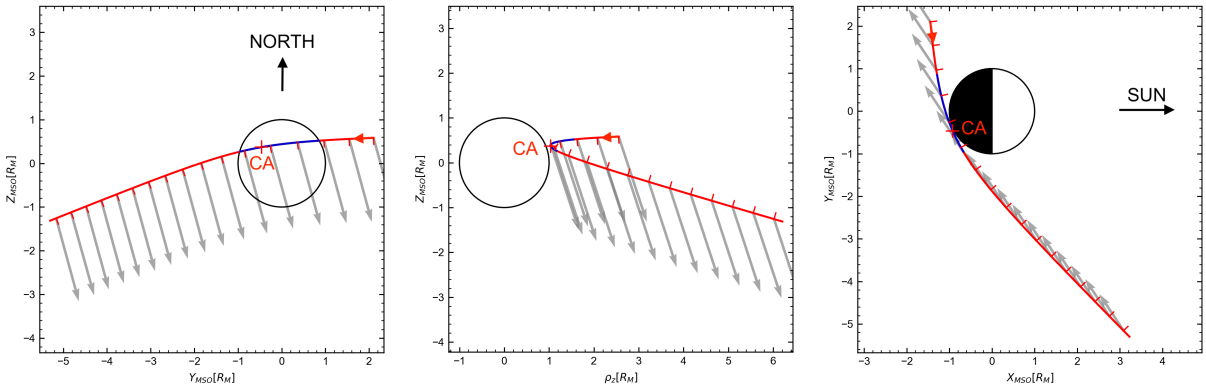

(a) (b) (c)

Figure 5.10: Geometry of the third flyby of Mercury. The black circle represents the planet, the gray arrows represent PHEBUS boresight, the red line represents the trajectory of BepiColombo and the blue line represents the transit in the shadow of Mercury.

5.2.4 Unexpected spikes

The spikes occur during the same acquisitions on both detectors, with the same magnitude. Some spikes are even spread over several acquisitions, especially during the first flyby. We suspect the spikes are due to either particles crossing the instrument or light. If light is the source of these spikes, it can occur in several ways:

- Light reflected on parts of the spacecraft stack (e.g. solar panels, antenna, MTM, magnetometer boom or Mio's Sunshield). However, the attitude of the satellite remained inertial during the flybys. This contribution of reflected light would therefore appear as a quasi-continuous signal and not as a sporadic one.

- Light from magnetospheric structures (magnetopause and bow shock), where ions accumulate. But this (these) ion(s) must have emission lines in the bandwidth of the two detectors. To determine if some spikes were related to these crossings, I compared the peak occurrence with the times of passage through these structures. They were deduced from the electron data of the MEA (Mercury Electron Analyzer) instrument on board Mio (S. Aizawa/L. Hadid/Mio team, personal communication). As it can be seen on Figure 5.11, the correlation is not obvious.

- Light reflected on particles released during outgassing of the spacecraft. As the spacecraft gets closer to the planet, the temperature increases, causing outgassing. If not from outgassing, the particles could also come from degradation of the thermal protection of the spacecraft, made of Nextel. This protection is found on the different sides of BepiColombo except on the radiator side (where PHEBUS is located), but PHEBUS has this type of protection on the baffle. During thermal tests on the ground, a cloud of dust coming from the thermal protection was released. However, we do not see any particle on the Monitoring Camera (M-CAM).

Apart from light, the other hypothesis is that particles pass through the detectors. These particles can come from the passage through magnetospheric structures. The problem with this hypothesis lies in the fact that the detectors are about 20 cm away from each other. It seems unlikely that a particle would pass through both detectors and this repeatedly. Moreover, this hypothesis is not valid for spikes that extend over several acquisitions.

The spikes occurring at the same time on both detectors and their intensity that is exactly proportional from one channel to the other seem to indicate that the phenomenon originates rather from light rather than from particles. The most probable hypothesis thus seems to be

that of outgassing. This could also explain why the frequency of the peaks is less important during the second and third flybys (as time goes by, there should be less outgassing occurring). The next flybys will hopefully allow to conclude on this hypothesis.

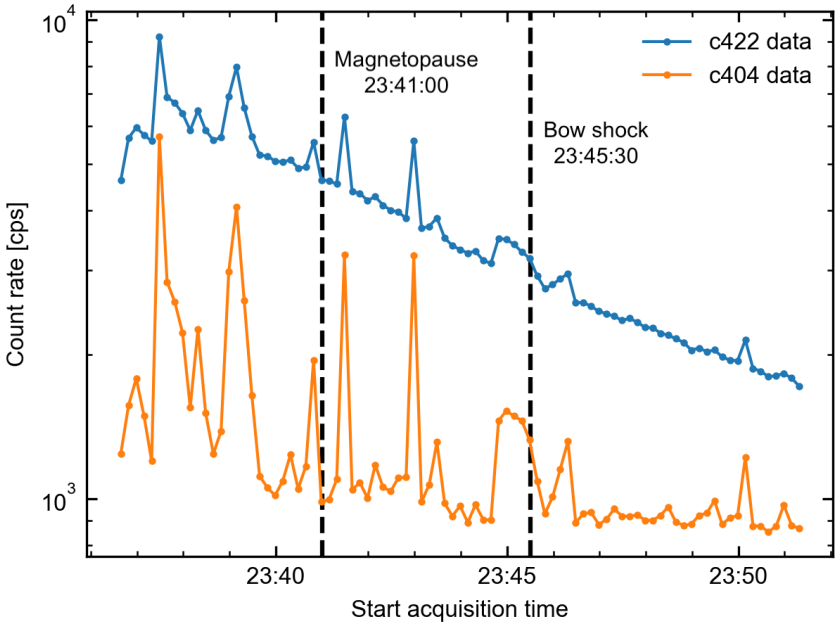

(a)

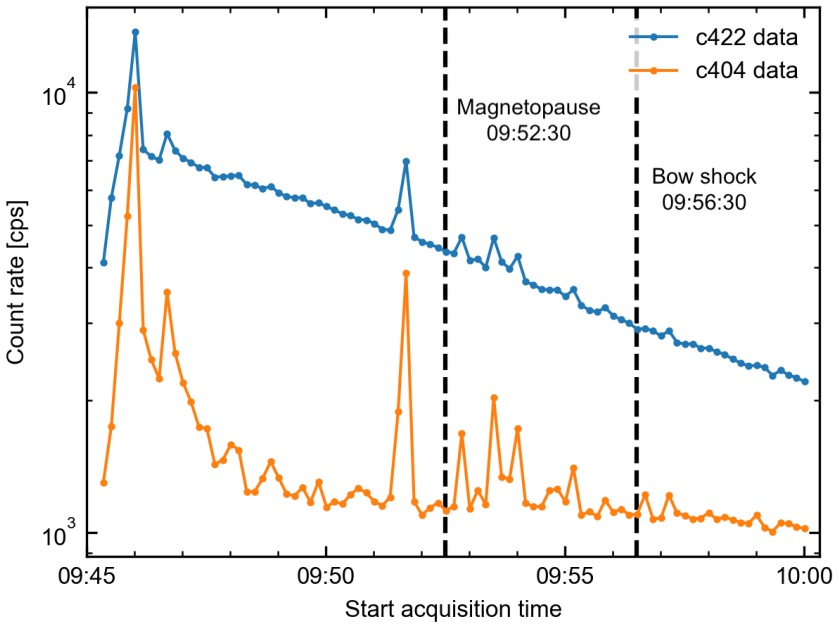

(b)

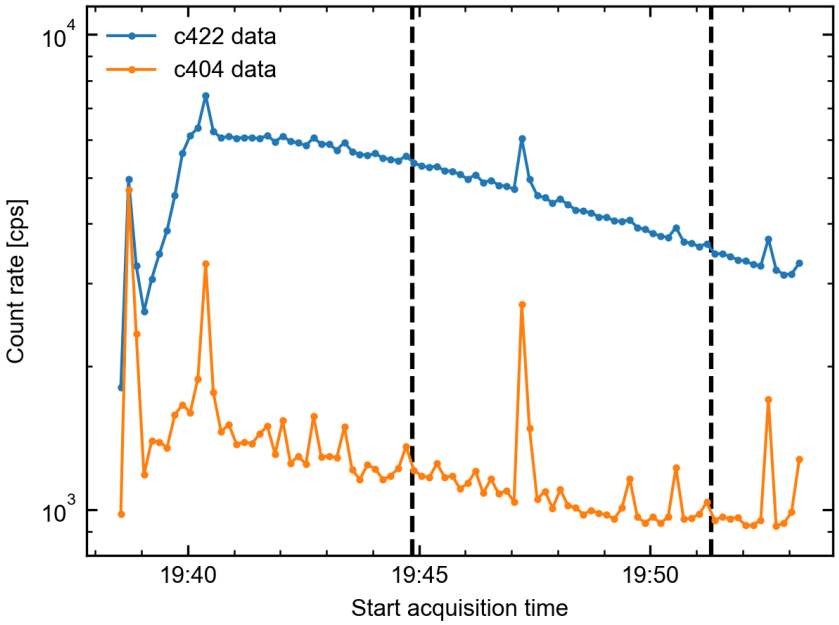

(c)

Figure 5.11: Close up on the count rate profile of the visible channels after the exit of Mercury's shadow during the first flyby (a), the second flyby (b) and third flyby (c) of Mercury. The blue (resp. orange) curve represents the c422 (resp. c404) count rate. The black dashed vertical lines indicate the magnetopause and bow shock crossing times. They were derived from MEA data.

5.3 Processing flybys data

In this section and in the following chapters, I will discuss the data of the first two flybys only.

To compare our data with those of MESSENGER and from ground-based observations of Mercury's exosphere, I need to convert the corrected count rate CR (Eq. 5.9) in radiance I_R (Eq. 5.2).

The radiance is expressed in Rayleigh (R), where 1 R is 10^6 photons emitted into 4π steradians in 1 second. When the source is large (as it is the case for Mercury's exosphere), the relation between the count rate CR (s^{-1}) and the measured emission brightness I ($ph.s^{-1}.cm^{-2}.sr^{-1}$) is given by:

$$CR = I\, A_{eff}\, \Omega \tag{5.9}$$

Where A_{eff} is the effective area (cm^2) and Ω is the instrument solid angle (sr). I have derived the effective area of both detectors in Section 4.2. When the slit is removed, the solid angle of the instrument is equal to 4.157 deg^2 (1 $deg^2 = (\pi/180)^2$ sr). The value of Ω is based on results from ground calibration. As for the count rate, I need to correct it for the background and the spikes. As mentioned in Section 4.2.4.2, the background of the signal consists of the dark current, the zodiacal light and the stellar contributions. Based on multiple observations made at the parking position during the cruise, I have estimated the contribution of the dark current at about 230 counts per second. During both flybys, PHEBUS was pointing towards the ecliptic North. The contribution of the zodiacal light is therefore estimated at ∼50 counts per second (Section 4.2.4.2.1). As there were no bright stars in PHEBUS FOV during both flybys (Figure 5.12), I considered the stellar contribution as null, or at least constant. I get a background estimate of ∼280 counts per second.

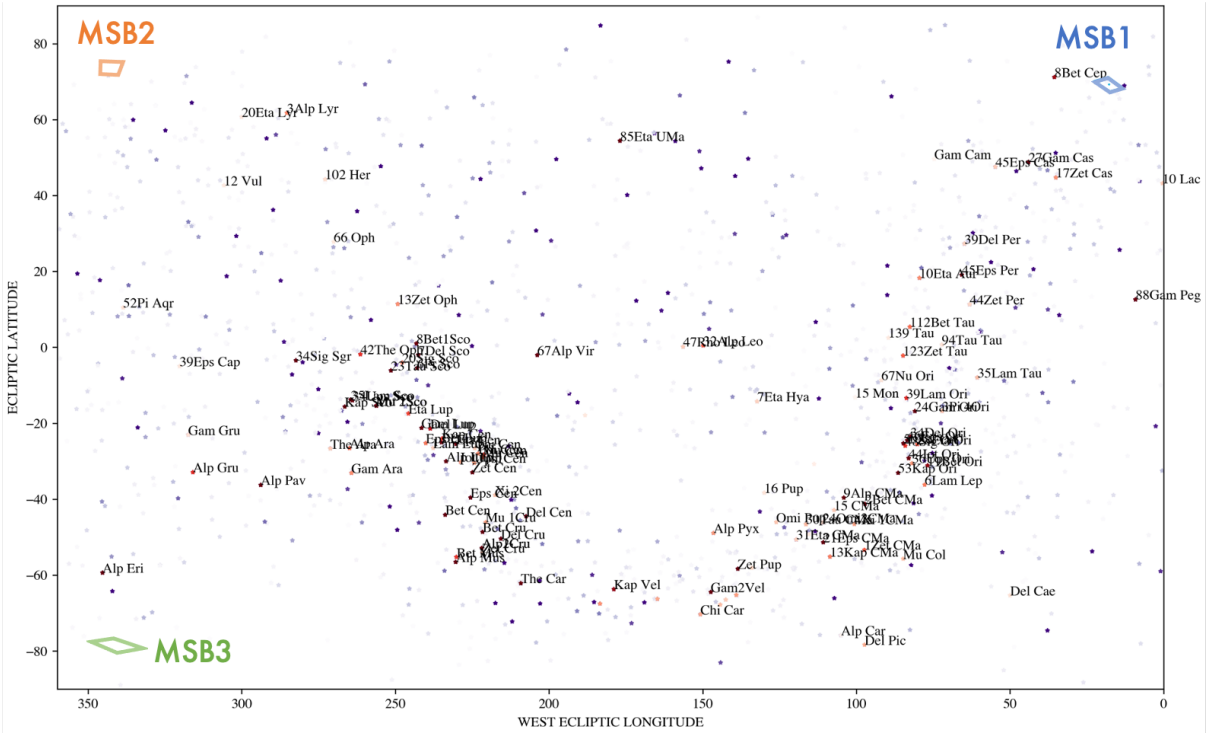

Figure 5.12: Projection of PHEBUS FoV on the sky for the three flybys of Mercury by BepiColombo.

During both flybys, the observation starts far from the planet (∼11,000 km for MSB1, ∼21,000 km for MSB2). At this distance, the exosphere is not yet observed, so the signal of both detectors should be close to the estimated background level i.e. ∼280 counts per second. However, the count rate of both detectors at the beginning of each flyby is well above this background value (Figure 5.13). This difference could potentially be due to particles, possibly related to electrons in the magnetosphere of Mercury. However, such assumption requires more investigation and in particular a comparison of the behavior of the detector in cruise and orbit.

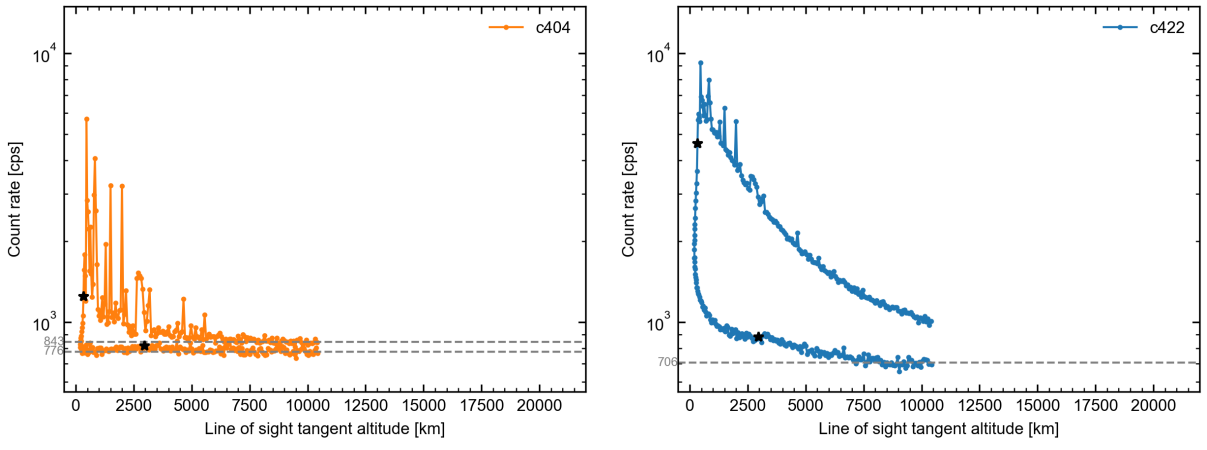

(a) **(b)**

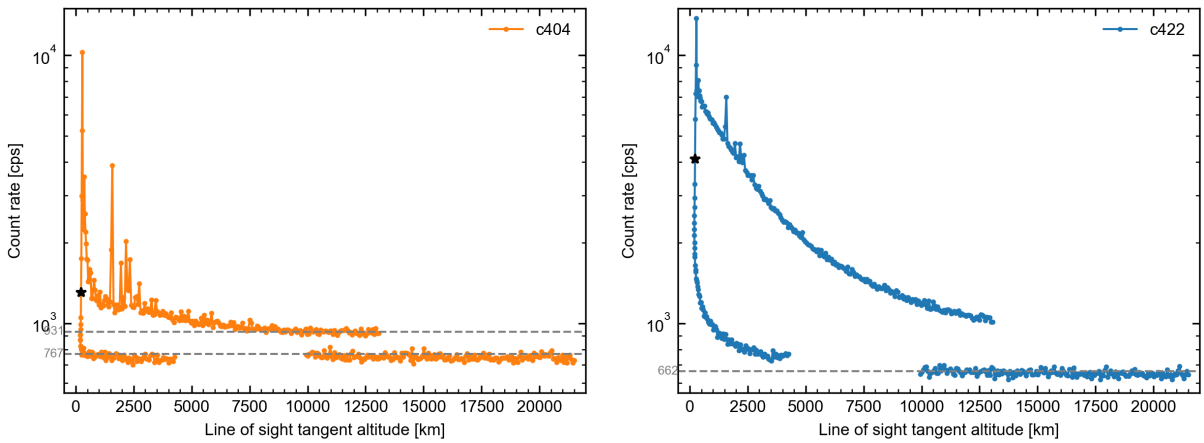

(c) **(d)**

Figure 5.13: c404 count rate as a function of the tangent altitude during MSB1 (a) and MSB2 (c). c422 count rate as a function of the tangent altitude during MSB1 (b) and MSB2 (d). The black stars depict the entry in Mercury's shadow and the exit. As we did not observe during the entry in Mercury's shadow for MSB2, only the exit is represented.

The mean value of the signal at the beginning of the flyby is different depending on the channel. Also, for the c404 channel, this value is different from the mean value at the end of the flyby. We suspect that this difference between the beginning and the end of the flyby is related to the lit surface of Mercury that reflects on certain parts of the BepiColombo stack spacecraft. Once the spacecraft is out of eclipse, the lit surface of Mercury can reflect on the spacecraft, providing an additional signal to the channels. This difference is not visible on the c422 signal as the channel still detects calcium at the end of the observation.

During both flybys, the pointing was inertial, so the stellar and zodiacal light contributions are constant. However, we saw that the background is much higher than the estimated value (based on observations made in cruise in the parking position) and that it is not constant (difference between the beginning and the end of the overflight on channel c404). Therefore, we can not simply remove a constant, we need to derive a background correction model specific to Mercury flybys. To do so, I use the data from the c404 channel. Let C_{404} be the number of counts registered by the c404 channel and C_{422} the number of counts registered the c422 channel. They can be expressed as follows:

$$C_{422} = N_{422} + B_{422} \tag{5.10}$$

$$C_{404} = N_{404} + B_{404} + CT \times N_{422} \tag{5.11}$$

Where N_{422} is the number of counts attributed to calcium, B_{422} the number of counts attributed to the background of the c422 channel, N_{404} the number of counts attributed to the species detected by the c404 channel, B_{404} the number of counts attributed to the background of the c404 channel and CT the coefficient of Ca cross-talk (Section 3.3.1).

We notice a constant difference between the signals of the two detectors at the beginning of the flyby. No species are detected on this part of the flyby so it is only the difference between the background of the two channels. Let's call this difference ΔB, thus:

$$\Delta B = B_{404} - B_{422} \tag{5.12}$$

I assume that this difference remains the same throughout the flyby. Replacing B_{422} in Eq. (5.10) by its expression derived from Eq. (5.12), we have:

$$C_{422} = N_{422} + (B_{404} - \Delta B) \tag{5.13}$$

To model the transition from the mean value at the beginning of the flyby to the mean value at the end of the flyby, I decided to use a sine function (Figure 5.14).

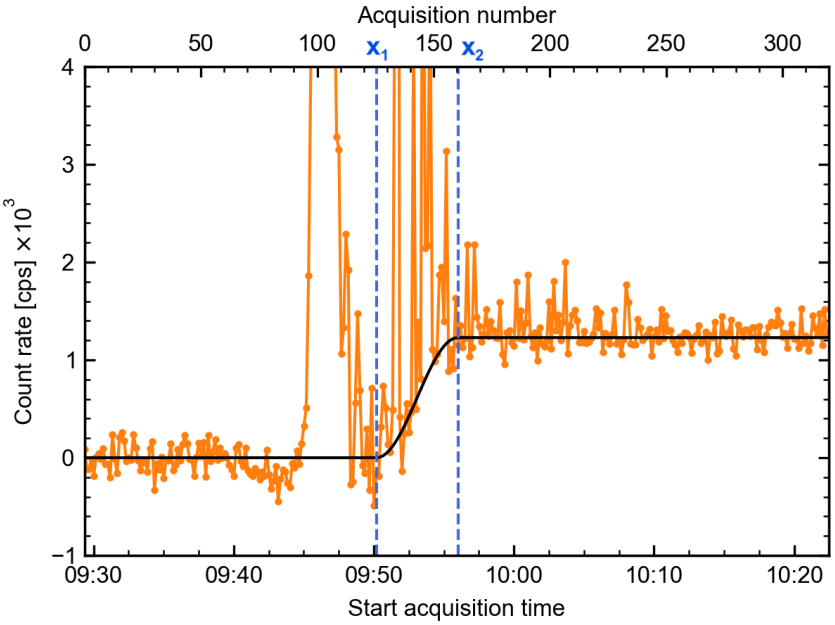

Figure 5.14: Background correction of the c404 signal during MSB2. In orange, the number of counts registered by the c404 channel to which I subtracted the mean value of the beginning of the flyover and the contribution of calcium cross-talk. In black, the background function.

Therefore, the background is modelled as follows:

$$B(x) = \begin{cases} b_1 & x < x_1 \\ b_1 + (b_2 - b_1) \times \sin^2\left(\frac{\pi}{2}\frac{(x-x_1)}{(x_2-x_1)}\right) & x_1 \leq x < x_2 \\ b_2 & x \geq x_2 \end{cases} \tag{5.14}$$

Where b_1 represents the number of counts to be removed from the start to index x_1, b_2 represents the number of counts to be removed from index x_2 to the end. b_1 corresponds to the mean value of the number of counts registered by the c404 channel at the beginning of the flyby. The values for both flybys are given in Table 5.4.

Table 5.4: Parameters of the background correction for both flybys. CT is the coefficient of the Ca cross-talk, b_1 is the number of counts to remove at the beginning of the flyby (before index x_1), b_2 is the number of counts to remove at the end of the flyby (after x_2) and ΔB is the average value of the difference between the number of counts registered by the c404 channel and those registered by the c422 channel over the first 30 points for MSB1, 75 first points for MSB2. b_1 is the average value of the number of counts registered by the c404 channel over the first 30 data points for MSB1, 75 first data points for MSB2.

Flyby n°	CT	b_1	b_2	x_1	x_2	ΔB
1	0.058	6233	6615	210	280	612
2	0.099	5960	7188	125	160	787

At the end of the flyby, from a certain altitude h (∼5,000 km), the c404 channel no longer detects any species. Its signal is then simply the sum of two components:

$$C_{404} = B_{404} + CT \times N_{422} \tag{5.15}$$

Combining Eq. (5.13) and (5.15), we have:

$$\begin{aligned} C_{404} &= B_{404} + CT \times (C_{422} + \Delta B - B_{404}) \\ &= CT \times C_{422} + (1 - CT) \times B_{404} + CT \times \Delta B \\ &= \alpha \times C_{422} + \beta \end{aligned} \tag{5.16}$$

To derive α and β (Figure 5.15), I perform a linear regression on the data for which the altitude h is higher than 5,000 km after the closest approach. I then deduce b_2:

$$b_2 = \frac{\beta - \alpha \times \Delta B}{1 - \alpha} \tag{5.17}$$

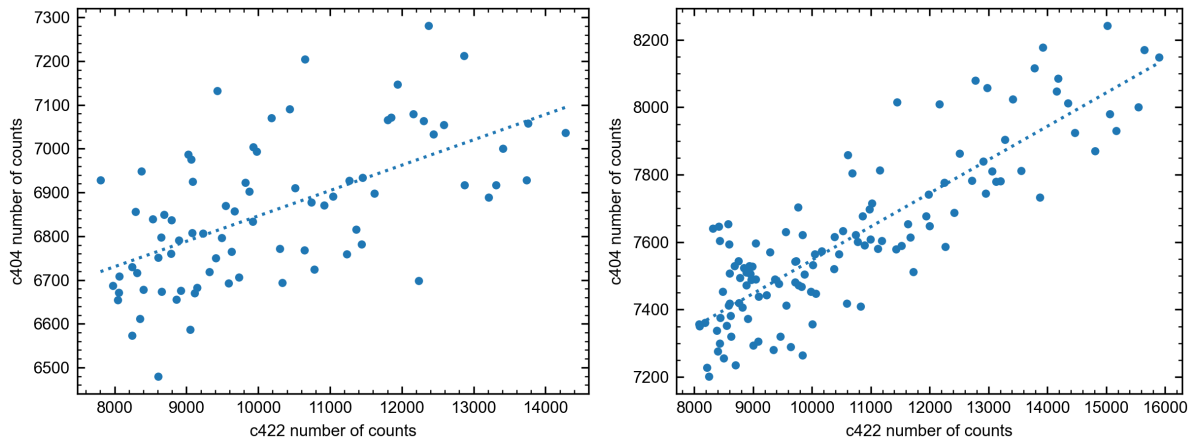

(a) **(b)**

Figure 5.15: Number of counts registered by the c404 channel as a function of the number of counts registered by the c422 channel after the CA of MSB1 (a) and MSB2 (b) with an altitude above 5,000 km. The dotted line represents the linear regression.

I thus obtain the "useful" information i.e. the signal related to the detected species:

$$\begin{aligned} C_{422_{corr}} &= N_{422} = C_{422} - (B - \Delta B) \\ C_{404_{corr}} &= N_{404} = C_{404} - B - CT \times N_{422} \end{aligned} \tag{5.18}$$

Once the data are corrected and the peaks removed, I calculate the uncertainty related to each measurement. Considering the propagation of errors (Eq. 4.5), we have:

$$\sigma^2_{I_R} = \left(\frac{4\pi}{10^6 \; A_{eff} \; \Omega} \right)^2 \sigma^2_{CR} + \left(\frac{-4\pi \; CR}{10^6 \; A^2_{eff} \; \Omega} \right)^2 \sigma^2_{A_{eff}} \tag{5.19}$$

The effective area A_{eff} and its associated uncertainty $\sigma_{A_{eff}}$ are given in Eq. (4.14) for both channels. Considering Eq. (4.8), (4.9), (4.10), (4.11) and (4.12), we get:

$$\sigma^2_{CR} = \frac{1}{\Delta t} \, CR + \frac{2}{\Delta t^2} \, \sigma^2_D \tag{5.20}$$

With:

$$\begin{aligned} CR_{404} &= \frac{C_{404_{corr}}}{\Delta t} \\ CR_{422} &= \frac{C_{422_{corr}}}{\Delta t} \end{aligned} \tag{5.21}$$

I compute the uncertainty σ_D associated with the dark current for both channels the same way I did in Section 4.2.4.3, i.e. considering all the observations conducted at the parking position with the slit removed and an exposure time of 8 s. This way, I get:

$$\begin{aligned} D_{404} &= 1566.3 \pm 162.8 \,\text{counts} \\ D_{422} &= 1574.9 \pm 159.8 \,\text{counts} \end{aligned} \tag{5.22}$$

The corrected count rate (Eq. 5.21) are then converted to radiance using Eq. (5.9). The derived radiance and associated error are used in Chapters 6 and 7.

Chapter 6

Calcium in the exosphere of Mercury

Calcium has been observed in Mercury's exosphere first from ground-based telescopes and later with MESSENGER. During the first two BepiColombo flybys of Mercury, PHEBUS also observed Ca with its visible channel c422. This chapter traces exospheric Ca studies from ground- and space-based observations and models. These studies focus on Ca distribution and its variations and seek to determine the potential source processes. Then, I analyze PHEBUS c422 channel data and compare it to MESSENGER results.

6.1 Ground-based observations

Calcium was first detected in Mercury's exosphere from observations made at the Keck Observatory (Bida et al., 2000) through its emission line at 422.8 nm. Bida et al. (2000) revealed a tenuous atmosphere of Ca that varies both temporally and spatially. The observed line widths were consistent with a temperature of ∼12,000 K. Bida et al. (2000) proposed three possible sources for the hot Ca: photon-stimulated desorption, micrometeoroid impact vaporization and ion sputtering, favouring the last more in line with the derived high temperature.

Killen et al. (2005) reported four years of observations of the Ca exosphere of Mercury acquired at the Keck Observatory. From the observed line width, they derived temperature between 12,000 and 20,000 K. Such a high temperature suggests that the neutral calcium derives from an energetic process. Killen et al. (2005) was the first to propose a two-step process to explain the energetic Ca: calcium is ejected by impact vaporization in molecular form, and subsequently photo-dissociated, producing high energy Ca atoms. Molecular compounds most likely involved are CaO, CaOH, $Ca(OH)_2$ (Killen et al., 2005; Berezhnoy and Klumov, 2008). Killen et al. (2005) also showed that ion sputtering is a likely source of exospheric calcium.

6.2 Space-based observations: MESSENGER/MASCS

MESSENGER/MASCS also observed this emission line during its three Mercury flybys (McClintock et al., 2008, 2009; Vervack et al., 2010). The tail observations over the nightside of the planet during the second and third flybys showed that the Ca emission peaks near the equatorial region, and declines towards higher latitudes. Ca is observed up to 4-5 R_M in the tail region. The Ca tail is more due to the lack of photoionization (increasing the lifetime of the exospheric Ca atoms) than to the radiation pressure. Knowing that the Ca photoionization lifetime is short[1] and that the effect of radiation pressure on Ca atoms is small, the Ca atoms must be released by a very energetic process (ion sputtering or meteoroid impact vaporization) to be able to travel to that extent before being ionized. The analysis of Mercury tail data during the

[1] Ca ionization lifetime varies from 23 min near perihelion to 52 min near aphelion (Burger et al., 2014).

second and the third flybys did not reveal a north/south asymmetry of the Ca emission (Burger et al., 2012).

Fantail[2] observations made during MESSENGER's flybys of Mercury revealed a large dawn /dusk asymmetry with a peak of Ca radiance at dawn. The intensity and location of the Ca dawnside peak were similar during all three flybys (Figure 6.1a) but the magnetospheric conditions were different, which tends to contradict ion sputtering as the process releasing Ca atoms. Vervack et al. (2010) additionally stated that the dawn/dusk asymmetry argues against meteoroid impact vaporization as the source of calcium "unless a systematic, and perhaps large, dawn-dusk asymmetry is shown to exist in the meteoroid flux".

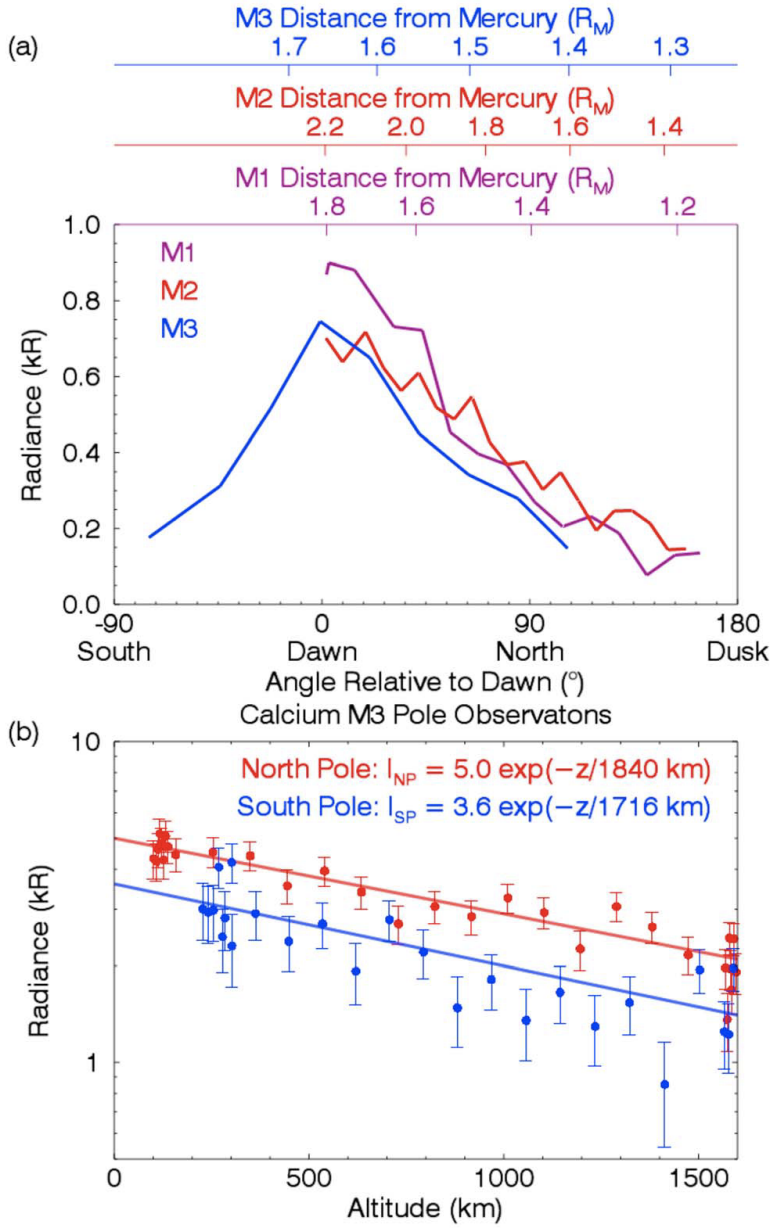

Figure 6.1: (a) Calcium fantail measurements performed during the three MESSENGER flybys of Mercury. (b) Ca emission profile over Mercury's north (red dots) and south (blue dots) poles observed by UVVS during MESSENGER third flyby of Mercury. Exponential fits to the data are represented by the solid lines. In the exponential fits, z is the altitude above the surface. From Burger et al. (2012).

[2]The fantail corresponds to a 180° roll of the spacecraft (McClintock et al.2008, 2009), similar to the Bepi-Colombo flip maneuvers (Section 4.2.2).

During the third flyby, altitude scans above north and south poles of Mercury were obtained (Vervack et al., 2010). The polar profiles revealed a north/south asymmetry in the release rate as a higher radiance is exhibited in the north. Exponential fits to these profiles yielded e-folding distances of 1,878 km in the north and 1,621 km in the south. These large scale heights indicate an energetic Ca source, which is consistent with ground-based observations. The analysis made by Burger et al. (2012) produced similar e-folding values (1,840 ± 140 km at the north pole and 1,716 ± 200 km at the south pole, Figure 6.1b).

Using Monte Carlo simulations, Burger et al. (2012) determined the Ca distribution to be consistent with temperatures of as much as 50,000 K. Observations were well fit by a persistent and energetic source of Ca located in Mercury's dawn equatorial region, which was confirmed later by Burger et al. (2014) with the analysis of the orbital observations.

Burger et al. (2014) discovered a seasonal dependence in the calcium source rate. Killen and Hahn (2015) later explained this seasonal variations of the exospheric Ca source rate by impact vaporization from interplanetary dust coming from a dust-disk, tipped less than 5° from Mercury's orbital plane. An additional source of dust was however required to explain a peak of Ca near Mercury TAA of ∼25°. Killen and Hahn (2015) and Christou et al. (2015) showed that this enhancement of Ca could be due to a meteor storm from comet 2P/Encke.

Although Burger et al. (2014) did not determine the process responsible for the Ca release in Mercury's exosphere, they concluded that impact followed by molecular dissociation is most consistent with their results. Killen (2016) investigated more in details the process producing highly energetic Ca, assuming the impact vaporization as the primary source. This process must explain not only the high temperature of the calcium exosphere but also its seasonal variations and dawnside enhancement. Assuming that the predominant form of the initial Ca ejecta is CaO, Killen (2016) examined the following mechanisms:

1. electron-impact dissociation,
2. spontaneous dissociation,
3. shock-induced dissociative ionization,
4. photodissociation,
5. sputtering.

Killen (2016) concluded that: (1) electron-impact dissociation can not produce the required abundance of Ca, (2) spontaneous dissociation is unlikely to result in energy high enough to accelerate Ca atoms to the altitudes where they are observed, (3) shock-induced dissociative ionization produces the required energy and comes close to producing the required abundance, but there a lot of uncertainties implied in the calculation, (4) photodissociation can produce the required abundance of Ca but can not reproduce the observed spatial distribution, and (5) sputtering can not reproduce the observed spatial and temporal variation that is measured. Berezhnoy (2018) also concluded that the observed temperatures of Ca atoms disagree with results of the simple model of photolysis of impact-produced molecules. Additional processes are necessary to explain the energetic Ca in Mercury's exosphere.

Other studies confirm the viability of this two-step process i.e. impact followed by molecular dissociation (e.g. Plainaki et al., 2017, Cassidy et al., 2021, Moroni et al., 2023). Plainaki et al. (2017) performed simulations of the spatial distribution of (1) micrometeoroid impact vaporization generated CaO exosphere and (2) thermal Ca exosphere, generated through the photodissociation of CaO. They found that the simulated morphology of the Ca exosphere is consistent with the available MESSENGER observations. According to Plainaki et al. (2017), the generation of a seasonal asymmetric CaO exosphere is expected, with the maximum surface release being on the dawnside-nightside hemisphere, near the equator. In addition, an exospheric energetic Ca component, derived from the dissociative ionization and neutralization of CaO, is

expected above the same region. The spatial distribution of the thermal Ca exosphere generated by photoionization of the CaO molecules in sunlight is expected to be asymmetric, exhibiting local maxima near the dawn region. Moreover, Cassidy et al. (2021) reported large transient exospheric enhancements observed by MESSENGER's UVVS on Mercury's nightside. The most likely source for these events is meteoroid impacts. During these events, exospheric Ca did not show obvious enhancement, which is consistent with earlier predictions that Ca is ejected in a neutral molecular form that is undetectable to UVVS. Another form of molecular Ca is CaS. Bennett et al. (2016) investigated the photon-stimulated desorption of Ca from calcium sulfide (CaS). They concluded that Ca photodesorbed from CaS is not energetic enough to contribute to the hot component of exospheric Ca but could contribute to the cold one at low altitudes. Limb scans taken above Mercury's dayside actually revealed a potential cold component of Ca (Cassidy, 2018). The cold component was only observed sporadically, at all dayside local times (8 A.M. to 4 P.M.) but not at dawn and dusk. Cassidy reported a temperature that is consistent with laboratory measurements of atomic Ca photodesorption from CaS.

Burger et al. (2014) concluded that ion sputtering and electron-stimulated desorption are unlikely to be the primary source of Ca owing to the year-to-year stability of the Ca exosphere compared with the solar-wind interaction with Mercury's magnetosphere. Moreover, Burger et al. (2014) showed no evidence for Ca enhancement at high latitudes (where ion sputtering predominantly occurs at Mercury). Pfleger et al. (2015) simulations of solar wind sputtered Ca also suggest that sputtering cannot explain the MESSENGER observations analyzed by Burger et al. (2014). Pfleger et al. (2015) however suggested that ion sputtering could provide a minor population of Ca.

6.3 Space-based observations: BepiColombo/PHEBUS

We have detected calcium in Mercury's exosphere with PHEBUS c422 channel during both flybys. The observations revealed for the first time a very extended Ca corona (up to 13,000 km) on the morning side. The peak of Ca was also measured near dawn for both flybys. The unexpected spikes that we have over the emission profile hinder a more accurate determination of the Ca peak location.

6.3.1 Exponential fit

To compare PHEBUS data to MASCS data, I computed an exponential fit to the data:

$$I_R(z) = I_0 \, e^{-z/H} \tag{6.1}$$

With I_0 the radiance at the surface (R), H the e-folding distance (km) and z the altitude (km). I only considered the data on the morning side and excluded the spikes to derive an exponential fit. For the first flyby, it was difficult to use data below ∼600 km as they are affected by the spikes. I thus used data starting at ∼600 km of altitude for the first flyby. For the second flyby, I used data starting at ∼260 km of altitude.

However, I could not fit the data with a single e-folding distance. Indeed, as the gravitational force acting on the atoms varies with the altitude, I cannot consider all the morning side data to compute this exponential fit, the altitude stretching over several orders of magnitude (∼600 to ∼10,000 km for MSB1 and ∼260 to ∼13,000 km for MSB2). Therefore, I have derived the exponential fit (Eq. 6.1) on the morning side data whose altitude is lower than the radius of Mercury R_M, based on the results from the same empirical analysis conducted on MESSENGER's orbital phase data. For the TAAs of BepiColombo's flybys, the derived radiance at the surface is ∼9 kR and the e-folding distance is between 1,500 and 2,000 km (Figure 6.2).

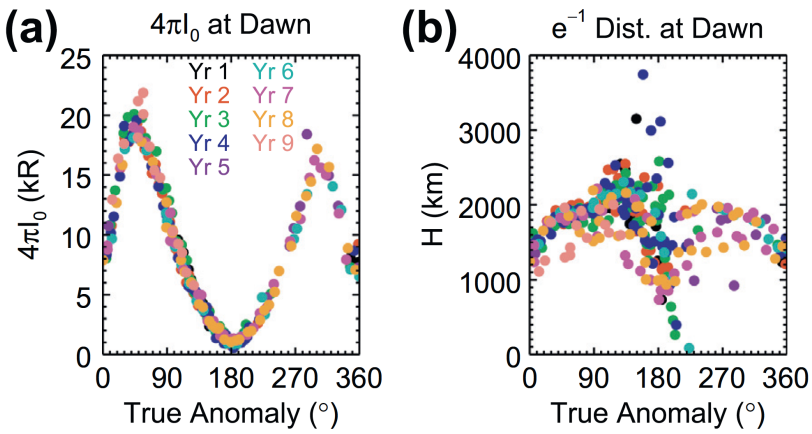

Figure 6.2: (a) Ca emission at the surface and (b) e-folding distance at dawn determined from exponential fits to radial limb profiles. From Burger et al. (2014).

Deriving an exponential fit is equivalent to performing a linear regression of the form:

$$y(x) = a + bx$$

With:

$$y = \ln(I_R)$$
$$a = \ln(I_0)$$
$$b = -\frac{1}{H}$$

Using the formulas given in Chapter 15.2 in Winkler (1993), I computed the best-fit model parameters a and b and the variances in the estimates of a and b i.e. σ_a^2 and σ_b^2. I deduced I_0 and H (Eq. 6.2) and their variances $\sigma_{I_0}^2$ and σ_H^2 (Eq. 6.3).

$$I_0 = e^a \qquad H = -\frac{1}{b} \tag{6.2}$$

$$\sigma_{I_0}^2 = (e^a)^2\,\sigma_a^2 \qquad \sigma_H^2 = \left(\frac{1}{b^2}\right)^2 \sigma_b^2 \tag{6.3}$$

The results for both flybys are given in Table 6.1 and represented on Figure 6.3. The values are quite consistent from one flyby to another. The second flyby dataset is more reliable as it includes data closer to the surface and less noisy.

Table 6.1: Derived values of the exponential fit to c422 data for both flybys.

Flyby n°	I_0 [kR]	H [km]
1	6.93 ± 0.26	2,555 ± 142
2	7.43 ± 0.21	2,777 ± 145

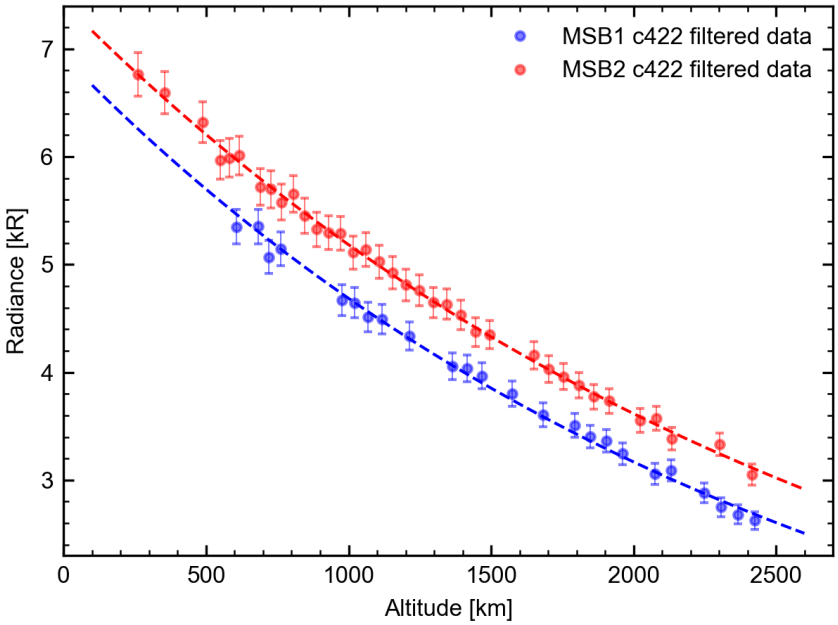

Figure 6.3: Low-altitude Ca emission profiles on dawn side. Blue (resp. red) dots correspond to the first (resp. second) flyby data that were considered to derive the exponential fit. The error bars represent the $\pm 1\sigma$ uncertainty. Exponential fits to the data are shown by the dashed lines.

6.3.2 Chamberlain model

The empirical approach of the previous section (exponential fit on the intensities) allowed us to compare our results with those of Burger et al. (2014). In this section, we take a physical approach using the Chamberlain exospheric model (Chamberlain, 1963) with a fit on the densities. The description of the model is given in Appendix A.

6.3.2.1 Application to c422 dayside data

For each flyby, I applied Chamberlain's theory to the c422 detector data. As for the exponential fit (Section 6.3.1), I first focused on the c422 data on the morning side at relatively low altitudes ($<1\mathrm{R_M}$). I sought to test several temperatures based on the temperatures deduced by Burger et al. (2012, 2014) i.e. 20,000 K and 50,000 to 90,000 K. For each LOS, I compute the density $n(r)$ (A.1) at each point of the LOS, considering $n_0 = 1$. For the calculations, I considered a variable step δ:

$$\delta(h) = \begin{cases} 1 & h < 1,000 \\ 5 & 1,000 \leq h < 5,000 \\ 10 & 5,000 \leq h < 10,000 \\ 25 & h \geq 10,000 \end{cases}$$

The calculation stops when the LOS exceeds the region of interest (i.e. a sphere of radius 10 R_M centered at Mercury). I subsequently integrate the density $n(r)$ along the LOS to obtain the column density N. From the column density N, I deduce the count rate CR using Eq. (5.3) and (5.9). I use the g-value of Ca emission line at 422.8 nm computed in section 5.1.4.1 (Table 5.3), the effective area of the c422 channel derived in section 4.2.4.3 (4.14) and the instrument solid angle Ω. To measure how well the model agrees with the data, I use the chi-square merit function:

$$\chi^2 = \sum \left(\frac{d_i - n_0\, m_i}{\sigma_i} \right)^2 \tag{6.4}$$

Where d_i corresponds to the count rate registered by c422, n_0 is the density at the surface (A.1) and m_i is the modelled count rate. Equation (6.4) is minimized to determine n_0. At its minimum, the derivative of χ^2 with respect to n_0 vanishes:

$$0 = \frac{\partial \chi^2}{\partial n_0} = -2 \sum \frac{m_i \, (d_i - n_0 \, m_i)}{\sigma_i^2} \tag{6.5}$$

For each tested temperature, I thus calculate the associated density n_0 and χ^2. Results are shown on Figure 6.4a and 6.4b. The χ^2 is minimal for $(n_0; T) = (2.2\,\mathrm{cm}^{-3}; 60,000\,\mathrm{K})$ for the first flyby and $(n_0; T) = (2.3\,\mathrm{cm}^{-3}; 70,000\,\mathrm{K})$ for the second one. The density, as well as the temperature, are very consistent from one flyby to the other. The exobase temperature is consistent with the temperatures derived by Burger et al. (2012, 2014).

Note that the temperature T is not well constrained: the low-altitude profile is equally well approximated by a Chamberlain model at temperatures above 50,000 K (Figure 6.4a and 6.4b).

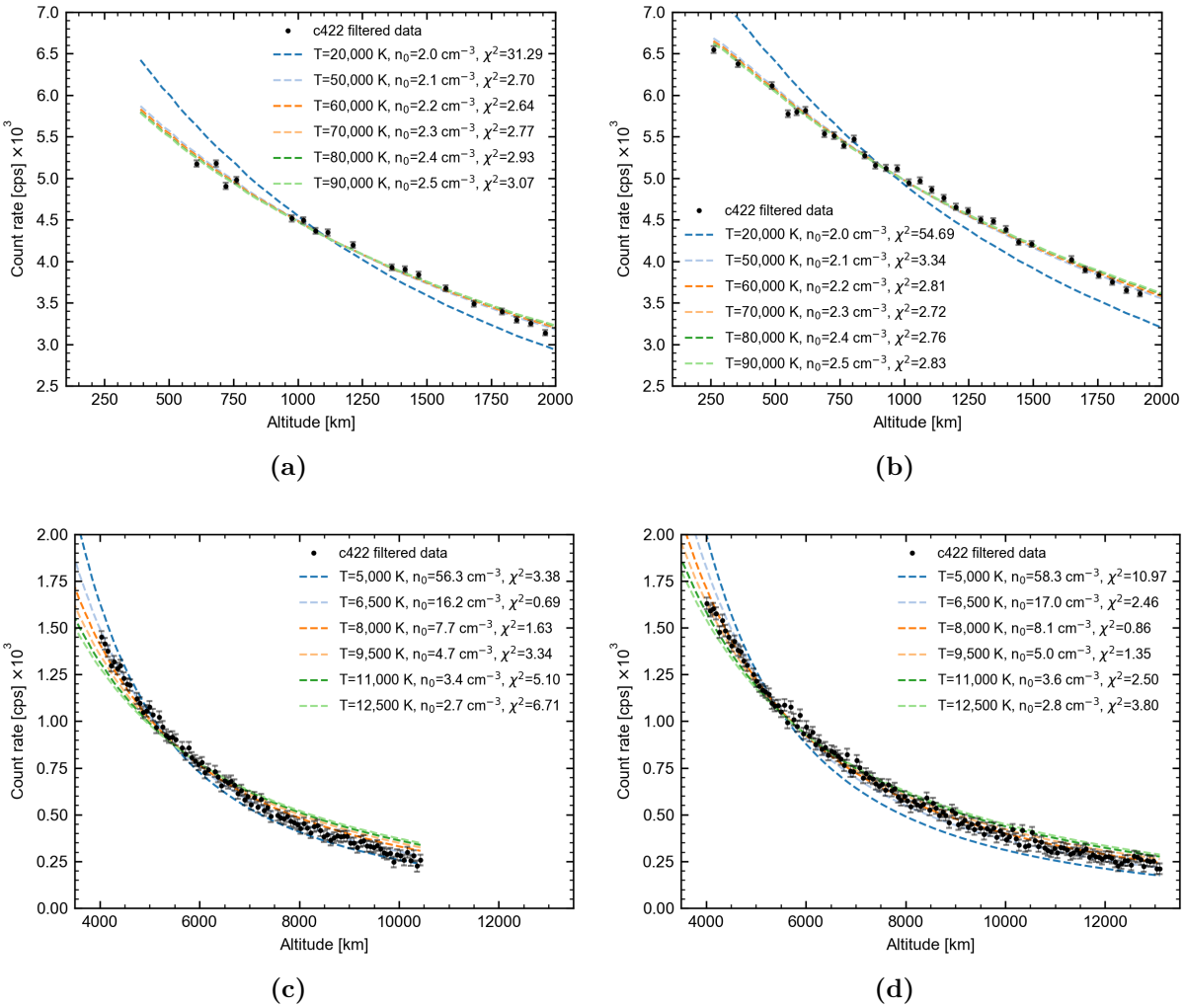

Figure 6.4: Ca Chamberlain model fits to c422 data at low altitudes on the dawn side during MSB1 (a) and MSB2 (b). Ca Chamberlain model fits to c422 data at high altitudes on the dawn side during MSB1 (c) and MSB2 (d). The colored dashed lines represent Ca Chamberlain models at different temperatures. The error bars represent the 1σ uncertainties.

Now, if I consider the c422 high-altitude data on the morning side, the profiles are well fitted by a Chamberlain model at temperatures between 5,000 and 10,000 K (Figure 6.4c and 6.4d), which is more in agreement with the values deduced from linewidth measurements by Bida et al. (2000) and Killen et al. (2005).

6.3.2.2 Application to c422 nightside data

For both flybys, we noticed that the Chamberlain model fit to c422 dawn side data at low altitudes did not fit the c422 nightside data (Figure 6.5), revealing a day/night asymmetry.

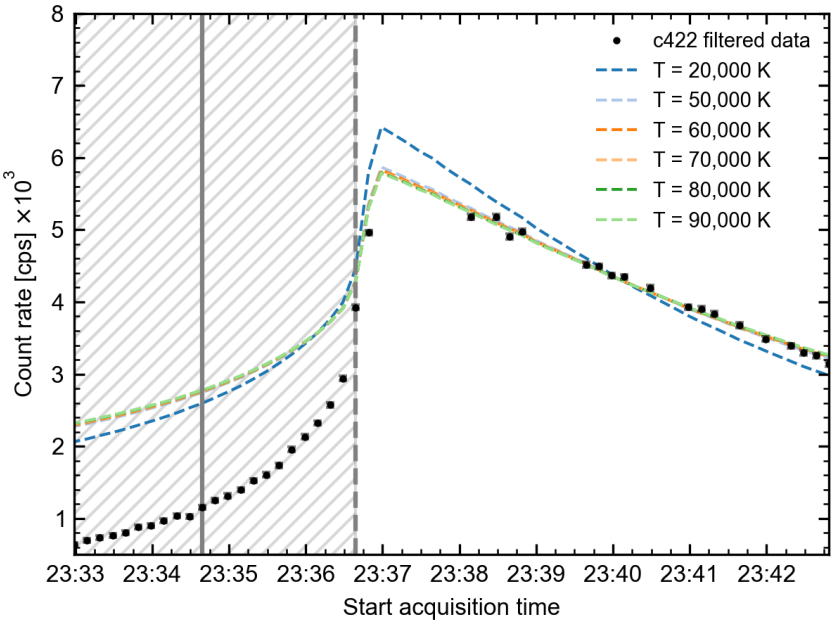

(a)

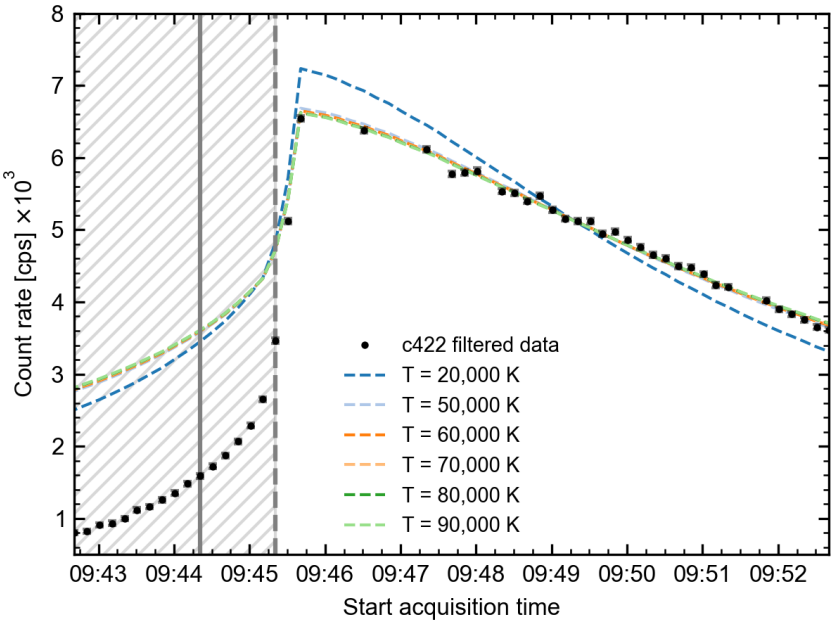

(b)

Figure 6.5: c422 count rate as a function of time. The colored dashed lines are Chamberlain models of Ca at different temperatures. The solid gray line represents the CA and the hatched area represents the time spent by the spacecraft in the shadow of Mercury.

I thus tested different temperatures with Chamberlain's model on the nightside data (Figure 6.6). The best-fit was obtained for $(n_0; T) = (6.0\,\mathrm{cm}^{-3}; 5,500\,\mathrm{K})$ for the first flyby and $(n_0; T) = (3.5\,\mathrm{cm}^{-3}; 6,000\,\mathrm{K})$ for the second one. The temperature at the exobase is ∼10 times lower than the one derived from morning side data and in good agreement from one flyby to the other. The densities, although different between the two flybys, are higher than those obtained on the

morning side.

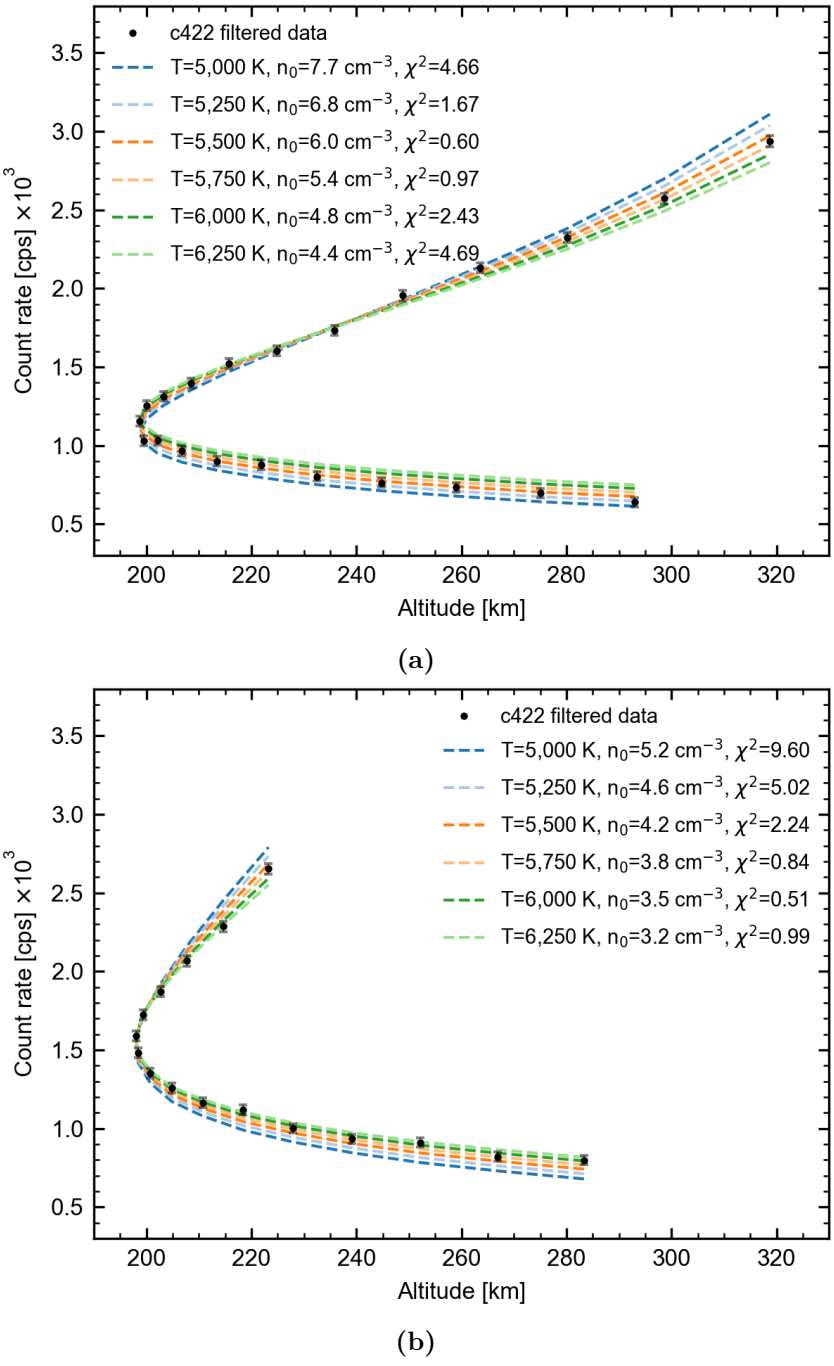

Figure 6.6: Ca Chamberlain model fits to c422 nightside profile during MSB1 (a) and MSB2 (b). The colored dashed lines represent Ca Chamberlain models at different temperatures. The error bars represent the 1σ uncertainties.

6.3.3 Discussion

During the first two flybys of Mercury, the c422 channel observations revealed a very extended calcium exosphere, up to 13,000 km altitude on the dayside. PHEBUS c422 data showed a dawn enhancement of Ca, supporting previous conclusions that the Ca source peaks in the dawn region (McClintock et al., 2009; Vervack et al., 2010; Burger et al., 2012).

At first, I focused on the morning side data and calculated an exponential fit to compare our results with MESSENGER. I obtained a relatively high e-folding distance (~2,600 km), in

agreement with the results of Burger et al. (2014), confirming the energetic nature of exospheric Ca.

To go further in the study and adopt a more physical point of view, I applied the Chamberlain model to the c422 data on the morning side (i.e. when MPO is out of eclipse) at relatively low altitudes (<1R_M). Both flybys give similar results, both in terms of exobase density n_0 and exobase temperature T. Note that there is not much difference in slope between profiles for temperatures >50,000 K. This result is consistent with the temperature derived by Burger et al. (2012, 2014) based on MESSENGER/MASCS data during the orbital phase.

Such a high temperature implies a high-energy process to release calcium in the exosphere of Mercury. Several processes have been discussed in the literature (including electron-stimulated desorption, photon-stimulated desorption, impact vaporization or sputtering) but none of them seem to be able to produce an exosphere that hot. Killen et al. (2005) was the first to propose a two-step process: the first one ejects Ca-bearing molecules and the second one produces highly energetic Ca atoms. A lot of studies support this process. First, Killen and Hahn (2015) showed that micrometeoroid impact vaporization as the primary source explains the seasonal variations of Ca. Pokorný et al. (2018) showed a strong dawn/dusk asymmetry in both meteoroid impact direction distribution and the impact vaporization pattern on the surface, which is consistent with the dawn/dusk asymmetry of the Ca exosphere. Furthermore, Ca-bearing molecules are more likely to be produced in impact vapor plumes than atomic Ca (Berezhnoy & Klumov, 2008), and the molecules expected to be produced (CaO, CaOH, and/or $Ca(OH)_2$, depending on the temperature of the vapor plume) quickly dissociate to release atomic Ca (Berezhnoy & Klumov, 2008). Killen (2016) discussed processes by which the Ca-bearing molecules produced by impact vaporization are then dissociated (including electron-impact dissociation, sputtering, spontaneous dissociation, shock-induced dissociative ionization or photodissociation) and concluded that shock-induced dissociative ionization is the most likely mechanism for creating high energy Ca atoms.

I subsequently focused on the morning side data at high altitudes (>4,000 km) to apply Chamberlain's model. The exobase density n_0 is quite different from one flyby to another, in contrast with the exobase temperature T which is similar from one flyby to the other. The exobase temperature I deduced from the data at high altitudes is ∼10 times lower than the exobase temperature I deduced from the data at relatively low altitudes for both flybys and in better agreement with the values derived from linewidth measurements by Bida et al. (2000) and Killen et al. (2005). This difference between low and high altitudes is likely due to the ionization that is not considered in the model of Chamberlain.

Finally, the temperature deduced from the low-altitude morning side data does not fit the predawn nightside data. This could indicate a day/night asymmetry with a source of Ca located predominantly on the dayside. Ca atoms observed on the nightside would then come mainly from the transport around the planet with a significant proportion of them being photoionized before reaching the nightside. Alternatively, the day/night asymmetry could also be the consequence of a shift of the main source of Ca away from the dawn region. Pokorný et al. (2018) showed that micrometeoroid impact vaporization flux does not peak systematically at 6 A.M. (i.e. at dawn). At TAA = 240° and TAA = 300°, which encompasses the TAAs of Mercury flybys, the impact vaporization flux peaks between 7 and 8 A.M. (Figure 6.7).

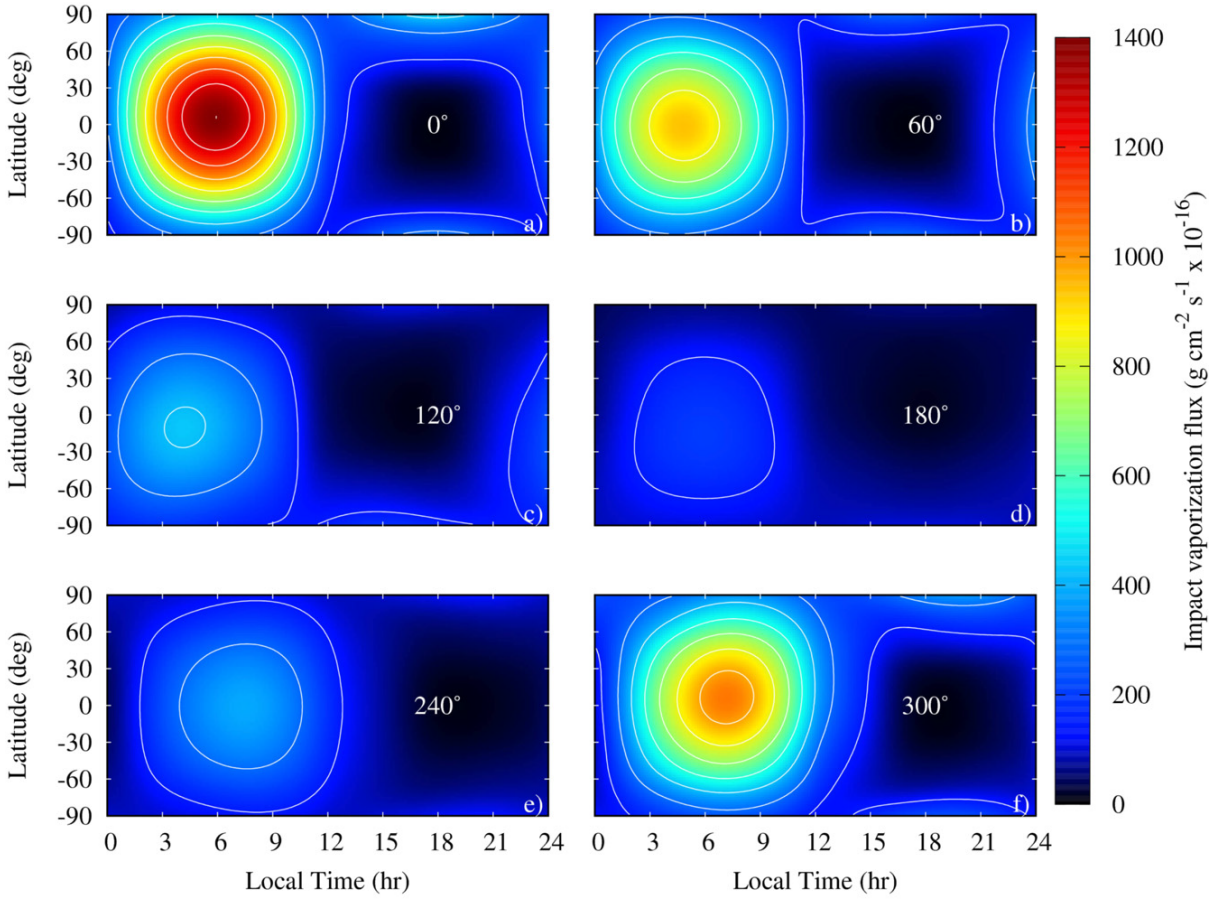

Figure 6.7: Impact vaporization flux on Mercury for six different TAAs. From Pokorný et al. (2018).

The model of Chamberlain presents some limitations when applied to the Ca exosphere. First, the model is a 1D spherical model, which does not appear to be suitable for the Ca exosphere as the Ca distribution seems to vary with the local time. Second, the model does not take into account radiation pressure or photoionization. The radiation pressure effect is considered negligible for Ca: due the short photoionization lifetime of Ca atoms, most of them are photoionized before being affected by the radiation pressure (McClintock et al., 2008; Chaufray et al., 2022). Photoionization, on the other hand, seems to play an important role in the formation of Mercury's Ca exosphere and should be considered in the exospheric model. Beyond the limits of the model, another potential source of error lies in the the g-value, since we assumed that the atoms are at rest with respect to Mercury. However, Moroni et al. (2023) concluded that the calculation of the acceleration due to the radiation pressure produced very little refinement of their simulated Ca profiles.

Chapter 7

Potassium (?) in Mercury's exosphere

In Section 5.2, I stated that we had detected species with the c404 channel during both flybys. It is now necessary to identify this (these?) species. For this, I made an inventory of the species previously observed in Mercury's exosphere which have emission lines in the detector bandwidth.

In the following sections, I will therefore describe the species considered and their previous detection in the exosphere of Mercury. Then, I will use the model of Chamberlain to compare our results to MESSENGER.

7.1 Ground and space based observations prior to BepiColombo

The c404 channel was built to detect potassium. It has been observed in Mercury's exosphere with ground-based telescopes via emission from its D lines at 766.49 and 769.89 nm. These two strong resonance lines were unfortunately outside the spectral range of MESSENGER/MASCS. Attempts to detect the potassium emission lines at 404.52 and 404.83 nm were not successful. Only an upper limit of a few Rayleigh was derived (Vervack et al., 2016). In contrast, using ground-based observations at 769.9 nm, Lierle et al. (2022) estimated the disk-averaged brightness for the K doublet at 404 nm of 50 R. They also reported the enhancement of exospheric K at low to midlatitudes and a north/south asymmetry, with the strongest emission in the south.

Other species having emission lines in c404 channel bandwidth have been detected in Mercury's exosphere by MESSENGER/MASCS: Ca^+, Al and Mn. Singly ionized calcium was first detected in Mercury's exosphere during the third MESSENGER flyby (Vervack et al., 2010). The ions were observed at approximately 1–2 R_M antiSunward of the planet and mostly near the equatorial plane. Vervack et al. (2016) confirmed the presence of Ca^+ in Mercury's exosphere with the observations of two lines at 393.48 and 396.96 nm. Bida and Killen (2011) and Bida and Killen (2017) reported ground-based measurements of Al via its emission line at 396.2 nm. Vervack et al. (2016) confirmed the presence of aluminum in Mercury's exosphere with the clear measurement of two lines of Al (394.51 and 396.26 nm) with MESSENGER/MASCS. Manganese was unexpectedly detected by MESSENGER/MASCS through its emission triplet at 403 nm (403.19, 403.42 and 403.56 nm) (Vervack et al., 2016).

The species have been sporadically detected both from the ground and from MESSENGER observations, pointing to a very high variability of their production. The detection of Ca^+ (apart from the third flyby), Al and Mn was made only towards the end of the mission, confined to a small region (predawn nightside region) and a limited range of Mercury season (TAA between 0° and 70°). The location and timing of these detections correspond to the intersection of Mercury with the comet 2P/Encke dust trail. Killen and Hahn (2015) indeed proposed this correlation to explain the spike in the Ca emission source rate observed over similar TAAs (Section 6.2). The

three species could then come from Encke dust impacting the dawn side of Mercury. But the observed Mn profile is far different from those of Al and Ca^+ (Figure 7.1), which could indicate that Mn perhaps derives from the cometary dust rather than the surface of the planet itself. The intensity of Mn rapidly decreases with the altitude in contrast to those of Al and Ca^+, suggesting that the temperature of Mn is lower than the temperature of Al and Ca^+. However, the Al profile observed by MESSENGER is quite different from that observed from ground. In the ground-based observations (Bida & Killen, 2017), Al shows an exponential decrease, consistent with a hot exosphere whereas the MESSENGER observations (Vervack et al., 2016) showed that Al may exhibit a flat to increasing profile with altitude. Note that the observations of Al do not cover the same altitude ranges: 860-2,100 km for ground-based observations and 250-650 km for MESSENGER observations. Bida and Killen (2017) estimated the temperature of Al atoms as 6,100 - 8,000 K, consistent with the presence of Al as a dissociation product of comparatively long-lived AlO (same process as discussed in Killen et al., 2005). A high-temperature Al exosphere is also predicted by Berezhnoy and Klumov (2008), a consequence of excess energy imparted to the atom in photodissociation of molecular compounds. In contrast, Berezhnoy (2018) concluded that the observed temperature of Al atoms disagrees with results of the photodissociation of impact-produced molecules. Sputtering can also be considered as an important source of Al atoms in Mercury's exosphere (Wurz et al., 2010).

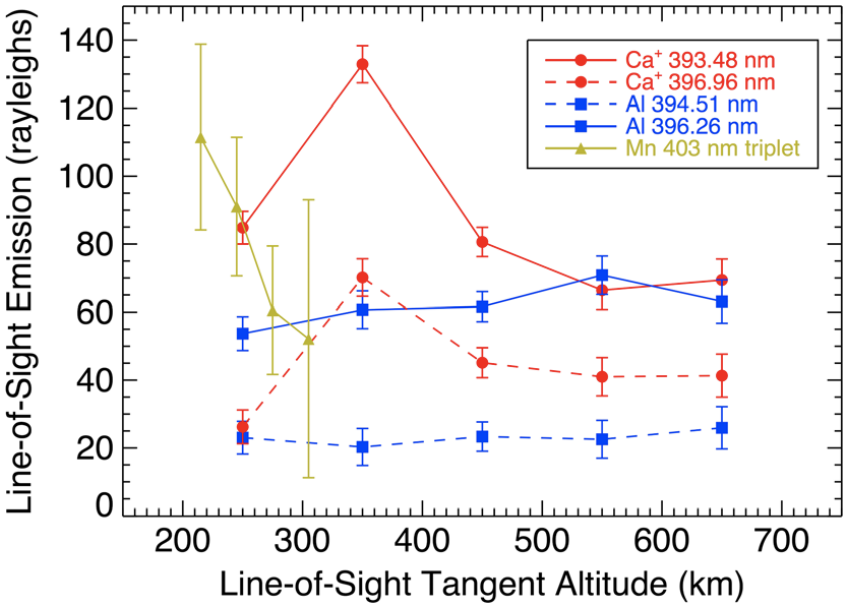

Figure 7.1: Profiles of Al, Ca^+ and Mn radiances as a function of the tangent altitude during one observation sequence of MESSENGER. From Vervack et al. (2016).

7.2 Space-based observations with BepiColombo/PHEBUS

7.2.1 Exponential fit

To compare PHEBUS data to MESSENGER's, I computed an exponential fit to the data, using the same process as for c422 data (Section 6.3.1). As mentioned in Section 5.2, the species was(were) detected at relatively low altitudes. Therefore, to derive the exponential fit, I only considered data with altitudes below 600 km. Unfortunately, during the first flyby, the data with altitudes below 600 km are too affected by the spikes, so I could not use them. The results for MSB2 are summarized in Table 7.1 and represented on Figure 7.2.

Among the species reported by Vervack et al. (2016), only the Mn profile shows an exponential decrease with the altitude (Figure 7.1). Therefore, I derived an exponential fit to this Mn

Table 7.1: Derived values of the exponential fit to c404 data during MSB2 and to MESSENGER's Mn radiance profile from Vervack et al. (2016).

Dataset	I_0 [kR]	H [km]
This study	9.60 ± 0.65	135 ± 3
Vervack et al. (2016)	0.95 ± 0.39	102 ± 17

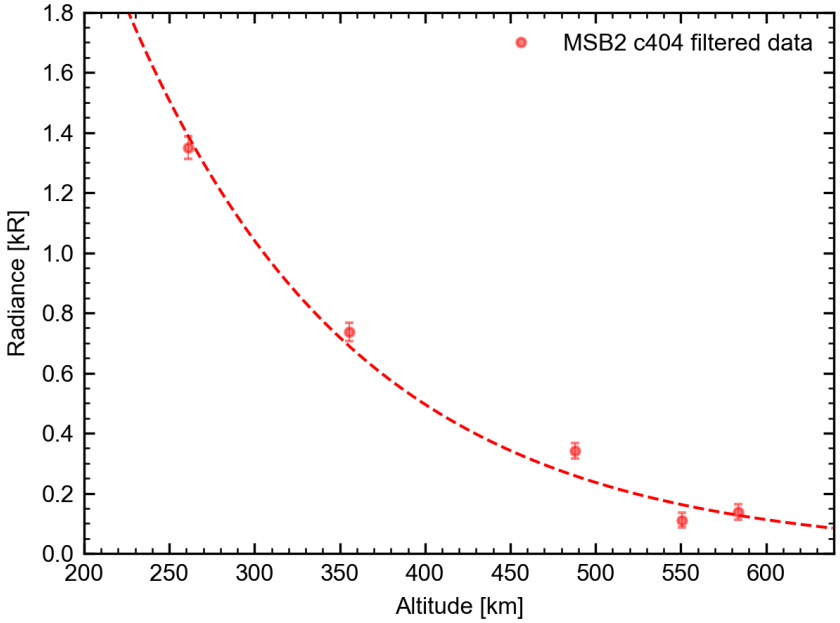

Figure 7.2: c404 emission profile on dawn side during MSB2. Red dots correspond to the data considered to derive the exponential fit. The error bars represent the $\pm 1\sigma$ uncertainty. Exponential fit to the data is shown by the red dashed line.

profile (Table 7.1). The exponential fit is derived from only four points at a very low altitude with high uncertainties. The e-folding distance is quite consistent with the one derived from c404 data during the second flyby but not the radiance at the surface. Moreover, BepiColombo flybys of Mercury were done at TAAs quite different from those for which the detection of Mn is reported (Table 5.2). Furthermore, during both BepiColombo flybys of Mercury, the detection was not confined to the predawn nightside region (local times from ∼2 to 5 A.M.), but extends from ∼4 to 6 A.M. i.e., towards the dawn/morning side region.

I could not compare profiles observed by PHEBUS to a potassium profile since MESSENGER did not detect its emission line. However, the estimate of brightness of Lierle et al. (2022) (50 R) is still far below the maximum emission observed during MSB2 (1,335 R). The spectra obtained during the observations described in Vervack et al. (2016) yield LOS radiances of 25.5 R (Al 394.51 nm), 63.0 R (Al 396.26 nm), 82.4 R (Ca^+ 393.48 nm), 41.2 R (Ca^+ 396.96 nm) and an average LOS radiance for Mn of 80.4 R, which is far below the values observed by PHEBUS c404 channel.

7.2.2 Chamberlain model

Regarding the c404 channel, I focused on the morning side data at low altitudes, where the instrument detected one (or more) species. To apply the Chamberlain, I selected the species that were potentially detected by the c404 channel, i.e. Al, K and Mn. Their spectral lines

have multiple components: a doublet for K (404.528 and 404.835 nm) and Al (394.512 and 396.264 nm), and a triplet for Mn (403.190, 403.421 and 403.563 nm). For each multiplet, I calculated the g-value for each wavelength of the multiplet and summed the contribution of each wavelength to obtain the g factor. The values are given in Table 7.2.

Table 7.2: g-values for the Al, Mn and K emission lines computed for the first three flybys of Mercury along with the oscillator strength and atomic mass assumed for the calculations. The g-values are given for Mercury heliocentric distance and TAA corresponding to each flyby.

Species	Wavelength in vacuum λ_0 [nm]	Oscillator strength f	Atomic mass m [u]	g value at MSB1 [s^{-1}]	g value at MSB2 [s^{-1}]	g value at MSB3 [s^{-1}]
Al	394.512	1.16×10^{-1}	26.98154	0.953	0.970	-
	396.264	1.16×10^{-1}		1.004	1.022	-
Mn	403.190	5.50×10^{-2}	54.93805	0.700	0.715	0.921
	403.421	4.03×10^{-2}		0.680	0.698	0.695
	403.563	2.57×10^{-2}		0.837	0.852	0.867
K	404.528	5.67×10^{-3}	39.0983	0.243	0.247	0.332
	404.835	2.63×10^{-3}		0.079	0.081	0.078

It is quite difficult to use the c404 data as they are very noisy, especially on the first flyby. Therefore, as for the exponential fit (Section 7.2.1), I only consider c404 data from the second flyby. For each species (Al, K and Mn), I have tested several temperatures. I was unable to fit the c404 morning side data with the temperatures reported for Al in Bida and Killen (2017) (Figure 7.3a). For potassium, the best-fit was achieved for $n_0 = 381.3\,\mathrm{cm}^{-3}$ and $T = 1,500\,\mathrm{K}$ (Figure 7.3b). For manganese, the best-fit was achieved for $n_0 = 34.3\,\mathrm{cm}^{-3}$ and $T = 2,500\,\mathrm{K}$ (Figure 7.3c).

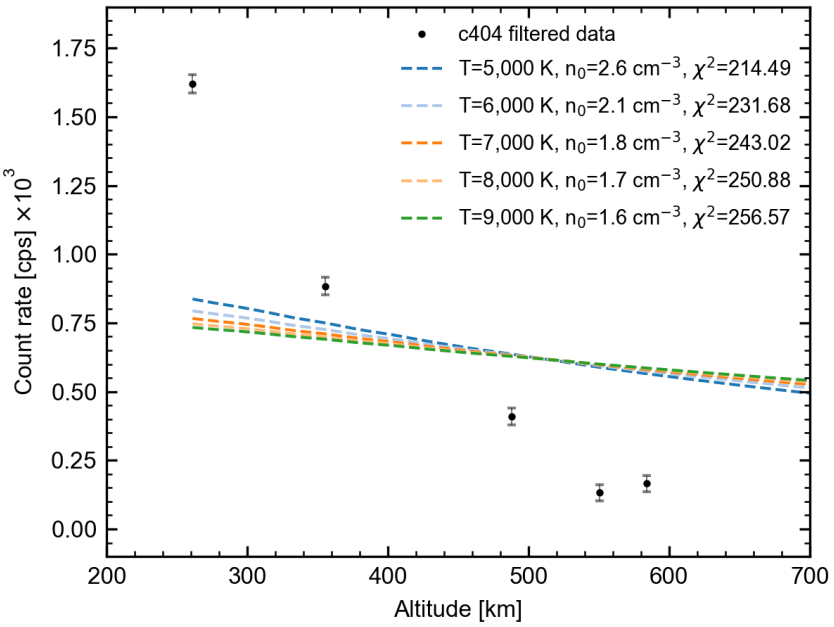

(a)

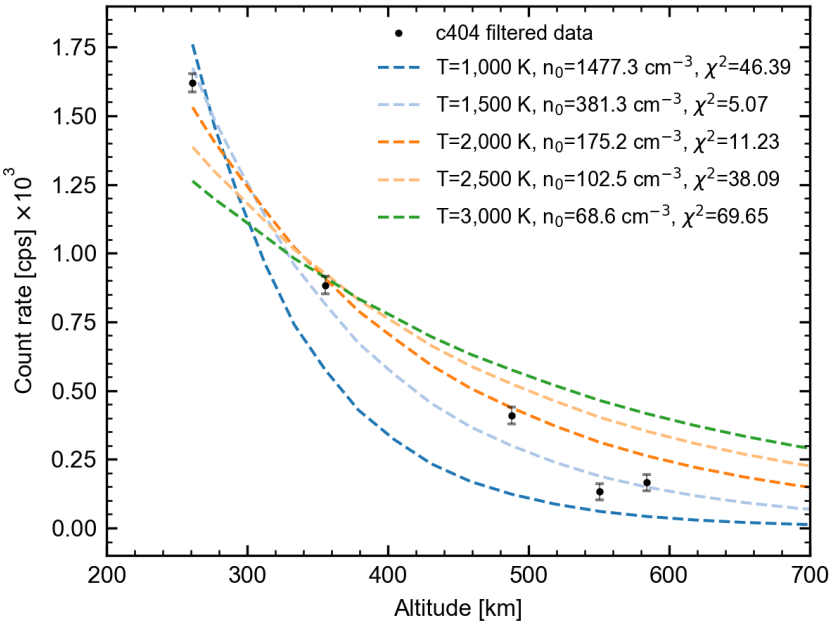

(b)

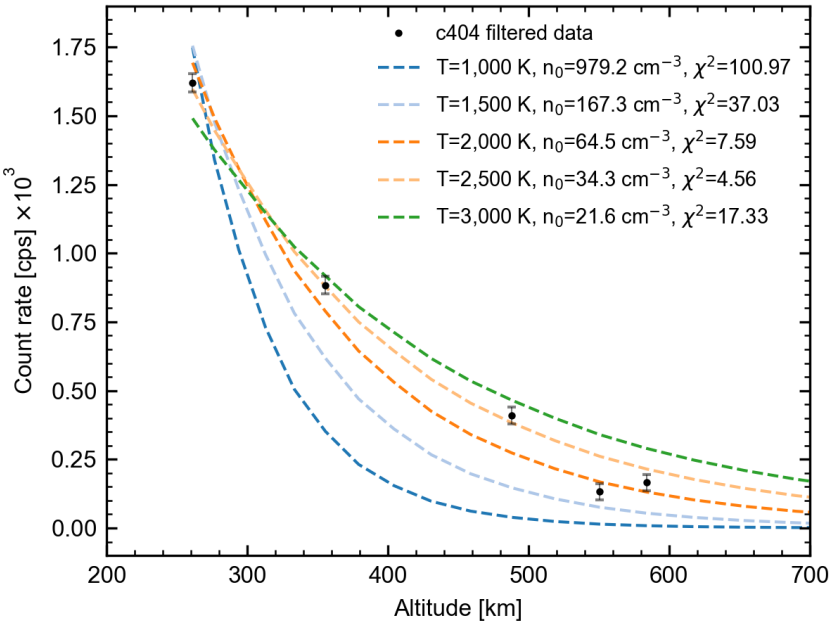

(c)

Figure 7.3: c404 count rate as a function of time. The colored dashed lines are Chamberlain models of Al (a), K (b) and Mn (c) at different temperatures.

For both manganese and potassium, Chamberlain's model applied to the dawn side data does not fit the night side data. However, it is very difficult to fit the data on the nightside. It will be necessary to wait for the orbital phase to accumulate data on the nightside.

7.2.3 Discussion

During both flybys, the c404 channel has detected species at low altitudes. The bandwidth of the channel is large enough to detect the emission lines of Ca^+ (393.48 and 396.96 nm), Al (394.51 and 396.26 nm), Mn (403.19, 403.42 and 403.56 nm) and K (404.52 and 404.83 nm).

Ca^+ was first detected in Mercury's exosphere by MESSENGER/MASCS during flybys (Vervack et al., 2010) and later during the orbital phase (Vervack et al., 2016). During the same observations, Vervack et al. (2016) reported the detection of Al and Mn. This was the first time manganese was detected in Mercury's exosphere. Aluminum was also observed from the ground (Bida & Killen, 2011; Bida & Killen, 2017). As for potassium, its doublet at 404 nm was never detected neither from ground nor in-flight but an upper limit was derived by Vervack et al. (2016). However, the K doublet at 766.49 and 769.9 nm was observed with ground-based telescopes (Killen et al., 2010; Lierle et al., 2022).

The profiles obtained with the c404 channel during both flybys show an exponential decrease with altitude. Data from the first flyby were unfortunately too affected by the spikes at low altitude. I therefore derived an exponential fit from the second flyby data only. This gave an estimate of the e-folding distance of 135 km.

Aluminum profile is different depending on the observations. In the observations reported by Vervack et al. (2016), Al shows a flat to increasing profile with altitude, which is not consistent with PHEBUS data. Nonetheless, Al observed with ground-based telescopes (Bida & Killen, 2017) shows exponential decrease, consistent with a hot exosphere. Using Chamberlain model, Bida and Killen (2017) derived a temperature T between 6,000 and 8,000 K. I have therefore applied a Chamberlain model to the c404 profile and tested temperatures ranging from 5,000 to 9,000 K. None of the temperatures could fit the c404 profile, ruling out Al as the species detected by PHEBUS c404 channel.

The Ca^+ profiles reported by Vervack et al. (2016) do not show an exponential decrease, which is not consistent with the profile obtained by PHEBUS c404 channel during MSB1 and MSB2.

In contrast with Al and Ca^+ profiles, Mn profile shows an exponential decrease (Vervack et al., 2016), suggesting that temperature of Mn is lower than the temperature of Al and Ca^+. The e-folding distance I deduced from the MESSENGER observations (i.e. 102 km) is similar to the one deduced from the c404 data (135 km) but not the radiance at the surface. The location and timing of Mn detection in Mercury's exosphere by MESSENGER suggest a relation with the comet Encke's dust trail (Vervack et al., 2016). We might then expect that the release of manganese is dominated by meteoroid impact vaporization. During impact events, Mn is produced mainly in the form of atoms (Berezhnoy, 2018). Thus, their temperature is assumed to be ∼3,000 K i.e. the typical temperature of the impact-produced cloud for Mn (Berezhnoy, 2018). The temperature I deduced using a Chamberlain model (∼2,500 K) is consistent with the expected temperature of impact-produced Mn. However, the observations of Mn reported by Vervack et al. (2016) were made only towards the end of the mission, over a limited range of TAAs (0-70°) and located in the predawn nightside region (local time from 2 to 5 A.M.). It is not consistent with the TAA of MSB2 (∼265°) and the location of the species during MSB2 is a bit different (local time from 4 to 6 A.M.).

For potassium, I fitted a Chamberlain model to the c404 profile and estimated a temperature at the exobase of 1,500 K. Recent results from Lierle et al. (2022) reveal K to be the coldest metallic constituent of Mercury's exosphere, with temperature between the surface temperature (i.e. 700 K) and 1,000 K. This temperature range favors thermal desorption or photodesorption

as the dominant mechanism for K release, as sputtered or meteoroid-vaporized K would appear much hotter.

Lierle et al. (2022) deduced a disk-averaged brightness for the K doublet at 404 nm of 50 R. The spectra obtained during the observations described in Vervack et al. (2016) yield LOS radiances of 25.5 R (Al 394.51 nm), 63.0 R (Al 396.26 nm), 82.4 R (Ca^+ 393.48 nm), 41.2 R (Ca^+ 396.96 nm) and an average LOS radiance for Mn of 80.4 R. The intensities observed with PHEBUS c404 channel are rather of the order of ∼1 kR.

In short, comparison with previous studies is inconclusive as to the species detected by the c404 channel during the flybys. We can only state that the e-folding distance is quite low (∼135 km) and that the temperature seems to be below 3,000 K.

General conclusion and perspectives

After the missions of NASA Mariner 10 in the 1970s and MESSENGER in the years 2000-2010, the ESA-JAXA joint mission BepiColombo is the third to explore Mercury. During its journey to Mercury, the BepiColombo spacecraft is to perform several gravity assist maneuvers, including six around Mercury. At the time of writing, three flybys have already taken place. During these flybys, PHEBUS, the UV spectrometer on board BepiColombo/MPO operated. For the first flyby on October 1, 2021, PHEBUS used its EUV detector (55-155 nm) as well as its visible channels c404 and c422, dedicated to K (404.7 nm) and Ca (422.8 nm) emission lines respectively. The instrument started the observations half an hour before the CA and was switched off half an hour after the CA. For the second flyby on June 23, 2022, both visible channels acquired data during half an hour, starting an hour before the CA. The instrument was then switched off and on again to operate the FUV detector (145-315 nm) along with the visible channels. The three detectors were then scheduled to acquire data during an hour, starting 15 min before the CA. The operation timeline for the third flyby on June 19, 2023 was very similar to that of the second flyby, the difference being that the FUV detector began to acquire a little earlier with respect to the CA ($\sim$20 min before the CA). This manuscript focused on the visible channels results of the first two flybys, the data of the third flyby having not yet been analysed at the time of writing this manuscript.

The geometric configuration of the two flybys was similar: the spacecraft approached the planet on the night side, crossed its shadow before exiting on the day side and moving away from Mercury. The CA occurred at an altitude of $\sim$200 km a few minutes before the spacecraft crossed the terminator. The count rate of both visible channels reflects this geometry, especially the eclipse.

Data analysis was complicated by sporadic spikes observed during both flybys on both visible channels. They occurred during the exact same acquisitions on both channels and occurred only when the spacecraft was out of eclipse on the morning side. Their origin remains undetermined. Another complication lies in the background signal that has to be removed from the exospheric signal. The background contains the contributions of the dark current, the zodiacal light and the stars in PHEBUS FOV. The background was well above the estimations made based on cruise observations and was not constant throughout each flyby. We have then developed an empirical correction that comes with uncertainties. This correction also had to consider the Ca cross-talk supposedly observed on the c404 channel signal.

The c422 channel clearly detected Ca, surprisingly extending far from the planet (up to 13,000 km) on the morning side. This is surprising given the short photoionization lifetime of Ca: the atoms are very likely to be photoionized before reaching these high altitudes. This implies that the release process of neutral Ca in the exosphere of Mercury is very energetic or that recombination of Ca^+ ions, either by electron impact or charge exchange, could occur far from the surface. The process currently favoured by the community is a two-step process where Ca is ejected from the surface in a molecular form that is subsequently dissociated. The

primary source considered is micrometeoroid impact vaporization. The process which dissociates the Ca-bearing molecules to produce energetic Ca atoms is still debated.

The e-folding distance we have derived from our radiance profiles of Ca close to the planet on the morning side is similar to that deduced from MESSENGER flybys, around 2,600 km. This result also implies a very energetic process releasing Ca in Mercury's exosphere.

We have used the model of Chamberlain despite its physical limitations when applied to the Ca exosphere. However, we could not fit the Ca radiance profiles on the morning side with a single temperature. We believe this is related to photoionization, which plays a major role in the Ca exosphere but is not considered in the model. We then fitted the low-altitude data on the morning side with a temperature above 50,000 K, in agreement with previous results from MESSENGER. Our fits revealed a day/night asymmetry, which could indicate that the source of Ca is mainly on the dayside or that the source of Ca is shifted away from the dawn region.

The next step is to include the effects of photoionization in Ca exospheric model. Ultimately, a 3D exospheric model would allow to better picture the spatial distribution of Ca and the local time effects.

Finally, during the flybys we did not observe a cold Ca component that MESSENGER possibly observed at low altitudes. The cold Ca component reported by MESSENGER (Cassidy, 2018) was seen sporadically at all dayside local times (from 8 A.M. to 4 P.M.) but not at dawn and dusk. The locations do not correspond to our flybys. This cold component must not extend to very high altitude, therefore we are more likely to detect it when performing low-altitudes observations. We plan on conducting low-altitude observations of the exosphere during the nominal phase of BepiColombo, mainly during the terminator seasons, covering all latitudes and local times around 6 A.M. and 6 P.M.. We will also have a better spatial resolution because the spacecraft velocity relative to Mercury will be lower than during the flybys.

The c404 channel detected species at low altitudes on the morning side during both flybys. The emission is weaker than that of Ca, the signal is therefore more affected by the sporadic spikes. The bandpass of the channel is large enough (especially when the slit of the instrument is removed) to detect the emission lines of Al, Ca^+, Mn and K. Comparing our results to those of MESSENGER, it appears that the detected species is potentially Mn and/or K.

The e-folding distance derived from our radiance profiles ($\sim$135 km) is similar to that of Mn ($\sim$100 km), which was derived from MESSENGER/MASCS radiance profile in the orbital phase. However, the detection location and the TAA are completely different. The temperature we deduced with the Chamberlain model (2,500 K) is in agreement with the typical temperature of impact-produced cloud ($\sim$3,000 K), but the origin of Mn is still unknown. The MESSENGER observations suggest that Mn could derive from cometary material rather than from the planet's surface.

For K, MESSENGER and ground-based telescopes have never detected this emission line in Mercury's exosphere. We derived a temperature of 1,500 K from the Chamberlain model, which is comparable to estimates from ground-based observations (between 700 and 1,000 K). Potter and Morgan (1997) and Killen et al. (2010) showed that the potassium emission is particularly strong in the southern hemisphere of Mercury, which was recently confirmed by Lierle et al. (2022). During the orbital phase, we can cover all latitudes and see if the emission of the species we detect with the c404 channel presents an excess in the southern hemisphere of Mercury. If so, it could indicate the detection of potassium.

To determine which species was observed with the c404 channel, we need to accumulate more data especially from the orbital phase. They will allow to observe any spatial and temporal variations and will help determine the release processes. Finally, ground-based measurements of the potassium emission lines in Mercury's exosphere could help differentiate potassium from manganese in the c404 channel measurements. In conclusion, more observations are needed to identify the species detected by the c404 channel.

The next flybys of Mercury in September and December 2024, and January 2025 will offer different geometries and will surely bring new information. I intend to remain invested in the preparation of PHEBUS operations and the analysis of visible channels data. Beyond the flybys, the orbital phase will offer various opportunities for PHEBUS to observe Mercury's exosphere (hopefully with all its detectors). We will make consecutive measurements with and without the slit, to monitor any variations (other than simply related to the ratio slit across/removed). As mentioned before, we will also make low-altitude observations. We intend to scan the exosphere at all local times and latitudes over the different seasons. Toward the end of the mission, we want to observe the planet's surface at the terminator to determine the albedo. We also intend to investigate the relation between neutral and ionised components in the exosphere of Mercury by qualitatively comparing in-situ measurements (heavy ions from MIA and MSA of Mio/MPPE) to our remote observations. We could also study how the different exospheric elements respond to space weathering events by comparing MPO/PHEBUS data and Mio/MSASI data (the MSASI instrument is dedicated to sodium). Meteoroid events were actually observed by MESSENGER/UVVS in 2011 and the response of three atomic species (Na, Mg and Ca) during one specific event were compared (Cassidy et al., 2021).

Finally, the orbital phase will also be an opportunity to conduct observations of the zodiacal light. The recent results obtained with PHEBUS visible channels during Lucas Gomez's internship indicate that the dust component in the inner solar system (i.e. <1 AU) is poorly constrained from past studies, and PHEBUS will be able to contribute with measurements for elongations varying from $\sim 10°$ to $100°$ along Mercury's orbit. We will then compare these measurements to those of the past mission HELIOS, which sampled similar regions of the zodiacal light (Leinert et al., 1981).

Mercury is not the only airless body in our solar system. Therefore, I became interested in the exosphere of other airless bodies such as Ganymede and Europa. We know that the processes (Figure 1.5) act differently according to the bodies, their physical and chemical properties, and their environment (type of surface, gravity, proximity with the Sun, magnetic field, plasma environment ...). For example, the solar wind is responsible for the sputtering on Mercury while on Ganymede or Europa, the Jovian plasma is. The meteoritic impacts are currently not considered as a contribution of Ganymede and Europa's exospheres in the Exospheric Global Model (EGM) developed at LATMOS (Leblanc et al., 2017; Oza et al., 2019). It is, however, taken into account in the exospheric model of Mercury (Leblanc et al., 2013). I have therefore decided to study the micro-meteoroid contribution to the exosphere formation of the Galilean moons, as a proxy to constrain the surface composition and evolution. In fact, the study of meteoritic impacts is important to understand the aging of the airless bodies surfaces (their renewal by mixing in particular) and the relationship between endogenous and exogenous sources of surface materials. I intend to adapt the vaporization model used for Mercury to the Galilean moons. I will conduct my research at ESAC as a research fellow and I intend to remain invested in the operations of PHEBUS.

Appendices

Appendix A

Chamberlain's theory

The theory of exospheres developed by Chamberlain (1963) is used to describe the composition and temperature of an exosphere. Chamberlain (1963) defines the exosphere as the portion of atmosphere above the critical level i.e. the height at which the collisions cease to be important. When it comes to Mercury, the critical level, also called exobase, corresponds to the surface of the planet. Chamberlain assumes that the exosphere is supplied by particles coming from below the exobase and having a Maxwellian velocity distribution.

The population of the exosphere is divided depending on the type of particle orbits:

1. ballistic particles – captive particles whose orbits intersect the exobase. Their energy is insufficient to allow them to escape. Their trajectory is elliptical.

2. satellite particles – captive particles orbiting above the exobase.

3. escaping particles – particles whose energy is sufficient enough to escape the attraction of the planet. Their trajectory is hyperbolic.

Because the exobase occurs at the surface of Mercury, collisions between atoms in the exosphere are improbable so only the ballistic and escaping partitions were considered.

The only force acting on the particles is the gravity. The only loss process considered is the Jeans escape. Moreover, the theory is developed for spherical symmetry.

In the exosphere where atomic collisions are rare, the spatial and momentum distribution is governed by Liouville's equation. The model of Chamberlain allows to determine the velocity distribution function at any point of the exosphere by solving the Liouville equation. The density is subsequently obtained by integrating this function on all the allowed trajectories (i.e. ballistic, satellite and escaping particles). The density $n(r)$ is written in the form:

$$n(r) = n_0 \, e^{-(\lambda_0 - \lambda)} \, \zeta(\lambda) \tag{A.1}$$

Where n_0 is the density at the critical level and λ is the absolute value of the potential energy:

$$\lambda(r) = \frac{GmM}{kT_0 r}$$

With:

G = gravitational constant
m = planetary mass (in our case, mass of Mercury)
M = atomic mass
k = Boltzmann constant
T_0 = temperature at the exobase

r = height

In (A.1), $\zeta(\lambda)$ is the partition function, which may be regarded as the fraction of the isotropic, Maxwellian distribution that is actually present. ζ is the sum of three terms (ζ_{bal}, ζ_{esc} and ζ_{sat}), describing the types of possible trajectories of exospheric particles. In Mercury's exosphere, ζ is simply the sum of ζ_{bal} and ζ_{esc}.

$$\zeta_{bal}(\lambda) = \frac{2}{\pi^{1/2}}\left[\gamma\left(\frac{3}{2},\lambda\right) - \frac{\left(\lambda_c^2-\lambda^2\right)^2}{\lambda_c}e^{-\psi_1}\gamma\left(\frac{3}{2},\lambda-\psi_1\right)\right] \tag{A.2}$$

$$\zeta_{esc}(\lambda) = \frac{1}{\pi^{1/2}}\left\{\Gamma\left(\frac{3}{2}\right) - \gamma\left(\frac{3}{2},\lambda\right) - \frac{\left(\lambda_c^2-\lambda^2\right)^2}{\lambda_c}e^{-\psi_1}\left[\Gamma\left(\frac{3}{2}\right) - \gamma\left(\frac{3}{2},\lambda-\psi_1\right)\right]\right\} \tag{A.3}$$

Where:

$$\psi_1 = \frac{\lambda^2}{\lambda+\lambda_c}$$

In (A.2) and (A.3), the function γ is the incomplete Γ-function:

$$\gamma(\alpha,x) = \int_0^x y^{\alpha-1}e^{y-1}dy$$

$$\Gamma(\alpha) = \int_0^\infty y^{\alpha-1}e^{-y}dy$$

Chamberlain's theory shows some limitations when applied to Mercury's exosphere. First, Mercury's exosphere is not spherically symmetric. Then, other processes are known to deplete Mercury's exosphere (e.g. surface sticking, ionization followed by transport along magnetic lines, acceleration by radiation pressure). Finally, the model considers gravity as the only force acting on the particles but we know that some atoms are accelerated by solar radiation pressure. The effect of radiation pressure on neutrals is however small at low altitudes. Moreover, "Radiation acceleration has the greatest effect on the motion of Na atoms and is not much of a factor when determining the motion of Mg atoms because of weak absorptions. For Ca, the trajectories are affected, although the short photoionization lifetime (...) results in a large fraction of Ca atoms being photoionized before radiation acceleration effects become significant." (Killen et al., 2018). Despite its limitations, Chamberlain's model provides a simple analytic description of the exosphere that requires only two independent parameters: the temperature and density at the exobase.

Appendix B

Mercury's exosphere is optically thin

Let's demonstrate the Ca exosphere of Mercury can be considered as an optically thin medium.

An optically thin medium is one which a typical photon of frequency ν can pass through without being absorbed. The chances are small that a photon will interact with a particle and even smaller that it will interact with more than one. A medium is considered optically thin when its optical depth $\tau_\nu \ll 1$. It is defined as follows:

$$\tau_\nu = \sigma_\nu N \tag{B.1}$$

Where N is the column density (cm^{-2}) and σ_ν is the cross section (cm^2) at the frequency ν.

At the line center, the cross section is given by:

$$\sigma_0 = \frac{\sigma_{tot}}{\sqrt{\pi}\Delta\nu_d} \tag{B.2}$$

Where $\Delta\nu_d$ is the Doppler width and σ_{tot} is the total cross section of the transition.

The Doppler width ($\Delta\nu_d$ in B.2) is defined as follows:

$$\Delta\nu_d = \frac{\nu_0}{c}\sqrt{\frac{2kT}{m}}$$

With ν_0 the frequency at line center, c the speed of light, k the Boltzmann constant, T the temperature and m the atomic mass.

The total cross section of the transition (σ_{tot} in B.2) is defined as follows:

$$\sigma_{tot} = \frac{\pi e^2}{m_e c} f$$

With e the elementary charge, m_e the electron mass, c the speed of light and f the oscillator strength factor. σ_{tot} is expressed in CGS units.

Considering (5.2), (5.3) and (B.1), I calculated the radiance up to which the medium is considered as thin for the emission line of Ca at 422.8 nm:

$$\begin{aligned} I_R &= \frac{4\pi I}{10^6} \\ &= \frac{gN}{10^6} \\ &= \frac{g}{10^6}\frac{\tau}{\sigma_0} \end{aligned}$$

I considered T = 12,000 K and the parameters listed in Table 5.3 for the emission line of Ca and obtained a radiance I_R = 618 kR for MSB1, 630 kR for MSB2 and 687 kR for MSB3. During MSB1 and MSB2, we have observed a maximum of ∼7 kR. Therefore, we can indeed consider the exosphere of Mercury as a optically thin.

Appendix C

List of publications and participation in conferences

C.1 Peer-reviewed papers

- Lee, Y. J., Muñoz, A. G., Yamazaki, A., Quémerais, E., Mottola, S., Hellmich, S., Granzer, T., Bergond, G., Roth, M., Gallego-Cano, E., Chaufray, J.-Y., **Robidel, R.**, Murakami, G., Masunaga, K., Kaplan, M., Erece, O., Hueso, R., Kabàth, P., Špokovà, M., Sánchez-Lavega, A., Kim, M.-J. and Mangano, V., Jessup, K.-L., Widemann, T., Sugiyama, K., Watanabe, S., Yamada, M., Satoh, T., Nakamura, M., Imai, M. & Cabrera, J. (2022). Reflectivity of Venus's Dayside Disk During the 2020 Observation Campaign: Outcomes and Future Perspectives. The Planetary Science Journal, 3(9), 209. https://doi.org/10.3847/PSJ/ac84d1

  Contribution: Processing data from different Venus observation campaigns (FUV detector calibration, dark current correction and spectrum extraction).

- Quémerais, E., Koutroumpa, D., Lallement, R., Sandel, B. R., **Robidel, R.**, Chaufray, J.-Y., Reberac, A., Leblanc, F., Yoshikawa, I., Yoshioka, K., Murakami, G., Korablev, O., Belyaev, D., Pelizzo, M. G., & Corso, A. J. (2023). Observation of Helium in Mercury's Exosphere by PHEBUS on Bepi-Colombo. Journal of Geophysical Research: Planets, 128 (6), e2023JE007743. https://doi.org/10.1029/2023JE007743

  Contribution: Preparation of observations and review of the paper.

- Chaufray, J.-Y., Quémerais, E., Koutroumpa, D., **Robidel, R.**, Leblanc, F., Reberac, A., Yoshikawa, I., Yoshioka, K., Murakami, G., Korablev, O., Belyaev, D., Pelizzo, M. G., & Corso, A. J. (2023). The EUV Reflectance of Mercury's Surface Measured by BepiColombo/PHEBUS. Journal of Geophysical Research: Planets, 128 (3). https://doi.org/10.1029/2022JE007669

  Contribution: Preparation of observations and review of the paper.

- **Robidel, R.**, Quémerais, E., Chaufray, J.-Y., Koutroumpa, D., Leblanc, F., Reberac, A., Yoshikawa, I., Yoshioka, K., Murakami, G., Korablev, O., Belyaev, D., Pelizzo, M. G., & Corso, A. J. (Under review). Mercury's Exosphere as seen by BepiColombo/PHEBUS Visible Channels during the First Two Flybys. Journal of Geophysical Research: Planets.

  Contribution: Processing and analysis of data from the first two flybys of Mercury and writing of paper.

C.2 Conferences

- AGU Fall Meeting 2020, held virtually 1-17 December 2020.
  - Faults network on Enceladus North Pole (Seignovert, B., Sotin, C., Tobie, G., Le Mouelic, S., & **Robidel, R.**)
- 5th Planetary Data Workshop & Planetary Science Informatics & Analytics, held virtually June 28-July 2, 2021.
  - Planning Science Opportunities with the JUICE Moon Coverage Tool. (Seignovert, B., Altobelli, N., Belgacem, I., **Robidel, R.**, Tobie, G., Vallat, C.)
- Mercury 2022, held 7-10 June, 2022 in Orléans, France.
  - PHEBUS observations of the He 58.4 nm emission during BepiColombo's first Mercury Flyby. (Koutroumpa, D., Quémerais, E., **Robidel, R.**, Chaufray, J. -Y., Phebus Team)
  - Observations of Mercury's Exosphere during BepiColombo First Mercury Flyby with PHEBUS' visible channels. (**Robidel, R.**, Quémerais, E., Koutroumpa, D., Chaufray, J. -Y.) - *Oral presentation*
  - EUV reflectance of Mercury measured by BepiColombo/PHEBUS. (Chaufray, J. -Y., Quémerais, E., Koutroumpa, D., **Robidel, R.**)
- 44th COSPAR Scientific Assembly, held 16-24 July, 2022 in Athens, Greece.
  - Observations of Mercury's Exosphere during BepiColombo First Mercury flyby (**Robidel, R.**, Quémerais, E., Koutroumpa, D., Leblanc, F., Chaufray, J. -Y.) - *Oral presentation*
  - UV Albedo of Mercury measured by BepiColombo/PHEBUS. (Chaufray, J. -Y., Quémerais, E., Koutroumpa, D., **Robidel, R.**, Leblanc, F.)
  - Global infrared mosaics of Enceladus based on new navigation and photometric correction function. (Ntinos, C., Rodriguez, S., Altobelli, N., Le Mouelic, S., **Robidel, R.**, Seignovert, B., Tobie, G., Cornet, T., Vallat, C.)
- 16th Europlanet Science Congress 2022, held 18-23 September, 2022 in Granada, Spain.
  - Observation of Mercury's Exosphere with the Visible Channels of PHEBUS during BEPICOLOMBO First Mercury's Flyby. (**Robidel, R.**, Quémerais, E., Koutroumpa, D., Leblanc, F., Chaufray, J. -Y.) - *Oral presentation*
  - First results of super-resolution mapping of Enceladus' surface, based on new navigation and photometric correction function. (Ntinos, C., Rodriguez, S., Altobelli, N., Le Mouelic, S., **Robidel, R.**, Seignovert, B., Tobie, G., Cornet, T., Vallat, C.)
- AGU Fall Meeting 2022, held 12-16 December, 2022 in Chicago, USA.
  - Mercury's exosphere as seen by BepiColombo/PHEBUS visible channels during the first two flybys. (**Robidel, R.**, Quémerais, E., Koutroumpa, D., Chaufray, J. -Y., Leblanc, F.) - *Oral presentation*
- AOGS 20th Annual Meeting, held July 30-August 4, 2023 in Singapore, Singapore.
  - Detection of Species in Mercury's Exosphere with the Visible Channels of PHEBUS During BepiColombo Flybys. (**Robidel, R.**, Quémerais, E., Chaufray, J. -Y., Koutroumpa, D., Leblanc, F., Reberac, A.) - *Poster presentation*
  - The UV Reflectance of Mercury Measured by BepiColombo/PHEBUS. (Chaufray, J. -Y., Quémerais, E., Koutroumpa, D., **Robidel, R.**, Leblanc, F., Reberac, A.)

C.3 Meetings

- PHEBUS distant observations of Venus, BepiColombo Cruise Science Study Group meeting, 28 September 2021 (online)
- PHEBUS visible channels operation during Mercury Swing-By 1, Mio Low Energy Particle consortium meeting, 24 March 2022 (online)
- PHEBUS team meeting, 13 June 2022, Montigny-le-Bretonneux, France
  - Visible channels in-flight performance and calibration
  - Summary of Mercury Swing-By 1 and plans for Mercury Swing-By 2
- Observation of Mercury's exosphere with PHEBUS visible channels during BepiColombo Mercury Swing-By 1 and 2, BepiColombo Science Working Team (SWT) meeting, 21-24 November 2022, Kobe, Japan

C.4 Other activities

- Chair of the *Young Planetary Scientists Group* in LATMOS - (2021 and 2022).
- Member of the Organizing Committee of the 2022 edition of the Elbereth Conference.
- Reviewer of a scientific paper published in Icarus (2021).
- Internship co-supervision:
  - Valentin Boullenger (2022) - Identification of the stellar contribution to PHEBUS visible channels.
  - Matthieu Didier (2022) - Spatial and temporal sampling study of the observations of the PHEBUS instrument orbiting Mercury.
  - Lucas Gomez (2023) - BepiColombo/PHEBUS cruise data analysis: contribution of zodiacal light
- Member of the defense jury of the students of the Master 2 Planetology and Master 2 NewSpace to validate their project of scientific definition of a space mission: Response to a bid for tenders similar to NASA SIMPLEx (Small Innovative Missions for Planetary Exploration) Announcement of Opportunity - (2022 and 2023).
- Presentation of the research professions
  - *Meet engineers and researchers night*, 7 January 2021, Lycée Clémanceau, Nantes. (Cancelled due to COVID-19)
  - Declics2021 - Speed meetings between scientists and students, Lycée Saint Sernin, Toulouse, 2 December 2021 (online)
  - Careers Fair, 14 January 2023, Collège Saint-Exupéry, Vélizy-Villacoublay

Bibliography

Anderson, B. J., Acuña, M. H., Lohr, D. A., Scheifele, J., Raval, A., Korth, H., & Slavin, J. A. (2007). The Magnetometer Instrument on MESSENGER. *Space Science Reviews*, *131*(1-4), 417–450. https://doi.org/10.1007/s11214-007-9246-7

Anderson, B. J., Johnson, C. L., Korth, H., Slavin, J. A., Winslow, R. M., Phillips, R. J., McNutt, R. L., & Solomon, S. C. (2014). Steady-state field-aligned currents at Mercury. *Geophysical Research Letters*, *41*(21), 7444–7452. https://doi.org/10.1002/2014GL061677

Anderson, B. J., Johnson, C. L., Korth, H., Winslow, R. M., Borovsky, J. E., Purucker, M. E., Slavin, J. A., Solomon, S. C., Zuber, M. T., & McNutt, J., Ralph L. (2012). Low-degree structure in Mercury's planetary magnetic field. *Journal of Geophysical Research: Planets*, *117*, E00L12. https://doi.org/10.1029/2012JE004159

Andrews, G. B., Zurbuchen, T. H., Mauk, B. H., Malcom, H., Fisk, L. A., Gloeckler, G., Ho, G. C., Kelley, J. S., Koehn, P. L., Lefevere, T. W., Livi, S. S., Lundgren, R. A., & Raines, J. M. (2007). The Energetic Particle and Plasma Spectrometer Instrument on the MESSENGER Spacecraft. *Space Science Reviews*, *131*(1-4), 523–556. https://doi.org/10.1007/s11214-007-9272-5

Baumjohann, W., Matsuoka, A., Magnes, W., Glassmeier, K.-H., Nakamura, R., Biernat, H., Delva, M., Schwingenschuh, K., Zhang, T., Auster, H.-U., Fornacon, K.-H., Richter, I., Balogh, A., Cargill, P., Carr, C., Dougherty, M., Horbury, T. S., Lucek, E. A., Tohyama, F., … Shinohara, M. (2010). Magnetic field investigation of Mercury's magnetosphere and the inner heliosphere by MMO/MGF. *Planetary and Space Science*, *58*(1), 279–286. https://doi.org/10.1016/j.pss.2008.05.019

Bednarski, T., Czerwiński, E., Moskal, P., Bialas, P., Giergiel, K., Kapłon, Ł., Kochanowski, A., Korcyl, G., Kowal, J., Kowalski, P., Kozik, T., Krzemien, W., Molenda, M., Moskal, I., Niedźwiecki, S., Palka, M., Pawlik, M., Raczyński, L., Rudy, Z., & Zon, N. (2014). Calibration of photomultipliers gain used in the J-PET detector. *Bio-Algorithms and Med-Systems*, *10*, 13–17. https://doi.org/10.1515/bams-2013-0110

Benkhoff, J., Murakami, G., Baumjohann, W., Besse, S., Bunce, E., Casale, M., Cremosese, G., Glassmeier, K.-H., Hayakawa, H., Heyner, D., Hiesinger, H., Huovelin, J., Hussmann, H., Iafolla, V., Iess, L., Kasaba, Y., Kobayashi, M., Milillo, A., Mitrofanov, I. G., … Zender, J. (2021). BepiColombo - Mission Overview and Science Goals. *Space Science Reviews*, *217*(8), 90. https://doi.org/10.1007/s11214-021-00861-4

Bennett, C. J., McLain, J. L., Sarantos, M., Gann, R. D., DeSimone, A., & Orlando, T. M. (2016). Investigating potential sources of Mercury's exospheric Calcium: Photon-stimulated desorption of Calcium Sulfide. *Journal of Geophysical Research: Planets*, *121*(2), 137–146. https://doi.org/10.1002/2015JE004966

Berezhnoy, A. A. (2018). Chemistry of impact events on Mercury. *Icarus*, *300*, 210–222. https://doi.org/10.1016/j.icarus.2017.08.034

Berezhnoy, A. A., & Klumov, B. A. (2008). Impacts as sources of the exosphere on Mercury. *Icarus*, *195*(2), 511–522. https://doi.org/10.1016/j.icarus.2008.01.005

Bida, T. A., & Killen, R. M. (2011). Observations of Al, Fe, and Ca^+ in Mercury's exosphere [Abstract EPSC-DPS2011-1621]. *EPSC-DPS Joint Meeting 2011*, *6*. https://meetingorganizer.copernicus.org/EPSC-DPS2011/EPSC-DPS2011-1621.pdf

Bida, T. A., & Killen, R. M. (2017). Observations of the minor species Al and Fe in Mercury's exosphere. *Icarus*, *289*, 227–238. https://doi.org/10.1016/j.icarus.2016.10.019

Bida, T. A., Killen, R. M., & Morgan, T. H. (2000). Discovery of calcium in Mercury's atmosphere. *Nature*, *404*(6774), 159–161. https://doi.org/10.1038/35004521

Blewett, D. T., Chabot, N. L., Denevi, B. W., Ernst, C. M., Head, J. W., Izenberg, N. R., Murchie, S. L., Solomon, S. C., Nittler, L. R., McCoy, T. J., Xiao, Z., Baker, D. M. H., Fassett, C. I., Braden, S. E., Oberst, J., Scholten, F., Preusker, F., & Hurwitz, D. M. (2011). Hollows on Mercury: MESSENGER Evidence for Geologically Recent Volatile-Related Activity. *Science*, *333*(6051), 1856–1859. https://doi.org/10.1126/science.1211681

Borin, P., Cremonese, G., Marzari, F., Bruno, M., & Marchi, S. (2009). Statistical analysis of micrometeoroids flux on Mercury. *Astronomy and Astrophysics*, *503*(1), 259–264. https://doi.org/10.1051/0004-6361/200912080

Broadfoot, A. L., Kumar, S., Belton, M. J. S., & McElroy, M. B. (1974). Mercury's Atmosphere from Mariner 10: Preliminary Results. *Science*, *185*(4146), 166–169. https://doi.org/10.1126/science.185.4146.166

Broadfoot, A. L., Shemansky, D. E., & Kumar, S. (1976). Mariner 10: Mercury atmosphere. *Geophysical Research Letters*, *3*(10), 577–580. https://doi.org/10.1029/GL003i010p00577

Bunce, E. J., Martindale, A., Lindsay, S., Muinonen, K., Rothery, D. A., Pearson, J., McDonnell, I., Thomas, C., Thornhill, J., Tikkanen, T., Feldman, C., Huovelin, J., Korpela, S., Esko, E., Lehtolainen, A., Treis, J., Majewski, P., Hilchenbach, M., Väisänen, T., ... Yeoman, T. (2020). The BepiColombo Mercury Imaging X-Ray Spectrometer: Science Goals, Instrument Performance and Operations. *Space Science Reviews*, *216*(8), 126. https://doi.org/10.1007/s11214-020-00750-2

Burger, M. H., Killen, R. M., McClintock, W. E., Merkel, A. W., Vervack, R. J., Cassidy, T. A., & Sarantos, M. (2014). Seasonal variations in Mercury's dayside calcium exosphere. *Icarus*, *238*, 51–58. https://doi.org/10.1016/j.icarus.2014.04.049

Burger, M. H., Killen, R. M., McClintock, W. E., Vervack, R. J., Merkel, A. W., Sprague, A. L., & Sarantos, M. (2012). Modeling MESSENGER observations of calcium in Mercury's exosphere. *Journal of Geophysical Research: Planets*, *117*, E00L11. https://doi.org/10.1029/2012JE004158

Burnashev, V. I. (1985). Catalogue of data on energy distribution in spectra of stars in a uniform spectrophotometric system. *Abastumanskaia Astrofizicheskaia Observatoriia Byulleten*, *59*, 83–89.

Byrne, P. K., Klimczak, C., Celâl Şengör, A. M., Solomon, S. C., Watters, T. R., & Hauck, I., Steven A. (2014). Mercury's global contraction much greater than earlier estimates. *Nature Geoscience*, *7*(4), 301–307. https://doi.org/10.1038/ngeo2097

Cassidy, T. A. (2018). Messenger MASCS/UVVS Observations of Cold Exospheric Calcium [Abstract #6108, LPI Contribution No. 2047]. *Mercury: Current and Future Science of the Innermost Planet*. https://www.hou.usra.edu/meetings/mercury2018/pdf/6108.pdf

Cassidy, T. A., Schmidt, C. A., Merkel, A. W., Jasinski, J. M., & Burger, M. H. (2021). Detection of Large Exospheric Enhancements at Mercury due to Meteoroid Impacts. *The Planetary Science Journal*, *2*(5), 175. https://doi.org/10.3847/PSJ/ac1a19

Cassidy, T. A., Merkel, A. W., Burger, M. H., Sarantos, M., Killen, R. M., McClintock, W. E., & Vervack, R. J. (2015). Mercury's seasonal sodium exosphere: MESSENGER orbital observations. *Icarus*, *248*, 547–559. https://doi.org/10.1016/j.icarus.2014.10.037

Cavanaugh, J. F., Smith, J. C., Sun, X., Bartels, A. E., Ramos-Izquierdo, L., Krebs, D. J., McGarry, J. F., Trunzo, R., Novo-Gradac, A. M., Britt, J. L., Karsh, J., Katz, R. B.,

Lukemire, A. T., Szymkiewicz, R., Berry, D. L., Swinski, J. P., Neumann, G. A., Zuber, M. T., & Smith, D. E. (2007). The Mercury Laser Altimeter Instrument for the MESSENGER Mission. *Space Science Reviews*, *131*(1-4), 451–479. https://doi.org/10.1007/s11214-007-9273-4

Chabot, N. L., Ernst, C. M., Denevi, B. W., Nair, H., Deutsch, A. N., Blewett, D. T., Murchie, S. L., Neumann, G. A., Mazarico, E., Paige, D. A., Harmon, J. K., Head, J. W., & Solomon, S. C. (2014). Images of surface volatiles in Mercury's polar craters acquired by the MESSENGER spacecraft. *Geology*, *42*(12), 1051–1054. https://doi.org/10.1130/G35916.1

Chabot, N. L., Ernst, C. M., Denevi, B. W., Harmon, J. K., Murchie, S. L., Blewett, D. T., Solomon, S. C., & Zhong, E. D. (2012). Areas of permanent shadow in Mercury's south polar region ascertained by MESSENGER orbital imaging. *Geophysical Research Letters*, *39*(9), L09204. https://doi.org/10.1029/2012GL051526

Chabot, N. L., Ernst, C. M., Harmon, J. K., Murchie, S. L., Solomon, S. C., Blewett, D. T., & Denevi, B. W. (2013). Craters hosting radar-bright deposits in Mercury's north polar region: Areas of persistent shadow determined from MESSENGER images. *Journal of Geophysical Research: Planets*, *118*(1), 26–36. https://doi.org/10.1029/2012JE004172

Chabot, N. L., Ernst, C. M., Paige, D. A., Nair, H., Denevi, B. W., Blewett, D. T., Murchie, S. L., Deutsch, A. N., Head, J. W., & Solomon, S. C. (2016). Imaging Mercury's polar deposits during MESSENGER's low-altitude campaign. *Geophysical Research Letters*, *43*(18), 9461–9468. https://doi.org/10.1002/2016GL070403

Chamberlain, J. W. (1963). Planetary coronae and atmospheric evaporation. *Planetary and Space Science*, *11*(8), 901–960. https://doi.org/10.1016/0032-0633(63)90122-3

Chassefière, E., Maria, J.-L., Goutail, J.-P., Quémerais, E., Leblanc, F., Okano, S., Yoshikawa, I., Korablev, O., Gnedykh, V., Naletto, G., Nicolosi, P., Pelizzo, M.-G., Correia, J.-J., Gallet, S., Hourtoule, C., Mine, P.-O., Montaron, C., Rouanet, N., Rigal, J.-B., … Yan, N. (2010). PHEBUS: A double ultraviolet spectrometer to observe Mercury's exosphere. *Planetary and Space Science*, *58*(1), 201–223. https://doi.org/10.1016/j.pss.2008.05.018

Chaufray, J.-Y., Leblanc, F., Robidel, R., Quémerais, E., & Koutroumpa, D. (2023). Simulation of the Ca emission at Mercury and comparison with the observations by PHEBUS/BepiColombo during the first two flybys, EGU–6164. https://doi.org/10.5194/egusphere-egu23-6164

Chaufray, J.-Y., Leblanc, F., Werner, A. I. E., Modolo, R., & Aizawa, S. (2022). Seasonal variations of Mg and Ca in the exosphere of Mercury. *Icarus*, *384*, 115081. https://doi.org/10.1016/j.icarus.2022.115081

Chaufray, J.-Y., Quémerais, E., Koutroumpa, D., Robidel, R., Leblanc, F., Reberac, A., Yoshikawa, I., Yoshioka, K., Murakami, G., Korablev, O., Belyaev, D., Pelizzo, M. G., & Corso, A. J. (2023). The EUV Reflectance of Mercury's Surface Measured by BepiColombo/PHEBUS. *Journal of Geophysical Research: Planets*, *128*(3), e2022JE007669. https://doi.org/10.1029/2022JE007669

Christou, A. A., Killen, R. M., & Burger, M. H. (2015). The meteoroid stream of comet Encke at Mercury: Implications for MErcury Surface, Space ENvironment, GEochemistry, and Ranging observations of the exosphere. *Geophysical Research Letters*, *42*(18), 7311–7318. https://doi.org/10.1002/2015GL065361

Cintala, M. J. (1992). Impact-induced thermal effects in the lunar and Mercurian regoliths. *Journal of Geophysical Research: Planets*, *97*(E1), 947–973. https://doi.org/10.1029/91JE02207

Coddington, O. M., Richard, E. C., Harber, D., Pilewskie, P., Woods, T. N., Snow, M., Chance, K., Liu, X., & Sun, K. (2023). Version 2 of the TSIS-1 Hybrid Solar Reference Spectrum and Extension to the Full Spectrum. *Earth and Space Science*, *10*(3), e2022EA002637. https://doi.org/10.1029/2022EA002637

Colombo, G. (1965). Rotational Period of the Planet Mercury. *Nature*, *208*(5010), 575. https://doi.org/10.1038/208575a0

Cremonese, G., Capaccioni, F., Capria, M. T., Doressoundiram, A., Palumbo, P., Vincendon, M., Massironi, M., Debei, S., Zusi, M., Altieri, F., Amoroso, M., Aroldi, G., Baroni, M., Barucci, A., Bellucci, G., Benkhoff, J., Besse, S., Bettanini, C., Blecka, M., ... Turrini, D. (2020). SIMBIO-SYS: Scientific Cameras and Spectrometer for the BepiColombo Mission. *Space Science Reviews*, *216*(5), 75. https://doi.org/10.1007/s11214-020-00704-8

Denevi, B. W., Ernst, C. M., Meyer, H. M., Robinson, M. S., Murchie, S. L., Whitten, J. L., Head, J. W., Watters, T. R., Solomon, S. C., Ostrach, L. R., Chapman, C. R., Byrne, P. K., Klimczak, C., & Peplowski, P. N. (2013). The distribution and origin of smooth plains on Mercury. *Journal of Geophysical Research: Planets*, *118*(5), 891–907. https://doi.org/10.1002/jgre.20075

Denevi, B. W., Robinson, M. S., Solomon, S. C., Murchie, S. L., Blewett, D. T., Domingue, D. L., McCoy, T. J., Ernst, C. M., Head, J. W., Watters, T. R., & Chabot, N. L. (2009). The Evolution of Mercury's Crust: A Global Perspective from MESSENGER. *Science*, *324*(5927), 613–618. https://doi.org/10.1126/science.1172226

Dunne, J. A., & Burgess, E. (1978). *The Voyage of Mariner 10: Mission to Venus and Mercury* (Vol. 424).

ESA. (1997). The HIPPARCOS and TYCHO catalogues. *ESA Special Publication*.

Evans, L. G., Peplowski, P. N., McCubbin, F. M., McCoy, T. J., Nittler, L. R., Zolotov, M. Y., Ebel, D. S., Lawrence, D. J., Starr, R. D., Weider, S. Z., & Solomon, S. C. (2015). Chlorine on the surface of Mercury: MESSENGER gamma-ray measurements and implications for the planet's formation and evolution. *Icarus*, *257*, 417–427. https://doi.org/10.1016/j.icarus.2015.04.039

Goldsten, J. O., Rhodes, E. A., Boynton, W. V., Feldman, W. C., Lawrence, D. J., Trombka, J. I., Smith, D. M., Evans, L. G., White, J., Madden, N. W., Berg, P. C., Murphy, G. A., Gurnee, R. S., Strohbehn, K., Williams, B. D., Schaefer, E. D., Monaco, C. A., Cork, C. P., Del Eckels, J., ... Witte, M. C. (2007). The MESSENGER Gamma-Ray and Neutron Spectrometer. *Space Science Reviews*, *131*(1-4), 339–391. https://doi.org/10.1007/s11214-007-9262-7

Harmon, J. K., & Slade, M. A. (1992). Radar Mapping of Mercury: Full-Disk Images and Polar Anomalies. *Science*, *258*(5082), 640–643. https://doi.org/10.1126/science.258.5082.640

Hawkins, S. E., Boldt, J. D., Darlington, E. H., Espiritu, R., Gold, R. E., Gotwols, B., Grey, M. P., Hash, C. D., Hayes, J. R., Jaskulek, S. E., Kardian, C. J., Keller, M. R., Malaret, E. R., Murchie, S. L., Murphy, P. K., Peacock, K., Prockter, L. M., Reiter, R. A., Robinson, M. S., ... Williams, B. D. (2007). The Mercury Dual Imaging System on the MESSENGER Spacecraft. *Space Science Reviews*, *131*(1-4), 247–338. https://doi.org/10.1007/s11214-007-9266-3

Head, J. W., Chapman, C. R., Strom, R. G., Fassett, C. I., Denevi, B. W., Blewett, D. T., Ernst, C. M., Watters, T. R., Solomon, S. C., Murchie, S. L., Prockter, L. M., Chabot, N. L., Gillis-Davis, J. J., Whitten, J. L., Goudge, T. A., Baker, D. M. H., Hurwitz, D. M., Ostrach, L. R., Xiao, Z., ... Nittler, L. R. (2011). Flood Volcanism in the Northern High Latitudes of Mercury Revealed by MESSENGER. *Science*, *333*(6051), 1853. https://doi.org/10.1126/science.1211997

Head, J. W., Murchie, S. L., Prockter, L. M., Robinson, M. S., Solomon, S. C., Strom, R. G., Chapman, C. R., Watters, T. R., McClintock, W. E., Blewett, D. T., & Gillis-Davis, J. J. (2008). Volcanism on Mercury: Evidence from the First MESSENGER Flyby. *Science*, *321*(5885), 69–72. https://doi.org/10.1126/science.1159256

Heyner, D., Auster, H.-U., Fornaçon, K.-H., Carr, C., Richter, I., Mieth, J. Z. D., Kolhey, P., Exner, W., Motschmann, U., Baumjohann, W., Matsuoka, A., Magnes, W., Berghofer,

G., Fischer, D., Plaschke, F., Nakamura, R., Narita, Y., Delva, M., Volwerk, M., ... Glassmeier, K.-H. (2021). The BepiColombo Planetary Magnetometer MPO-MAG: What Can We Learn from the Hermean Magnetic Field? *Space Science Reviews*, *217*(4), 52. https://doi.org/10.1007/s11214-021-00822-x

Hiesinger, H., Helbert, J., Alemanno, G., Bauch, K. E., D'Amore, M., Maturilli, A., Morlok, A., Reitze, M. P., Stangarone, C., Stojic, A. N., Varatharajan, I., Weber, I., & Mertis Co-I Team. (2020). Studying the Composition and Mineralogy of the Hermean Surface with the Mercury Radiometer and Thermal Infrared Spectrometer (MERTIS) for the BepiColombo Mission: An Update. *Space Science Reviews*, *216*(6), 110. https://doi.org/10.1007/s11214-020-00732-4

Ho, G. C., Krimigis, S. M., Gold, R. E., Baker, D. N., Anderson, B. J., Korth, H., Slavin, J. A., McNutt, J., Ralph L., Winslow, R. M., & Solomon, S. C. (2012). Spatial distribution and spectral characteristics of energetic electrons in Mercury's magnetosphere. *Journal of Geophysical Research: Space Physics*, *117*, A00M04. https://doi.org/10.1029/2012JA017983

Huovelin, J., Vainio, R., Kilpua, E., Lehtolainen, A., Korpela, S., Esko, E., Muinonen, K., Bunce, E., Martindale, A., Grande, M., Andersson, H., Nenonen, S., Lehti, J., Schmidt, W., Genzer, M., Vihavainen, T., Saari, J., Peltonen, J., Valtonen, E., ... Oleynik, P. (2020). Solar Intensity X-Ray and Particle Spectrometer SIXS: Instrument Design and First Results. *Space Science Reviews*, *216*(5), 94. https://doi.org/10.1007/s11214-020-00717-3

Iess, L., Asmar, S. W., Cappuccio, P., Cascioli, G., De Marchi, F., di Stefano, I., Genova, A., Ashby, N., Barriot, J. P., Bender, P., Benedetto, C., Border, J. S., Budnik, F., Ciarcia, S., Damour, T., Dehant, V., Di Achille, G., Di Ruscio, A., Fienga, A., ... Zannoni, M. (2021). Gravity, Geodesy and Fundamental Physics with BepiColombo's MORE Investigation. *Space Science Reviews*, *217*(1), 21. https://doi.org/10.1007/s11214-021-00800-3

Jasinski, J. M., Cassidy, T. A., Raines, J. M., Milillo, A., Regoli, L. H., Dewey, R., Slavin, J. A., Mangano, V., & Murphy, N. (2021). Photoionization Loss of Mercury's Sodium Exosphere: Seasonal Observations by MESSENGER and the THEMIS Telescope. *Geophysical Research Letters*, *48*(8), e2021GL092980. https://doi.org/10.1029/2021GL092980

Kasaba, Y., Bougeret, J.-L., Blomberg, L., Kojima, H., Yagitani, S., Moncuquet, M., Trotignon, J.-G., Chanteur, G., Kumamoto, A., Kasahara, Y., Lichtenberger, J., Omura, Y., Ishisaka, K., & Matsumoto, H. (2010). The Plasma Wave Investigation (PWI) onboard the BepiColombo/MMO: First measurement of electric fields, electromagnetic waves, and radio waves around Mercury. *Planetary and Space Science*, *58*(1), 238–278. https://doi.org/10.1016/j.pss.2008.07.017

Killen, R. M., Shemansky, D., & Mouawad, N. (2009). Expected Emission from Mercury's Exospheric species, and their Ultraviolet-Visible signatures. *The Astrophysical Journal Supplement Series*, *181*(2), 351–359. https://doi.org/10.1088/0067-0049/181/2/351

Killen, R. M. (2016). Pathways for energization of Ca in Mercury's exosphere. *Icarus*, *268*, 32–36. https://doi.org/10.1016/j.icarus.2015.12.035

Killen, R. M., Bida, T. A., & Morgan, T. H. (2005). The calcium exosphere of Mercury. *Icarus*, *173*(2), 300–311. https://doi.org/10.1016/j.icarus.2004.08.022

Killen, R. M., Burger, M. H., Vervack, R. J., & Cassidy, T. A. (2018). Understanding Mercury's Exosphere: Models Derived from MESSENGER Observations. In S. C. Solomon, L. R. Nittler, & B. J. Anderson (Eds.), *Mercury: The view after messenger* (pp. 407–429). Cambridge University Press. https://doi.org/10.1017/9781316650684.016

Killen, R. M., & Hahn, J. M. (2015). Impact vaporization as a possible source of Mercury's calcium exosphere. *Icarus*, *250*, 230–237. https://doi.org/10.1016/j.icarus.2014.11.035

Killen, R. M., Potter, A. E., Vervack, R. J., Bradley, E. T., McClintock, W. E., Anderson, C. M., & Burger, M. H. (2010). Observations of metallic species in Mercury's exosphere. *Icarus*, *209*(1), 75–87. https://doi.org/10.1016/j.icarus.2010.02.018

Kramida, A., Ralchenko, Y., Reader, J., & Team, N. A. (2022). Nist Atomic Spectra Database. https://doi.org/10.18434/T4W30F

Laskar, J. (1989). A numerical experiment on the chaotic behaviour of the Solar System. *Nature*, *338*(6212), 237–238. https://doi.org/10.1038/338237a0

Laskar, J. (1990). The chaotic motion of the solar system: A numerical estimate of the size of the chaotic zones. *Icarus*, *88*(2), 266–291. https://doi.org/10.1016/0019-1035(90)90084-M

Laskar, J. (1994). Large-scale chaos in the solar system. *Astronomy and Astrophysics*, *287*, L9–L12.

Laskar, J. (2008). Chaotic diffusion in the solar system. *Icarus*, *196*(1), 1–15. https://doi.org/10.1016/j.icarus.2008.02.017

Lawrence, D. J., Feldman, W. C., Goldsten, J. O., Maurice, S., Peplowski, P. N., Anderson, B. J., Bazell, D., McNutt, R. L., Nittler, L. R., Prettyman, T. H., Rodgers, D. J., Solomon, S. C., & Weider, S. Z. (2013). Evidence for Water Ice Near Mercury's North Pole from MESSENGER Neutron Spectrometer Measurements. *Science*, *339*(6117), 292. https://doi.org/10.1126/science.1229953

Le Verrier, U. J. (1859). Théorie du mouvement de Mercure. *Annales de l'Observatoire de Paris*, *5*, 1.

Leblanc, F., Oza, A., Leclercq, L., Schmidt, C., Cassidy, T., Modolo, R., Chaufray, J., & Johnson, R. (2017). On the orbital variability of Ganymede's atmosphere. *Icarus*, *293*, 185–198. https://doi.org/10.1016/j.icarus.2017.04.025

Leblanc, F., Chaufray, J.-Y., Doressoundiram, A., Berthelier, J.-J., Mangano, V., López-Ariste, A., & Borin, P. (2013). Mercury exosphere. III: Energetic characterization of its sodium component. *Icarus*, *223*(2), 963–974. https://doi.org/10.1016/j.icarus.2012.08.025

Lee, Y. J., Muñoz, A. G., Yamazaki, A., Quémerais, E., Mottola, S., Hellmich, S., Granzer, T., Bergond, G., Roth, M., Gallego-Cano, E., Chaufray, J.-Y., Robidel, R., Murakami, G., Masunaga, K., Kaplan, M., Erece, O., Hueso, R., Kabàth, P., Špokovà, M., ... Cabrera, J. (2022). Reflectivity of Venus's Dayside Disk During the 2020 Observation Campaign: Outcomes and Future Perspectives. *The Planetary Science Journal*, *3*(9), 209. https://doi.org/10.3847/PSJ/ac84d1

Leinert, C., Richter, I., Pitz, E., & Planck, B. (1981). The zodiacal light from 1.0 to 0.3 A.U. as observed by the HELIOS space probes. *Astronomy and Astrophysics*, *103*(1), 177–188.

Leinert, C., Bowyer, S., Haikala, L. K., Hanner, M. S., Hauser, M. G., Levasseur-Regourd, A.-C., Mann, I., Mattila, K., Reach, W. T., Schlosser, W., Staude, H. J., Toller, G. N., Weiland, J. L., Weinberg, J. L., & Witt, A. N. (1998). The 1997 reference of diffuse night sky brightness. *Astronomy and Astrophysics Supplement Series*, *127*(1), 1–99. https://doi.org/10.1051/aas:1998105

Lierle, P., Schmidt, C., Baumgardner, J., Moore, L., Bida, T. A., & Swindle, R. (2022). The Spatial Distribution and Temperature of Mercury's Potassium Exosphere. *The Planetary Science Journal*, *3*(4), 87. https://doi.org/10.3847/PSJ/ac5c4d

Mangano, V., Milillo, A., Mura, A., Orsini, S., De Angelis, E., Di Lellis, A. M., & Wurz, P. (2007). The contribution of impulsive meteoritic impact vapourization to the Hermean exosphere. *Planetary and Space Science*, *55*(11), 1541–1556. https://doi.org/10.1016/j.pss.2006.10.008

Mangano, V., Dósa, M., Fränz, M., Milillo, A., Oliveira, J. S., Lee, Y. J., McKenna-Lawlor, S., Grassi, D., Heyner, D., Kozyrev, A. S., Peron, R., Helbert, J., Besse, S., de la Fuente, S., Montagnon, E., Zender, J., Volwerk, M., Chaufray, J.-Y., Slavin, J. A., ... Baumjohann, W. (2021). Bepicolombo Science Investigations During Cruise and Flybys at the Earth,

Venus and Mercury. *Space Science Reviews*, *217*(1), 23. https://doi.org/10.1007/s11214-021-00797-9

Mangano, V., Massetti, S., Milillo, A., Mura, A., Orsini, S., & Leblanc, F. (2013). Dynamical evolution of sodium anisotropies in the exosphere of Mercury. *Planetary and Space Science*, *82-83*, 1–10. https://doi.org/10.1016/j.pss.2013.03.002

Marchi, S., Morbidelli, A., & Cremonese, G. (2005). Flux of meteoroid impacts on Mercury. *Astronomy & Astrophysics*, *431*(3), 1123–1127. https://doi.org/10.1051/0004-6361:20041800

Mariscal, J.-F., Rouanet, N., Maria, J.-L., Lustrement, B., Bertran, E., Montaron, C., Guignan, G., Reberac, A., Quémerais, E., Zuppella, P., Pelizzo, M. G., Corso, A. J., Yoshikawa, I., Yoshioka, K., & Murakami, G. (2019). PHEBUS UV spectrometer on board ESA-BepiColombo Mission: Instrument design & performance results. *International Conference on Space Optics — ICSO 2018*. https://doi.org/10.1117/12.2536020

McAdams, J. V., Moessner, D. P., Williams, K. E., Taylor, A. H., Page, B. R., & O'Shaughnessy, D. J. (2011). Messenger - Six Primary Maneuvers, Six Planetary Flybys, and 6.6 Years to Mercury Orbit. *Astrodynamics 2011: Pt III, Advances in the Astronautical Sciences*, *142*, 2191–2209.

McClintock, W. E., Bradley, E. T., Vervack, R. J., Killen, R. M., Sprague, A. L., Izenberg, N. R., & Solomon, S. C. (2008). Mercury's Exosphere: Observations During MESSENGER's First Mercury Flyby. *Science*, *321*(5885), 92–94. https://doi.org/10.1126/science.1159467

McClintock, W. E., Cassidy, T. A., Merkel, A. W., Killen, R. M., Burger, M. H., & Vervack, R. J. (2018). Observations of Mercury's Exosphere: Composition and Structure. In S. C. Solomon, L. R. Nittler, & B. J. Anderson (Eds.), *Mercury: The view after messenger* (pp. 371–406). Cambridge University Press. https://doi.org/10.1017/9781316650684.015

McClintock, W. E., & Lankton, M. R. (2007). The Mercury Atmospheric and Surface Composition Spectrometer for the MESSENGER Mission. *Space Science Reviews*, *131*(1-4), 481–521. https://doi.org/10.1007/s11214-007-9264-5

McClintock, W. E., Vervack, R. J., Bradley, E. T., Killen, R. M., Mouawad, N., Sprague, A. L., Burger, M. H., Solomon, S. C., & Izenberg, N. R. (2009). MESSENGER Observations of Mercury's Exosphere: Detection of Magnesium and Distribution of Constituents. *Science*, *324*(5927), 610–613. https://doi.org/10.1126/science.1172525

Merkel, A. W., Cassidy, T. A., Vervack, R. J., McClintock, W. E., Sarantos, M., Burger, M. H., & Killen, R. M. (2017). Seasonal variations of Mercury's magnesium dayside exosphere from MESSENGER observations. *Icarus*, *281*, 46–54. https://doi.org/10.1016/j.icarus.2016.08.032

Milillo, A., Mangano, V., Massetti, S., Mura, A., Plainaki, C., Alberti, T., Ippolito, A., Ivanovski, S. L., Aronica, A., De Angelis, E., Kazakov, A., Noschese, R., Orsini, S., Rispoli, R., Sordini, R., & Vertolli, N. (2021). Exospheric Na distributions along the Mercury orbit with the THEMIS telescope. *Icarus*, *355*, 114179. https://doi.org/10.1016/j.icarus.2020.114179

Minovitch, M. A., Laboratory (U.S.), J. P., Aeronautics, U. S. N., & Administration, S. (1963). *The Determination and Characteristics of Ballistic Interplanetary Trajectories Under the Influence of Multiple Planetary Attractions*. Jet Propulsion Laboratory, California Institute of Technology.

Mitrofanov, I. G., Kozyrev, A. S., Lisov, D. I., Litvak, M. L., Malakhov, A. A., Mokrousov, M. I., Benkhoff, J., Owens, A., Schulz, R., & Quarati, F. (2021). The Mercury Gamma-Ray and Neutron Spectrometer (MGNS) Onboard the Mercury Planetary Orbiter of the BepiColombo Mission: Design Updates and First Measurements in Space. *Space Science Reviews*, *217*(5), 67. https://doi.org/10.1007/s11214-021-00842-7

Moroni, M., Mura, A., Milillo, A., Plainaki, C., Mangano, V., Alberti, T., Andre, N., Aronica, A., De Angelis, E., Del Moro, D., Kazakov, A., Massetti, S., Orsini, S., Rispoli, R., & Sordini, R. (2023). Micro-meteoroids impact vaporization as source for Ca and CaO exosphere along Mercury's orbit. *Icarus*, *401*, 115616. https://doi.org/10.1016/j.icarus.2023.115616

Murakami, G., Hayakawa, H., Ogawa, H., Matsuda, S., Seki, T., Kasaba, Y., Saito, Y., Yoshikawa, I., Kobayashi, M., Baumjohann, W., Matsuoka, A., Kojima, H., Yagitani, S., Moncuquet, M., Wahlund, J.-E., Delcourt, D., Hirahara, M., Barabash, S., Korablev, O., & Fujimoto, M. (2020). Mio—First Comprehensive Exploration of Mercury's Space Environment: Mission Overview. *Space Science Reviews*, *216*(7), 113. https://doi.org/10.1007/s11214-020-00733-3

Murchie, S. L., Klima, R. L., Denevi, B. W., Ernst, C. M., Keller, M. R., Domingue, D. L., Blewett, D. T., Chabot, N. L., Hash, C. D., Malaret, E., Izenberg, N. R., Vilas, F., Nittler, L. R., Gillis-Davis, J. J., Head, J. W., & Solomon, S. C. (2015). Orbital multispectral mapping of Mercury with the MESSENGER Mercury Dual Imaging System: Evidence for the origins of plains units and low-reflectance material. *Icarus*, *254*, 287–305. https://doi.org/10.1016/j.icarus.2015.03.027

Murchie, S. L., Vervack, R. J., Ernst, C. M., & Strom, R. G. (2014). Chapter 13 - Mercury. In T. Spohn, D. Breuer, & T. V. Johnson (Eds.), *Encyclopedia of the Solar System (Third Edition)* (Third Edition, pp. 283–304). Elsevier. https://doi.org/10.1016/B978-0-12-415845-0.00013-X

Murchie, S. L., Watters, T. R., Robinson, M. S., Head, J. W., Strom, R. G., Chapman, C. R., Solomon, S. C., McClintock, W. E., Prockter, L. M., Domingue, D. L., & Blewett, D. T. (2008). Geology of the Caloris Basin, Mercury: A View from MESSENGER. *Science*, *321*(5885), 73–76. https://doi.org/10.1126/science.1159261

Murray, B. C., Strom, R. G., Trask, N. J., & Gault, D. E. (1975). Surface history of Mercury: Implications for terrestrial planets. *Journal of Geophysical Research*, *80*(B17), 2508–2514. https://doi.org/10.1029/JB080i017p02508

Murray, B. C., Belton, M. J. S., Danielson, G. E., Davies, M. E., Gault, D. E., Hapke, B., O'Leary, B., Strom, R. G., Suomi, V., & Trask, N. (1974). Mercury's Surface: Preliminary Description and Interpretation from Mariner 10 Pictures. *Science*, *185*(4146), 169–179. https://doi.org/10.1126/science.185.4146.169

Ness, N. F., Behannon, K. W., Lepping, R. P., & Whang, Y. C. (1975). The magnetic field of Mercury, 1. *Journal of Geophysical Research*, *80*(19), 2708–2716. https://doi.org/10.1029/JA080i019p02708

Ness, N. F., Behannon, K. W., Lepping, R. P., & Whang, Y. C. (1976). Observations of Mercury's Magnetic Field. *Icarus*, *28*(4), 479–488. https://doi.org/10.1016/0019-1035(76)90121-4

Ness, N. F., Behannon, K. W., Lepping, R. P., Whang, Y. C., & Schatten, K. H. (1974). Magnetic Field Observations near Mercury: Preliminary Results from Mariner 10. *Science*, *185*(4146), 151–160. https://doi.org/10.1126/science.185.4146.151

Neumann, G. A., Cavanaugh, J. F., Sun, X., Mazarico, E. M., Smith, D. E., Zuber, M. T., Mao, D., Paige, D. A., Solomon, S. C., Ernst, C. M., & Barnouin, O. S. (2013). Bright and Dark Polar Deposits on Mercury: Evidence for Surface Volatiles. *Science*, *339*(6117), 296. https://doi.org/10.1126/science.1229764

Nittler, L. R., Starr, R. D., Weider, S. Z., McCoy, T. J., Boynton, W. V., Ebel, D. S., Ernst, C. M., Evans, L. G., Goldsten, J. O., Hamara, D. K., Lawrence, D. J., McNutt, R. L., Schlemm, C. E., Solomon, S. C., & Sprague, A. L. (2011). The Major-Element Composition of Mercury's Surface from MESSENGER X-ray Spectrometry. *Science*, *333*(6051), 1847–1850. https://doi.org/10.1126/science.1211567

Nogami, K., Fujii, M., Ohashi, H., Miyachi, T., Sasaki, S., Hasegawa, S., Yano, H., Shibata, H., Iwai, T., Minami, S., Takechi, S., Grün, E., & Srama, R. (2010). Development of the

Mercury dust monitor (MDM) onboard the BepiColombo mission. *Planetary and Space Science*, *58*(1), 108–115. https://doi.org/10.1016/j.pss.2008.08.016

Ogilvie, K. W., Scudder, J. D., Hartle, R. E., Siscoe, G. L., Bridge, H. S., Lazarus, A. J., Asbridge, J. R., Bame, S. J., & Yeates, C. M. (1974). Observations at Mercury Encounter by the Plasma Science Experiment on Mariner 10. *Science*, *185*(4146), 145–151. https://doi.org/10.1126/science.185.4146.145

Orsini, S., Livi, S. A., Lichtenegger, H., Barabash, S., Milillo, A., De Angelis, E., Phillips, M., Laky, G., Wieser, M., Olivieri, A., Plainaki, C., Ho, G., Killen, R. M., Slavin, J. A., Wurz, P., Berthelier, J.-J., Dandouras, I., Kallio, E., McKenna-Lawlor, S., … Zampieri, S. (2021). SERENA: Particle Instrument Suite for Determining the Sun-Mercury Interaction from BepiColombo. *Space Science Reviews*, *217*(1), 11. https://doi.org/10.1007/s11214-020-00787-3

Orsini, S., Mangano, V., Milillo, A., Plainaki, C., Mura, A., Raines, J. M., De Angelis, E., Rispoli, R., Lazzarotto, F., & Aronica, A. (2018). Mercury sodium exospheric emission as a proxy for solar perturbations transit. *Scientific Reports*, *8*(1), 928. https://doi.org/10.1038/s41598-018-19163-x

Oza, A. V., Leblanc, F., Johnson, R. E., Schmidt, C., Leclercq, L., Cassidy, T. A., & Chaufray, J.-Y. (2019). Dusk over dawn O_2 asymmetry in Europa's near-surface atmosphere. *Planetary and Space Science*, *167*, 23–32. https://doi.org/10.1016/j.pss.2019.01.006

Paige, D. A., Siegler, M. A., Harmon, J. K., Neumann, G. A., Mazarico, E. M., Smith, D. E., Zuber, M. T., Harju, E., Delitsky, M. L., & Solomon, S. C. (2013). Thermal Stability of Volatiles in the North Polar Region of Mercury. *Science*, *339*(6117), 300. https://doi.org/10.1126/science.1231106

Paige, D. A., Wood, S. E., & Vasavada, A. R. (1992). The thermal stability of water ice at the poles of Mercury. *Science*, *258*(5082), 643–646. https://doi.org/10.1126/science.258.5082.643

Peplowski, P. N., Lawrence, D. J., Evans, L. G., Klima, R. L., Blewett, D. T., Goldsten, J. O., Murchie, S. L., McCoy, T. J., Nittler, L. R., Solomon, S. C., Starr, R. D., & Weider, S. Z. (2015). Constraints on the abundance of carbon in near-surface materials on Mercury: Results from the MESSENGER Gamma-Ray Spectrometer. *Planetary and Space Science*, *108*, 98–107. https://doi.org/10.1016/j.pss.2015.01.008

Peplowski, P. N., Lawrence, D. J., Feldman, W. C., Goldsten, J. O., Bazell, D., Evans, L. G., Head, J. W., Nittler, L. R., Solomon, S. C., & Weider, S. Z. (2015). Geochemical terranes of Mercury's northern hemisphere as revealed by MESSENGER neutron measurements. *Icarus*, *253*, 346–363. https://doi.org/10.1016/j.icarus.2015.02.002

Peplowski, P. N., Lawrence, D. J., Rhodes, E. A., Sprague, A. L., McCoy, T. J., Denevi, B. W., Evans, L. G., Head, J. W., Nittler, L. R., Solomon, S. C., Stockstill-Cahill, K. R., & Weider, S. Z. (2012). Variations in the abundances of potassium and thorium on the surface of Mercury: Results from the MESSENGER Gamma-Ray Spectrometer. *Journal of Geophysical Research: Planets*, *117*, E00L04. https://doi.org/10.1029/2012JE004141

Pfleger, M., Lichtenegger, H. I. M., Wurz, P., Lammer, H., Kallio, E., Alho, M., Mura, A., McKenna-Lawlor, S., & Martín-Fernández, J. A. (2015). 3D-modeling of Mercury's solar wind sputtered surface-exosphere environment. *Planetary and Space Science*, *115*, 90–101. https://doi.org/10.1016/j.pss.2015.04.016

Plainaki, C., Mura, A., Milillo, A., Orsini, S., Livi, S., Mangano, V., Massetti, S., Rispoli, R., & De Angelis, E. (2017). Investigation of the possible effects of comet Encke's meteoroid stream on the Ca exosphere of Mercury. *Journal of Geophysical Research: Planets*, *122*(6), 1217–1226. https://doi.org/10.1002/2017JE005304

Pokorný, P., Sarantos, M., & Janches, D. (2018). A Comprehensive Model of the Meteoroid Environment around Mercury. *The Astrophysical Journal*, *863*(1), 31. https://doi.org/10.3847/1538-4357/aad051

Potter, A. E., Killen, R. M., & Morgan, T. H. (2002). The sodium tail of Mercury. *Meteoritics & Planetary Science*, *37*(9), 1165–1172. https://doi.org/10.1111/j.1945-5100.2002.tb00886.x

Potter, A. E., Killen, R. M., & Morgan, T. H. (2007). Solar radiation acceleration effects on Mercury sodium emission. *Icarus*, *186*(2), 571–580. https://doi.org/10.1016/j.icarus.2006.09.025

Potter, A. E., & Morgan, T. H. (1985). Discovery of Sodium in the Atmosphere of Mercury. *Science*, *229*(4714), 651–653. https://doi.org/10.1126/science.229.4714.651

Potter, A. E., & Morgan, T. H. (1986). Potassium in the atmosphere of Mercury. *Icarus*, *67*(2), 336–340. https://doi.org/10.1016/0019-1035(86)90113-2

Potter, A. E., & Morgan, T. H. (1997). Sodium and potassium atmospheres of Mercury. *Planetary and Space Science*, *45*(1), 95–100. https://doi.org/10.1016/S0032-0633(96)00100-6

Quémerais, E., Chaufray, J.-Y., Koutroumpa, D., Leblanc, F., Reberac, A., Lustrement, B., Montaron, C., Mariscal, J.-F., Rouanet, N., Yoshikawa, I., Murakami, G., Yoshioka, K., Korablev, O., Belyaev, D., Pelizzo, M. G., Corso, A., & Zuppella, P. (2020). PHEBUS on Bepi-Colombo: Post-launch Update and Instrument Performance. *Space Science Reviews*, *216*(4), 67. https://doi.org/10.1007/s11214-020-00695-6

Quémerais, E., Koutroumpa, D., Lallement, R., Sandel, B. R., Robidel, R., Chaufray, J.-Y., Reberac, A., Leblanc, F., Yoshikawa, I., Yoshioka, K., Murakami, G., Korablev, O., Belyaev, D., Pelizzo, M. G., & Corso, A. J. (2023). Observation of Helium in Mercury's Exosphere by PHEBUS on Bepi-Colombo. *Journal of Geophysical Research: Planets*, *128*(6), e2023JE007743. https://doi.org/https://doi.org/10.1029/2023JE007743

Raines, J. M., Gershman, D. J., Zurbuchen, T. H., Sarantos, M., Slavin, J. A., Gilbert, J. A., Korth, H., Anderson, B. J., Gloeckler, G., Krimigis, S. M., Baker, D. N., McNutt Jr., R. L., & Solomon, S. C. (2013). Distribution and compositional variations of plasma ions in Mercury's space environment: The first three Mercury years of MESSENGER observations. *Journal of Geophysical Research: Space Physics*, *118*(4), 1604–1619. https://doi.org/10.1029/2012JA018073

Robinson, M. S., & Lucey, P. G. (1997). Recalibrated Mariner 10 Color Mosaics: Implications for Mercurian Volcanism. *Science*, *275*(5297), 197–200. https://doi.org/10.1126/science.275.5297.197

Robinson, M. S., Murchie, S. L., Blewett, D. T., Domingue, D. L., Hawkins, S. E., Head, J. W., Holsclaw, G. M., McClintock, W. E., McCoy, T. J., McNutt, R. L., Prockter, L. M., Solomon, S. C., & Watters, T. R. (2008). Reflectance and Color Variations on Mercury: Regolith Processes and Compositional Heterogeneity. *Science*, *321*(5885), 66–69. https://doi.org/10.1126/science.1160080

Rodriguez, J. A. P., Leonard, G. J., Kargel, J. S., Domingue, D., Berman, D. C., Banks, M., Zarroca, M., Linares, R., Marchi, S., Baker, V. R., Webster, K. D., & Sykes, M. (2020). The Chaotic Terrains of Mercury Reveal a History of Planetary Volatile Retention and Loss in the Innermost Solar System. *Scientific Reports*, *10*, 4737. https://doi.org/10.1038/s41598-020-59885-5

Saito, Y., Sauvaud, J., Hirahara, M., Barabash, S., Delcourt, D., Takashima, T., & Asamura, K. (2010). Scientific objectives and instrumentation of Mercury Plasma Particle Experiment (MPPE) onboard MMO. *Planetary and Space Science*, *58*(1), 182–200. https://doi.org/10.1016/j.pss.2008.06.003

Santoli, F., Fiorenza, E., Lefevre, C., Lucchesi, D. M., Lucente, M., Magnafico, C., Morbidini, A., Peron, R., & Iafolla, V. (2020). ISA, a High Sensitivity Accelerometer in the Interplanetary Space. *Space Science Reviews*, *216*(8), 145. https://doi.org/10.1007/s11214-020-00768-6

Schlemm, C. E., Starr, R. D., Ho, G. C., Bechtold, K. E., Hamilton, S. A., Boldt, J. D., Boynton, W. V., Bradley, W., Fraeman, M. E., Gold, R. E., Goldsten, J. O., Hayes, J. R., Jaskulek,

S. E., Rossano, E., Rumpf, R. A., Schaefer, E. D., Strohbehn, K., Shelton, R. G., Thompson, R. E., ... Williams, B. D. (2007). The X-Ray Spectrometer on the MESSENGER Spacecraft. *Space Science Reviews*, *131*(1-4), 393–415. https://doi.org/10.1007/s11214-007-9248-5

Simpson, J. A., Eraker, J. H., Lamport, J. E., & Walpole, P. H. (1974). Electrons and Protons Accelerated in Mercury's Magnetic Field. *Science*, *185*(4146), 160–166. https://doi.org/10.1126/science.185.4146.160

Slade, M. A., Butler, B. J., & Muhleman, D. O. (1992). Mercury Radar Imaging: Evidence for Polar Ice. *Science*, *258*(5082), 635–640. https://doi.org/10.1126/science.258.5082.635

Slavin, J. A., Anderson, B. J., Baker, D. N., Benna, M., Boardsen, S. A., Gold, R. E., Ho, G. C., Imber, S. M., Korth, H., Krimigis, S. M., McNutt Jr., R. L., Raines, J. M., Sarantos, M., Schriver, D., Solomon, S. C., Trávníček, P., & Zurbuchen, T. H. (2012). MESSENGER and Mariner 10 flyby observations of magnetotail structure and dynamics at Mercury. *Journal of Geophysical Research: Space Physics*, *117*(A1). https://doi.org/10.1029/2011JA016900

Solomon, S. C., & Anderson, B. J. (2018). The MESSENGER Mission: Science and Implementation Overview. In S. C. Solomon, L. R. Nittler, & B. J. Anderson (Eds.), *Mercury: The View after MESSENGER* (pp. 1–29). Cambridge University Press. https://doi.org/10.1017/9781316650684.002

Solomon, S. C., McNutt, R. L., Gold, R. E., Acuña, M. H., Baker, D. N., Boynton, W. V., Chapman, C. R., Cheng, A. F., Gloeckler, G., Head III, J. W., Krimigis, S. M., McClintock, W. E., Murchie, S. L., Peale, S. J., Phillips, R. J., Robinson, M. S., Slavin, J. A., Smith, D. E., Strom, R. G., ... Zuber, M. T. (2001). The MESSENGER mission to Mercury: Scientific objectives and implementation. *Planetary and Space Science*, *49*(14), 1445–1465. https://doi.org/10.1016/S0032-0633(01)00085-X

Solomon, S. C., McNutt, R. L., Gold, R. E., & Domingue, D. L. (2007). Messenger Mission Overview. *Space Science Reviews*, *131*(1-4), 3–39. https://doi.org/10.1007/s11214-007-9247-6

Srinivasan, D. K., Perry, M. E., Fielhauer, K. B., Smith, D. E., & Zuber, M. T. (2007). The Radio Frequency Subsystem and Radio Science on the MESSENGER Mission. *Space Science Reviews*, *131*(1-4), 557–571. https://doi.org/10.1007/s11214-007-9270-7

Strom, R. G. (1977). Origin and relative age of lunar and Mercurian intercrater plains. *Physics of the Earth and Planetary Interiors*, *15*(2-3), 156–172. https://doi.org/10.1016/0031-9201(77)90028-0

Strom, R. G., Trask, N. J., & Guest, J. E. (1975). Tectonism and volcanism on Mercury. *Journal of Geophysical Research*, *80*(17), 2478–2507. https://doi.org/10.1029/JB080i017p02478

Strom, R. G., Murray, B. C., Belton, M. J. S., Danielson, G. E., Davies, M. E., Gault, D. E., Hapke, B., O'Leary, B., Trask, N., Guest, J. E., Anderson, J., & Klaasen, K. (1975). Preliminary imaging results from the second Mercury encounter. *Journal of Geophysical Research*, *80*(17), 2345–2356. https://doi.org/10.1029/JB080i017p02345

Sturms, F. M., & Cutting, E. (1966). Trajectory analysis of a 1970 mission to Mercury via a close encounter with Venus. *Journal of Spacecraft and Rockets*, *3*(5), 624–631. https://doi.org/10.2514/3.28505

Thomas, N., Hussmann, H., Spohn, T., Lara, L. M., Christensen, U., Affolter, M., Bandy, T., Beck, T., Chakraborty, S., Geissbuehler, U., Gerber, M., Ghose, K., Gouman, J., HosseiniArani, S., Kuske, K., Peteut, A., Piazza, D., Rieder, M., Servonet, A., ... Metz, B. (2021). The BepiColombo Laser Altimeter. *Space Science Reviews*, *217*(1), 25. https://doi.org/10.1007/s11214-021-00794-y

Vervack, R. J., Hurley, D. M., Pryor, W., & Killen, R. M. (2018). MESSENGER Orbital Observations of Mercury's Hydrogen Exosphere [Abstract #6025, LPI Contribution No.

2047]. *Mercury: Current and Future Science of the Innermost Planet*. https://www.hou.usra.edu/meetings/mercury2018/pdf/6025.pdf

Vervack, R. J., Killen, R. M., McClintock, W. E., Merkel, A. W., Burger, M. H., Cassidy, T. A., & Sarantos, M. (2016). New discoveries from MESSENGER and insights into Mercury's exosphere. *Geophysical Research Letters*, *43*(22), 11, 545–11, 551. https://doi.org/10.1002/2016GL071284

Vervack, R. J., McClintock, W. E., Killen, R. M., Sprague, A. L., Anderson, B. J., Burger, M. H., Bradley, E. T., Mouawad, N., Solomon, S. C., & Izenberg, N. R. (2010). Mercury's Complex Exosphere: Results from MESSENGER's Third Flyby. *Science*, *329*(5992), 672–675. https://doi.org/10.1126/science.1188572

Watters, T. R., Solomon, S. C., Robinson, M. S., Head, J. W., André, S. L., Hauck, S. A., & Murchie, S. L. (2009). The tectonics of Mercury: The view after MESSENGER's first flyby. *Earth and Planetary Science Letters*, *285*(3-4), 283–296. https://doi.org/10.1016/j.epsl.2009.01.025

Weider, S. Z., Nittler, L. R., Starr, R. D., Crapster-Pregont, E. J., Peplowski, P. N., Denevi, B. W., Head, J. W., Byrne, P. K., Hauck, S. A., Ebel, D. S., & Solomon, S. C. (2015). Evidence for geochemical terranes on Mercury: Global mapping of major elements with MESSENGER's X-Ray Spectrometer. *Earth and Planetary Science Letters*, *416*, 109–120. https://doi.org/10.1016/j.epsl.2015.01.023

Wilhelms, D. E. (1976). Mercurian Volcanism Questioned. *Icarus*, *28*(4), 551–558. https://doi.org/10.1016/0019-1035(76)90128-7

Winkler, J. R. (1993). Numerical recipes in C: The art of scientific computing, second edition. *Endeavour*, *17*(4), 201. https://doi.org/10.1016/0160-9327(93)90069-F

Wurz, P., Fatemi, S., Galli, A., Halekas, J., Harada, Y., Jäggi, N., Jasinski, J., Lammer, H., Lindsay, S., Nishino, M. N., Orlando, T. M., Raines, J. M., Scherf, M., Slavin, J., Vorburger, A., & Winslow, R. (2022). Particles and Photons as Drivers for Particle Release from the Surfaces of the Moon and Mercury. *Space Science Reviews*, *218*(3), 10. https://doi.org/10.1007/s11214-022-00875-6

Wurz, P., Whitby, J. A., Rohner, U., Martín-Fernández, J. A., Lammer, H., & Kolb, C. (2010). Self-consistent modelling of Mercury's exosphere by sputtering, micro-meteorite impact and photon-stimulated desorption. *Planetary and Space Science*, *58*(12), 1599–1616. https://doi.org/10.1016/j.pss.2010.08.003

Yakshinskiy, B. V., Madey, T. E., & Ageev, V. N. (2000). Thermal desorption of sodium atoms from thin SiO_2 films. *Surface Review and Letters*, *7*, 75–87. https://doi.org/10.1142/S0218625X00000117

Yen, C.-W. L. (1989). Ballistic Mercury orbiter mission via Venus and Mercury gravity assists. *Journal of the Astronautical Sciences*, *37*, 417–432.

Yoshikawa, I., Korablev, O., Kameda, S., Rees, D., Nozawa, H., Okano, S., Gnedykh, V., Kottsov, V., Yoshioka, K., Murakami, G., Ezawa, F., & Cremonese, G. (2010). The Mercury sodium atmospheric spectral imager for the MMO spacecraft of Bepi-Colombo. *Planetary and Space Science*, *58*(1), 224–237. https://doi.org/10.1016/j.pss.2008.07.008